

TECHNOLOGIES TO ENHANCE THE OPERATION OF EXISTING NATURAL GAS COMPRESSION INFRASTRUCTURE

**FINAL REPORT
SwRI® Project No. 18.06223
DOE Award No. DE-FC26-02NT41646**

**Reporting Period
October 1, 2002 – February 28, 2006**

Prepared by

**Anthony J. Smalley
Ralph E. Harris
Gary D. Bourn
Ford A. Phillips
Danny M. Deffenbaugh**

Prepared for

**U.S. Department of Energy
National Energy Technology Laboratory
3610 Collins Ferry Road
P.O. Box 880
Morgantown, WV 26507-0880**

May 31, 2006



SOUTHWEST RESEARCH INSTITUTE®

This page left intentionally blank.

SOUTHWEST RESEARCH INSTITUTE®
6220 Culebra Road
San Antonio, Texas 78238

TECHNOLOGIES TO ENHANCE THE OPERATION OF EXISTING NATURAL GAS COMPRESSION INFRASTRUCTURE

FINAL REPORT
SwRI® Project No. 18.06223
DOE Award No. DE-FC26-02NT41646

Reporting Period
October 1, 2002 – February 28, 2006

Prepared by

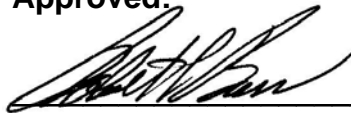
Anthony J. Smalley
Ralph E. Harris
Gary D. Bourn
Ford A. Phillips
Danny M. Deffenbaugh

Prepared for

U.S. Department of Energy
National Energy Technology Laboratory
3610 Collins Ferry Road
P.O. Box 880
Morgantown, WV 26507-0880

May 31, 2006

Approved:



Robert L. Bass, Vice President
Mechanical and Materials Engineering



SOUTHWEST RESEARCH INSTITUTE®

DISCLAIMER

This report was prepared as an account of work sponsored by an agency of the United States Government. Neither the United States nor any agency thereof, nor any of their employees, makes any warranty, express or implied, or assumes any legal liability or responsibility for the accuracy, completeness, or usefulness of any information, apparatus, product, or process disclosed, or represents that its use would not infringe privately owned rights. Reference herein to any specific commercial product, process, or service by trade name, trademark, manufacturer, or otherwise does not necessarily constitute or imply its endorsement, recommendation, or favoring by the United States Government or any agency thereof. The views and opinions of authors expressed herein do not necessarily state or reflect those of the United States Government or any agency thereof.

TABLE OF CONTENTS

<u>Section</u>	<u>Page</u>
1. EXECUTIVE SUMMARY	1
2. INTRODUCTION	3
2.1 The U.S. Gas Transmission Compression Infrastructure	3
2.2 The Compression Infrastructure Project.....	6
2.3 Project Accomplishment.....	6
2.3.1 Integrity.....	6
2.3.2 Efficiency	6
2.3.3 Capacity	7
2.4 Field Test Program Overview.....	8
2.5 Project Emphasis	8
2.6 Air Imbalance	9
3. EXPERIMENTAL	11
3.1 Overview	11
3.2 Field Test Instrumentation.....	11
3.2.1 Sensors and Data Channels for Field Measurement.....	11
3.2.2 Transducer Installation	13
3.2.3 Field Data System	21
3.2.4 Selection of Test Engine Models for Field Testing	22
3.3 Air Balance Facilities	23
3.3.1 GMVH-6 Test Bed	23
3.3.2 Cylinder Flow Test Rig	30
3.3.3 Computational Model	32
4. RESULTS AND DISCUSSION: CHARACTERISTICS, METHODS, NEEDS, TECHNOLOGIES	33
4.1 Section Overview	33
4.2 Characteristics of Integral Engine Compressors	33
4.2.1 Cylinder-to-Cylinder Combustion Imbalance	33
4.2.2 Cycle-to-Cycle Combustion Variability	37
4.2.3 Cylinder-to-Cylinder Air Imbalance.....	39
4.2.4 Cycle-to-Cycle Air Imbalance	41
4.2.5 Dynamic Variability in Manifold Pressures	42
4.2.6 Variability in Equivalence Ratio	44
4.2.7 Influence of Load on Heat rate	45
4.2.8 Influence of Timing on Heat Rate	46
4.2.9 Influence of Timing on Crank Strain	48
4.2.10 Influence of Combustion Balancing on Engine Heat Rate.....	48
4.2.11 Influence of Combustion Balancing on Crank Strain	51
4.2.12 System-Wide Variation in Compressor Efficiency	51
4.2.13 Mechanical Efficiency	52
4.2.14 Installation Losses.....	54

TABLE OF CONTENTS (Cont'd)

<u>Section</u>		<u>Page</u>
	4.2.15 System Thermal Efficiency	54
	4.2.16 Capacity	56
	4.2.17 Observed Influence of Time from a Cold Start on Power Transmission Efficiency.....	57
	4.2.18 Pulsations from Reciprocating Compressor Action	58
	4.2.19 Speed/Power Modulation (Multiple Compressors “Beating” Against Each Other)	60
	4.2.20 Square Law Losses in Valves, Orifices, and Pipe Area Changes	61
4.3	Methods for Testing, Characterization, and Monitoring.....	62
	4.3.1 Suite of Instruments and Data Acquisition System.....	62
	4.3.2 Assessing How Operating Changes Influence Heat Rate Variation with Load	62
	4.3.3 Monitoring Rod Load	63
	4.3.4 Isolating Mechanical Losses with the Rod Load Measurement.....	64
	4.3.5 Monitoring Compressor Cylinder Temperature Rise	67
	4.3.6 Monitoring Frame Vibration	68
	4.3.7 Monitoring Instantaneous Rotational Velocity	69
	4.3.8 Isolating Installation Losses.....	69
	4.3.9 Monitoring Crank Strain.....	72
4.4	Needs (Technology, Data, Methods) of Integral Engine/Compressors	72
	4.4.1 Combustion Balancing	73
	4.4.2 Balanced Air to Each Power Cylinder.....	73
	4.4.3 Accurate Monitoring of Power and Torque	74
	4.4.4 Unit Throughput Monitoring and Measurement	75
	4.4.5 Protection Against the Damage of Detonation	76
	4.4.6 Low Loss Pulsation Control	77
	4.4.7 Capacity and Horsepower Recovery on Low Efficiency Compressors	77
	4.4.8 Refined Knowledge of Mechanical Losses.....	78
4.5	Technologies	78
	4.5.1 Standard Deviation Balancing	78
	4.5.2 Combustion Pressure Ratio Balancing.....	79
	4.5.3 Closed Loop Waste-Gate Control.....	82
	4.5.4 Closed Loop Fuel Rate Control for Carbureted Four-Stroke Engines	84
	4.5.5 Rod Load Monitor	86
	4.5.6 Strain Data Capture Module	87
	4.5.7 High Pressure Fuel Injection	88
	4.5.8 Detonation Detector	90
	4.5.9 Digital Simulation of Interaction Between Compressor and Installed Piping	93

TABLE OF CONTENTS (Cont'd)

<u>Section</u>	<u>Page</u>
4.5.10	Side Branch Absorbers for Pulsation Control 96
4.5.11	In-Line Filter Bottles 97
5.	RESULTS AND DISCUSSION: AIR BALANCE STUDY 99
5.1	Engine Measurement, Testing, And Simulation 99
5.1.1	The GMVH-6 Engine 99
5.1.2	GMVH-6 Baseline Testing 105
5.1.3	Geometric Analysis 110
5.1.4	Port Flow Testing 124
5.1.5	Computational Modeling 135
5.1.6	GMVH-6 Component Swap Testing 142
5.1.7	Detailed Analysis of Cylinder Pressure Data 144
5.1.8	Investigation of Fuel Valves and Fueling Rate 148
5.2	Conceptual Manifold Designs 151
5.2.1	Individual Tuned Expansion Chamber Concept 152
5.2.2	Multi-Cylinder Coupling Tuned Manifold Concept 154
5.2.3	Exhaust Side Branch Absorber (SBA) 156
5.2.4	Intake Manifold Modifications 160
5.3	EXHAUST SIDE BRANCH ABSORBER DESIGN, CONSTRUCTION, AND VALIDATION TESTING 163
5.4	Component Variability 168
6.	CONCLUSIONS 171
7.	REFERENCES 175
8.	LIST OF ACRONYMS AND ABBREVIATIONS 177

This page left intentionally blank.

LIST OF FIGURES

<u>Figure</u>		<u>Page</u>
Figure 2-1	TLA6 (2,000 HP) and GMW10 (2,500 HP) in Pipeline Service	3
Figure 2-2	Install Dates: Over 50% of Pipeline Compressors Exceed 45 Years Old.....	4
Figure 2-3	Industry Fuel Consumption (~7.7 MCF/HP-Hr ±20% – Need to Lower the High Values).....	4
Figure 2-4	Compressor Thermal Efficiency Histogram Based on GMRC Survey.....	5
Figure 2-5	Integrity: Crankshaft Failure Examples – Need Methods of Avoidance	5
Figure 3-1	Compressor Cylinder and Pressure Transducers on Each End (Williams’ Station 40 (Sour Lake); August 2003)	14
Figure 3-2	Details of Power Cylinder Pressure Transducer Installation (Williams’ Station 40 (Sour Lake); August 2003)	14
Figure 3-3	Initial Site Test Showing Air Manifold Sensor (HBA-6T; TGP Kinder Station (El Paso Station 823); April 2003).....	15
Figure 3-4	Pressure Transducer in Air Intake Manifold (GMW10; Williams’ Station 40 (Sour Lake); August 2003)	15
Figure 3-5	Pressure Transducer in Exhaust Manifold (GMW10; Williams’ Station 40 (Sour Lake); August 2003)	16
Figure 3-6	Encoder, Outboard of Flywheel on Mounting Tripod (GMW10; Williams’ Station 40 (Sour Lake); August 2003)	16
Figure 3-7	Detailed View of Encoder and Connection to Flywheel (GMW10; Williams’ Station 40 (Sour Lake); August 2003)	17
Figure 3-8	Accelerometer Mounted on Frame (GMW10; Williams’ Station 40 (Sour Lake); August 2003)	17
Figure 3-9	Strain Data Capture Module Installed (GMW10; Williams’ Station 40 (Sour Lake); August 2003)	18
Figure 3-10	SDCM Installation for Crankshaft Strain Measurements (HBA-6T; Kinder Station (El Paso Station 823); April 2003).....	18
Figure 3-11	O ₂ /NO _x Sensor and Connection to Line from Stack (GMW10; Williams’ Station 40 (Sour Lake); August 2003)	19
Figure 3-12	Installations of the RLM on HBA-6T (April 2003) and GMW10 (August 2003)	19
Figure 3-13	Cable from RLM Antenna (GMW10; Williams’ Station 40 (Sour Lake); August 2003).....	20
Figure 3-14	Self-Powered Rod Load Monitor (RLM)	20
Figure 3-15	Fuel Flow Measurement Using Emerson Flobas 103 Transmitter (HBA-6T; Kinder Station (El Paso Station 823); April 2004)	21
Figure 3-16	Front View of Field Data Acquisition System (DAS).....	21
Figure 3-17	Rear View of Field Data Acquisition System (DAS)	22
Figure 3-18	Photograph of GMVH-6 Laboratory Research Engine	24
Figure 3-19	Photograph of Dynamic Pressure Sensor Installation for Engine Cylinder	25
Figure 3-20	Photograph of Dynamic Exhaust Pressure Sensor in Exhaust Runner.....	25

LIST OF FIGURES (Cont'd)

<u>Figure</u>		<u>Page</u>
Figure 3-21	Comparison of Dynamic Exhaust Pressure Sensor to Kistler Piezo-Resistive Sensor at End of Measurement Channel in Exhaust Runner	26
Figure 3-22	Comparison of FFT-Filtered Dynamic Exhaust Pressure Sensor to Flush-Mounted Kistler Piezo-Resistive Sensor in Exhaust Runner	26
Figure 3-23	Photograph of Dynamic Exhaust Pressure Sensor in Exhaust Manifold	28
Figure 3-24	Photograph of Dynamic Intake Pressure Sensor in Intake Manifold	28
Figure 3-25	Photograph of Pitot Tubes in Cylinder 1L Intake Runner	29
Figure 3-26	Photographs of GMVH Cylinder Flow Bench	31
Figure 3-27	Virtual Two-Stroke Computational Model Schematic of GMVH-6	32
Figure 4-1	Pressure Traces for All Six Power Cylinders on an HBA-6T, Pulsating the Average Spread in Peak Pressure (Test #1 at Kinder Station (El Paso Station 823); April 2003).....	35
Figure 4-2	Representative Pressure Data for Ten Power Cylinders; GMW10 with a Turbocharger, High-Pressure Fuel Injection and Automated Peak Pressure Control (Williams' Station 60, Unit 6; August 25, 2004)	36
Figure 4-3	KVG103 – Peak Firing Pressure Averaged for All Cylinders and for Cylinder 10 Alone, with Global Equivalence Ratio Superimposed (Duke Thomaston Station; Wed., Nov. 3, 2004)	36
Figure 4-4	Typical 20 Successive Cycles, Illustrating Cycle-to-Cycle Variation in Peak Pressure for a GMW10 with a Turbocharger and High-Pressure Fuel Injection (Power Cylinder 2; Williams' Station 40 (Sour Lake); August 2003)	37
Figure 4-5	Engine Average Cycle-to-Cycle Standard Deviation in Peak Firing Pressure; and Ratio of Peak Firing Pressure to Compression Pressure (CPR) for an Unmodified GMW10 (Williams' Station 60; February 2004).....	38
Figure 4-6	CPR and Standard Deviation for Peak Firing Pressure; Averaged Across the Six Power Cylinders for a Turbocharged HBA-6T (Kinder (El Paso Station 823); April 21, 2004).....	38
Figure 4-7	Coefficient of Variation for Cycle-to-Cycle Variation in Peak Firing Pressure—Comparison of Five Engines	39
Figure 4-8	Cylinder Pressure 20 Degrees Before TDC (Compression Pressure for HBA-6T) (Kinder Station (El Paso Station 823); April 2003)	40
Figure 4-9	Power Cylinder Compression Pressure for GMW10 with a Turbocharger and High-Pressure Fuel Injection (Williams' Station 40 (Sour Lake); August 2003)	40
Figure 4-10	Power Cylinder Compression Pressure for GMW10; After Modification (Williams' Station 60; August 26, 2004).....	41
Figure 4-11	Mean and Standard Deviation for P20 (Pressure 20 DBTDC) as a Function of Cylinder for GMW10 Unmodified (Williams' Station 60; February 2004).....	42
Figure 4-12	Time and Frequency Modulation of Inlet Air Manifold Pressure; HBA-6T (Kinder Station (El Paso Station 823); April 2003)	42

LIST OF FIGURES (Cont'd)

<u>Figure</u>	<u>Page</u>
Figure 4-13	Variation in Inlet and Exhaust Pressures in a GMW10 with a Turbocharger and High-Pressure Fuel Injection (Williams' Station 40 (Sour Lake); August 2003) 43
Figure 4-14	Inlet Manifold Pressure; Time Wave and Order Spectrum in an Unmodified GMW10 (Williams' Station 60; February 2004)..... 44
Figure 4-15	Variation in Equivalence Ratio in an HBA-6T (Kinder Station (El Paso Station 823); April 2003)..... 44
Figure 4-16	Heat Rate for Days 1 and 2 <i>versus</i> Indicated Compressor Horsepower (IHP) Without Compression Pressure Ratio or Timing Tests or Speed Tests..... 45
Figure 4-17	Heat Rate <i>versus</i> Torque for a GMW10 After Modifications (Williams' Station 60; August 2004)..... 45
Figure 4-18	Normalized Rate of Change of Heat Rate with Load—Comparison for Four Tests 46
Figure 4-19	Heat Rate Tests for a GMW10; Unit 6; After Modifications (Williams' Station 60; August 25, 2004)..... 47
Figure 4-20	Heat Rate <i>versus</i> Timing for a GMW10 After Modifications (Williams' Station 60; August 2004)..... 47
Figure 4-21	Variation in Peak-to-Peak Crankshaft Strain for a Modified GMW10 (Williams' Station 60; February 2004) 48
Figure 4-22	Heat Rate <i>versus</i> Indicated Compressor Horsepower; Series 2 Adds in the CPR Balancing Data, and Series 3 Adds in the Advanced Timing Data for a HBA-6T (Kinder Station (El Paso Station 823); April 22, 2004) 49
Figure 4-23	Instantaneous and Average Spread for HBA-6T (Kinder Station (El Paso Station 823); April 22, 2004)..... 50
Figure 4-24	Heat Rate; Day 2 Tests for a GMW10; Unit 6; After Modification (Williams' Station 60; August 26, 2004)..... 50
Figure 4-25	Peak-to-Peak Dynamic Variation in Crankshaft Microstrain; Unit 6 for a GMW10; After Modification (Williams' Station 60; August 26, 2004)..... 51
Figure 4-26	Compressor Efficiency – Project Summary 52
Figure 4-27	Flow of Power from Fuel to Header, Showing Percentage of Fuel Power on Each Column; Losses Stated in HP, % of Total, and % of Available at that Point 53
Figure 4-28	Compressor Loss Comparison – Installation and Total Losses 54
Figure 4-29	Overall System Efficiency Summary 55
Figure 4-30	Cylinder Flow (MMSCFD); Dresser-Rand TCVC10 (Dominion Groveport Station; Unit 1; April 20, 2005) 56
Figure 4-31	Engine HP, Compressor HP, and Inferred Mechanical Efficiency; (Kinder Station (El Paso Station 823); Test 1; April 2003)..... 57
Figure 4-32	Oil Outlet Temperature <i>versus</i> Time from Station Records (Note Increase Over 5 Hours Matches Mechanical Efficiency Trend); (Kinder Station (El Paso Station 823); Test 1; April 2003)..... 58

LIST OF FIGURES (Cont'd)

<u>Figure</u>		<u>Page</u>
Figure 4-33	Suction Nozzle Pulsation – Comparison of Single-Acting and Double-Acting Operation; Clark HBA-6; Unit 4 (Duke Energy’s Bedford Station; March 1, 2005)	59
Figure 4-34	Illustrative Channel Corrected Data from Cylinder 2 Under All Double-Acting Operation; Clark HBA-6; Unit 4 (Duke Energy’s Bedford Station; March 1, 2005)	59
Figure 4-35	Discharge Nozzle Pulsation Levels; Dresser-Rand TCVC10 (Dominion Groveport Station; Unit 1; April 20, 2005).....	60
Figure 4-36	Cylinder 1 Suction and Discharge Nozzle Pulsations <i>versus</i> Time in Seconds; Cylinders 1 and 4 Single-Acting; Clark HBA-6 Unit 4 Compressor Cylinders (Duke Energy’s Bedford Station; March 1, 2005)	61
Figure 4-37	Cylinder Total DIP; Dresser-Rand TCVC10 (Dominion Groveport Station; Unit 1; April 20, 2005).....	62
Figure 4-38	Representative Unloaded Cylinder and RLM Data (250 RPM)	65
Figure 4-39	Unloaded Frictional Losses as a Function of Speed	65
Figure 4-40	Unloaded Frictional Loss as Percent of Compressor Cylinder IHP	66
Figure 4-41	Comparison of Inferred Values for Friction, Valves (DIP) and Installation Losses as a Percentage of Indicated Power	66
Figure 4-42	Temperature Rise <i>versus</i> Ratio for 3 Cylinders on a GMW10	67
Figure 4-43	Average Cylinder Td <i>versus</i> Header Td; Days 1 and 2	68
Figure 4-44	Vibration Bearing Centerline (Throw 1); (Kinder Station (El Paso Station 823); April 2003).....	69
Figure 4-45	Engine Cylinder Power Over 20 Revolutions	70
Figure 4-46	Instantaneous Rotational Velocity, as a Function of Crank Angle Over 20 Revolutions.....	70
Figure 4-47	Heated Pressure Sensor Installed on Suction Nozzle; Dresser-Rand TCVC10 (Dominion Groveport Station; Unit 1; April 20, 2005)	71
Figure 4-48	Heated Pressure Sensor (Suction Lateral); Dresser-Rand TCVC10 (Dominion Groveport Station; Unit 1; April 20, 2005)	71
Figure 4-49	Pressure as a Function of Crank Angle; Cylinder 3 Head End, Crank End, Nozzles, and Laterals; Dresser-Rand TCVC10; 330 RPM Operation (Dominion Groveport Station; Unit 1; April 20, 2005)	72
Figure 4-50	Spectral Orders of Crankshaft Dynamic Microstrain Variation; Unit 6; After Modification (Williams’ Station 60; Day 2; August 26, 2004)	73
Figure 4-51	Typical Lean-Burn Spark-Ignited Gas Engine Operating Boundaries	74
Figure 4-52	Comparison of Station BHP to BHP from Cylinder Pressure (Using 0.95 Mechanical Efficiency).....	75
Figure 4-53	Pressure-Based BHP <i>versus</i> Station Data	75
Figure 4-54	Predicted Power Losses at Pulsation Control Orifices TCVC10 Compressor	77

LIST OF FIGURES (Cont'd)

<u>Figure</u>		<u>Page</u>
Figure 4-55	Comparison of Key PFP Statistics (Instantaneous Speed – Average Spread); and Time from Last 70+ Microstrain Event; HBA-6T; Test #1; (Kinder Station (El Paso Station 823); April 2003)	79
Figure 4-56	Unbalanced Engine Simulation – Spread in Compression Pressure Induced by Even Increment Spread in AMP – 15% Random Spread in A/F Ratio	80
Figure 4-57	Ratio of PFP to Compression Pressure for Three Different Balancing Situations.....	81
Figure 4-58	Cylinder-to-Cylinder Variation in Combustion Pressure Ratio (CPR); Day 1 (Williams’ Station 60; February 2004)	81
Figure 4-59	Cylinder-to-Cylinder Variation in Combustion Pressure Ratio after CPR Balancing (Williams’ Station 60; February 2004).....	82
Figure 4-60	Element of Waste-Gate Control for Equivalence Ratio; HBA-6T at Kinder Station (El Paso Station 823); April 2004	83
Figure 4-61	Equivalence Ratio <i>versus</i> Speed; Comparison of Open-Loop and Closed-Loop Control (Kinder Station (El Paso Station 823); April 2004).....	83
Figure 4-62	Mean Cylinder Cycle-to-Cycle Standard Deviation <i>versus</i> Speed; Comparison of Open-Loop and Closed-Loop Control of Waste-Gate (Kinder Station (El Paso Station 823); April 2004)	84
Figure 4-63	MEC-L Flo-Tech Control Valve.....	85
Figure 4-64	MEC-L Controller and Sensors.....	85
Figure 4-65	Simple Test of Closed-Loop	86
Figure 4-66	Self-Powered Rod Load Monitor (RLM)	86
Figure 4-67	Comparison of Horsepower Based on the Rod Load Monitor and on Cylinder Pressure; Unit 6; After Modification (Williams’ Station 60; Day 1; August 25, 2004)	88
Figure 4-68	Percentage Difference Between Horsepower Based on Rod Load Monitor and on Cylinder Pressure; Unit 6; After Modification (Williams’ Station 60; Day 1; August 25, 2004).....	88
Figure 4-69	High-Pressure Fuel Injection System Installed on a GMW10 (Williams’ Station 60)	89
Figure 4-70	Turbocharger Installed as Part of a Modification on a GMW10 (Williams’ Station 60)	89
Figure 4-71	Evaluation of Adding High Pressure Fuel and Turbo to a GMW10	90
Figure 4-72	Detonation Detector Mounted on Power Cylinder 7 on a KVG103.....	90
Figure 4-73	Knock Detector Output (Williams’ Station 60)	91
Figure 4-74	Knock Detector Output (Kinder Station (El Paso Station 823)).....	92
Figure 4-75	Power Cylinder 4 (Left); Average Peak Firing Pressure; Unit 6; After Modification (Williams’ Station 60; Day 1; August 25, 2004).....	92
Figure 4-76	Detonation Detector Signal Corresponding to Figure 4-75 (Williams Station 60; Unit 6; After Modification).....	93

LIST OF FIGURES (Cont'd)

<u>Figure</u>		<u>Page</u>
Figure 4-77	Photograph of TCVC 10 as Tested Showing Compressor Cylinders, Suction Bottle, and Suction Piping	94
Figure 4-78	Summary of Comparisons in Pulsation Levels Before and After Modifications Under Single-Acting Conditions (Duke Energy’s Bedford Station; Data from March 2005 and January 2006).....	95
Figure 4-79	Acoustic Model of Existing System.....	95
Figure 4-80	Comparison of Predicted Shaking Forces – Suction and Discharge Bottles	96
Figure 4-81	Schematic of Side Branch Absorber to be Connected to Suction Lateral Line.....	97
Figure 4-82	Suction Side Branch Absorber (SBA).....	97
Figure 4-83	Schematic of Redesigned Bottles.....	98
Figure 5-1	Cross-Section of a Cooper-Bessemer GMVH Integral Compressor Engine	99
Figure 5-2	Kinematic Model Illustration of GMVH-6 Articulation.....	100
Figure 5-3	Kinematic Model Results of Left and Right Bank Piston Travel <i>versus</i> Crank Angle Degree	100
Figure 5-4	Nominal Exhaust Port Timings for Left and Right Banks.....	101
Figure 5-5	Nominal Intake Port Timings for Left and Right Banks.....	101
Figure 5-6	GMVH Cylinder Pressure <i>versus</i> Crank Angle – Scavenging and Fuel Admission Events Noted	103
Figure 5-7	GMVH Cylinder Pressure <i>versus</i> Cylinder Volume on Logarithmic Scale – Scavenging and Fuel Admission Events Noted.....	103
Figure 5-8	Top-View Schematic of GMVH-6 Engine	104
Figure 5-9	Comparison of Cylinder-to-Cylinder Compression Pressure (20 Degrees BTDC) at All Operating Conditions.....	105
Figure 5-10	Open Chamber Fuel Efficiency <i>versus</i> Engine Speed at Constant NO _x	106
Figure 5-11	Open Chamber Fuel Efficiency <i>versus</i> Engine Load and Ignition Timing at Constant NO _x	106
Figure 5-12	Prechamber Fuel Efficiency <i>versus</i> Engine Load, Speed, and Ignition Timing at Constant NO _x	107
Figure 5-13	Prechamber and Open Chamber NO _x – Efficiency Trade-Off.....	108
Figure 5-14	Cylinder 1L Pressure Comparison for Prechamber and Open Chamber	108
Figure 5-15	Cylinder 1L Apparent Heat Release Rate Comparison for Prechamber and Open Chamber	109
Figure 5-16	Cylinder 1L Cumulative Heat Release Comparison for Prechamber and Open Chamber.....	109
Figure 5-17	CAD Model of Base Air Chest (air volume shown as solid).....	111
Figure 5-18	Photograph of GMVH Base with Cylinder Removed – Air Chest Ports Highlighted	112
Figure 5-19	Exhaust Port Shapes.....	113

LIST OF FIGURES (Cont'd)

<u>Figure</u>		<u>Page</u>
Figure 5-20	Cylinder Inlet Volume Measurements.....	113
Figure 5-21	GMVH Cross-Section with Inlet (blue) and Exhaust (red) Highlights	114
Figure 5-22	Photographs of External Inlet Air System.....	115
Figure 5-23	Photographs of External Exhaust System.....	115
Figure 5-24	Photographs of Internal Geometry of Exhaust Manifold.....	115
Figure 5-25	Measured Left Bank Piston Motions <i>versus</i> Calculated Motion	116
Figure 5-26	Measured Right Bank Piston Motions <i>versus</i> Calculated Motion	117
Figure 5-27	Measured Piston Stroke per Cylinder Compared to Drawing Mean Values.....	117
Figure 5-28	Measured Distances from Cylinder Top to Exhaust Port Top	118
Figure 5-29	Calculated TDC Clearance Volumes and Effective Compression Ratios for Each Cylinder.....	119
Figure 5-30	Calculated Exhaust Port Opening Timings for Each Cylinder	120
Figure 5-31	Calculated Exhaust Port Closing Timings for Each Cylinder.....	120
Figure 5-32	Calculated Exhaust Port Areas for Each Cylinder.....	121
Figure 5-33	Calculated Intake Port Open Timings for Each Cylinder	122
Figure 5-34	Calculated Intake Port Closing Timings for Each Cylinder.....	122
Figure 5-35	Calculated Intake Port Areas for Each Cylinder	123
Figure 5-36	Schematic of Intake Port Geometry.....	123
Figure 5-37	Measured Fuel Valve Travel.....	124
Figure 5-38	Cylinder 1L Intake – Mass Flow <i>versus</i> Piston Travel from BDC.....	125
Figure 5-39	Cylinder 1L Intake – Mass Flow <i>versus</i> Plenum Pressure	126
Figure 5-40	Cylinder 1L Exhaust – Mass Flow <i>versus</i> Piston Travel from BDC.....	127
Figure 5-41	Cylinder 1L Exhaust – Mass Flow <i>versus</i> Plenum Pressure.....	127
Figure 5-42	Comparison of Intake Mass Flow <i>versus</i> Area Ratio (Pressure Ratio=1.05).....	128
Figure 5-43	Comparison of Exhaust Mass Flow <i>versus</i> Area Ratio (Pressure Ratio=1.05).....	129
Figure 5-44	Intake Port Flow Area Schematic.....	129
Figure 5-45	Exhaust Port Flow Area Schematic.....	130
Figure 5-46	Cylinder 1L Intake Discharge Coefficient <i>versus</i> Area Ratio at Tested Pressure Ratios.....	131
Figure 5-47	Cylinder 1L Exhaust Discharge Coefficient <i>versus</i> Area Ratio at Tested Pressure Ratios.....	131
Figure 5-48	Intake Discharge Coefficient <i>versus</i> Area Ratio for Tested Cylinders (Pressure Ratio=1.05)	132
Figure 5-49	Intake Discharge Coefficient <i>versus</i> Area Ratio for Tested Cylinders (Pressure Ratio=1.2)	132
Figure 5-50	Exhaust Discharge Coefficient <i>versus</i> Area Ratio for Tested Cylinders (Pressure Ratio=1.05)	133

LIST OF FIGURES (Cont'd)

<u>Figure</u>		<u>Page</u>
Figure 5-51	Exhaust Discharge Coefficient <i>versus</i> Area Ratio for Tested Cylinders (Pressure Ratio=1.2)	133
Figure 5-52	Model Generated Exhaust Discharge Coefficients.....	134
Figure 5-53	Model Generated Intake Discharge Coefficients.....	134
Figure 5-54	Initial Simulation to Measurement Comparison – Cylinder 1L Pressure	136
Figure 5-55	Initial Simulation to Measurement Comparison – Intake Manifold Pressure	137
Figure 5-56	Initial Simulation to Measurement Comparison – Exhaust Manifold Pressure	137
Figure 5-57	Revised Simulation to Measurement Comparison – Cylinder Pressure.....	138
Figure 5-58	Revised Simulation to Measurement Comparison – Inlet, Exhaust, and Cylinder Pressure	138
Figure 5-59	Identical Cylinder Simulation to Measurement Comparison – Cylinder Compression Pressure at TDC.....	139
Figure 5-60	Simulation Predictions of Compression Pressure with Variation in Port Opening Height (Timing)	140
Figure 5-61	Simulation Predictions of Compression Pressure with Variation in Port Discharge Coefficient	141
Figure 5-62	Simulation Predictions of Compression Pressure with Variation in Compression Ratio.....	142
Figure 5-63	100-Cycle Average Cylinder Pressures at 20 Degrees BTDC <i>versus</i> Air Manifold Pressure – Post Power Assembly Swap.....	143
Figure 5-64	Cylinder Pressures at 20 Degrees BTDC for Air Manifold Pressure of 20 inHg – Before and After Power Assembly Swap	143
Figure 5-65	Measured and Simulated Cylinder Pressure for Cylinder 1L Showing Effects of Thermal Shock	145
Figure 5-66	logP-logV Diagram for Cylinder 1L Showing “Dip” in Initial Compression.....	146
Figure 5-67	logP-logV Diagram for Cylinder 3L Showing No “Dip” in Initial Compression	146
Figure 5-68	logP-logV Diagrams for Cylinders 1L and 3L Showing Effect of “Dip” on Resulting Compression Pressure.....	147
Figure 5-69	Cylinder Pressure for All Cylinders – Before 1L-3L Fuel Valve Swap.....	148
Figure 5-70	Cylinder Pressure for All Cylinders – After 1L-3L Fuel Valve Swap	149
Figure 5-71	Cylinder Pressure and Fuel Valve Pressure for Cylinder 1L	150
Figure 5-72	Cylinder Pressure and Fuel Valve Pressure for Cylinder 3L	150
Figure 5-73	Flowchart of Current Conceptual Manifold Designs	152
Figure 5-74	Photographs of Expansion Chambers (Motorcycle Application at Left & AJAX™ Application on Right [16]).....	153
Figure 5-75	Design Parameters of an Individual Expansion Chamber Manifold	153
Figure 5-76	Multi-Cylinder Coupling Tuned Manifold Concept	154
Figure 5-77	Phasing and Coupling of Cylinders on the GMVH-6 Engine	155

LIST OF FIGURES (Cont'd)

<u>Figure</u>	<u>Page</u>
Figure 5-78	Dimensions for Optimized Multi-Cylinder Coupled Exhaust Manifold Concept 156
Figure 5-79	Dynamic Pressure Data Recorded on Cylinder 1L of the GMVH-6 Engine..... 157
Figure 5-80	Frequency Analysis of Recorded Engine Data for Left Bank Cylinders 158
Figure 5-81	Conceptual Exhaust SBA Design for GMVH-6..... 158
Figure 5-82	IPPS Model Results for SBA Concept..... 159
Figure 5-83	Simulated Mass Air Flow from Base Plenum, Intake Manifold, and Through the Intake Ports 160
Figure 5-84	Photograph and Sketch of Intake Manifold Showing Region of Concern for Flow Disturbance and Restriction..... 161
Figure 5-85	Three-Dimensional CAD Image of Prototype SBA Design..... 163
Figure 5-86	Photograph of Prototype SBA Housing Prior to Installation 164
Figure 5-87	Photograph of Prototype SBA Housing Installed on Engine..... 164
Figure 5-88	Photograph of Prototype SBA Housing Prior Installed on Engine 165
Figure 5-89	Comparison of Cylinder 1L Dynamic Exhaust Pressure Before and After SBA Installed 166
Figure 5-90	Comparison of Cylinder 1L Pressure and Dynamic Exhaust Pressure Before and After SBA Installed..... 167
Figure 5-91	Comparison of Humidity Corrected NO _x versus Air Manifold Pressure Before and After SBA Installed..... 168
Figure 5-92	Photograph of Cylinder Showing Location of Casting Number 169
Figure 5-93	Photograph of Cylinder Head Showing Location of Casting Number 170
Figure 5-94	Schematic of Cylinder Measurements (with head removed) for Geometric Variability Investigation..... 170

This page left intentionally blank.

LIST OF TABLES

<u>Table</u>		<u>Page</u>
Table 3-1	High Count Engines in Gas Transmission—Sorted by Number (From 1998 Coerr Database).....	23
Table 3-2	High Count Engines in Gas Transmission—Sorted by Horsepower (From 1998 Coerr Database).....	23
Table 3-3	Time-Averaged and Crank-Angle Resolved Measurements on GMVH	27
Table 3-4	Static Measurements on Each Cylinder of GMVH.....	30
Table 3-5	GMVH Cylinder Flow Bench Measurements	31
Table 4-1	Categorization of Topics and Technologies Discussed and Illustrated in Section 4	34

This page left intentionally blank.

1. EXECUTIVE SUMMARY

This project has documented and demonstrated the feasibility of technologies and operational choices for companies who operate the large installed fleet of integral engine compressors in pipeline service. Continued operations of this fleet is required to meet the projected growth of the U.S. gas market. Applying project results will meet the goals of the DOE-NETL Natural Gas Infrastructure program to enhance integrity, extend life, improve efficiency, and increase capacity, while managing NO_x emissions. These benefits will translate into lower cost, more reliable gas transmission, and options for increasing deliverability from the existing infrastructure on high demand days.

The power cylinders on large bore slow-speed integral engine/compressors do not in general combust equally. Variations in cylinder pressure between power cylinders occur cycle-to-cycle. These variations affect both individual cylinder performance and unit average performance. The magnitude of the variations in power cylinder combustion is dependent on a variety of parameters, including air/fuel ratio. Large variations in cylinder performance and peak firing pressure can lead to detonation and misfires, both of which can be damaging to the unit. Reducing the variation in combustion pressure, and moving the high and low performing cylinders closer to the mean is the goal of engine balancing. The benefit of improving the state of the engine “balance” is a small reduction in heat rate and a significant reduction in both crankshaft strain and emissions.

A new method invented during the course of this project is combustion pressure ratio (CPR) balancing. This method is more effective than current methods because it naturally accounts for differences in compression pressure, which results from cylinder-to-cylinder differences in the amount of air flowing through the inlet ports and trapped at port closure. It also helps avoid compensation for low compression pressure by the addition of excess fuel to achieve equalizing peak firing pressure, even if some of the compression pressure differences are attributed to differences in cylinder and piston geometry, clearance, and kinematics.

The combination of high-pressure fuel injection and turbocharging should produce better mixing of fuel and air in lean mixtures. Test results documented modest improvements in heat rate and efficiency and significant improvements in emissions.

The feasibility of a closed-loop control of waste-gate setting, which will maintain an equivalence ratio set point, has been demonstrated. This capability allows more direct tuning to enhance combustion stability, heat rate, or emissions.

The project has documented the strong dependence of heat rate on load. The feasibility of directly measuring power and torque using the GMRC Rod Load Monitor (RLM) has been demonstrated. This capability helps to optimize heat rate while avoiding overload.

The crankshaft Strain Data Capture Module (SDCM) has shown the sensitivity to changes in operating conditions and how they influence crankshaft bending strain. The results indicate that: balancing reduces the frequency of high-strain excursions, advanced timing directly increases crankshaft dynamic strain, reduced speed directly reduces strain, and high-pressure fuel injection reduces crankshaft strain slightly.

The project demonstrated that when the timing is advanced, the heat rate is reduced, and when the timing is retarded, the heat rate is increased. One reason why timing is not advanced as much as it might be is the potential for detonation on hot days. A low-cost knock detector was

demonstrated that allowed active control to use timing to allow the heat rate benefit to be realized safely.

High flow resistance losses in the pulsation control systems installed on some compressors have been shown to hurt efficiency of both compressor and engine/compressor system. Improved pulsation control systems have the potential to recover almost 10% of available engine power.

Integrity enhancements and reduced component failure probability will enhance aggregate deliverability. In addition to improving the efficiency of fuel conversion, all increases in compressor efficiency will reduce the fraction of available engine power that must go to overcome losses and, thereby, will add to deliverability. Project results confirm an earlier survey of a large range of compressor efficiency. If the bottom half of the efficiency range is upgraded with improved technology, such that the resulting performance approaches the best documented efficiency, the aggregate system-wide capacity could be increased by 10% with no new installed compression.

An additional phase was added to the original scope of work to investigate the perceived imbalance in airflow between power cylinders in two-stroke integral compressor engines. Results of a geometric analysis and simulations on the effects of geometric variation showed that a large percentage (50% to 60%) of the spread in compression pressure is due to component geometry variation. Several conceptual manifold designs and retrofits to the existing manifolds were developed. The exhaust Side Branch Absorber (SBA) concept was selected for detailed design and testing. Testing showed a reduction in amplitude of exhaust pulsations, an increase in scavenge airflow, and consistently lower NO_x.

This program has provided an in-depth assessment of operating methods and technologies that can enhance the operation of integral engine/compressors in natural gas pipeline service. Applying these technologies will meet the goals of the Natural Gas Infrastructure program to increase the capacity of the existing pipeline by 10%, reduce fuel consumption by 10%, reduce operational costs by enhancing mechanical integrity, and reducing NO_x emissions by 90%.

2. INTRODUCTION

This report presents the results of a multi-year program to characterize slow speed integral engine compressors in pipeline service, and to quantify, through measurement and analysis, the influence of operating practice and technology options on their component and system efficiencies, their integrity, their capacity, and their emissions.

2.1 THE U.S. GAS TRANSMISSION COMPRESSION INFRASTRUCTURE

The gas transmission industry operates over 4,000 integral engine compressors, which play a major role in pumping natural gas through the U.S. pipeline system. Although the use of centrifugal compressors in the U.S. pipeline industry has grown, these integral reciprocating units still represent over 70% of the fleet in numbers and over one-half of the installed power. These “slow-speed” integral engine compressors have been the workhorses of the industry for over 50 years, providing the reliable gas compression needed by the pipeline system. Figure 2-1 shows two such units: a 48-year old TLA6 and a 50-year old GMW10.



Figure 2-1. TLA6 (2,000 HP) and GMW10 (2,500 HP) in Pipeline Service

Figure 2-2 shows the age distribution of the current infrastructure. Over one-half of the fleet is well over 45 years old, but replacing all these units with currently available technology would incur a huge cost and disruption to service with insufficient improvement in overall performance of the pipeline system to justify this cost and disruption. For these reasons, wholesale replacement remains unlikely (although selective replacement driven by factors such as environmental regulations can be expected). Growth to a 30-TCF-plus gas market in the U.S., anticipated over the next 10 to 20 years, must come on the backs of the existing compression infrastructure; therefore, it will depend on continued integrity, enhanced capacity, and efficiency of the existing integral engine/compressors under all loads. The industry needs demonstrated technology options and operating methods, which will cost-effectively maximize the capacity of these old units, and reduce their fuel consumption, while respecting or improving their integrity.

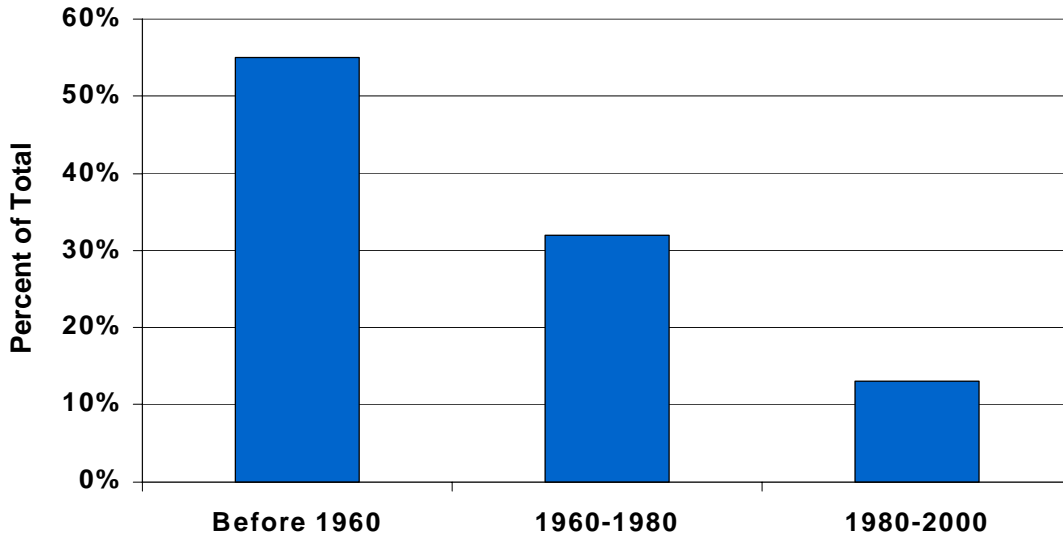
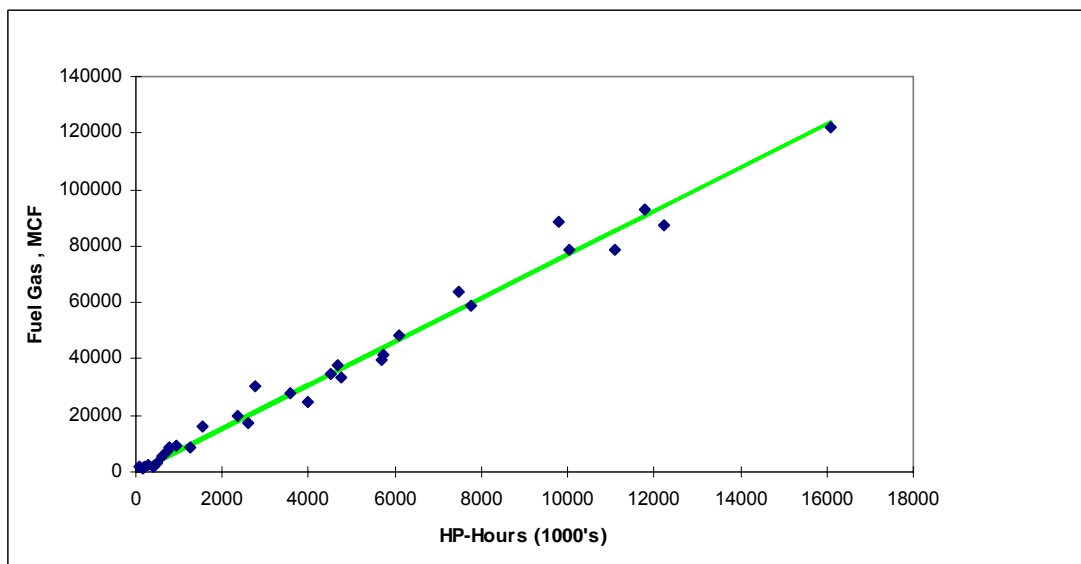


Figure 2-2. Install Dates: Over 50% of Pipeline Compressors Exceed 45 Years Old

Figure 2-3, Figure 2-4, and Figure 2-5 exemplify these needs of the existing infrastructure.

Figure 2-3 shows how annual fuel consumption at a number of individual compressor stations in the pipeline system varies with the number of horsepower hours delivered by the engine to the compressor cylinders at that station. Points on the high side of the mean slope represent stations, which are burning more than the industry average. In addition, with a regressed slope of 7.7 MCF/HP-Hr for Figure 2-3, the industry burns significantly more fuel than the most efficient current technology natural gas engines (as little as 6 MCF/HP-Hr).



**Figure 2-3. Industry Fuel Consumption
(~7.7 MCF/HP-Hr ±20% – Need to Lower the High Values)**

Figure 2-4 presents a distribution of compressor thermal efficiency for the industry created by the Gas Machinery Research Council (GMRC) from a quantitative survey a number of years ago. This is the efficiency with which the compressors convert piston face HP-Hr to useful compression. The width of the range and the 12 points by which the 79% median lies below the best achieved (91% to 92%) represents not only gas, which is burnt rather than delivered, but also engine capacity, which must overcome losses rather than deliver useful compression of the transported gas.

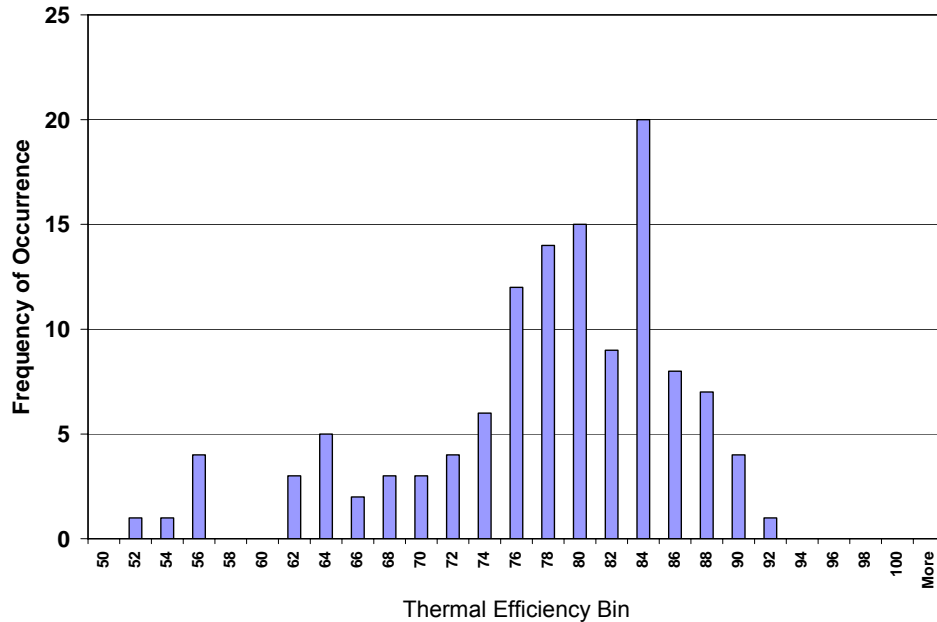


Figure 2-4. Compressor Thermal Efficiency Histogram Based on GMRC Survey

Figure 2-5 shows a number of failed crankshafts. This problem continues to occur at an undesirable rate for the pipeline industry as a whole (about one failure per thousand engines per year). This rate may not seem excessive, but for the compressor station and company, which incurs such a failure, the disruption, cost, and loss of capacity at the time is significant. The chance of this rate increasing as a penalty for improved performance and increased capacity must be avoided, as well as any increase in problems, such as bearing failure, or damage caused by detonation, or unintended overload.



Figure 2-5. Integrity: Crankshaft Failure Examples – Need Methods of Avoidance

2.2 THE COMPRESSION INFRASTRUCTURE PROJECT

Six years ago, the U.S. Department of Energy (DOE) National Energy Technology Laboratory (NETL) initiated a Natural Gas Infrastructure (NGI) program whose goals included increasing capacity of the existing pipeline infrastructure (by 10%) and reducing operational costs (50% by 2010). As part of this program, Southwest Research Institute[®] (SwRI[®]) undertook the project described in this report. GMRC co-funded and provided the industry oversight for this program. The project objective is:

To develop and substantiate methods for operating integral engine/compressors in gas pipeline service that reduce *fuel consumption*, increase *capacity*, and enhance mechanical *integrity*.

2.3 PROJECT ACCOMPLISHMENT

This project has documented and demonstrated the feasibility of technologies and operational choices for companies who operate the large installed fleet of integral engine compressors in pipeline service. Applying project results will enhance integrity, extend life, improve efficiency, and increase capacity, while managing NO_x emissions. These benefits will translate into lower cost, more reliable gas transmission, and options for increasing deliverability from the existing infrastructure on high demand days. The following documents the project's value and contribution to DOE goals.

2.3.1 INTEGRITY

Increasing integrity and reducing statistical likelihood of component failure reduces transmission cost and enhances aggregate deliverability. Detonation represents a damaging threat to an engine. Applying the detonation detection technology tested under the project will mitigate this threat, which widely inhibits potentially beneficial operation with advanced timing. The newly defined CPR balancing method, which has proved quick and convenient to apply, will help equalize air/fuel ratio across cylinders and reduce the tendency to detonate. The low-cost control method demonstrated for maintaining a global equivalence ratio set point provides another option for maximizing the margin between misfire and detonation limits and using commercially available controllers and could contribute to an effective detonation avoidance system. The crank Strain Data Capture Module (SDCM) applied on all engines tested in the first two phases of the project has shown its value for defining conditions when crank damage rate increases. Measuring crankshaft torsional velocity has complemented the SDCM, particularly in documenting the influence of speed changes, showing also that torsional velocity data respond detectably to loss of torque from a misfire. The Rod Load Monitor (RLM) evaluated and enhanced on every major test promises to avoid overload of engines and resulting damage by improving consistency of load torque values used in load step control.

2.3.2 EFFICIENCY

As much as 3% of the natural gas consumed goes toward fuel gas for engines and turbines to drive compressors. This fuel gas would cost over \$3 billion at current rates—the single most significant cost of gas transportation. Increasing the aggregate efficiency with which engine/compressors convert fuel energy into useful compression work will reduce this cost and leave more of the gas in the pipeline system available to the end user. The project has documented how high-pressure fuel injection, coupled with the addition of a turbocharger on old

GMW engines, reduces their heat rate by about 7%. The demonstrated air/fuel ratio control on a rich burn, carbureted, four-stroke engine can replace manual adjustment based on indirect measurement, allowing optimization for minimum fuel, or for minimum emissions without a three-way catalyst, or for optimum catalyst performance if one is installed. The Rod Load Monitor will allow engine operation at the point of highest efficiency (100% torque) with greatly reduced risk of overload. The detonation detector, if integrated into a detonation avoidance system, will safely allow more efficient engine operation with timing advanced.

Comparison of the heat rate versus load characteristic has shown value as a graphical method to compare fuel conversion efficiency achieved by different engine technologies or operating decisions. This heat rate versus load comparison has revealed small potential benefits in brake thermal efficiency by applying CPR balancing. Mapping of overall system thermal efficiency has made clear the importance of considering both compressor and engine when evaluating how operational decisions will impact fuel conversion efficiency; speed/load combinations that favor heat rate may, at the same time, hurt compressor efficiency, so maximizing efficiency requires careful choices based on data. The project has identified ways to enhance this efficiency, with emphasis on the compressor and pulsation control. The project has prototyped and demonstrated a methodology for use of Differential Indicated Power (DIP) to distinguish valve and installation losses and their contribution to compressor efficiency. Results show DIP based efficiency and enthalpy based efficiency track each other quite closely. The project has also made clear the need for more information about mechanical losses and has added to this knowledge with a new interpretation of the rod load data.

Valve leaks represent a significant loss of compressor efficiency system-wide. Engine/compressor operators know the sensitivity of temperature rise to valve leaks, and the project has re-emphasized this sensitivity; the data normalization and statistical process control techniques already promoted by McKee, et al. [2], would lend themselves very effectively to monitoring of cylinder temperature rise and associated decision making based on the economic significance of valve leakage.

High flow resistance losses in the pulsation control systems installed on some compressors have been shown to hurt efficiency of both compressor and engine/compressor system. A design study using the GMRC-SwRI Interactive Pulsation Prediction Software (IPPS) has demonstrated the potential to recover almost 10% of available engine power by eliminating high flow resistance orifices, by adding a side branch absorber, and by adding a common chamber to enhance filtering of suction and discharge bottles, all of which combine to provide effective, low loss, pulsation control.

2.3.3 CAPACITY

As discussed above, integrity enhancement and reduced component failure probability will enhance aggregate deliverability. In addition to improving the efficiency of fuel conversion, all increases in compressor efficiency will reduce the fraction of available engine power that must go to overcome losses and, thereby, will add to deliverability. Project results obtained on seven different units encompass a compressor efficiency range from 76% to 91%, and add to an earlier GMRC survey for a larger base of compressors with a range from 52% to 92%! The highest compressor efficiency values found present a benchmark that will add greatly to system capacity, if more widely achieved. Phase III of the project has sought to re-emphasize compressor efficiency by tests and analysis to characterize and reduce compressor losses, both

mechanical and thermodynamic. Measurements of temperature rise, and dynamic pressure in the cylinder nozzles (as well as in the cylinders themselves) have quantified and characterized inherent thermodynamic losses—a first step in their reduction. Survey tests on the project have confirmed the contribution of pulsations to these losses; design analysis has illustrated options to reduce pulsations, to increase compressor thermal efficiency, and thereby to increase system capacity as discussed above.

Installation losses comparable to valve losses have been documented, together with just slightly lower mechanical losses. The project has validated the prediction capability of the IPPS software, and the effectiveness of the side branch absorber as a low loss tool for pulsation control.

2.4 FIELD TEST PROGRAM OVERVIEW

The project has performed detailed tests and analyses on five different units covering two different two-stroke engine models from two manufacturers and one four-stroke engine model: a Cooper GMW10 with three compressor cylinders, a Dresser-Clark HBA-6T with four compressor cylinders, and an Ingersoll-Rand KVG103 with three compression cylinders. The HBA is a straight six with a turbocharger. The GMW is a V-10 and has been tested both with and without the combination of a turbocharger and high-pressure fuel injection system. The KVG is a V-10 carbureted four-stroke engine. Survey tests and follow-up design analysis on the compressor piping have been performed on two additional two-stroke models, a naturally aspirated HBA-6 and a 5,000 HP TCVC10.

The engines were selected based on detailed quantitative analysis of the engine population using a database prepared for the pipeline industry. This analysis shows all tested models are in the top seven, measured by horsepower installed, and in the top eight by number of units installed. The two highest by installed HP (TCV, GMW) and by Number (GMW, KVG) are included. In addition, the GMVH6 used for air balance studies is seventh in installed power and ninth in number installed. Thus, marked diversity has been achieved in the process of testing widely deployed engine models.

The suite of instruments and data acquisition systems used has allowed characterization of heat rate, overall system efficiency, and rod load power, as a function of measured power, speed, compression ratio, timing, balance method and condition, and boost pressure, together with parameters which have value for condition monitoring, including crankshaft strain, suction and discharge temperature, detonation severity, frame vibration, and instantaneous rotational velocity (IRV).

2.5 PROJECT EMPHASIS

The original project was proposed as a three-phase effort. The first phase of the project emphasized two-stroke engines, demonstrated balancing options, and tested for the influence of operational decisions on component and system performance, on emissions, and on integrity. The second project phase documented results of adding high-pressure fuel and turbocharger to older two-stroke engines and evaluated an early four-stroke engine. Throughout the first two phases, the value of engine/compressor system thermal efficiency was emphasized, and methods for its evaluation were refined. In the third phase, methodologies were developed and demonstrated for quantifying compressor side efficiency, and for distinguishing losses in cylinder and piping; state-of-the-art design methods were demonstrated, which provide options

for reducing compressor pulsations and for enhancing compressor integrity, thermal efficiency, and capacity.

2.6 AIR IMBALANCE

During the course of the original effort, field testing showed many of the integral engines to have inconsistent performance between cylinders on a given unit. This inconsistency has been exhibited by the tendency of one or two of the cylinders in a given unit to be more prone to either misfire or knock (detonation) than the other cylinders. Dynamic cylinder pressure measurements have shown a spread in peak firing pressure and the pressure during the compression stroke. This spread in compression pressure and the tendency for misfire or detonation in one or two cylinders indicated that the air/fuel ratio between cylinders is varied. A variance, or spread, in air/fuel ratio would lead to excessive emissions and fuel consumption.

It was theorized that the spread in compression pressures in the various engines tested was caused in large part to dynamics in either or both of the intake or exhaust manifolds. This theory was qualitatively based on measurements of high amplitude pressure pulsations in the manifolds and the tendency of the low compression pressure cylinder to be located at the first junction of the intake manifold, nearest the turbocharger outlet. If this theory was correct, then redesigning the manifolds based on actual fluid dynamics of the particular engine should alleviate the spread and create balanced trapped mass between cylinders.

Other factors that could cause this spread in compression pressure relate to cylinder geometry. The geometric parameters include mechanical compression ratio, port flow coefficients, and port timings. The uncertainty was to what magnitude each of these parameters contributes to the spread, what is the likely variation existing in field engines, and whether or not these factors dominate over fluid dynamics effects.

As a result, an additional phase was added to the project to specifically investigate the perceived imbalance in airflow between power cylinders, develop potential solutions, and experimentally validate these solutions.

The industry co-funders for this additional phase of work were different than the original effort. Separate industry reports are being developed to cover each effort. Since DOE's contribution was provided through a single contract, the combined results are included in this report.

This page left intentionally blank.

3. EXPERIMENTAL

3.1 OVERVIEW

This section describes the facilities and suite of instruments with the associated data acquisition, which have been assembled and used for intensive testing of the power and compression sides of integral engine compressors. Section 3.2 describes the suite of instruments used in Phases I, II, and III of the project. Section 3.3 describes the facilities and instrumentation for the Air Balance effort.

3.2 FIELD TEST INSTRUMENTATION

3.2.1 SENSORS AND DATA CHANNELS FOR FIELD MEASUREMENT

Sensors and data acquisition capabilities have been assembled to record the following data on large integral engine compressors.

- *Dynamic Pressure in the Compressor Cylinders* – These measurements are used for compressor horsepower and flow determination. Both ends of each compressor cylinder have been instrumented for dynamic pressure in each major test series. The sensors are Sensotec piezo-restrictive transducers. They are calibrated prior to each test by deadweight loading to generate known force per unit area in the test fluid applied to the sensing element.
- *Dynamic Pressure in the Engine Cylinders* – These measurements are used for engine horsepower determination, engine balancing, and to calculate engine statistics. All power cylinders have been instrumented for dynamic pressure in each major test series. The sensors are Kistler quartz piezoelectric transducers. Because they are dynamic sensors, they are calibrated prior to each test by suddenly applied deadweight loading to generate known force per unit area in the test fluid applied to the sensing element.
- *Dynamic Pressure in the Engine Air Intake Manifold* – These measurements are used to correlate dynamic effects in the inlet manifolds, which deliver air for each cylinder with the dynamic statistics within each cylinder. They also provide the time-averaged value for air manifold pressure whose influence on engine heat rate and emissions is assessed. Air manifolds have been instrumented in each major test series. The sensors are Kistler piezo-resistive pressure transducers with factory provided calibration.
- *Dynamic Pressure in the Engine Exhaust Manifold* – These measurements are used to determine dynamic variation of pressure in the engine manifolds, which capture hot exhaust gas from each cylinder, and to correlate these dynamic pressure variations with the dynamics within each cylinder. The sensors are Kistler piezo-resistive transducers with factory provided calibration; they are water-cooled to reduce uncertainty resulting from temperature influence on the sensor readings.
- *Torsional Vibrations (IRV)* – This measures the dynamic variation in speed of rotation of the flywheel. The sensor is a BEI 512 pulse encoder driven through a flexible coupling by a shaft connected by a friction drive to the flywheel. The frequency of its output pulse train directly reflects instantaneous flywheel angular

velocity, which varies within each cycle of the engine because of dynamic load variation. Rather than digitally time the variation in the period between pulses (which imposes unrealistic period discrimination requirements), a frequency to voltage analog circuit is used to determine the continuous variation in flywheel speed. The frequency-to-voltage measurement is calibrated by supplying the analog circuitry with a pulse train of known frequency from a signal generator. The torsional vibration has been measured in this way on all major tests. The torsional vibration data have been assessed as a potential indicator of engine dynamic loading severity.

- *Data Acquisition Triggering* – The BEI encoder signal is also used to trigger acquisition of samples from all dynamic transducers. The phasing of the pulse train to top dead center (TDC) is important. A pre-established top dead center mark for power Cylinder 1 is used as a reference, and the angular setting within the DAS corresponding to Cylinder 1 TDC is adjusted, as the engine runs, until a strobe light triggered by the DAS at this angle shows that the mark on the flywheel coincides with the stationary mark.
- *Bearing Centerline Vibration* – This measurement is assessed as an indicator of engine dynamic loading severity. The sensors are PCB velocimeters with factory provided calibration. The sensors have been located to measure lateral vibration at each end of the engine/compressor frame.
- *Crankshaft Dynamic Strain* – This measurement is used as a direct indicator of shaft loading and to provide a link between engine statistical quantities and potential for crankshaft fatigue damage (Harris, et al., [3]). The strain gage is placed on the crankshaft web as close as possible to the crank pin—at the point most sensitive to opening and closing of the crank throw faces under load from engine and compressor rods. Data are acquired by the Strain Data Capture Module (SDCM), which rides on the shaft within the engine during each day of testing and from which data are downloaded at the end of each day. This is calibrated using a calibration resistance.
- *Engine Fuel Flow* – This measurement is used to document overall engine efficiency. The sensor is an Emerson Flobas 103 transmitter that implements the AGA3 flow measurement based on a differential pressure measurement and is factory calibrated with a certificate. It is connected to taps on the already installed engine fuel flow orifice, which has been available on all engines tested. The fuel flow, coupled with a gas analysis, provides the basis for determining fuel energy consumed by the engine and for determining heat rate and overall system efficiency.
- *Pressures and Temperatures in Headers and Laterals (Suction, Discharge)* – These measurements are used for installation efficiency determination. Pressures are measured with Sensotec piezo-restrictive transducers.
- *Engine Exhaust O₂ Level* – This measurement is used to determine global equivalence ratio, both as an independent variable influencing engine performance, and where the loop is closed between this sensor’s output and the turbocharger waste-gate (two-stroke) or fuel rate valve (four-stroke) for active control. The

sensor used is an NGK fast-response transducer, which provides a continuous variation of voltage with exhaust oxygen level. It is calibrated against a standard.

- *Engine Exhaust NO_x Level* – This measurement is used to provide comparative emissions data. The sensor used is an NGK fast-response transducer that provides a continuous variation of voltage with exhaust NO_x level. It is calibrated against a standard. This report presents no absolute NO_x data on any of the engine's data. All NO_x data presented is normalized so that the sensitivity to operating conditions is apparent.
- *Compressor Rod Load* – This measurement is used for both mechanical integrity and loading optimization. The sensor uses a pair of strain gages mounted on either side of the rod, which are bridged additively to cancel bending and to produce a signal proportional to axial load on the piston rod. The signal is transmitted using RF from a moving antenna to a stationary antenna. The strain gage and signal transmission can be powered by a battery or by a generator driven by rod motion. The battery power is adequate and simpler to set up for short-term tests, but for continuous monitoring and control, self-powering is needed. The horsepower measurement from the compressor cylinder, based on cylinder pressure transducer, has been used for calibration, in conjunction with a nominal load based on the product of strain, modulus, and rod area.
- *Knock Detection* – This sensor, provided as a loan to the project by Metrix, counts occurrences of dynamic acceleration levels above a threshold, to detect detonation.

3.2.2 TRANSDUCER INSTALLATION

Figure 3-1 shows a compressor cylinder with pressure transducers installed on head and crank end. As discussed above, these are Sensotec piezo-resistive sensors.

Figure 3-2 shows the details of the power cylinder pressure transducer installation on one cylinder of the first GMW10 tested. Close examination reveals two pressure transducers installed—the one nearest the cylinder was already installed at test time as part of the high-pressure fuel injection system; the one further removed from the cylinder provided the data for SwRI's test on the engine with high-pressure fuel.

Figure 3-3 shows the unit tested at El Paso's Station 823. Close examination reveals the pressure transducer located in its air manifold. Figure 3-4 shows rather more clearly the pressure transducer in the air manifold for the GMW10 with high-pressure fuel injection.

Figure 3-5 shows the pressure transducer in the exhaust manifold of the GMW10 at Williams' Station 40. Close examination also shows the tubes carrying cooling water to the transducer.

Figure 3-6 and Figure 3-7 show an overview and close-up of the installation for the encoder. As discussed above, the encoder provides the multiple functions of torsional vibration measurement and triggering of data acquisition for all dynamic channels. The bracket holding the encoder is mounted on the tripod shown in Figure 3-7, and the shaft connecting the encoder to the flywheel is also apparent in both figures. The cable evident in these figures connects the encoder to the DAS.



Figure 3-1. Compressor Cylinder and Pressure Transducers on Each End (Williams' Station 40 (Sour Lake); August 2003)

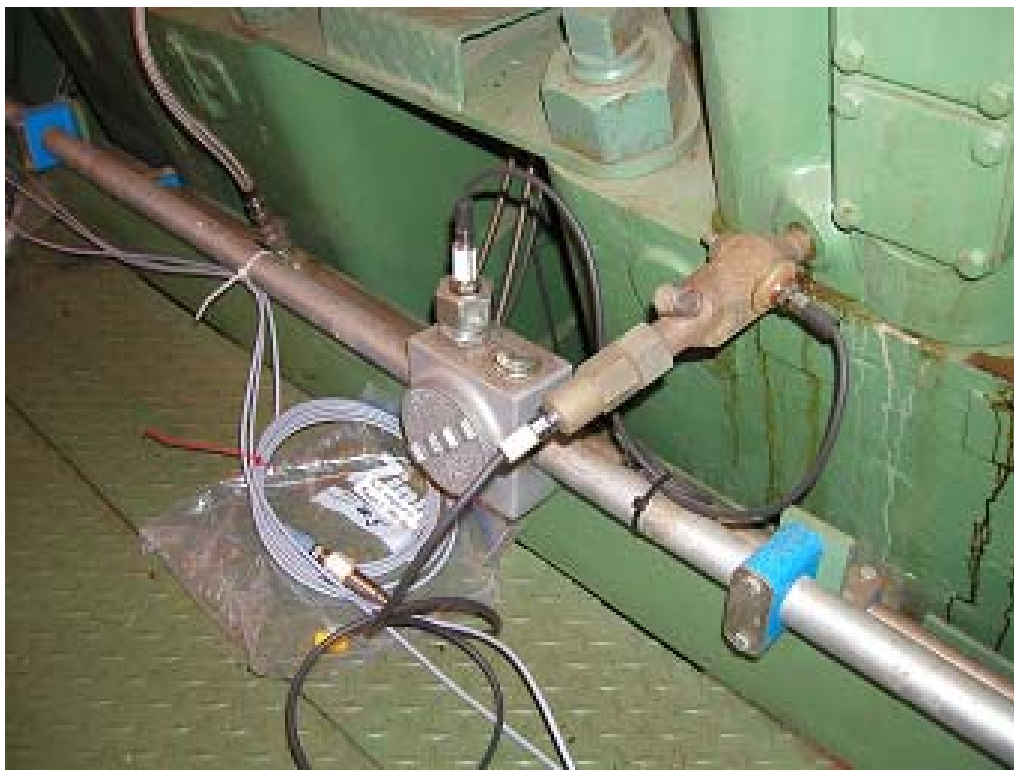


Figure 3-2. Details of Power Cylinder Pressure Transducer Installation (Williams' Station 40 (Sour Lake); August 2003)



Figure 3-3. Initial Site Test Showing Air Manifold Sensor (HBA-6T; TGP Kinder Station (El Paso Station 823); April 2003)



Transducer

Figure 3-4. Pressure Transducer in Air Intake Manifold (GMW10; Williams' Station 40 (Sour Lake); August 2003)

Transducer



Figure 3-5. Pressure Transducer in Exhaust Manifold (GMW10; Williams' Station 40 (Sour Lake); August 2003)



Figure 3-6. Encoder, Outboard of Flywheel on Mounting Tripod (GMW10; Williams' Station 40 (Sour Lake); August 2003)



Figure 3-7. Detailed View of Encoder and Connection to Flywheel (GMW10; Williams’ Station 40 (Sour Lake); August 2003)

Figure 3-8 shows one of the velocity probes mounted on the back of the compressor to measure lateral vibration of the frame; there are two such installations, one at each end of the compressor.



Figure 3-8. Accelerometer Mounted on Frame (GMW10; Williams’ Station 40 (Sour Lake); August 2003)

Figure 3-9 shows an installation of the crankshaft Strain Data Capture Module (SDCM) on a GMW10 at Williams’ Station 40 (Sour Lake). The data acquisition system dedicated to one channel of crankshaft strain is seen in this figure mounted on the unstressed flat part of the crank throw. The lead from the strain gage is seen attached to the face of the crank web. The strain gage itself is hidden by the rod—since it is pushed so far up into the space between rod and web

face. As previously described, the strain gage, cable, and single channel data acquisition system represent a standalone system with battery power, which captures data unattended throughout a day of testing.



Figure 3-9. Strain Data Capture Module Installed (GMW10; Williams' Station 40 (Sour Lake); August 2003)

Figure 3-10 shows the SDCM installed on two throws at the Kinder Station (El Paso Station 823)—one throw with power rod only connected, and one throw with both power and compressor cylinders attached. In Figure 3-9, two connectors may be seen attached to the data acquisition system; this temporary condition allows the data acquired over the preceding day's testing to be downloaded to a computer for analysis, and to make the onboard memory available for another day's testing.



**Throw 3
(Power & Compressor)**

**Throw 2
(Power Only)**

Figure 3-10. SDCM Installation for Crankshaft Strain Measurements (HBA-6T; Kinder Station (El Paso Station 823); April 2003)

Figure 3-11 shows the NGK combined O₂/NO_x sensor connected to a pipe already installed, which connects to the exhaust stack.



Figure 3-11. O₂/NO_x Sensor and Connection to Line from Stack (GMW10; Williams' Station 40 (Sour Lake); August 2003)

Figure 3-12 shows installations of the Rod Load Monitor on the first HBA-6T tested, and on the first GMW10 tested. These installations are visible with the “dog-house” cover removed for installation. Once the installation is checked out and the cover re-installed, Figure 3-13 shows that only the antenna connection remains visible. The antenna connection is then cabled to the DAS. Both installations photographed show the Rod Load Monitor in a battery-powered version, which is satisfactory for short-term testing. As a device for long-term monitoring, however, the Rod Load Monitor must be self-powered. Figure 3-14 shows the self-powered Rod Load Monitor installed on the second HBA-6T tested. This was the first successful operation of the RLM in self-powered data telemetry mode.



Figure 3-12. Installations of the RLM on HBA-6T (April 2003) and GMW10 (August 2003)



**Figure 3-13. Cable from RLM Antenna
(GMW10; Williams' Station 40 (Sour Lake); August 2003)**

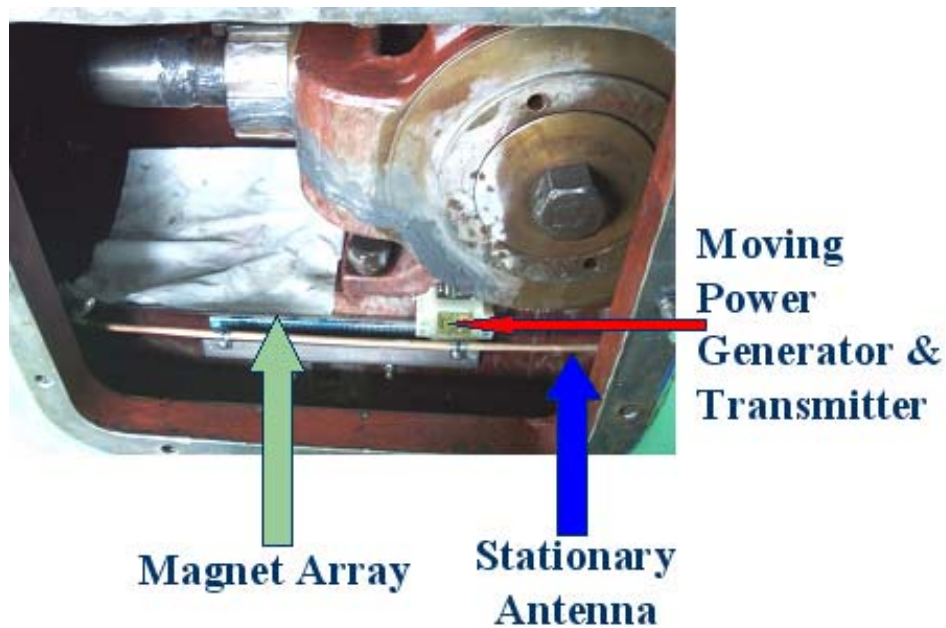


Figure 3-14. Self-Powered Rod Load Monitor (RLM)

Figure 3-15 shows the flow transmitter connected to the orifice taps in the fuel flow gas flow line for the second set of tests on an HBA-6T.



Figure 3-15. Fuel Flow Measurement Using Emerson Flobas 103 Transmitter (HBA-6T; Kinder Station (El Paso Station 823); April 2004)

3.2.3 FIELD DATA SYSTEM

Figure 3-16 and Figure 3-17 show photographs of the Field Data Acquisition System (DAS). The system comprises an industrially hardened computer, a flat screen for display, and a separate box with connectors to which cables from individual sensors are connected. The DAS box has analog-to-digital converters of appropriate speed for over 50 different channels.

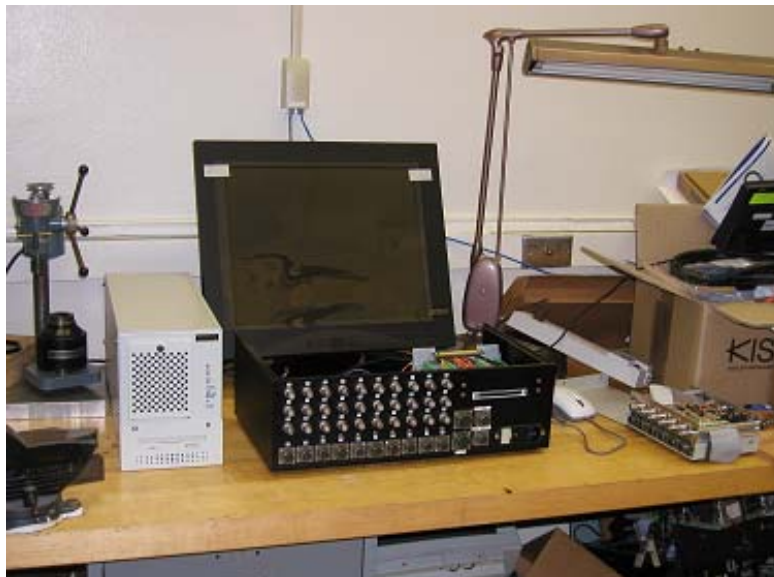


Figure 3-16. Front View of Field Data Acquisition System (DAS)



Figure 3-17. Rear View of Field Data Acquisition System (DAS)

The individual power cylinder transducers (up to 10) are connected to a box with connectors on the deck near the cylinders. A single cable from this box carries the signals from all the power cylinder transducers to the main data acquisition box. A similar approach is used for the compressor cylinders. In this way, the complexity of the cabling and system checkout is minimized. Signals from rod load monitors from other system pressures and from temperature sensors are acquired by the DAS, concurrently, and a database of the sensor values throughout each test is created by the DAS.

3.2.4 SELECTION OF TEST ENGINE MODELS FOR FIELD TESTING

In Phase I, two different engine models (HBA and GMW) were selected for testing and two different engines of each model have been tested. Data to guide this selection were obtained from an industry database of engines and compressors in gas transmission service, supported by the Pipeline Research Council International (PRCI) and GRI. Table 3-1 and Table 3-2 were obtained by appropriate sorting of the database to show the top 10 engine models in terms of number installed (Table 3-1), and in terms of horsepower installed (Table 3-2). It may be seen that the GMW has the highest count (336) and the second highest installed power (708,336 HP). The HBA is in the top six for both count (sixth with 223) and installed power (fifth with 372,414 HP). Thus, these two engines rank highly in terms of pipeline industry deployment. They also achieve diversity; one is made by Cooper and one by Clark; one is a straight six and one is a V-10. The HBA-6T is turbocharged; two different GMW units have been tested—one at Williams' Station 40 already had a turbocharger and high-pressure fuel injection; the other at Williams' Station 60 had no turbocharger and standard fuel pressure when initially tested; a turbocharger and high-pressure fuel were added and this second unit was tested again in Phase II.

In Phase II of the project, a four-stroke engine was also added to the previously selected two-stroke engines—a KVG103. As Table 3-1 shows, this is the most widely deployed four-stroke in gas transmission service (296 units), and Table 3-2 shows it is the seventh highest in terms of HP.

In Phase III of the project, survey tests were performed on a naturally aspirated HBA-6 and a TCVC10. The population of the HBA was discussed above in relation to Phase I (223 units, 372,414 HP). Table 3-1 and Table 3-2 show the TCV family is eighth in number installed (155) and first in installed power.

**Table 3-1. High Count Engines in Gas Transmission—Sorted by Number
(From 1998 Coerr Database)**

MODEL	Sum Of Rated HP	Count	Cumulative			Comments
GMW	708336	336	336	Top 6 by HP or #	Top 10 by HP or #	Just GMW, no GMWA, GMWC
KVG	330918	296	632		Top 10 by HP or #	
TLA	672085	280	912	Top 6 by HP or #	Top 10 by HP or #	
GMV	270489	269	1181		Top 10 by HP or #	Just GMV - No GMVB, GMVH
KVS	441455	233	1414	Top 6 by HP or #	Top 10 by HP or #	
HBA	372414	223	1637	Top 6 by HP or #	Top 10 by HP or #	
GMVH	302242	179	1816		Top 10 by HP or #	
TCV	872106	155	1971		Top 10 by HP or #	includes TCV thru TCVD
L-7042	154528	150	2121			Small High Speed Waukesha
BA	207271	140	2261			Old & Small

**Table 3-2. High Count Engines in Gas Transmission—Sorted by Horsepower
(From 1998 Coerr Database)**

MODEL	Sum Of Rated HP	Count	Cumulative HP			
TCV	872106	155	872106		Top 10 by HP or #	High HP
GMW	708336	336	1580442	Top 6 by HP or #	Top 10 by HP or #	
TLA	672085	280	2252527	Top 6 by HP or #	Top 10 by HP or #	
KVS	441455	233	2693982	Top 6 by HP or #	Top 10 by HP or #	
HBA	372414	223	3066396	Top 6 by HP or #	Top 10 by HP or #	
V-250	335450	93	3401846			
KVG	330918	296	3732764		Top 10 by HP or #	
W-330	315656	56	4048420			High HP, Recent
GMVH	302242	179	4350662		Top 10 by HP or #	
GMV	270489	269	4621151		Top 10 by HP or #	

Note: If we total all GMW, GMWA, thru GMWS, we get 1,189,736 HP and 511 Units.

3.3 AIR BALANCE FACILITIES

3.3.1 GMVH-6 TEST BED

The test bed for the work was a Cooper-Bessemer GMVH six-cylinder turbocharged integral compressor engine. This engine belongs to Cooper Compression and is installed at Southwest Research Institute for research and product development to support the gas transmission industry. The compressors have been removed and a dynamometer has been connected to the flywheel to apply load. The remainder of the engine setup, including the foundation, was designed to mimic a typical compressor station installation as much as possible. A photograph of the test engine installation is provided in Figure 3-18.

The GMVH-6 research engine has standard mechanical fuel valves and a pneumatically controlled fuel regulator. The governor has been removed, and the dynamometer controller is set up to maintain engine speed. Load is controlled by adjusting the fuel header pressure with a PID controller. Cooper configured the engine in a standard Cleanburn™ configuration with Jet-Cell igniters prior to installation. Testing in an open-chamber configuration was accomplished by replacing the Jet-Cells with spark plug adapters. An Altronic CPU-2000 was used for ignition, and Altronic software was installed on the data acquisition computer to command spark timing.



Figure 3-18. Photograph of GMVH-6 Laboratory Research Engine

The GMVH engine was highly instrumented prior to utilization for the air balance investigation. The instrumentation package included a variety of pressure, temperature, frequency, flow, and crankshaft position sensors. Each cylinder was instrumented with flush mount Kistler piezo-electric dynamic pressure sensors through modified start-valve dummy plugs as shown in Figure 3-19. An emissions bench featuring compliance grade analyzers for THC, CO, NO_x, CO₂, and O₂ was utilized for all emissions measurements. Additionally, a ThermoNicolet FTIR was available for hydrocarbon speciation. Additional dynamic pressure measurements were required for proper simulation with the computational model within the air balance tasks. The additional instrumentation is as follows:

- *Dynamic Pressure in Exhaust Manifold Runners* – Prior to the air balance investigation, only Cylinder 1L was instrumented for dynamic exhaust pressure. Additional dynamic pressure sensors were added to the remaining five cylinders to capture the dynamic pressure pulsations of the exhaust from each cylinder’s ports. These sensors are of a thin-film strain gage type, typically used for absolute pressure measurement of manifold pressure in automotive electronic engine control systems. Special heat exchangers were constructed to cool the exhaust gas slightly to minimize damage of these sensors. Each sensor was calibrated and a comparison test to a Kistler piezo-resistive sensor was performed on the running engine to validate transient response. A photograph of the exhaust manifold runner dynamic pressure transducer is depicted in Figure 3-20. A graph showing the comparison of signals from the Kistler piezo-resistive and dynamic exhaust runner pressure sensors is shown in Figure 3-21. These measurements were taken at the end of the measurement channel. An FFT filter was developed to remove the channel resonance and provide a comparison to the FFT-filtered signal from the dynamic exhaust runner pressure sensor to a flush-mounted Kistler piezo-resistive sensor shown in Figure 3-22 as final validation of the sensor and filter performance.

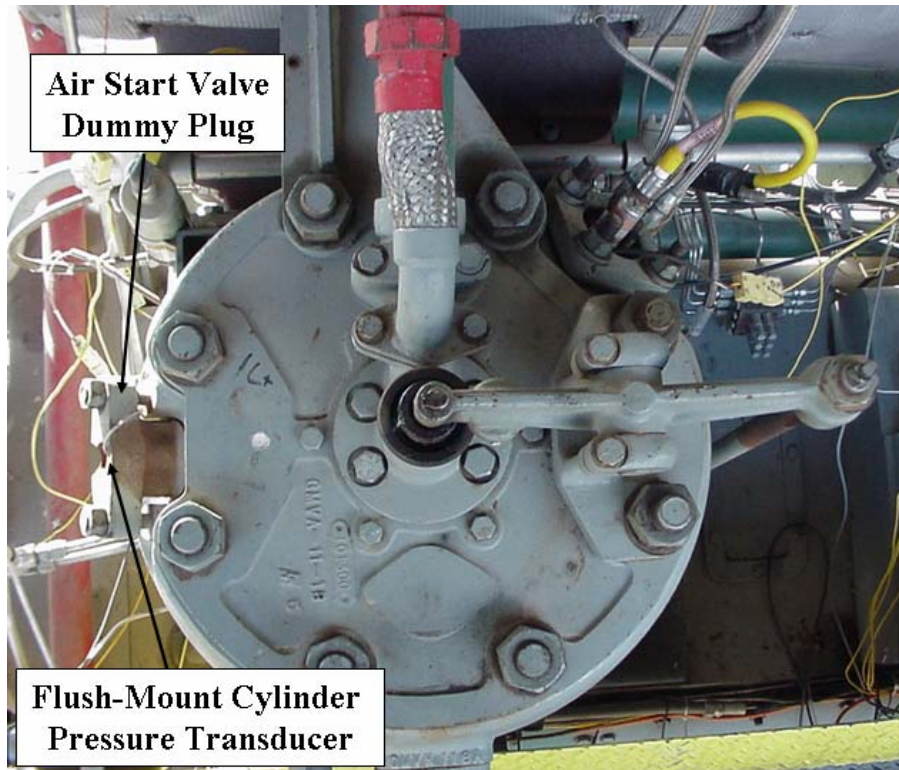


Figure 3-19. Photograph of Dynamic Pressure Sensor Installation for Engine Cylinder

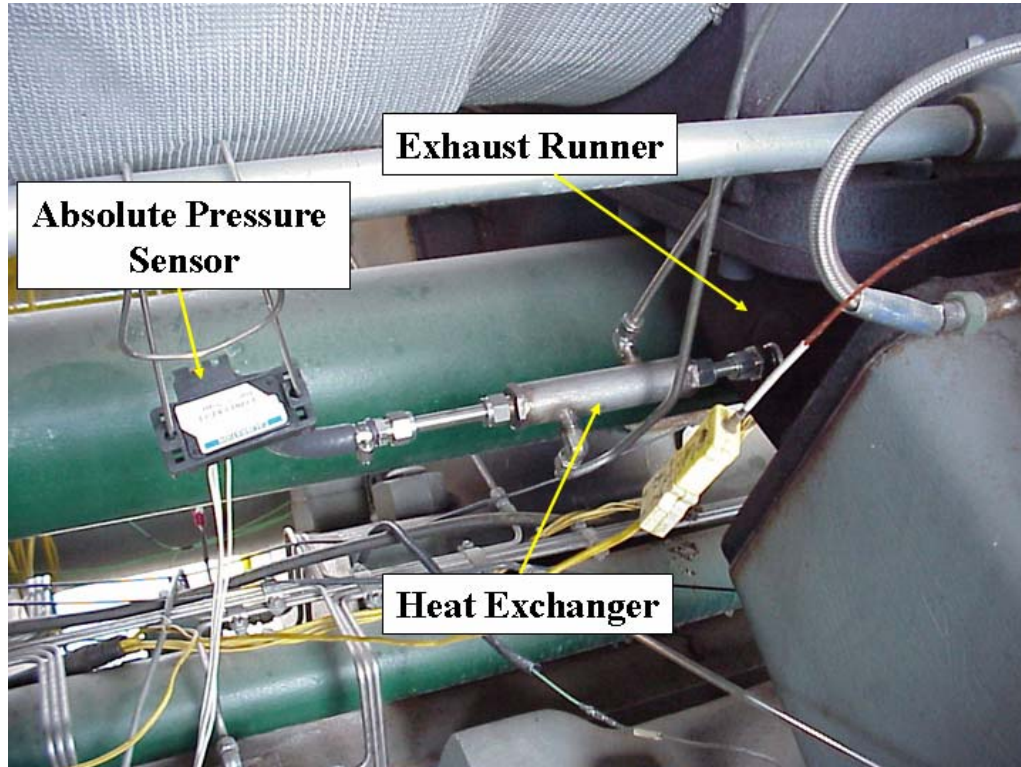


Figure 3-20. Photograph of Dynamic Exhaust Pressure Sensor in Exhaust Runner

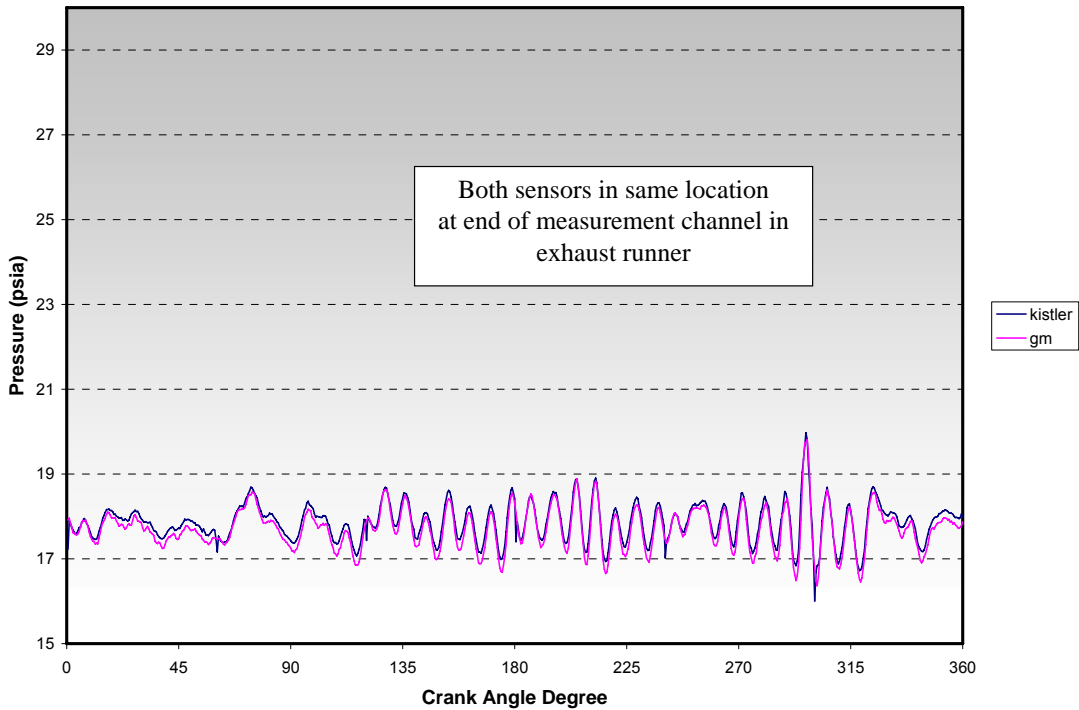


Figure 3-21. Comparison of Dynamic Exhaust Pressure Sensor to Kistler Piezo-Resistive Sensor at End of Measurement Channel in Exhaust Runner

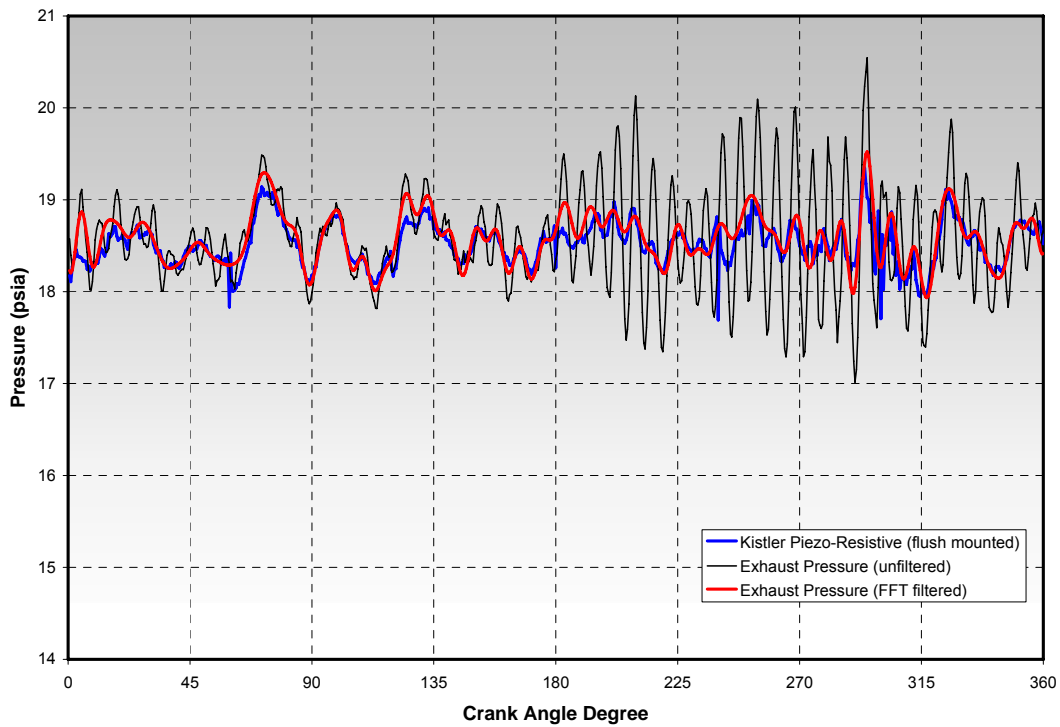


Figure 3-22. Comparison of FFT-Filtered Dynamic Exhaust Pressure Sensor to Flush-Mounted Kistler Piezo-Resistive Sensor in Exhaust Runner

- *Dynamic Pressure in Exhaust Manifold Plenum* – A new sensor was installed in the exhaust manifold plenum near the turbocharger. This measurement is required to capture the dynamic pressure pulsations in the exhaust manifold plenum and provide data to characterize the dynamic flow through the exhaust manifold. A Kistler piezo-resistive absolute pressure transducer was utilized for this measurement. This sensor was calibrated via a deadweight tester. A photograph of the exhaust manifold dynamic pressure sensor as installed for testing is provided in Figure 3-23.
- *Dynamic Pressure in Inlet Manifold Plenums* – Prior to the air balance investigation, only the left inlet manifold was instrumented for dynamic inlet plenum pressure. An additional dynamic pressure sensor was added to the right inlet manifold plenum to capture the dynamic pressure pulsations of the exhaust from each cylinder’s ports. These sensors are of a thin-film strain gage type, like those utilized in the exhaust manifold runners. A photograph of the left bank inlet manifold dynamic pressure sensor as installed for testing is provided in Figure 3-24.
- *Pitot Tubes in Inlet Manifold Runners* – Pitot tubes were installed in the inlet runners from the manifold log to Cylinders 1L and 3L. The pitot tubes were connected to delta-pressure sensors referencing the intake manifold log pressure. The delta-pressure sensors used were Sensotec strain-gage type transducers. A photograph of the pitot tubes installed in Cylinder 1L intake runner is provided in Figure 3-25.
- *Dynamic Pressure in Fuel Valves* – Dynamic pressure sensors were installed in the supply elbows to fuel valves in Cylinders 1L and 3L. The sensors used were Kistler piezo-resistive 4045A5 absolute pressure transducers. Measurement of the dynamic fuel pressure in these cylinders was desired to investigate the fuel admission rate and resulting effect on the cylinder pressure traces. This data was also desired to investigate variance in cylinder-to-cylinder air/fuel ratio.

The complete instrumentation package on the laboratory GMVH-6 engine is listed in Table 3-3.

In addition to the many measurements for engine performance and emissions, several static measurements were made of the engine geometry. These geometric measurements have been determined to be of critical importance for proper simulation of the engine. The key geometric parameters are compression ratio, port timing, and port area for each cylinder of the test engine. In order to conduct the many detailed measurements, the engine was disassembled. A list of the many static measurements taken on each cylinder is provided in Table 3-4. From these measurements, several calculated parameters were derived and discussed in the next section.

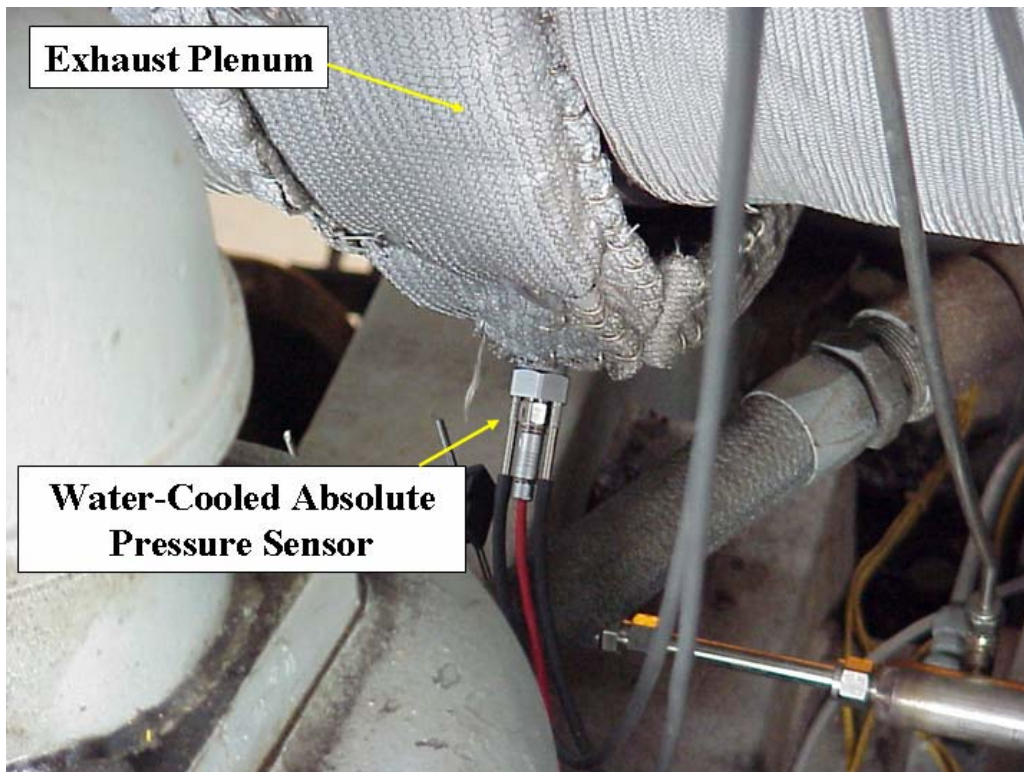


Figure 3-23. Photograph of Dynamic Exhaust Pressure Sensor in Exhaust Manifold

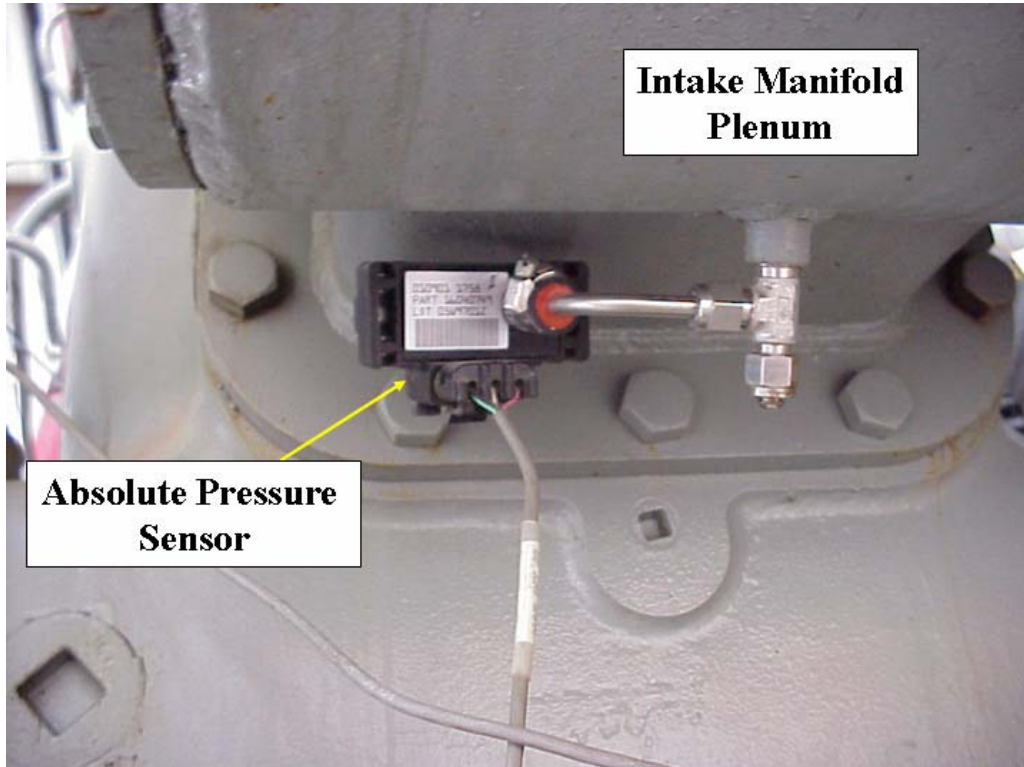


Figure 3-24. Photograph of Dynamic Intake Pressure Sensor in Intake Manifold



Figure 3-25. Photograph of Pitot Tubes in Cylinder 1L Intake Runner

Table 3-3. Time-Averaged and Crank-Angle Resolved Measurements on GMVH

Time-Averaged Measurements	
Engine Speed	Oil Pressure
Turbocharger Shaft Speed	Turbocharger Oil Pressure
Turbocharger Wastegate Position	Coolant Inlet & Outlet Pressure
Engine Torque	Pre-Turbine Pressure
Total Fuel Flow	Stack Pressure
Pre-Chamber Fuel Flow	Compressor Inlet Temperature
Fuel Gas Composition	Compressor Left & Right Outlet Temperatures
Fuel Gas Heating Value	Inlet Manifold Left & Right Temperatures
Total Air Flow	Fuel Header Temperature
Barometric Pressure	Pre-Chamber Header Temperature
Ambient Temperature	Individual Cyl. Exhaust Runner Temperatures
Ambient Humidity	Pre-Turbine Temperature
Exhaust NOx Concentration	Post-Turbine Temperature
Exhaust CO Concentration	I/C Inlet Left & Right Water Temperatures
Exhaust HC Concentration	I/C Outlet Left & Right Water Temperatures
Exhaust CO2 Concentration	Oil Sump Temperature
Exhaust O2 Concentration	Oil Inlet Temperature
Exhaust Equivalence Ratio	Turbocharger Oil Inlet Temperature
Inlet Manifold Left & Right Pressures	Coolant Inlet & Outlet Temperatures
Fuel Header Pressure	Individual Cyl. Head Temperatures
Pre-Chamber Header Pressure	Dynomometer Inlet & Outlet Temperatures
Crank-Angle Resolved (Dynamic) Measurements	
Cylinder 1L Firing Pressure	Cylinder 1L Exhaust Runner Pressure
Cylinder 2L Firing Pressure	Cylinder 2L Exhaust Runner Pressure
Cylinder 3L Firing Pressure	Cylinder 3L Exhaust Runner Pressure
Cylinder 1R Firing Pressure	Cylinder 1R Exhaust Runner Pressure
Cylinder 2R Firing Pressure	Cylinder 2R Exhaust Runner Pressure
Cylinder 3R Firing Pressure	Cylinder 3R Exhaust Runner Pressure
Left Inlet Manifold Plenum Pressure	Right Inlet Manifold Plenum Pressure
Cylinder 1L Pre-Chamber Firing Pressure	Exhaust Manifold Plenum Pressure

Table 3-4. Static Measurements on Each Cylinder of GMVH

Piston Stroke (BDC to TDC)	Cylinder Bore (~1" from top)
Connecting Rod C-C (cyl 1L only)	Piston TDC Height (from cylinder top)
Pre-Chamber Volume	Piston Top Ring Land Diameter
Cylinder Inlet Volume (inc.ports)	Piston Top Ring Land Height
Cylinder Intake Flange Width	Piston Dome Angle
Cylinder Intake Flange Height	Piston Dome Height from edge
Cylinder Exhaust Flange Width	Piston Bowl Depth
Cylinder Exhaust Flange Height	Piston Bowl Volume (inc puller-hole)
Cylinder Head Volume	Piston Pin Center to Crown Height
Cylinder Head Gasket Step	Top Int Port to Gasket Step - A
Cylinder Head Gasket Thickness	Top Int Port to Gasket Step - B
Exhaust Port "Shape" - A	Top Int Port to Gasket Step - C
Exhaust Port "Shape" - B	Top Int Port to Gasket Step - D
Exhaust Port "Shape" - C	Top Int Port to Gasket Step - E
Exhaust Port "Shape" - D	Top Int Port to Gasket Step - F
Exhaust Port "Shape" - E	Top Int Port to Gasket Step - G
Top Exh Port to Gasket Step - A	Top Int Port to Gasket Step - H
Top Exh Port to Gasket Step - B	Intake Port to Edge Width - A
Top Exh Port to Gasket Step - C	Intake Port to Edge Width - B
Top Exh Port to Gasket Step - D	Intake Port to Edge Width - C
Top Exh Port to Gasket Step - E	Intake Port to Edge Width - D
Exhaust Port Edge Width - A	Intake Port to Edge Width - E
Exhaust Port Edge Width - B	Intake Port to Edge Width - F
Exhaust Port Edge Width - C	Intake Port to Edge Width - G
Exhaust Port Edge Width - D	Intake Port to Edge Width - H
Exhaust Port Edge Width - E	Intake Port Edge Height - A
Exhaust Port Min Width - A	Intake Port Edge Height - B
Exhaust Port Min Width - B	Intake Port Edge Height - C
Exhaust Port Min Width - C	Intake Port Edge Height - D
Exhaust Port Min Width - D	Intake Port Edge Height - E
Exhaust Port Min Width - E	Intake Port Edge Height - F
Exhaust Port Edge Height - A	Intake Port Edge Height - G
Exhaust Port Edge Height - B	Intake Port Edge Height - H
Exhaust Port Edge Height - C	Intake Port Angle - A
Exhaust Port Edge Height - D	Intake Port Angle - B
Exhaust Port Edge Height - E	Intake Port Angle - C
Exhaust Port Min Height - A	Intake Port Angle - D
Exhaust Port Min Height - B	Intake Port Angle - E
Exhaust Port Min Height - C	Intake Port Angle - F
Exhaust Port Min Height - D	Intake Port Angle - G
Exhaust Port Min Height - E	Intake Port Angle - H

3.3.2 CYLINDER FLOW TEST RIG

Cylinders 1L and 3L, representing a high and low compression pressure on a given bank, were removed from the base and flow tested. During disassembly, it was found that Cylinder 1R had a different exhaust port shape from the other cylinders and was removed to be flow tested as well. The flow testing was conducted to measure the discharge coefficient of both intake and exhaust ports versus open area. Accurate discharge coefficients were required for simulation. In addition, a review of allowable port shape on the manufacturing drawings gave concern that variance in port shape from cylinder-to-cylinder could be a large contributor to flow imbalance. The effects of port shape also needed to be characterized and accounted for in the simulations.

A flow test rig was assembled specifically for this effort. This test rig featured a compressed air storage and regulation system, meter run, data acquisition, and cylinder stand. Photographs of the flow bench rig are shown together in Figure 3-26. The compressed air system featured three 1,050-gallon cylinders, charged to 250 psig. The outlet of the compressed air cylinders was connected to a regulator and control valve for setting the desired pressure versus mass flow of air into the flow bench. The meter run was fabricated from Schedule 40 PVC pipe and featured an ASME nozzle for flow measurement. Two sizes of flow nozzles, 2 and 4 inch, were interchangeably used for low and high flows. Mass flow was calculated from the volumetric flow measurements using standard equations given in ASME codes. The cylinder stand was fabricated to hold and seal the cylinder during testing. An adjusting screw protruded from the bottom of the stand to allow for adjustment of piston height to achieve the desired port open fraction. A Vernier scale mounted on the bottom of the stand was used for measuring piston travel. A fixture was later fabricated to mount on the cylinder studs to lock the piston and prevent lifting due to air pressure leaking past the rings and under the piston. The data acquisition system acquired data at a rate of 6 Hz and included the measurements given in Table 3-5.

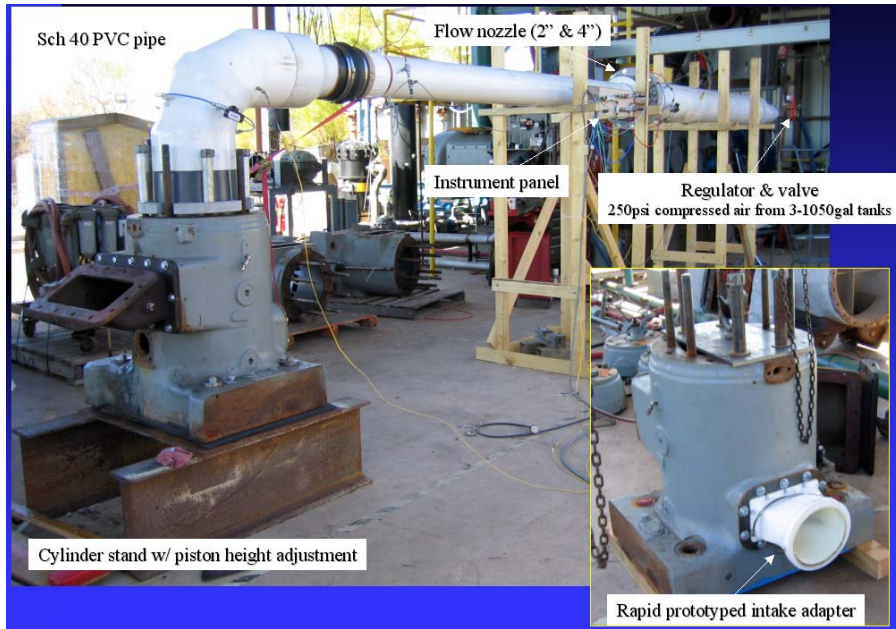


Figure 3-26. Photographs of GMVH Cylinder Flow Bench

Table 3-5. GMVH Cylinder Flow Bench Measurements

Supply Static Pressure (upstream)	Ambient Pressure
Supply Temperature (upstream)	Ambient Temperature
4" Nozzle delta-Pressure	Ambient Dewpoint Temperature
2" Nozzle delta-Pressure	Air Tank Pressure
Plenum Static Pressure (downstream)	Piston Travel from BDC
Plenum Temperature (downstream)	

4. RESULTS AND DISCUSSION: CHARACTERISTICS, METHODS, NEEDS, TECHNOLOGIES

4.1 SECTION OVERVIEW

The project has addressed a series of characteristics, methods, needs, and technologies, associated with slow speed integral engines/compressors. It has defined characteristics of these machines, using one or more methods of testing, monitoring, and evaluation; it has identified and documented a number of associated technology needs; and it has enhanced, developed, or evaluated a number of technologies, which potentially benefit the operation of such compressors. This report section presents and discusses the body of knowledge developed by this project under these headings and illustrates this knowledge with graphical or tabular results from the various tests. Table 4-1 lists and sorts the topics presented in this section into Characteristics, Methods, Needs, and Technologies. In addition, Table 4-1 identifies which of the project goals most directly relate to each topic:

- To Reduce Fuel Consumption
- To Enhance Capacity
- To Enhance Integrity

Inevitably a project of this magnitude does not set to rest all questions it raises or that existed at the start of the project. This section notes such open questions. In some cases, the project has reinforced existing knowledge with new quantitative data.

The remainder of this section contains four main additional sub-sections and, within each sub-section, a discussion of the topics listed in Table 4-1. Table 4-1 identifies the paragraph or “sub-sub-section” number within each sub-section for each topic.

This project has sought throughout to view the integral engine compressor as a system. This system has several components, and past research projects have often focused on a single component such as engine, compressor, power transmission path, or compressor piping. This project has endeavored to provide significant attention both to each component and to the system as a whole. In discussing measurement methods, component and system characteristics, and limitations in state of the art methods for the entire system, it is believed the project and report provide a unique window on the entire compression system represented by an integral engine/compressor and the piping, which connects it to the pipeline.

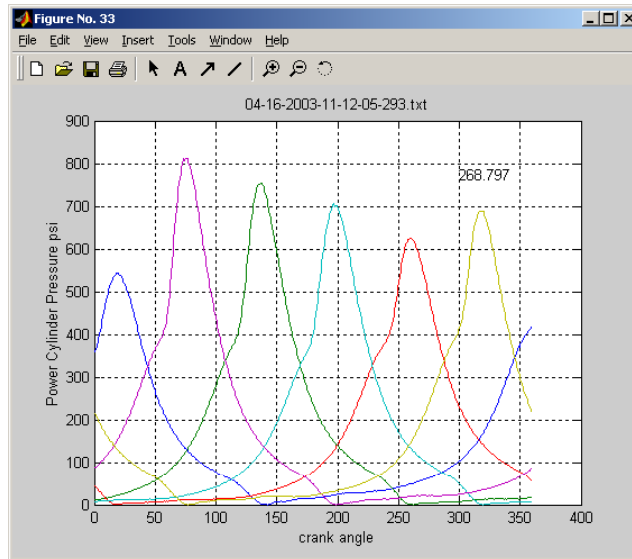
4.2 CHARACTERISTICS OF INTEGRAL ENGINE COMPRESSORS

4.2.1 CYLINDER-TO-CYLINDER COMBUSTION IMBALANCE

The power cylinders on large bore slow speed integral engine/compressors do not in general combust equally. Figure 4-1 illustrates this characteristic with pressure traces for all six-power cylinders on an HBA-6T, tested in April 2003, which exhibits widely varying peak pressures from a low of 550 to a high of 810 PSI. Each trace represents the result of averaging 32 cycles for the cylinder in question, so the differences arise in the average behavior of each cylinder; as subsequent data will show additional variability arises from cycle-to-cycle. This report will refer to the difference between minimum and maximum values for cycle averaged peak pressure as the average spread.

Table 4-1. Categorization of Topics and Technologies Discussed and Illustrated in Section 4

SUB-SECTION	TOPICS AND TECHNOLOGIES	RELATED PROJECT OBJECTIVE		
		REDUCE FUEL CONSUMPTION	INCREASE CAPACITY	ENHANCE INTEGRITY
	CHARACTERISTICS OF INTEGRAL ENGINE/COMPRESSORS			
4.2.1	Cylinder-to-Cylinder Combustion Imbalance	X		X
4.2.2	Cycle-to-Cycle Combustion Variability	X		X
4.2.3	Cylinder-to-Cylinder Air Imbalance	X		X
4.2.4	Cycle-to-Cycle Air Imbalance	X		
4.2.5	Dynamic Variability in Manifold Pressures	X		
4.2.6	Variability in Equivalence Ratio	X		
4.2.7	Influence of Load on Heat Rate	X		
4.2.8	Influence of Timing on Heat Rate	X		
4.2.9	Influence of Timing on Crank Strain			X
4.2.10	Influence of Combustion Balancing on Heat Rate	X		
4.2.11	Influence of Combustion Balancing on Crank Strain			X
4.2.12	System-Wide Variation in Compressor Efficiency	X	X	
4.2.13	Mechanical Efficiency	X	X	
4.2.14	Installation Losses	X	X	
4.2.15	System Thermal Efficiency	X	X	
4.2.16	Capacity		X	
4.2.17	Influence of Time from Cold Start on Power Transmission Efficiency	X	X	
4.2.18	Pulsations from Reciprocating Compressor Action			X
4.2.19	Speed/Power Modulation (Multiple Compressors "Beating" Against Each Other)	X	X	X
4.2.20	Square Law Losses in Valves, Orifices, and Pipe Area Changes	X	X	
	METHODS FOR TESTING, CHARACTERIZATION, AND MONITORING			
4.3.1	Suite of Instruments and Data Acquisition System	X	X	X
4.3.2	Assessing How Operating Changes Influence Heat Rate Variation with Load	X		
4.3.3	Monitoring Rod Load	X	X	X
4.3.4	Isolating Mechanical Losses with Rod Load Measurement	X	X	
4.3.5	Monitoring Compressor Cylinder Temperature Rise	X	X	
4.3.6	Monitoring Frame Vibration			X
4.3.7	Monitoring Instantaneous Rotational Velocity			X
4.3.8	Isolating Installation Losses	X	X	
4.3.9	Monitoring Crank Strain			X
	TECHNOLOGY NEEDS OF INTEGRAL ENGINE/COMPRESSORS			
4.4.1	Combustion Balancing	X		X
4.4.2	Balanced Air to Each Power Cylinder	X		X
4.4.3	Accurate Monitoring of Power & Torque	X		X
4.4.4	Unit Throughput Monitoring and Measurement		X	
4.4.5	Protection Against Damaging Detonation	X		X
4.4.6	Low Loss Pulsation Control	X	X	X
4.4.7	Capacity and Horsepower Recovery on Low Efficiency Compressors	X	X	
4.4.8	Refined Knowledge of Mechanical Losses			
	TECHNOLOGIES DEVELOPED, ENHANCED, OR EVALUATED			
4.5.1	Standard Deviation Balancing	X		X
4.5.2	Combustion pressure Ratio Balancing	X		X
4.5.3	Closed Loop Waste-Gate Control	X		
4.5.4	Closed Loop Fuel Rate Control for Carbureted 4-Stroke	X		
4.5.5	Rod Load Monitor	X		X
4.5.6	Strain Data Capture Module			X
4.5.7	High Pressure Fuel Injection	X		
4.5.8	Detonation Detector	X		X
4.5.9	Digital Simulation of Interaction Between Compressor and Installed Piping			X
4.5.10	Side Branch Absorbers for Pulsation Control	X	X	X
4.5.11	In-Line Filter Bottles	X	X	X



Power Cylinder Pressures

Figure 4-1. Pressure Traces for All Six Power Cylinders on an HBA-6T, Illustrating the Average Spread in Peak Pressure (Test #1 at Kinder Station (El Paso Station 823); April 2003)

The potential causes for such imbalance include unequal fuel quantities injected into each cylinder, differences in the amount of air supplied to each cylinder, differences in residual exhaust gas, differences in slider-crank kinematics, or differences in port, cylinder, and piston geometry.

Figure 4-2 illustrates the imbalance for the cylinders of a GMW10 engine, which has had a turbocharger and high-pressure fuel injection installed. This engine also has an automatic balancing system installed which adjusts the amount of fuel injected to each cylinder as guided by an internal algorithm to equalize the cycle averaged peak pressure; as a result, these cylinders exhibit only 70 PSI difference between the minimum of 465 and the maximum of 535 PSI—a spread of less than 15%, which most practitioners of power cylinder balancing would regard as reasonably well balanced.

As long as the difference in peak pressures results from differences in fuel supplied to cylinders with equal cylinder-piston geometries, equal kinematics, equal trapped exhaust, and equal trapped air, the balancing process described above makes sense and should equalize both peak firing pressure and air/fuel ratio. However, the existence of such equality is unlikely, and this balancing process will in many cases inappropriately compensate; by equalizing peak firing pressure, it will force the air/fuel ratios to differ, and inherently force the combustion process to differ from cylinder-to-cylinder. In general, only surrogates exist for measured cylinder-by-cylinder trapped air/fuel ratio; the report will discuss alternative balancing strategies, which seek to equalize combustion using such surrogates.

Even carbureted four-stroke engines can exhibit cylinder-to-cylinder differences in peak pressure. Figure 4-3 demonstrates this for a KVG103, with ten power cylinders, by comparing the average peak pressure for cylinders one through nine with the average peak pressure for cylinder ten. Throughout most of the tests on this engine, for which standard practice kept

operation lean, Cylinder 10 burnt with 100 PSI lower peak pressure than the other cylinders, in spite of the fact that the carburetor should deliver the same fuel/air mixture to a common manifold. Only with significantly richened operation would Cylinder 10 exhibit peak pressure similar to the other cylinders. With no adjustment possible on the fuel/air mixture to an individual cylinder, some extreme dynamic flow phenomenon under lean conditions seems the most likely explanation.

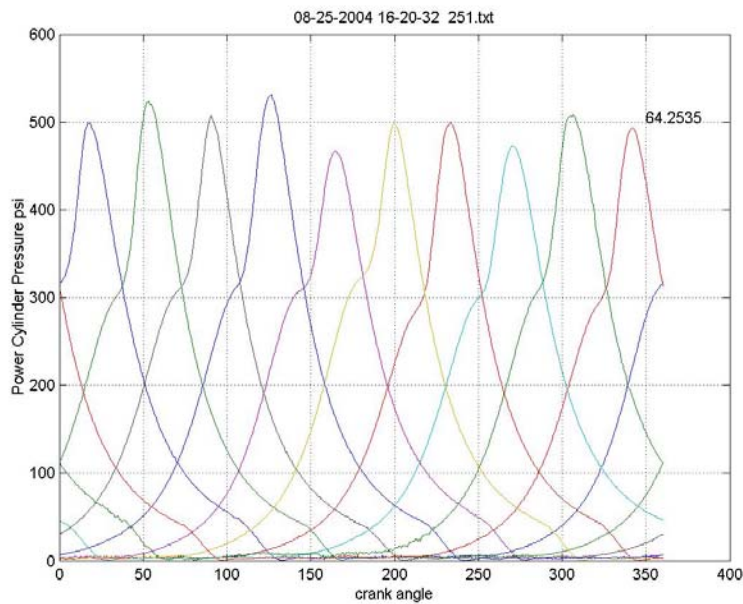


Figure 4-2. Representative Pressure Data for Ten Power Cylinders; GMW10 with a Turbocharger, High-Pressure Fuel Injection and Automated Peak Pressure Control (Williams' Station 60, Unit 6; August 25, 2004)

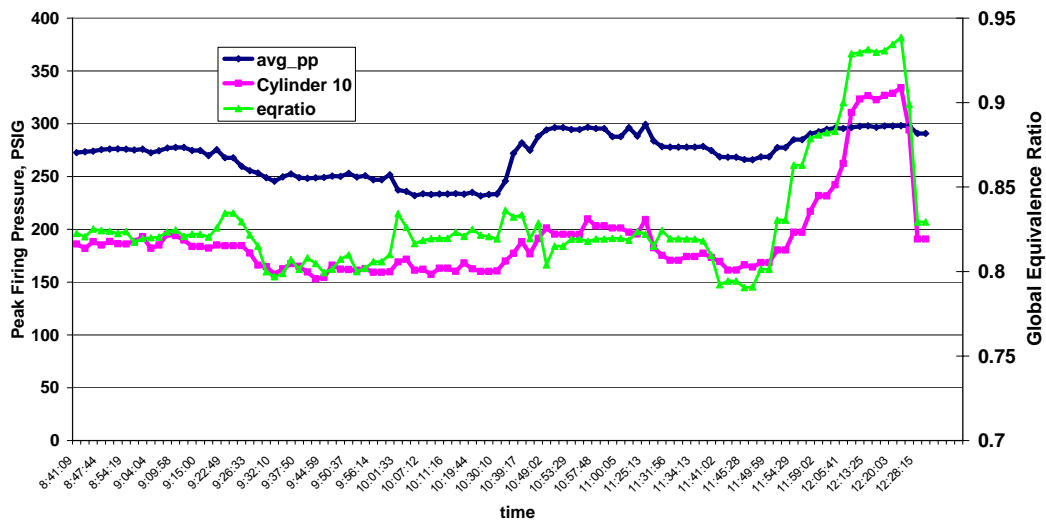


Figure 4-3. KVG103 – Peak Firing Pressure Averaged for All Cylinders and for Cylinder 10 Alone, with Global Equivalence Ratio Superimposed (Duke Thomaston Station; Wed., Nov. 3, 2004)

In general, high and low peak pressure cylinders are not expected to precisely balance each other out, whether we consider potential damage from overload, the influence of low and high equivalence ratio, the extremes of misfire and detonation, or the influence of high and low temperature. Bringing high and low cylinder peak pressures closer to the mean is the rationale for combustion balancing; however, the expected benefit in reduced fuel consumption or overload damage essentially depends on the non-linearity in how the quantity in question varies about the mean. The discussion in subsequent sub-sections will further quantify some of these factors.

4.2.2 CYCLE-TO-CYCLE COMBUSTION VARIABILITY

In addition to varying from cylinder-to-cylinder, combustion varies from cycle-to-cycle in any cylinder. Figure 4-4 provides a clear illustration of this characteristic with 20 successive combustion cycles for a single power cylinder (Cylinder 2) of a GMW10 with turbocharger and high-pressure fuel injection. The 20 cycles vary substantially, with even successive cycles differing by 180 PSI in peak pressure about an average of about 450 PSI. Figure 4-5 presents this variability for an unmodified GMW10, in terms of standard deviation for cycle-to-cycle variation of peak pressure (averaged across the cylinders). This standard deviation ranges from 75 to 85 PSI during about five hours of testing. With the average peak pressure at about 600 PSI most of the time, the coefficient of variation of peak pressure (standard deviation/mean) is about 13.3%. Thus, the cycle-to-cycle variation has the same order of magnitude as the cylinder-to-cylinder variation for this and for most two-stroke engines. The other trace on Figure 4-5 is combustion pressure ratio, which will be discussed subsequently.

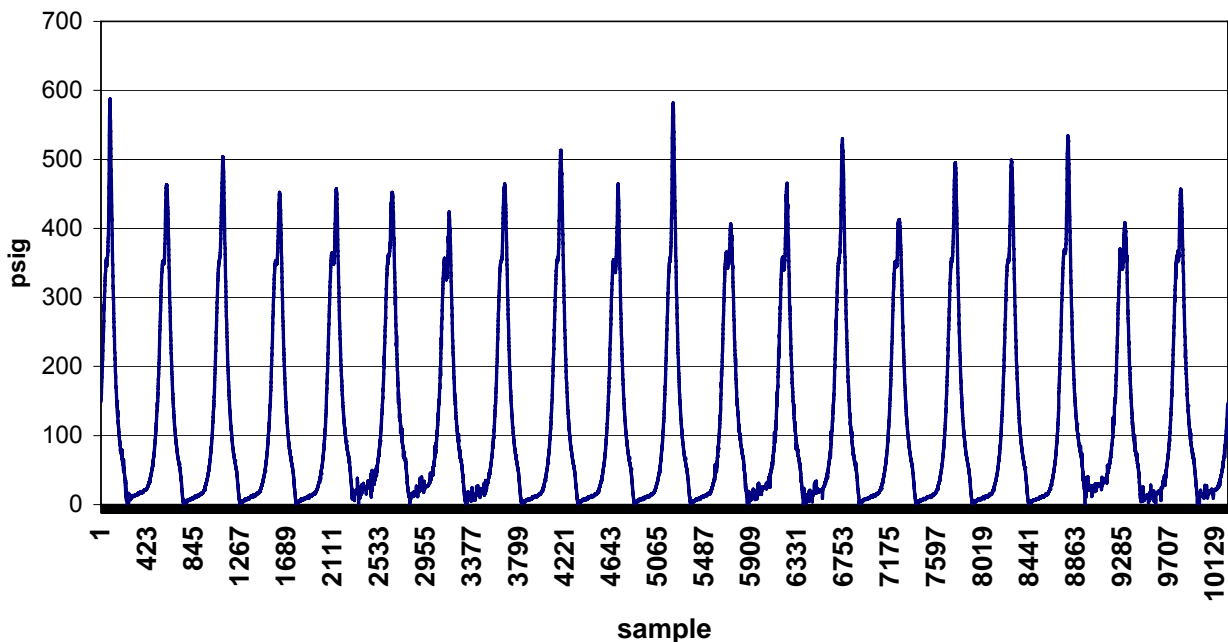


Figure 4-4. Typical 20 Successive Cycles, Illustrating Cycle-to-Cycle Variation in Peak Pressure for a GMW10 with a Turbocharger and High-Pressure Fuel Injection (Power Cylinder 2; Williams' Station 40 (Sour Lake); August 2003)

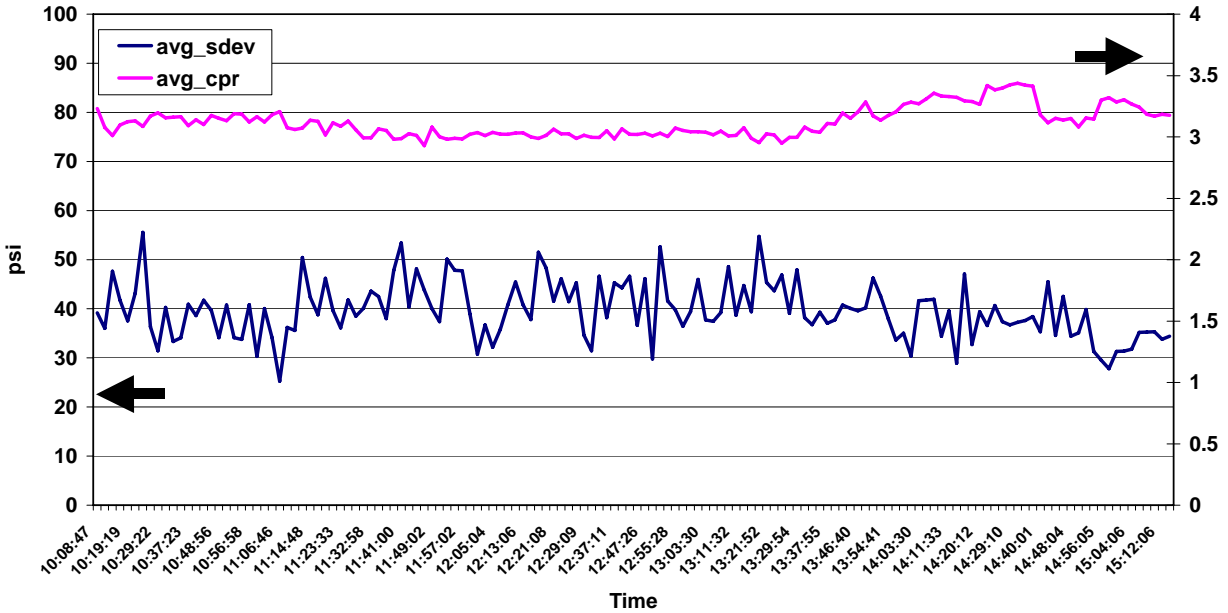


Figure 4-5. Engine Average Cycle-to-Cycle Standard Deviation in Peak Firing Pressure; and Ratio of Peak Firing Pressure to Compression Pressure (CPR) for an Unmodified GMW10 (Williams' Station 60; February 2004)

Figure 4-6 shows in similar format to Figure 4-5 that the standard deviation for a turbocharged HBA-6T during tests in April 2004 was around 60 PSI. With a typical peak pressure of around 520 PSI, the coefficient of variation of 11.5% is only slightly less than for the GMW10.

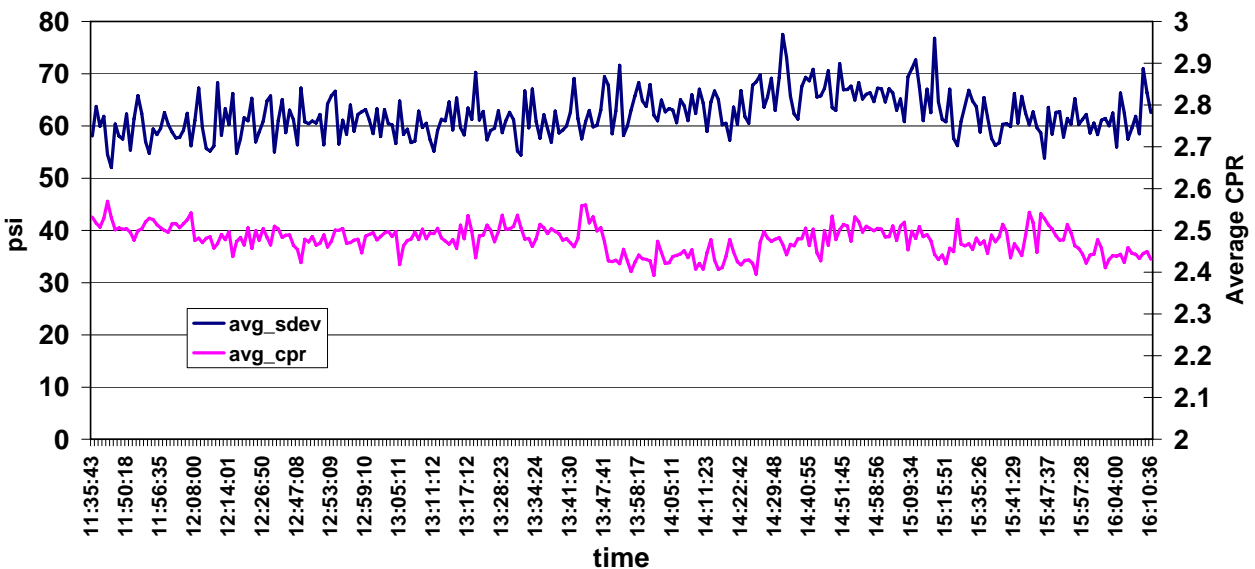


Figure 4-6. CPR and Standard Deviation for Peak Firing Pressure; Averaged Across the Six Power Cylinders for a Turbocharged HBA-6T (Kinder (El Paso Station 823); April 21, 2004)

Figure 4-7 compares the coefficients of variation for cycle-to-cycle variation in peak firing pressure of five different engines or engine conditions: an HBA-6T; a modified GMW10 (Station 40); another GMW10 both before and after modification (Station 60); and a KVG103. The range of COV is from 8.5% to 13.3%. The two modified GMW10 engines exhibit different COV values, with the lower COV corresponding to richer operation (0.42 measured equivalence ratio compared to 0.27).

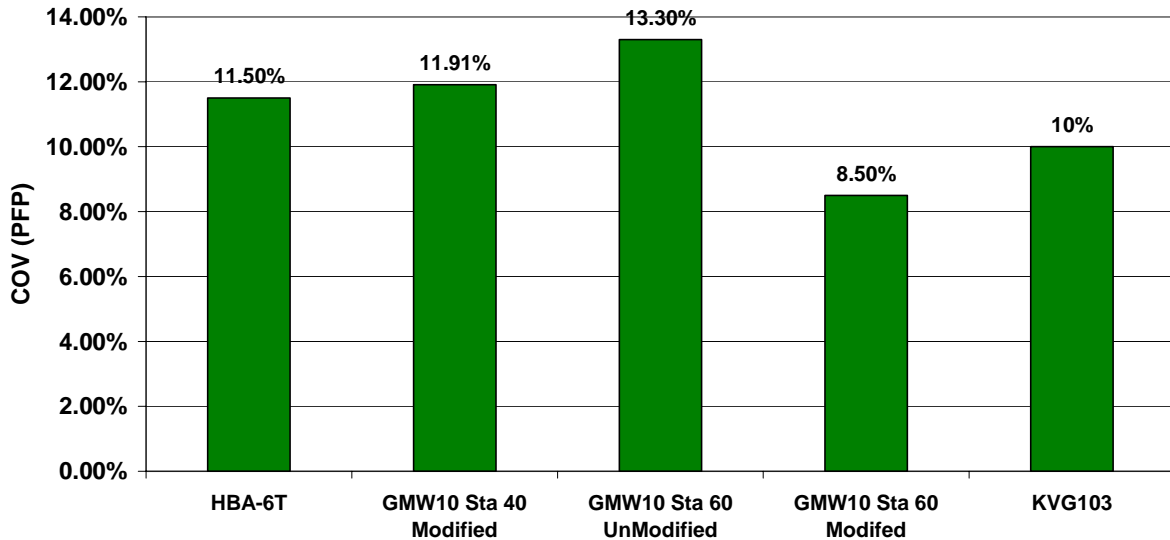


Figure 4-7. Coefficient of Variation for Cycle-to-Cycle Variation in Peak Firing Pressure—Comparison of Five Engines

The cycle-to-cycle variability complicates the process of balancing by making it difficult to define a cylinder’s peak firing pressure without substantial averaging and, therefore, providing imprecise indication of the fuel adjustments required to equalize peak firing pressure. Since it implies swings in peak pressure on both the low and high sides of the mean, this variability makes these engines prone to misfires on the lean side and to detonation on the high side.

4.2.3 CYLINDER-TO-CYLINDER AIR IMBALANCE

Prior to ignition, the development of pressure within a power cylinder depends on the air and fuel gas trapped in the cylinder after the inlet port closes and the subsequent change in cylinder volume with rotation of the crankshaft. Throughout the work reported here, the cylinder pressure at a point 20 degrees before Top Dead Center has been termed “compression pressure.” While consistently before ignition, this point reflects substantial compression of trapped air as a result of reduction in cylinder volume. Ideally, such a pressure would be equal across the cylinders, but Figure 4-8 makes clear that cylinder compression pressure can vary by 30 PSI from 280 to 310 PSI for the six cylinders of this HBA-6T, a range of 10% for the engine. Figure 4-9 shows the cylinder-to-cylinder difference in compression pressure for a GMW10 with Turbocharger and high-pressure fuel. The range from 245 PSI or below, to 275 PSI or above represents over 11% of the mean. Figure 4-10 for another GMW10 shows a very similar range in compression pressure.

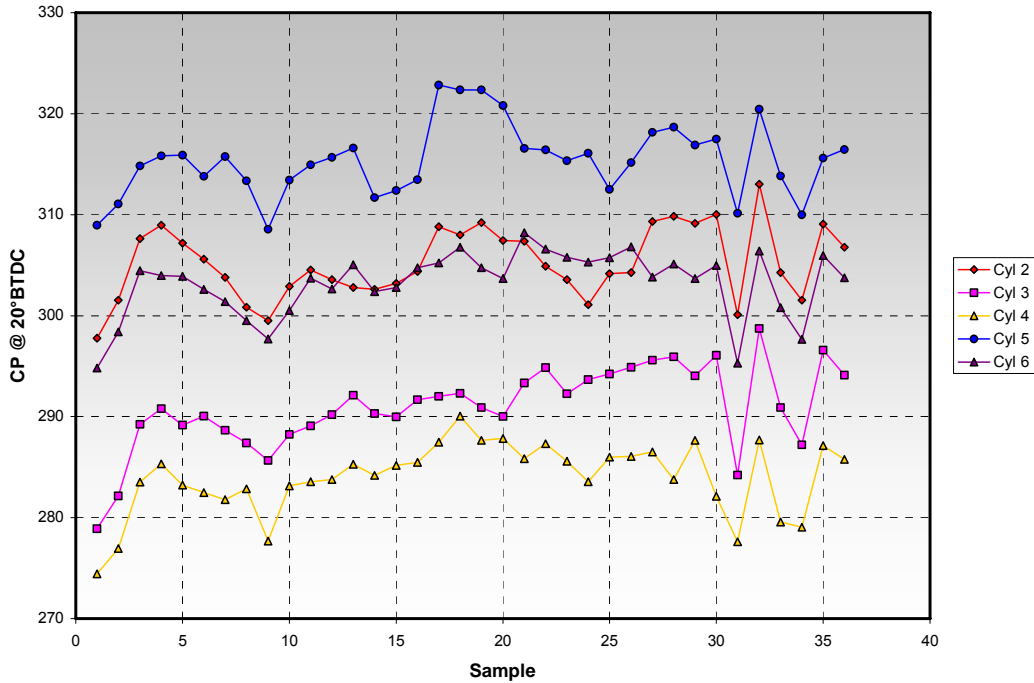


Figure 4-8. Cylinder Pressure 20 Degrees Before TDC (Compression Pressure for HBA-6T) (Kinder Station (EI Paso Station 823); April 2003)

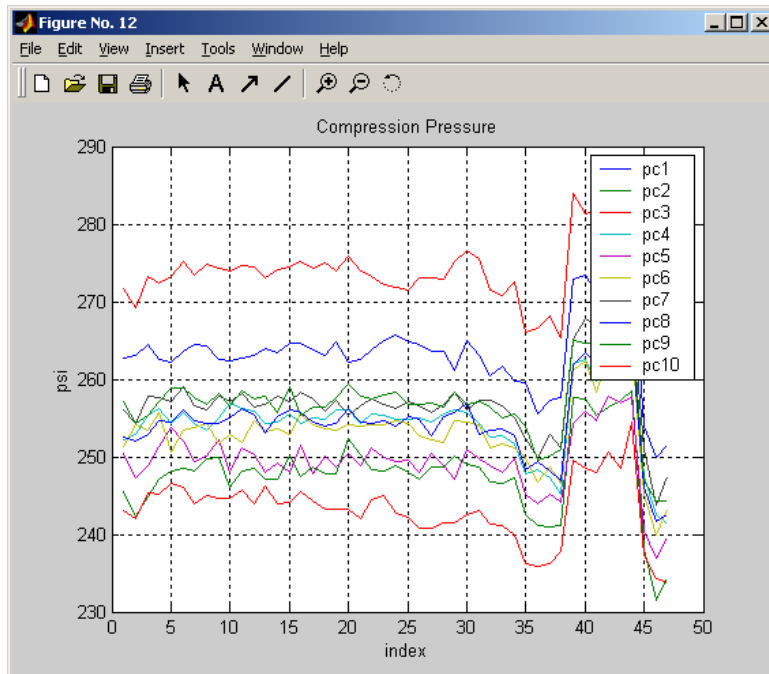


Figure 4-9. Power Cylinder Compression Pressure for GMW10 with a Turbocharger and High-Pressure Fuel Injection (Williams' Station 40 (Sour Lake); August 2003)

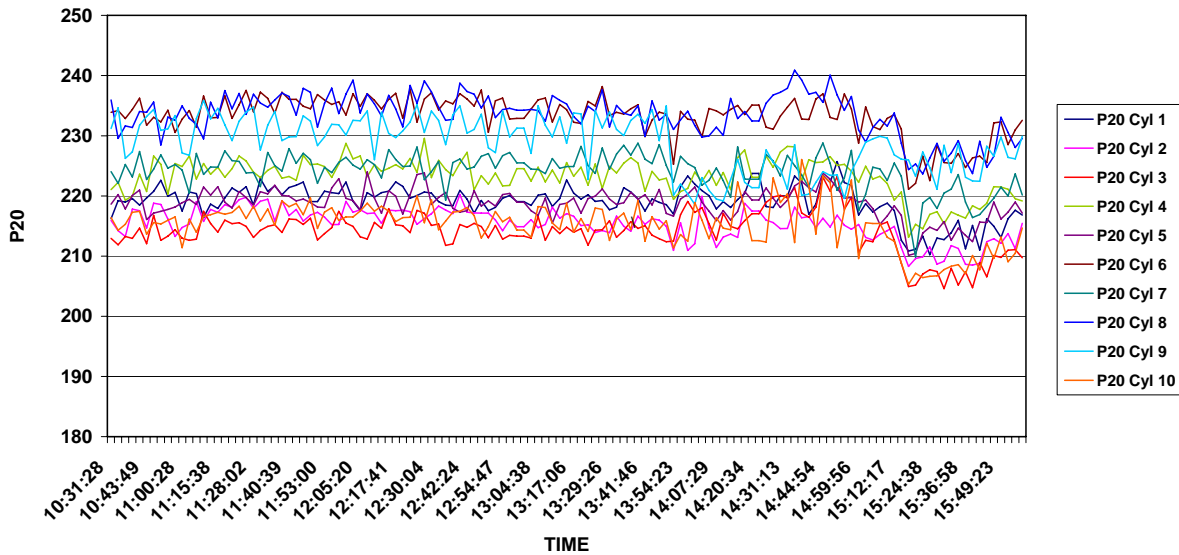


Figure 4-10. Power Cylinder Compression Pressure for GMW10; After Modification (Williams’ Station 60; August 26, 2004)

This range of compression pressure for three tested units appears very typical for this class of two-stroke engine. Since it results from compression of trapped air before combustion, a likely contributor to compression pressure imbalance is cylinder-to-cylinder difference in the mass of trapped air (Air Imbalance). This re-emphasizes that differences in peak firing pressure may result from differences other than just unequal fuel to the individual cylinders; compensating for such differences by balancing on peak pressure will tend to make the fuel/air equivalence ratios correspondingly unequal.

The widespread existence of compression pressure and trapped air imbalance led to an additional project phase whose objective was to investigate reasons for air imbalance and, guided by this investigation, to seek modifications, which would provide operators of these engines with options for reducing air imbalance.

4.2.4 CYCLE-TO-CYCLE AIR IMBALANCE

With wide variation in combustion both from cycle-to-cycle and from cylinder-to-cylinder, variation in compression pressure might be expected from cycle-to-cycle. However, Figure 4-11 makes clear that this is not the case. The standard deviations in compression pressure lie in the range 2.8 to 4.4 PSI—clearly one to two orders of magnitude lower than cycle-to-cycle standard deviation in peak firing pressure and one order of magnitude lower than the cylinder-to-cylinder variability in compression pressure. Interestingly, this set of data for cycle-to-cycle variability in compression pressure, obtained on an unmodified GMW10, was identical for every cylinder. This cycle-to-cycle consistency in the compression pressure indicates that compression pressure is a characteristic of the cylinder itself or of its location on the common manifolds for air and exhaust.

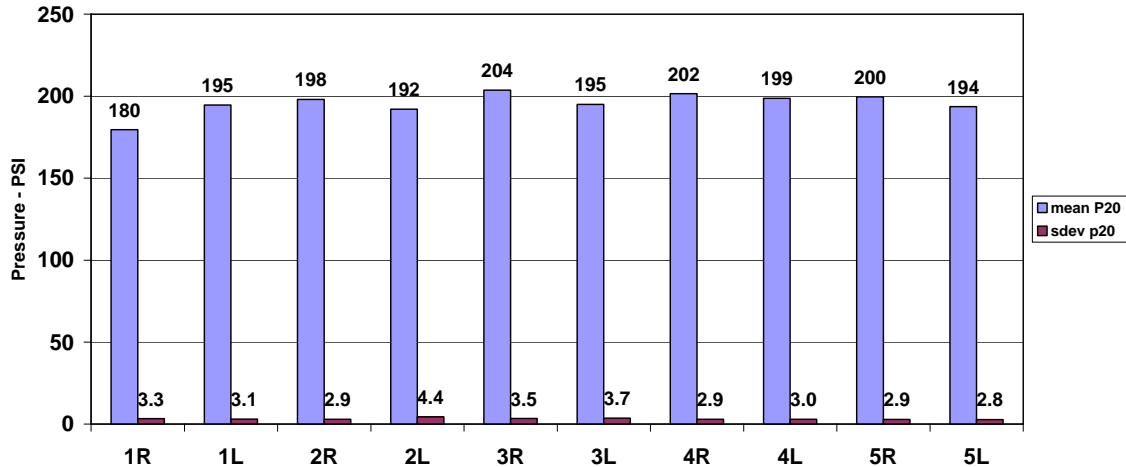


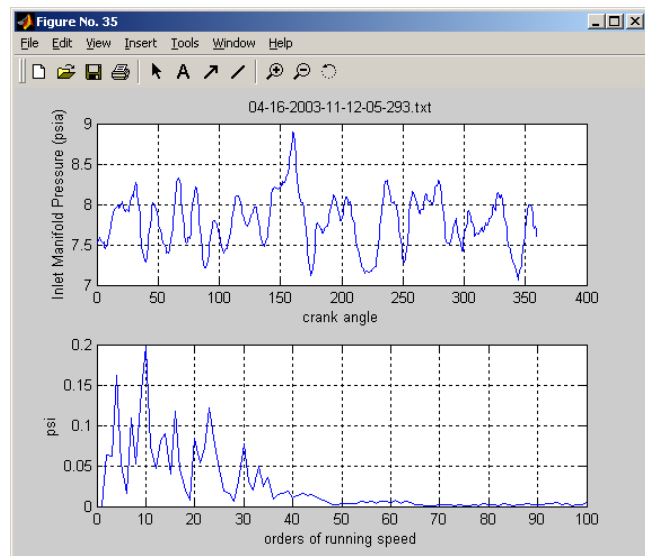
Figure 4-11. Mean and Standard Deviation for P20 (Pressure 20 DBTDC) as a Function of Cylinder for GMW10 Unmodified (Williams’ Station 60; February 2004)

To repeat the observations of the preceding paragraphs, compression pressure varies from cylinder-to-cylinder by 30 PSI or more, but varies from cycle-to-cycle by a factor of ten less. The factors leading to compression pressure differences should be better understood, but the difference in trapped air mass is a likely contributor; it will be shown in the next sub-section that the magnitudes of air and exhaust manifold dynamics indicate a likely source of air imbalance.

4.2.5 DYNAMIC VARIABILITY IN MANIFOLD PRESSURES

On two-stroke engines, one or two common manifolds deliver air to the power cylinders and the cylinders discharge exhaust gas to another common manifold. The flow modulations induced by the cylinder distributed along the length of each manifold cause pressure modulations with a range of engine order related frequencies and, if any of these frequencies tunes up with an acoustic length natural frequency of the manifold system, acoustic resonance will occur and amplify the pressure modulations. Figure 4-12 shows time and frequency domain modulation of inlet air manifold pressure, measured at one end of the air manifold for an HBA-6T engine. In this figure, the peak-to-peak variation of pressure approaches 2 PSI—about 25% of the mean air manifold pressure.

With only one pressure measurement location, the actual waveforms of pressure variation along the manifold length cannot be explicitly documented; however, it can be strongly argued, based on typical acoustic response



Inlet Air Manifold Pressure

Figure 4-12. Time and Frequency Modulation of Inlet Air Manifold Pressure; HBA-6T (Kinder Station (El Paso Station 823); April 2003)

characteristics that the pressure will vary along the length with similar amplitude to the variation with time. A 25% variation in air manifold pressure will have a distinct influence on the air pushed into a cylinder and represents a likely contributor to the variation observed in trapped air from cylinder-to-cylinder on this and other engines.

Figure 4-13 shows the peak-to-peak variation in both exhaust and inlet air manifold pressure during tests on a GMW10 with turbocharger and Enignuity’s high-pressure fuel injection system installed at Williams Sour Lake station (Station 40). The independent variable, “index,” in this figure represents the count for data sets obtained over a period of several hours testing. The exhaust manifold variation exceeds 50% of the average exhaust manifold pressure, and the air manifold variation is close to or above 20%. Based on the rationale presented in the previous paragraph, the implied variation of inlet and exhaust pressure from cylinder-to-cylinder would be expected to cause cylinder-to-cylinder variation in trapped air as observed on all engines tested with power cylinder pressure instrumentation on this project (typically 10% cylinder-to-cylinder variation in compression pressure).

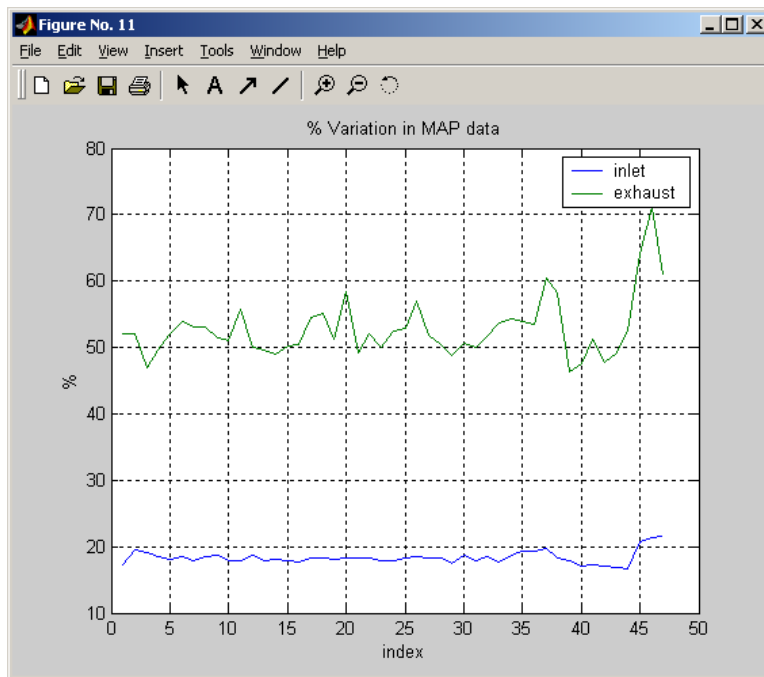


Figure 4-13. Variation in Inlet and Exhaust Pressures in a GMW10 with a Turbocharger and High-Pressure Fuel Injection (Williams’ Station 40 (Sour Lake); August 2003)

Figure 4-14 shows the instantaneous time and frequency domain variation for inlet air manifold pressure on an unmodified GMW10 (no turbo, flapper valve, normal fuel pressure). Here the peak-to-peak air manifold pressure variation approaches 50% of the mean. Based on this and the previously discussed figures, dynamic variation in time and along the length of air and exhaust manifolds is a widely observable characteristic of two-stroke engines, and likely contributes to cylinder-wise variation in compression pressure, trapped air, and combustion.

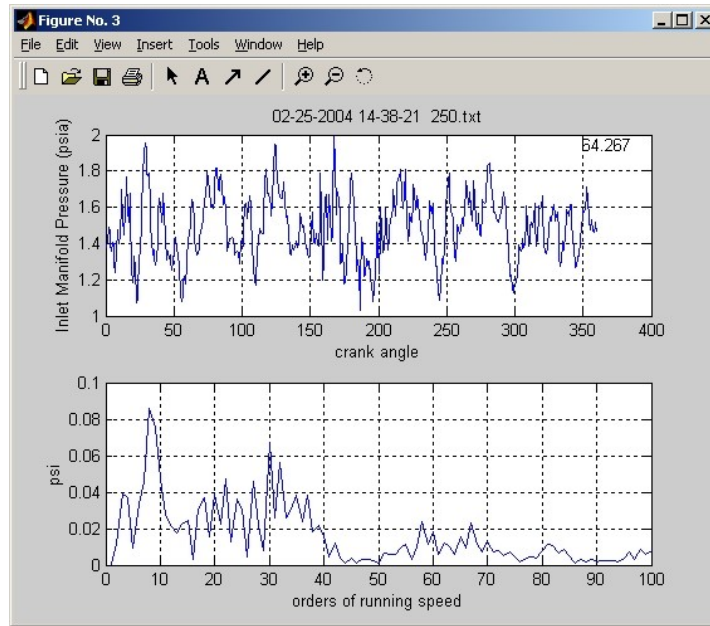


Figure 4-14. Inlet Manifold Pressure; Time Wave and Order Spectrum in an Unmodified GMW10 (Williams' Station 60; February 2004)

4.2.6 VARIABILITY IN EQUIVALENCE RATIO

During most tests under this program, a universal exhaust gas oxygen (UEGO) sensor was installed in the stack, which provides a direct measure of equivalence ratio (actual fuel-to-air ratio divided by stoichiometric fuel-to-air ratio). Figure 4-15 shows the extent of variation of equivalence ratio during the first series of tests at El Paso's Kinder Station on an HBA-6T. Some of the high extremes late in the day result from intentional changes in air manifold pressure. However, some other significant changes result from changes in conditions not

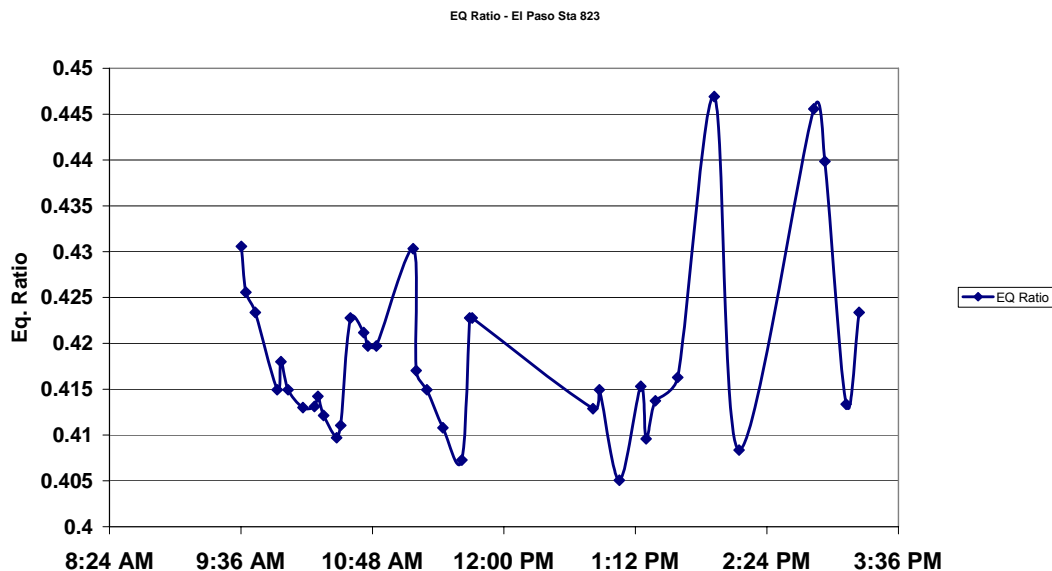


Figure 4-15. Variation in Equivalence Ratio in an HBA-6T (Kinder Station (El Paso Station 823); April 2003)

imposed by the test program or from changes unrelated to air manifold pressure. The range of 5% to 6% observed in the early part of the day's testing is significant and can influence engine operation. Similar observations could be made about equivalence ratio data obtained in other tests. These data prompted the observation that for turbocharged engines the feasibility of controlling equivalence ratio with low cost, state-of-the-art, commercially available sensors and controls should be evaluated; this feasibility was demonstrated in a subsequent test, and will be discussed further.

4.2.7 INFLUENCE OF LOAD ON HEAT RATE

Increasing load reduces heat rate, and if load drops below 100%, the heat rate increases above the value, which can be achieved if the engine is kept fully loaded. Figure 4-16 presents this variation based on test data for an HBA-6T and Figure 4-17 presents heat rate as a function of percentage torque for a modified GMW10. The sensitivity and the fuel consumption benefit of fully loading an engine to 100% while avoiding overload are clear.

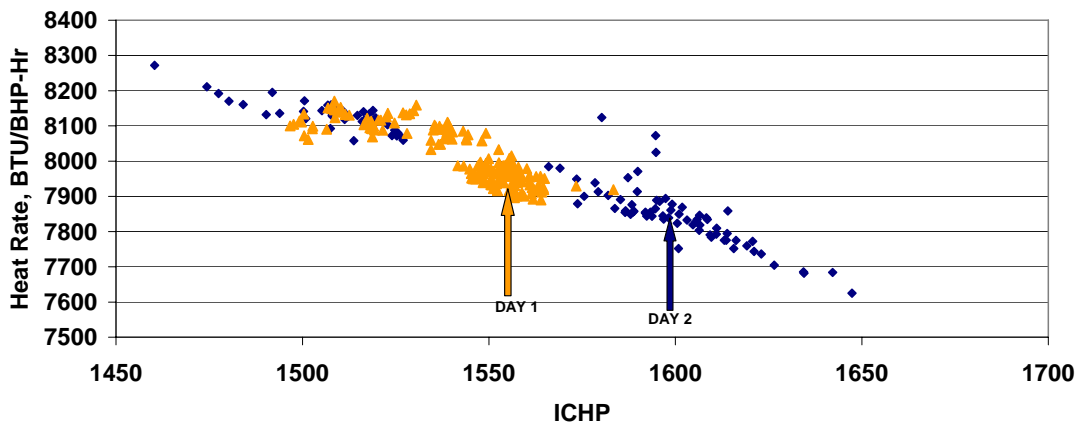


Figure 4-16. Heat Rate for Days 1 and 2 versus Indicated Compressor Horsepower (ICHP) Without Compression Pressure Ratio or Timing Tests or Speed Tests

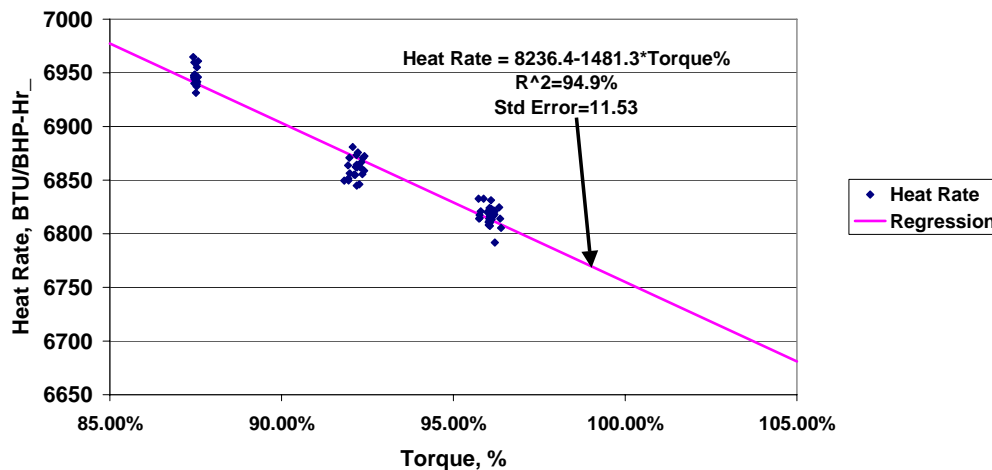


Figure 4-17. Heat Rate versus Torque for a GMW10 After Modifications (Williams' Station 60; August 2004)

A characteristic calculated for several units is the normalized rate of change of heat rate with load:

$$\left[\frac{\text{Load}}{\text{Heat Rate}} \right] \left[\frac{d(\text{Heat Rate})}{d(\text{Load})} \right]$$

The generally negative number expresses the percentage increase in heat rate for a one percent reduction in load. It provides a convenient way to rank engines in terms of their sensitivity to load changes

Figure 4-18 compares this normalized rate of change for four engine tests performed during the project, on a Modified GMW10, an unmodified GMW10, a KVG103, and an HBA-6T. The range for this measure of sensitivity to part loading is quite wide from -0.2 to -0.61 for the four sets of data compared on these four different engines. This data is intended to be illustrative rather than a generic evaluation of the engine models tested. However, obtaining this information for the specific fleet of engines deployed along a pipeline would help indicate which of them would experience the biggest increase in heat rate if pipeline conditions dictated choosing one or more engines to part load. As a numerical example, if the choice were to unload one of these four engines to 95% and to run the other four at 100%, the increase in heat rate for the partially loaded engine could vary between 1% and 3% according to which was chosen.

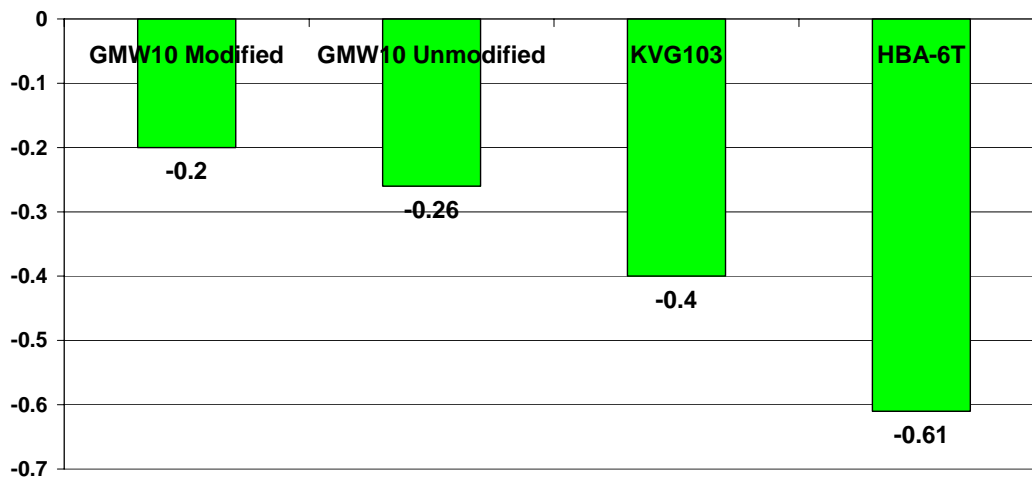


Figure 4-18. Normalized Rate of Change of Heat Rate with Load—Comparison for Four Tests

4.2.8 INFLUENCE OF TIMING ON HEAT RATE

For all the two-stroke engines tested, changes in timing exhibited a strong influence on heat rate. Figure 4-19 emphasizes this with sharp drops or increases in heat rate for each timing change tested. Figure 4-20 shows that the regressed rate of decrease of heat rate is 73.2 BTU/HP-Hour per degree of advance. As a percentage change in heat rate around 8 degrees of advance, this is just over one percent decrease in heat rate per degree of advance for this engine as tested on this day.

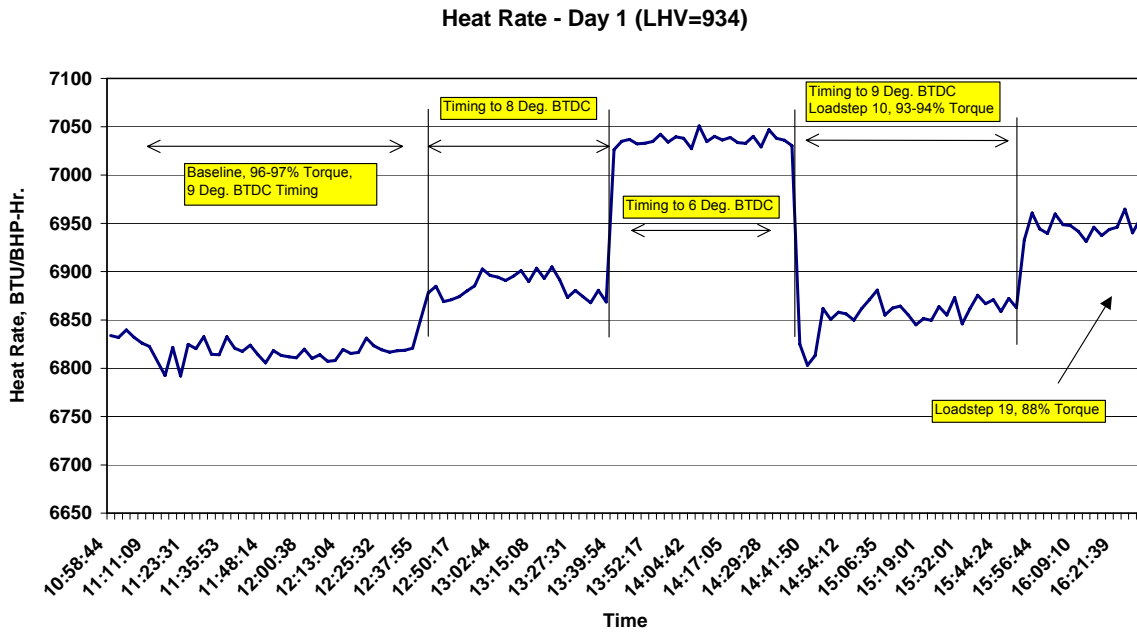


Figure 4-19. Heat Rate Tests for a GMW10; Unit 6; After Modifications (Williams' Station 60; August 25, 2004)

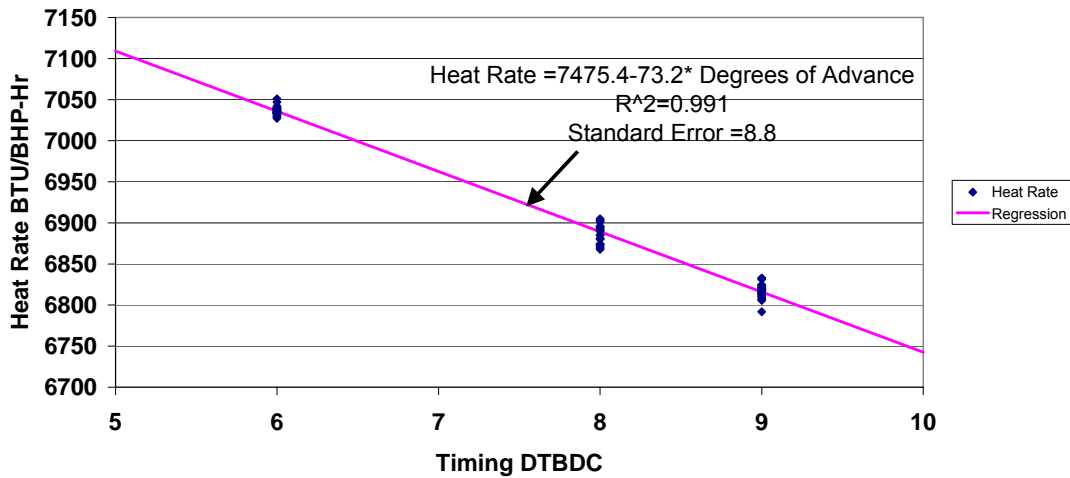


Figure 4-20. Heat Rate versus Timing for a GMW10 After Modifications (Williams' Station 60; August 2004)

While less exhaustive, test data on the HBA-6T tests in April 2004 showed 184 BTU/BHP-Hour reduction in heat rate, between time averaged values of 8,164 and 7,980, as a result of 2 degrees advance in timing from 10 to 12 degrees. These data give a rate of change in heat rate of 92 BTU/BHP-Hour per degree or 1.13% per degree.

Data from the four-stroke KVG103 tests is less precise, but indicate approximately 250 BTU/BHP-Hr heat rate reduction for between 2 and 3 degrees of timing advance—that is roughly 100 BTU/BHP-Hr reduction per degree of advance or 1.1% reduction per degree advance.

The similarity of these results for tests on three different engines indicates, as a working approximation, 1% heat rate reduction per degree of timing advance. This approximation deserves further and more widespread validation.

4.2.9 INFLUENCE OF TIMING ON CRANK STRAIN

Along with the benefits of timing advance on heat rate, this project's ability to measure crank strain enabled the possibly less desirable influence of timing advance on engine integrity to be quantified. Figure 4-21 shows the influence of an increase in timing first from 6 degrees to 8 degrees and then to 9 degrees for the modified GMW10. The full 3 degrees of advance approximately increases the strain from 115 microstrains to 135 microstrains—that is about 5.3% increase in crankshaft strain per degree of timing advance. Tests on an HBA-6T indicated approximately 6.6% increase in strain for a 2-degree advance from 10 to 12 degrees, or 3.3% per degree of advance.

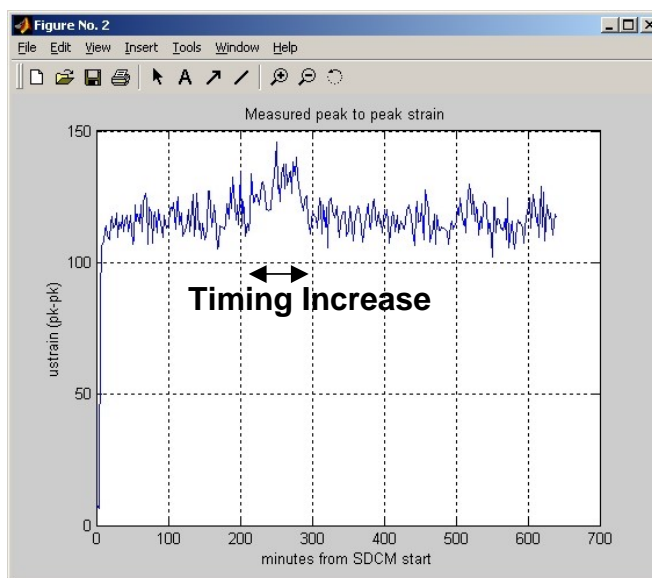


Figure 4-21. Variation in Peak-to-Peak Crankshaft Strain for a Modified GMW10 (Williams' Station 60; February 2004)

4.2.10 INFLUENCE OF COMBUSTION BALANCING ON ENGINE HEAT RATE

The natural variability in combustion from cylinder-to-cylinder for two-stroke engines has been documented and discussed, together with the variability from cycle-to-cycle. If the cycle-averaged combustion of each cylinder could be equalized, some benefits would be expected in terms of reduced heat rate (BTU/BHP-Hour). During this project, a balancing method termed Combustion Pressure Ratio (CPR) balancing was invented (with patent Number 6,981,488 issued January 3, 2006). This technology seeks to equalize air/fuel ratio across the cylinders by equalizing the ratio of peak firing pressure to compression pressure and will be subsequently documented, defined, and discussed in more detail.

Tests were performed on CPR balancing, peak pressure balancing, and standard deviation balancing technology, which also seeks to equalize air/fuel ratio rather than peak pressure.

Figure 4-22 shows heat rate as a function of engine load. As has been discussed, the line defining nominal variation of heat rate with load provides a reference for evaluating how changed operating conditions influences heat rate; its use helps avoid the uncertainty introduced by uncontrolled load variations from small changes in pipeline conditions. This figure includes heat rate data obtained during a CPR balancing test on an HBA-6T, in which combustion pressure ratio spread was reduced by a factor of four.

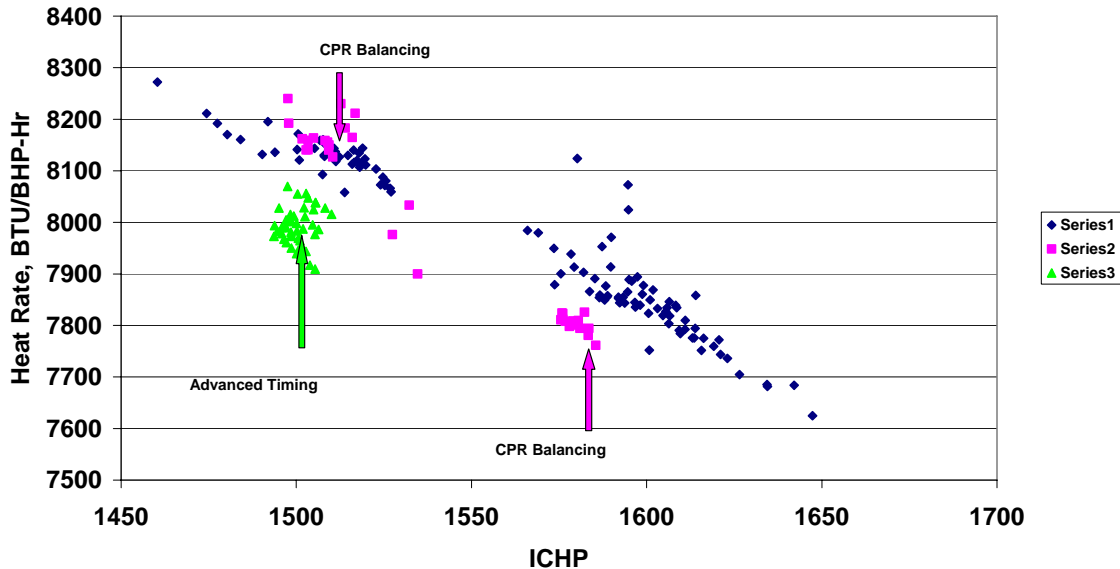


Figure 4-22. Heat Rate versus Indicated Compressor Horsepower; Series 2 Adds in the CPR Balancing Data, and Series 3 Adds in the Advanced Timing Data for a HBA-6T (Kinder Station (El Paso Station 823); April 22, 2004)

Figure 4-22 shows that for the CPR data near 1,560 ICHP, heat rate reduced by as much as 100 BTU/BHP-Hour out of 7,900 (1.25%), and for the CPR data near 1,510 ICHP, the CPR points lie essentially on top of the nominal heat rate variation. Thus, the influence of CPR balancing on heat rate is rather small, but in the preferred direction (down). On average, the results presented here indicate CPR to have about 0.625% influence on heat rate.

Figure 4-23 helps explain the small influence of balancing on heat rate. It shows the average and instantaneous spreads in peak firing pressure. The average spread is the difference from highest to lowest cylinder in cycle averaged peak pressure. The instantaneous spread is the difference between highest and lowest peak firing pressures during each cycle, averaged over many cycles. It can be argued that instantaneous spread reflects the true cylinder-to-cylinder variability in combustion. Figure 4-23 shows that between 12:40 and 13:20 the average spread distinctly drops from 50 to 40 PSI. Although CPR balancing only indirectly works on peak firing pressure, this reduction in average spread is a partial measure of how combustion was equalized (CPR spread was actually reduced by a factor of 4 during this CPR balancing test). Figure 4-23 shows no matching reduction in instantaneous spread—so this measure of cylinder-to-cylinder variability was not influenced by balancing. Any expected reduction in heat rate as a result of balancing would have to come from reduction in extremity of outliers and no such reduction is apparent from the instantaneous spread data.

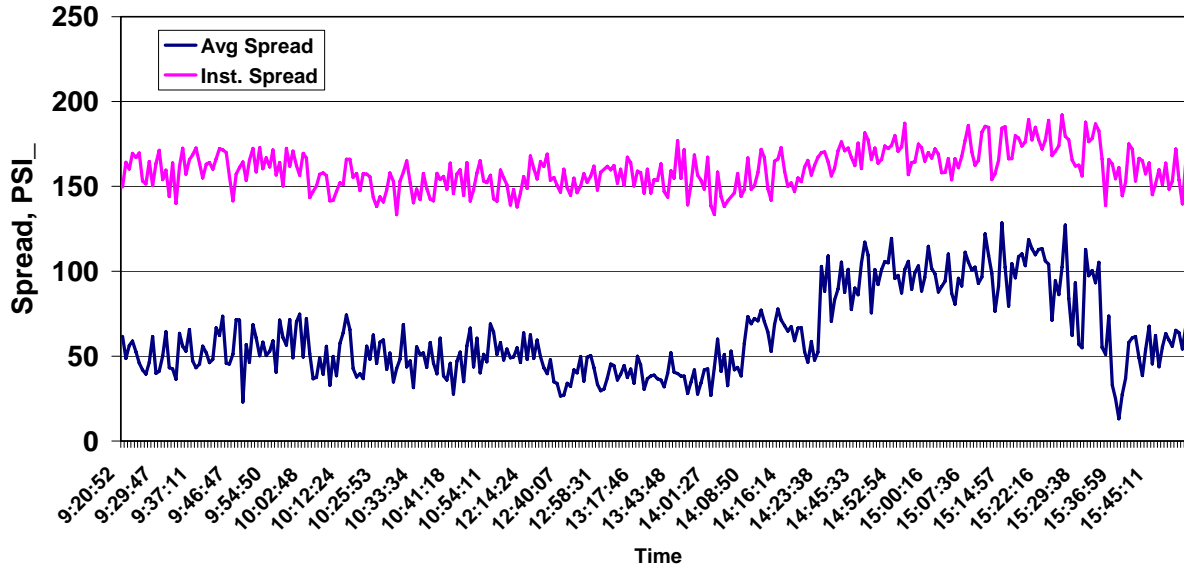


Figure 4-23. Instantaneous and Average Spread for HBA-6T (Kinder Station (El Paso Station 823); April 22, 2004)

Figure 4-24 provides another indication of small but beneficial influence of balancing on heat rate. It records how heat rate changed during a CPR balancing process in which CPR spread was reduced by a factor of 5. This figure indicates a possible 25 BTU/BHP-Hour reduction in heat rate during the CPR balancing process. Records showed no change in load during this test period, so this benefit can reasonably be attributed to CPR balancing, but it is clearly small—in this case between 0.3% and 0.4%.

Heat Rate - Day 2 (LHV=934)

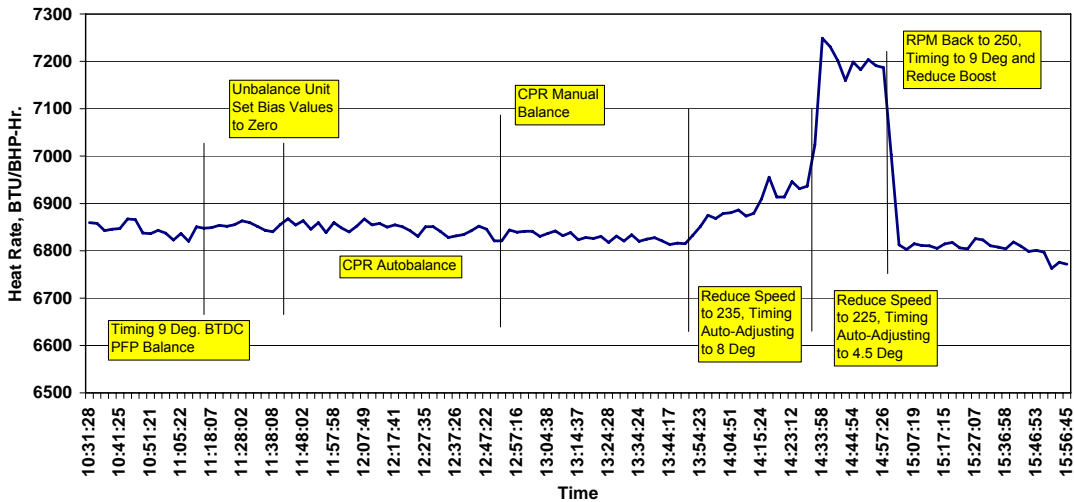


Figure 4-24. Heat Rate; Day 2 Tests for a GMW10; Unit 6; After Modification (Williams' Station 60; August 26, 2004)

4.2.11 INFLUENCE OF COMBUSTION BALANCING ON CRANK STRAIN

Balancing should reduce the highest outlier values for peak pressure and the highest peak pressure would be expected to have an influence on how severely the crankshaft is loaded and thereby on crankshaft integrity. Figure 4-25 provides clear documentation that balancing beneficially influences crankshaft dynamic strain, with data taken during two balancing events on a modified GMW10 at Williams Station 60.

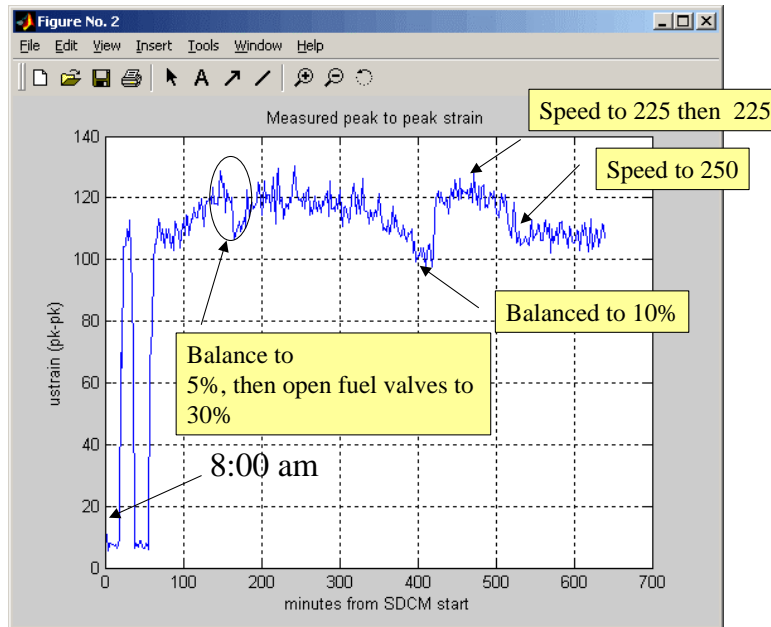


Figure 4-25. Peak-to-Peak Dynamic Variation in Crankshaft Microstrain; Unit 6 for a GMW10; After Modification (Williams' Station 60; August 26, 2004)

The first balancing event occurs during the period 150 to 170 minutes in Figure 4-25; this was peak firing pressure balancing, in which peak firing pressure spread was reduced to 5%. The crankshaft dynamic strain clearly responds, with a reduction from over 120 microstrains to about 108 microstrains—10% influence, approximately.

The second balancing event occurs between 350 and 420 minutes on this chart. This was CPR balancing in which the spread in CPR was reduced to 5%. The corresponding strain reduction was from 120 to 100—an even stronger influence (close to 20%) for CPR balancing.

Thus, in addition to small benefits in heat rate, CPR balancing has a distinct positive influence on crankshaft integrity.

4.2.12 SYSTEM-WIDE VARIATION IN COMPRESSOR EFFICIENCY

Compressor efficiency has a very significant influence on compressor capacity as well as on the overall fuel efficiency for a unit. Low compressor efficiency means that a high percentage of the available engine power is consumed in overcoming losses, and conversely as these losses are reduced more of the available horsepower becomes available for useful compression of the flowing gas. Thus, there is substantial leverage in improving compressor efficiency—it improves overall system efficiency and it increases capacity.

As discussed in the Introduction to this report, GMRC in the early 1990s undertook a wide ranging survey of compressor efficiency in the pipeline industry—gathering a substantial data set by having operating companies submit pressure and temperature data logged on operating units, which allowed calculation of isentropic efficiency. Figure 2-4 presented the resulting efficiency histogram, which showed a median of about 79% and a range from 52% to 92%.

This project also developed data on compressor efficiency for a number of units, and Figure 4-26 summarizes the results for ten different combinations of unit and operating conditions. Clearly the data set is smaller than for the GMRC survey, but the maximum efficiency of 91% sets a good industry benchmark similar to that for the previous survey. The lowest efficiency of this data set is just over 75% and the median is about 84%. The monitoring of compressor efficiency deterioration with time, based on temperature rise (suggested as part of a PRCI project—Smalley, McKee, et al. [4]), will be discussed in a later sub-section, and represents one approach to keeping the efficiency of compressors on a pipeline as high as possible, and to optimizing the sequence with which engines are started and shut down as demand varies. In addition, the identification and targeting of units with inherently low compressor efficiency for changes to reduce compressor losses represents an opportunity to increase aggregate compressor efficiency. As will be subsequently discussed, compression losses include losses in the attached piping as well as losses in the cylinder, valves, and in mechanical power transmission; the losses outside the cylinder may present the most productive opportunity for loss reduction.

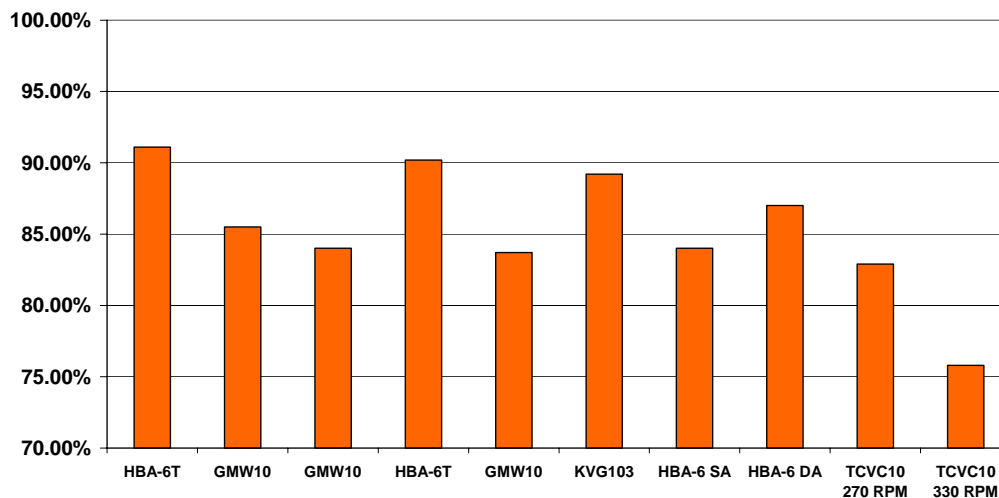


Figure 4-26. Compressor Efficiency – Project Summary

4.2.13 MECHANICAL EFFICIENCY

As normally applied in relation to integral engine compressors, mechanical efficiency represents the efficiency with which crankshaft power is transmitted to the face of the compressor pistons. The losses involved in this transmission of power include crank pin bearings, wrist pin bearings at the crosshead, crosshead slider bearings, packing resistance to motion, piston ring friction, and rider band friction; all these losses rob the available power at the crankshaft before it can reach the faces of the compressor pistons. In general, these losses have not been a target for reduction in past research. To pipeline users, these losses mainly represent

a quantity to be accounted for in inferring crankshaft power (brake horsepower) from indicated compressor horsepower, so that the engine heat rate (often referred to as the brake specific fuel consumption) can be calculated as the ratio of fuel energy consumption rate to brake horsepower. The value most widely used in integral engine/compressors for mechanical efficiency is 95% and so the indicated compressor horsepower based on cylinder pressure measurement is usually divided by 0.95 to obtain brake horsepower.

Under this project, some first steps were made towards the quantification of piston friction and packing friction, using the Rod Load Monitor (illustrated in Figure 4-66) during tests on a KVG 103 four-stroke engine/compressor. With the compressor isolated by valves from the headers, piston friction power was inferred as the difference between measured values for cylinder power and rod load power. This will be described subsequently in more detail, but Figure 4-27 incorporates the result in a system power flow diagram. This power flow chart indicates bearing mechanical losses in series with piston friction losses, valve losses, and installation losses; the combination of bearing and piston friction losses (over 49 HP) is comparable in magnitude to valve losses and the installation losses and clearly of a magnitude worthy of analysis and test to better define these losses, their drivers, and to seek technologies for reduction.

As an example of opportunities for mechanical loss reduction a “free floating piston” (FFP) has been developed by Thomassen and described by Koop [5]. This device separates the piston from the cylinder wall by means of a pressurized gas film achieved by valving compressed gas into the cylinder and out of appropriately sized small holes in the rider bands to form a pressurized gas bearing. In addition to the potential for loss reduction by reduction in frictional resistance, the FFP will reduce wear of rider bands.

Another potential opportunity to reduce mechanical losses for evaluation is the reduction in oil viscosity in bearings by increasing the temperature fed to main, crankpin, wrist pin, and crosshead slider bearings, and will be discussed in a later sub-section. Of course, the corresponding potential for reduced bearing load capacity has to be considered and managed.

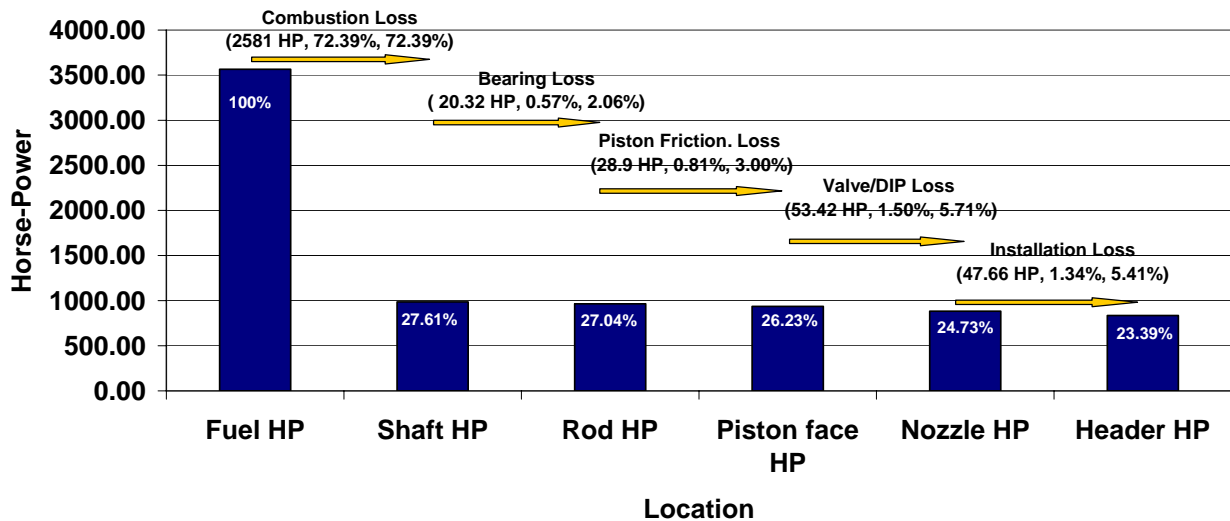


Figure 4-27. Flow of Power from Fuel to Header, Showing Percentage of Fuel Power on Each Column; Losses Stated in HP, % of Total, and % of Available at that Point

4.2.14 INSTALLATION LOSSES

The contribution of installation losses to compressor losses has been discussed. This term implies losses in the nozzles, in primary and secondary pulsation dampener bottles, in the laterals, and in pipe area changes between and within these system components. The most significant of these losses normally occur at orifices, which may be inserted at the cylinder flange connection to the nozzle, or in the nozzle at exit into the bottle, or in the line (e.g., at exit from the primary suction bottle). The project has quantified such losses in several installations by use of added pressure instrumentation and by taking advantage of installed temperature transducers. Figure 4-28 summarizes the results and makes a comparison, for three compressors, of installation losses and total losses (valves + installation). This figure shows total losses ranging from 10.81% to 22.64% and installation losses typically about half the total losses and varying from 5.1% to 12.36%. In the latter case, a major contributor to losses was orifices in nozzles and piping. The need to reduce such losses and to recover the available horsepower for useful compression is discussed subsequently together with an approach, for a TCVC10, using pulsation predictions and a significantly different pulsation control system without orifices.

4.2.15 SYSTEM THERMAL EFFICIENCY

The term system thermal efficiency is used in this report as the efficiency with which fuel energy is converted into useful compression work. It measures the efficiency of operation for the entire compression system: engine; compressor; power transmission between the two; compressor manifold; and gas piping. Its emphasis in this report recognizes that integral engine/compressors are a system whose performance can suffer as a result of low engine efficiency, low mechanical efficiency of power transmission and low compressor efficiency.

Determining system thermal efficiency requires accurate measurement of the following quantities as a minimum:

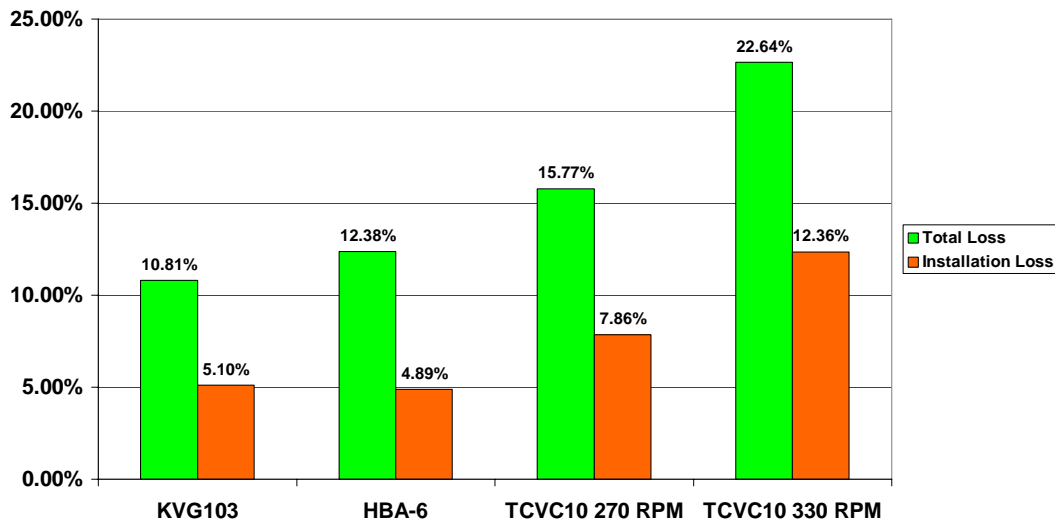


Figure 4-28. Compressor Loss Comparison – Installation and Total Losses

- Fuel flow
- Gas composition, yielding LHV for the fuel gas

- Indicated compressor piston face power
- Suction and discharge temperatures
- Suction and discharge pressures

With this data, system thermal efficiency can be calculated as:

$$\text{Fuel (BTU/ICHP-Hour)} * \text{Compressor Isentropic Efficiency}$$

Where BTU/Hour is fuel flow multiplied by fuel Lower Heating Value (LHV); ICHP is the indicated compressor horsepower obtained from the measurement and appropriate integration of cylinder pressure and crank angle. Isentropic efficiency is obtained as the isentropic enthalpy rise from suction conditions (Ps, Ts) to discharge pressure (Pd) divided by the actual enthalpy rise from suction conditions (Ps, Ts) to Discharge conditions (Pd, Td).

Alternatively, if compression pressure losses in valves, nozzles, pulsation dampeners, and lateral piping can be accurately determined, the associated power losses may be converted to a compressor efficiency, which replaces the isentropic efficiency referred to above.

It should be noted that this measure of system performance does not depend on an assumed value for mechanical efficiency to convert shaft power to compressor piston face power. Of course, such mechanical efficiency does influence the system thermal efficiency, but since the system thermal efficiency represents a calculation of “energy out divided by energy in,” it depends only on directly measurable quantities. If diagnostics are required to isolate the component values of heat rate for the engine and compressor efficiency, then mechanical efficiency shows up in the calculation of engine brake thermal efficiency.

Figure 4-29 makes a comparison of all engine compressors where the necessary measurements were available using either pressure based or enthalpy based compressor efficiency. It is seen to range from 24% to 31.3% in this figure. For the KVG, it is low mainly because of a low engine brake thermal efficiency (high heat rate); for the GMW10 with advanced timing, it is high mainly as the result of high engine brake thermal efficiency (low heat rate).

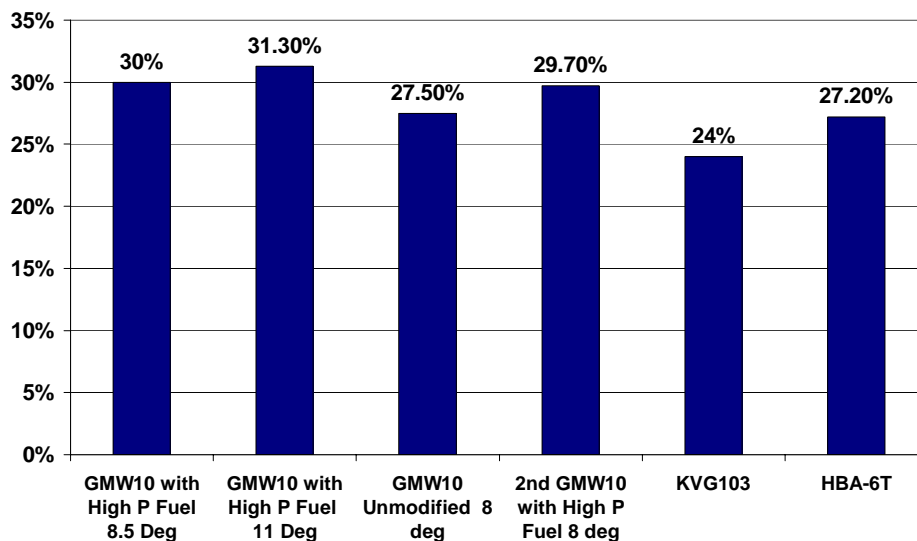


Figure 4-29. Overall System Efficiency Summary

Quantifying system thermal efficiency can guide operational decisions, horsepower replacements, and decisions on modifications directed at pipeline efficiency and capacity enhancements. Considered in this way, the engine/compressor system thermal efficiency for a single unit becomes a component of the broader system thermal efficiency of the pipeline, including station-to-station flow resistance losses and the combined losses of multiple units up and down the pipeline.

4.2.16 CAPACITY

The limited ability to directly measure capacity (throughput) for individual reciprocating compressors represents a major technological limitation for the pipeline industry. The primary objective of pipeline compressors is to flow gas, yet this essential item of performance cannot be directly measured.

It is, of course, possible to infer the throughput from the suction and discharge conditions in combination with knowledge of the clearance and kinematics of piston motion. Such inference was performed for the HBA-6 and TCVC10 tested under this project. However, there is some inevitable bias in this inference with the true flow tending to fall slightly below the predicted flow since the effective suction gas temperature tends to be slightly hotter than measured suction temperature and because it is assumed that all cylinders are in good condition. If there is a leak through suction valve, discharge valve, or rings, these malfunctions will tend to further reduce the flow relative to the inferred value.

Figure 4-30 presents the inferred flow for each cylinder of a TCVC10 and shows how inferred flow increases in near direct proportion to speed.

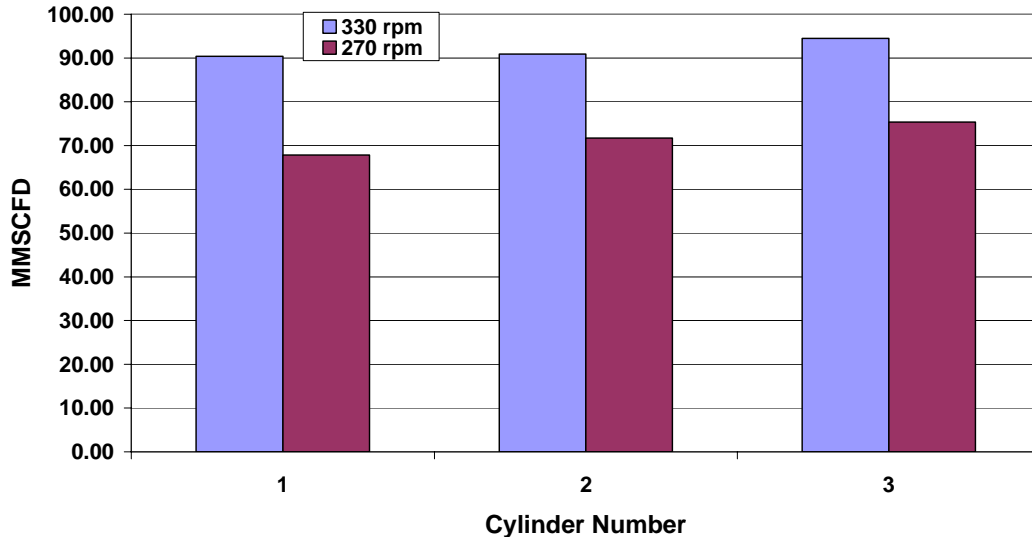


Figure 4-30. Cylinder Flow (MMSCFD); Dresser-Rand TCVC10 (Dominion Groveport Station; Unit 1; April 20, 2005)

There are limited options for measuring flow, because the flow measurement for a single unit tends to incur errors from pulsations when placed in the laterals, unless some specialized techniques are applied, which have not yet appeared as commercial products, or some restricted station operation is employed for a short-term test. Options will be discussed subsequently in this section.

Available capacity for given pipeline conditions are limited first by available engine power or torque, and at low compression ratio, the available power may be limited below nameplate by the minimum clearance with all pockets closed. The available power at the crankshaft is then used in part to overcome mechanical losses, in part to overcome flow resistance losses in valves, passages, and piping, and only the power remaining after these losses is used to elevate pressure of the flowing gas. Thus, with no leaks, mechanical and flow resistance losses have a very direct impact in limiting capacity. Leaks represent deterioration from design conditions, which further rob capacity.

4.2.17 OBSERVED INFLUENCE OF TIME FROM A COLD START ON POWER TRANSMISSION EFFICIENCY

It was observed during the first test of an HBA-6T that the ratio of compressor power to engine power (based both on cylinder pressure measurements) increased almost continuously over about five hours of testing. Figure 4-31 shows this. In fact, while the compressor power stays relatively constant, the engine power drops, and if we define an implied system mechanical efficiency for transmission of power from power piston faces to compressor piston faces as the ratio of compressor and engine indicated power, then this ratio increases over this time from 80% to over 92%. A rational explanation for this change is that the sump oil temperature is known to increase over time on this engine (Smalley [6]). While no measurement was made of sump temperature on this test unit, the station records provided data on bearing oil outlet temperature, which is plotted as a function of time in Figure 4-32. It is apparent that this oil temperature increased in a manner comparable to the variation of power transmission efficiency. The viscosity of the oil in the bearings must have an influence on friction resistance of these bearings and viscosity drops as oil temperature increases. The evidence is somewhat circumstantial, but the benefits of such a significant change in power transmission deserves further investigation, together with the potential for intentional control of oil temperature (subject to bearing integrity issues).

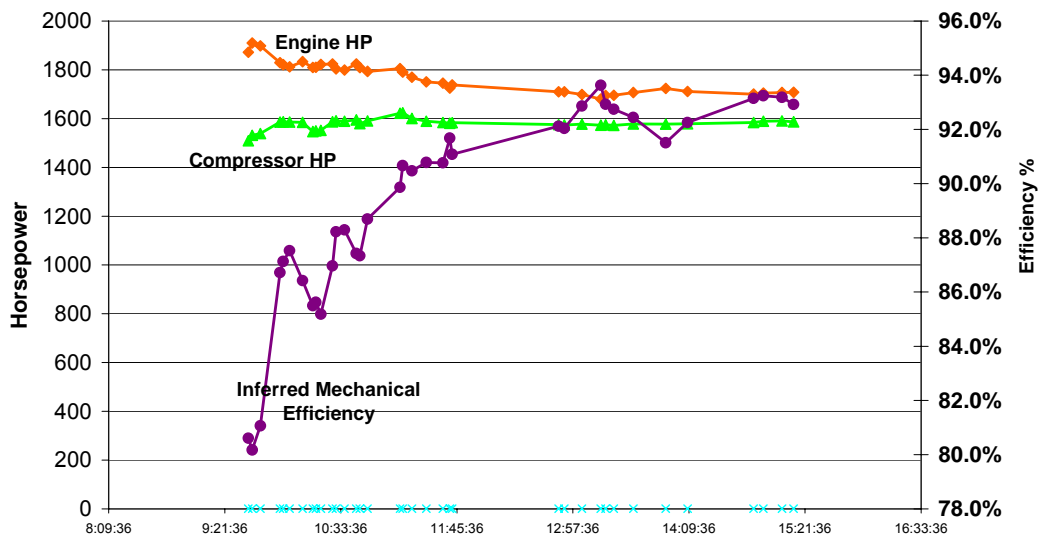


Figure 4-31. Engine HP, Compressor HP, and Inferred Mechanical Efficiency; (Kinder Station (El Paso Station 823); Test 1; April 2003)

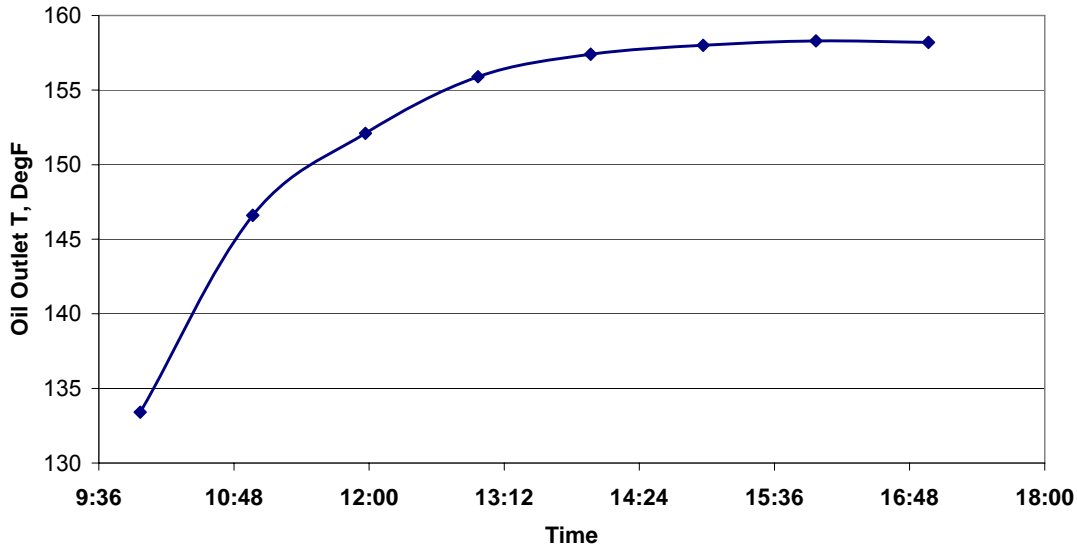


Figure 4-32. Oil Outlet Temperature versus Time from Station Records (Note Increase Over 5 Hours Matches Mechanical Efficiency Trend); (Kinder Station (El Paso Station 823); Test 1; April 2003)

4.2.18 PULSATIONS FROM RECIPROCATING COMPRESSOR ACTION

The cylinders of a reciprocating compressor impose on the compressor nozzles, connecting manifold, and compressor piping system, a dynamic modulation in flow to which these flow passages respond. The coincidence of any frequency component of the overall flow modulation to an acoustic natural frequency of the flow system means the potential exists for acoustic resonance and amplification of the flow modulation at this frequency.

Such flow modulation is a natural characteristic of all reciprocating compressors, but a number of devices exist by which resonance can be avoided or its severity reduced:

- Acoustic filtering limits the maximum frequency of significant flow modulation downstream of the filter.
- Choosing inlet and exit points in the manifold which correspond to nodes of the acoustic natural frequency limits the ability of flow modulations at these exit/entry points to excite that natural frequency.
- Orifices located at velocity maxima for the acoustic natural frequency offer resistive damping of an acoustic resonance and attenuate the severity with which it responds.
- “Side branch resonators” split an acoustic natural frequency into two frequencies, one above and one below the original natural frequency.

Designers of pulsation control systems have all these tools available to limit damaging pulsations and the severity of acoustic resonances. Some tools incur a penalty in flow resistance:

- Orifices directly add to the mean flow resistance, and this disadvantage increases in direct proportion to effectiveness of the attenuation.
- Filters are primarily reactive (employing chokes and volumes) as opposed to resistive devices, but the area changes for flow to and from the chokes adds some mean flow resistance.

- Controlling the location of junctions carries a low penalty, but is effective only for certain modes.
- Side branch resonators carry no mean flow, but dissipate a small amount of energy as dynamic flow into the device modulates about zero.

Pulsations have been documented at various points in the compressor’s flow path between piston face and headers. Figure 4-33 compares pulsations in the four suction nozzles of an HBA-6 under single-acting and double-acting conditions for that compressor. Figure 4-34 shows the pulsations in the suction and discharge traces of the pressure versus crank angle traces in Cylinder 2 for the same compressor under double-acting conditions. Figure 4-35 shows measured pulsations in the discharge nozzles of a TCVC10 at two speeds (270 and 330 RPM).

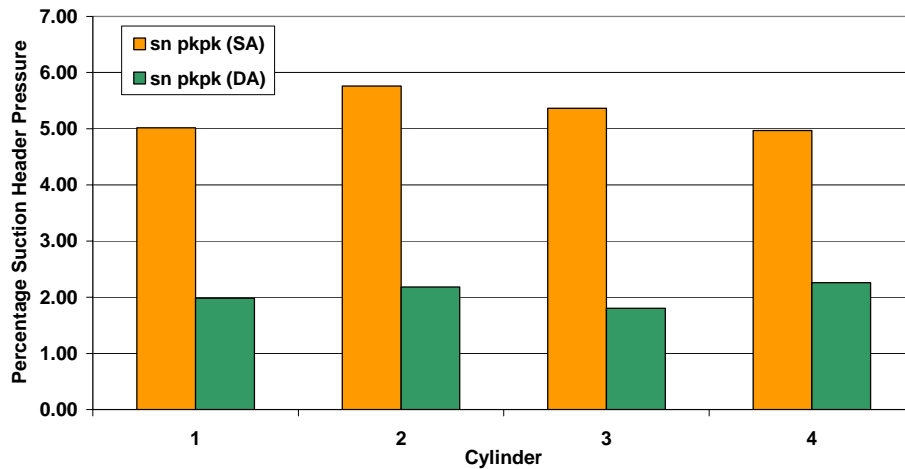


Figure 4-33. Suction Nozzle Pulsation – Comparison of Single-Acting and Double-Acting Operation; Clark HBA-6; Unit 4 (Duke Energy’s Bedford Station; March 1, 2005)

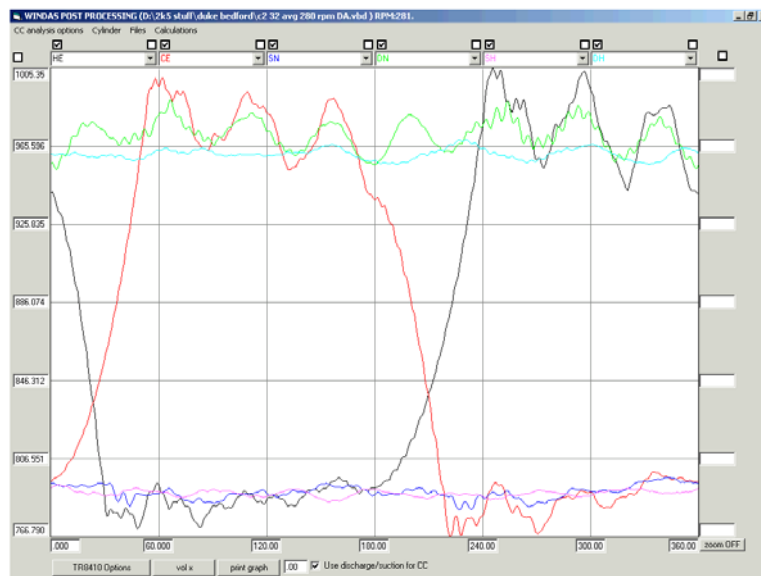


Figure 4-34. Illustrative Channel Corrected Data from Cylinder 2 Under All Double-Acting Operation; Clark HBA-6; Unit 4 (Duke Energy’s Bedford Station; March 1, 2005)

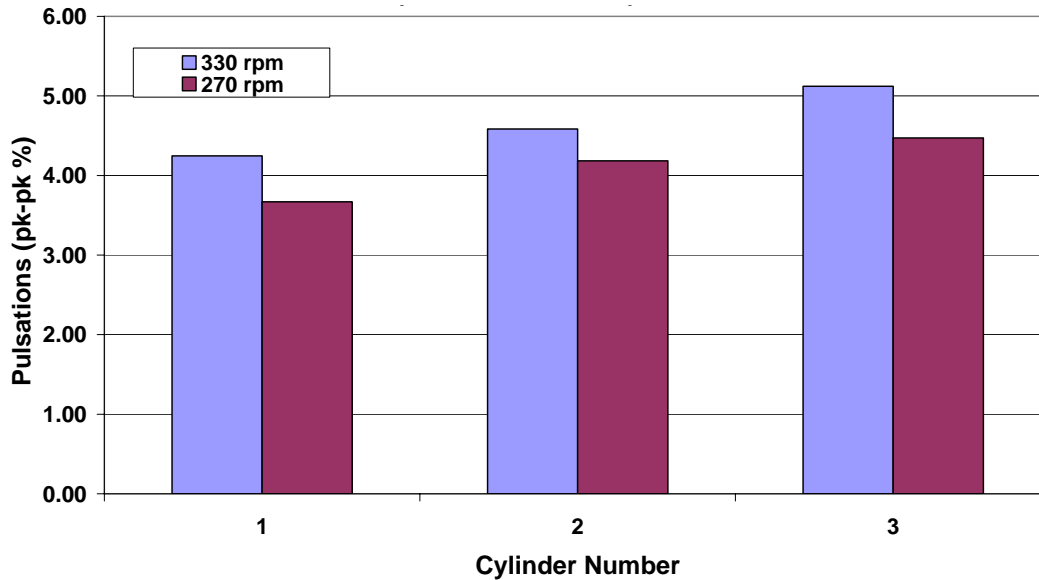


Figure 4-35. Discharge Nozzle Pulsation Levels; Dresser-Rand TCVC10 (Dominion Groveport Station; Unit 1; April 20, 2005)

Design analysis guided by this data has focused on the challenge of achieving effective control of pulsations while minimizing the mean flow resistance. Mean flow resistance is one contributor to compressor system losses so that minimizing this resistance has the potential to increase available capacity.

4.2.19 SPEED/POWER MODULATION (MULTIPLE COMPRESSORS “BEATING” AGAINST EACH OTHER)

Flow modulation and the potential for pulsations are features of all individual reciprocating compressors. With multiple reciprocating compressors operating concurrently and connected to a common header, small differences in speed of different units can create a situation where pulsations from individual units successively reinforce and cancel each other. The symptom of this phenomenon is referred to as “beating” and can exaggerate the pulsations from a single unit and can drive modulations in speed or power. Ineffective filtering of an inherent frequency of significant flow modulation from a series of compressors is a likely cause of beating.

The project has clearly documented the beating phenomenon, and through design and test of a solution has confirmed its cause and demonstrated the accuracy of acoustic pulsation predictions. Figure 4-36 shows the variation with time of measured pulsations in the suction and discharge nozzles of the HBA-6 under single-acting conditions. The period of these modulations is about 5 seconds; the range is from 2% to 8% of line pressure. The speed and power on this unit were also measured several times per second with data averaging switched off. Variation over time was observed with the same period. The compressors at this station were initially installed with acoustic filtering to cut off pulsations whose frequency exceeded second order (10 Hz), because they always operated in double-acting conditions. After some changes in pipeline operation led to higher-pressure differentials, it was necessary to operate the compressors under single-acting conditions, which produces pulsations at 5 Hz. The acoustic

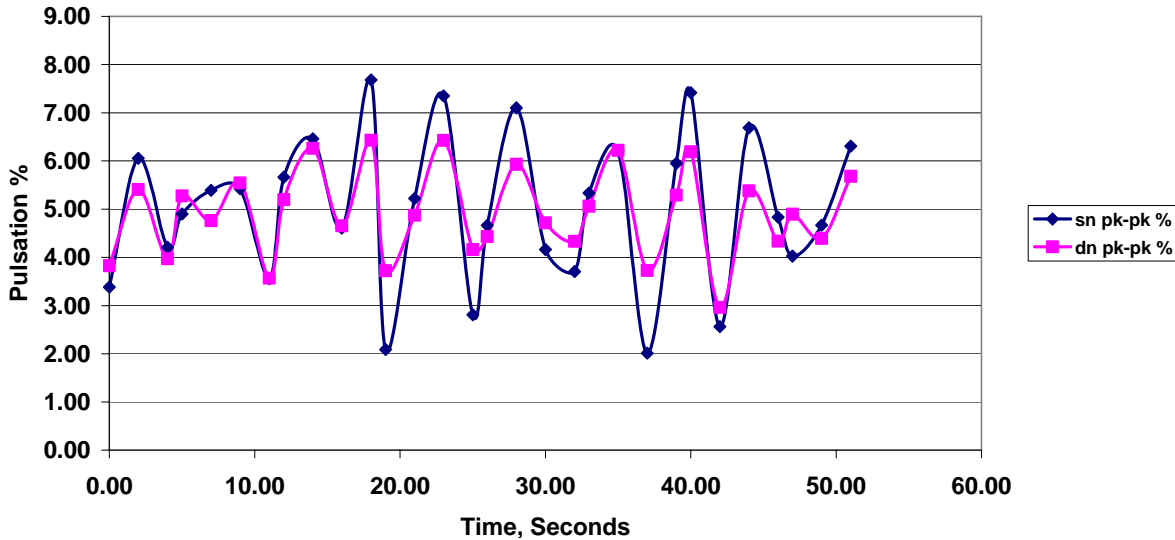


Figure 4-36. Cylinder 1 Suction and Discharge Nozzle Pulsations versus Time in Seconds; Cylinders 1 and 4 Single-Acting; Clark HBA-6 Unit 4 Compressor Cylinders (Duke Energy’s Bedford Station; March 1, 2005)

filtering was ineffective at this frequency, and significant pulsations from the multiple single-acting units with slight differences in speed produced the observed beating, which could only be eliminated by double-acting the compressors—an unacceptable solution.

4.2.20 SQUARE LAW LOSSES IN VALVES, ORIFICES, AND PIPE AREA CHANGES

Flow through orifices, piping area changes, and compressor valves all incur pressure drops, which vary predominantly as the square of flow velocity ($\rho V^2/2$). They are referred to here as “square law” loss components.

The first negative feature of such square law loss components is that when throughput is increased (normally by an increase in rotational speed), losses increase at twice the rate of the flow increase as illustrated in Figure 4-37 for a TCVC10 (in comparison with the capacity data of Figure 4-30); as a result efficiency falls as flow rate increases and capacity, while higher from increased speed, is not as high as it should be based on lower speed efficiency data, because an increasing fraction of available power has to go to overcoming losses.

A second negative feature of square law loss components is that flow modulation themselves incur a flow resistance penalty at each such component. This is because flow modulations produce a flow history with flow alternately higher then lower than the mean flow. The reduced losses when flow is at its lowest do not fully offset the increased losses when flow is at its highest; thus, flow modulation about a mean flow produces a net pressure drop in square law components.

The magnitude of square law flow resistance for the TCVC10 motivated the design of a pulsation control system, which would remove the orifices but remain effective and, therefore, eliminate over 400 HP in losses in a 5,000 HP compressor.

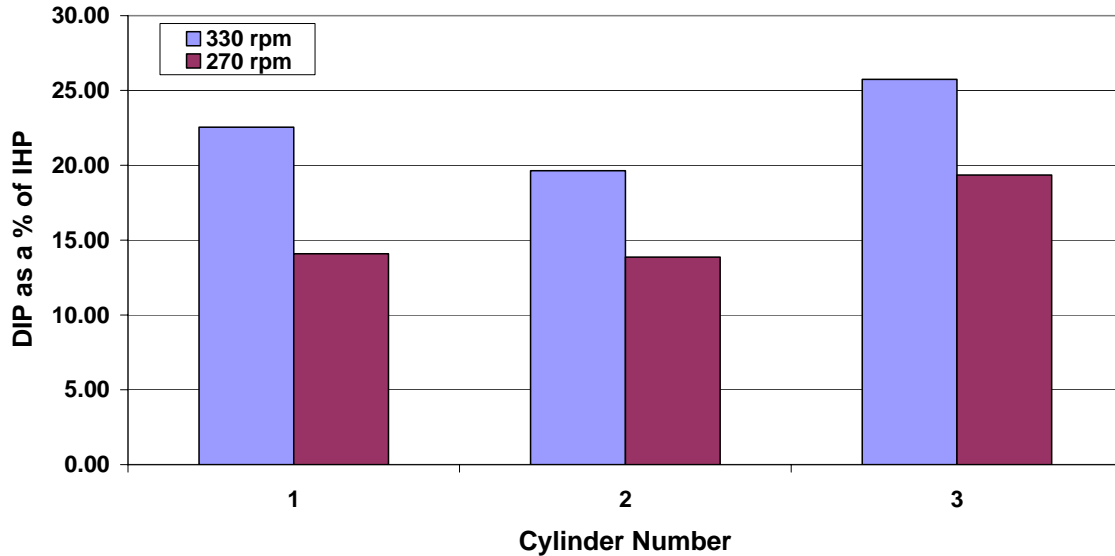


Figure 4-37. Cylinder Total DIP; Dresser-Rand TCVC10 (Dominion Groveport Station; Unit 1; April 20, 2005)

4.3 METHODS FOR TESTING, CHARACTERIZATION, AND MONITORING

4.3.1 SUITE OF INSTRUMENTS AND DATA ACQUISITION SYSTEM

The suite of instruments, associated data system, and selective use of installed station instrumentation documented in Section 3 of this report and used during this project were designed to provide concurrent performance data from multiple cylinder engine/compressors, avoiding the uncertainty and imprecision associated with movement of transducers from cylinder-to-cylinder.

Such concurrency enables meaningful use of the variation of heat rate with load to assess the influence of operational changes on performance, as previously discussed. Measuring fuel flow concurrently with pressure in each cylinder end enabled “end-to-end” determination of system thermal efficiency from compressor piston face heat rate coupled with isentropic efficiency. The acquisition of pressure from heated transducers in the nozzles and laterals concurrently with compressor cylinder pressure enabled isolation of losses.

Although the project is complete, this suite of instruments remains available for the documentation of performance of other integral engine/compressors, and for further research and investigation, the need for which the current project has highlighted.

4.3.2 ASSESSING HOW OPERATING CHANGES INFLUENCE HEAT RATE VARIATION WITH LOAD

As discussed, the inevitability of changes in conditions during testing greatly complicates the assessment of how a particular intentional change (e.g., timing advance or balancing) affects heat rate, because the unintentional changes from varying conditions may have had an equal or greater or opposite effect. However, assessing how this intentional change affects the variation of heat rate with load documents the influence of the intentional change much more convincingly because the variation of heat rate with load is closer to an inherent characteristic. The data

acquisition and recording practice for the project results in regular logging of all parameters from which load and heat rate are determined. The project showed the value of this method of assessment, particularly in evaluations of how balancing and timing affect heat rate. Figure 4-22 has already illustrated this approach graphically for the test of an HBA-6T.

The method deserves refinement beyond the illustrations of its value in Figure 4-22. For example, the data defining the baseline variation of heat rate with load could be processed to yield a regression model, with slope, intercept and an algebraic equation. Figure 4-17 illustrates such a regression model (with torque as the independent variable), which has been supplemented on this figure with a value for the coefficient of determination (R^2) and a value for standard error.

The equation from the regression model would then provide an “Expected Value” for any load; the difference between expected value and each test value obtained, after the imposition of an intentional change, would quantify the influence of the intentional change. This could then be compared to the standard error. The significance of the quantified influence can then be assessed by comparing the difference to the standard error; a consistent difference of 2 or 3 standard errors would be significant.

4.3.3 MONITORING ROD LOAD

As mentioned several times in the above discussion, quantifying the brake horsepower or load on the engine requires some inference because state-of-the-art instrumentation cannot measure this quantity directly; the closest meaningful measurement is compressor piston face horsepower, which has to be divided by an assumed mechanical efficiency (typically 0.95) to obtain a value for the brake horsepower available from the engine, to drive the compressor, at the crankshaft.

The experimental Rod Load Monitor (RLM) evaluated and refined on this project comes very close to a measurement of this brake power. The measurement is actually made at the piston rod, rather than the crankshaft, so there are still some fluid film bearing losses between the resulting power and the crankshaft. Specifically, some assumption about efficiency of power transmission from crankshaft to piston rod is needed, involving losses in the crank pin bearing, the wrist pin bearing at the crosshead, and the crosshead guide slider bearing. It is reasonable to expect that each of these losses involves full fluid films and is relatively small. The RLM removes the losses in the packing, the rider bands, and the rings as uncertainties, and these are expected to be higher than the pin and slider bearing losses.

Consistent knowledge of engine load is needed for a number of reasons. One of these has been discussed in detail already; engine heat rate is a strong function of load—increasing load reduces heat rate with substantial benefit in fuel consumption. However, exceeding 100% load has implications for engine integrity, with potential for damage to critical components, such as bearings and the crankshaft. Thus, the ability to minimize fuel consumption while not overloading the engine depends on accurate knowledge of engine torque or horsepower, and on appropriate control of that load whenever it is determined to deviate low or high from 100%.

Another reason for accurate knowledge of engine load is regulation of engine emissions. Engines are permitted on the basis of load and documentable ability to state the load on engines is needed.

Most operating companies determine load based on operating conditions, load step, and models of the compression process, which predict engine load as a function of condition. These

models are usually calibrated by compressor performance testing, but always need an assumed correction to account for mechanical losses in rings, rider bands, and packing.

The Rod Load Monitor, appropriately deployed and acted upon, can meet the need to reduce uncertainty in engine load.

4.3.4 ISOLATING MECHANICAL LOSSES WITH THE ROD LOAD MEASUREMENT

The uncertainty in the mechanical losses between power available at the crankshaft and power delivered to the piston face has been discussed. In addition to reducing this uncertainty better, knowledge of the mechanical losses will provide a measurable target for reduction. Mechanical losses represent engine power unavailable for useful compression of the transported gas, so their reduction has a direct potential benefit in increased capacity.

The project has demonstrated for the first time how subtracting accurate values for power at different points in the transmission path can reveal the power loss between these points. Specifically, subtracting rod load power from compressor piston face power provided data on the combined power loss from packing, rings, and rider bands. This test method was only performed once during one of the late tests, and then for essentially unloaded conditions under which the cylinder indicated power reflected only the flow resistance losses as non-flowing gas was forced successively in and out of the cylinder through the valves. Thus, the mechanical losses measured involved the difference between two relatively small power values.

Figure 4-38 shows a typical cylinder pressure measurement during this test, with the rod load variation superimposed. The cylinder pressure variation is clearly low as is the variation of rod load power since it reflects the indicated cylinder power with the ring, rider band, and packing losses subtracted off. Figure 4-39 shows the frictional loss horsepower inferred from the difference in cylinder and rod load power as a function of speed. The variation with speed is as expected—faster sliding increases friction power and matches closely to a linear fit. Figure 4-40 shows how the measured friction power under unloaded conditions compares to different realistic cylinder power values for the compressor under typical operation. Based on this analysis friction loss from rings, rider bands, and packing vary from 2.5% to 4.5%, a range comparable to typically assumed values.

Figure 4-41 compares the 3% mechanical loss at the middle of this range to the measured valve (5.71%) and installation (5.1%) losses on this unit. The valve and installation losses each exceed the mechanical losses, but all are significant enough to justify further efforts aimed at isolation and reduction.

This test method for isolating mechanical losses needs refinement and evaluation under different load levels, but has the potential to meet the need for reduced uncertainty in mechanical losses and to guide research, which will reduce mechanical losses.

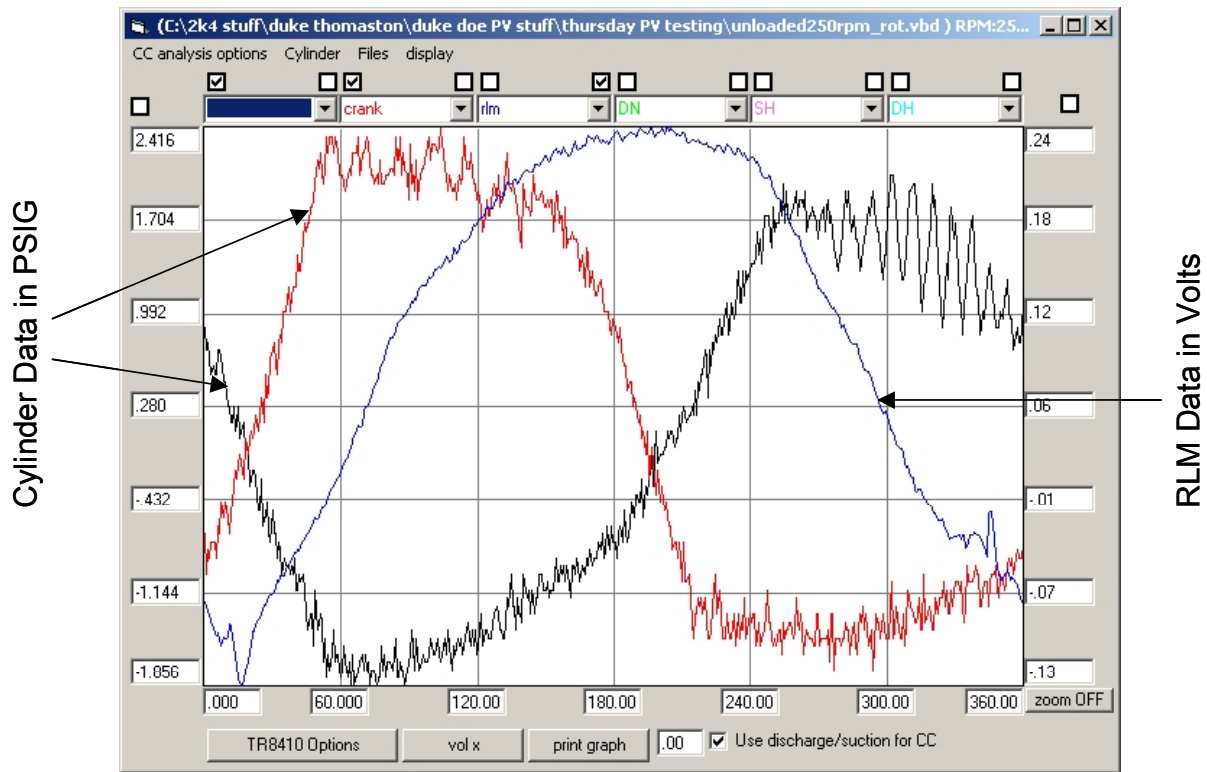


Figure 4-38. Representative Unloaded Cylinder and RLM Data (250 RPM)

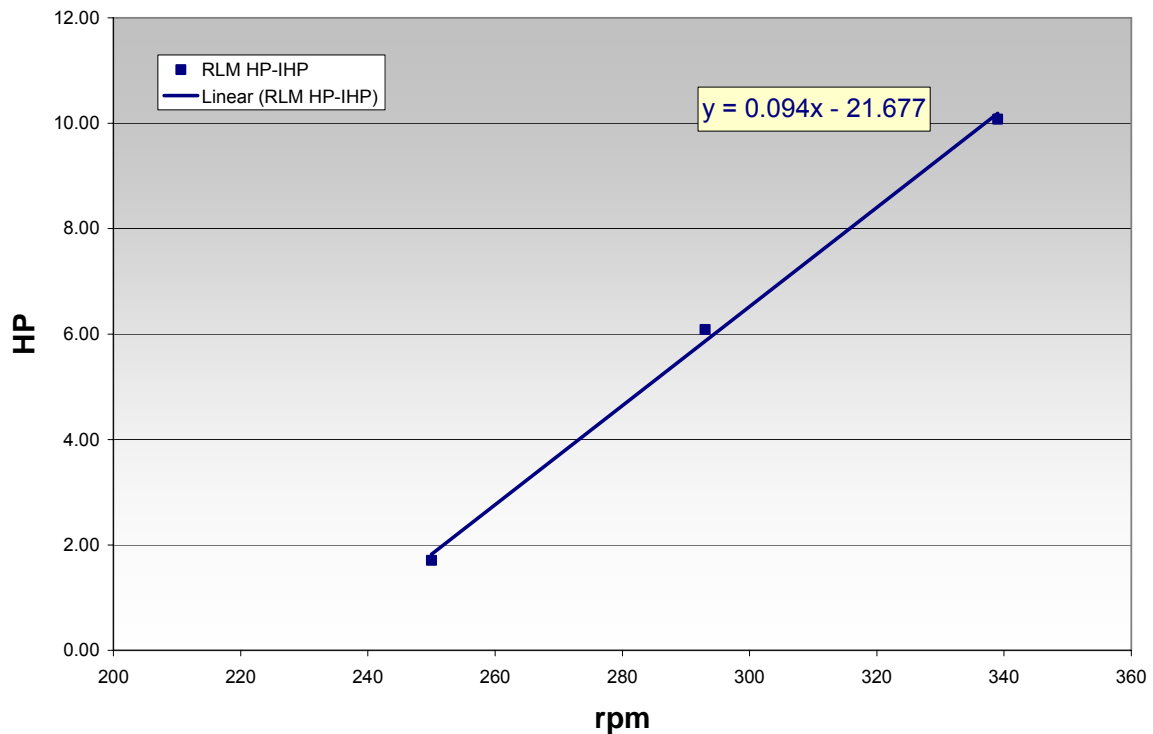


Figure 4-39. Unloaded Frictional Losses as a Function of Speed

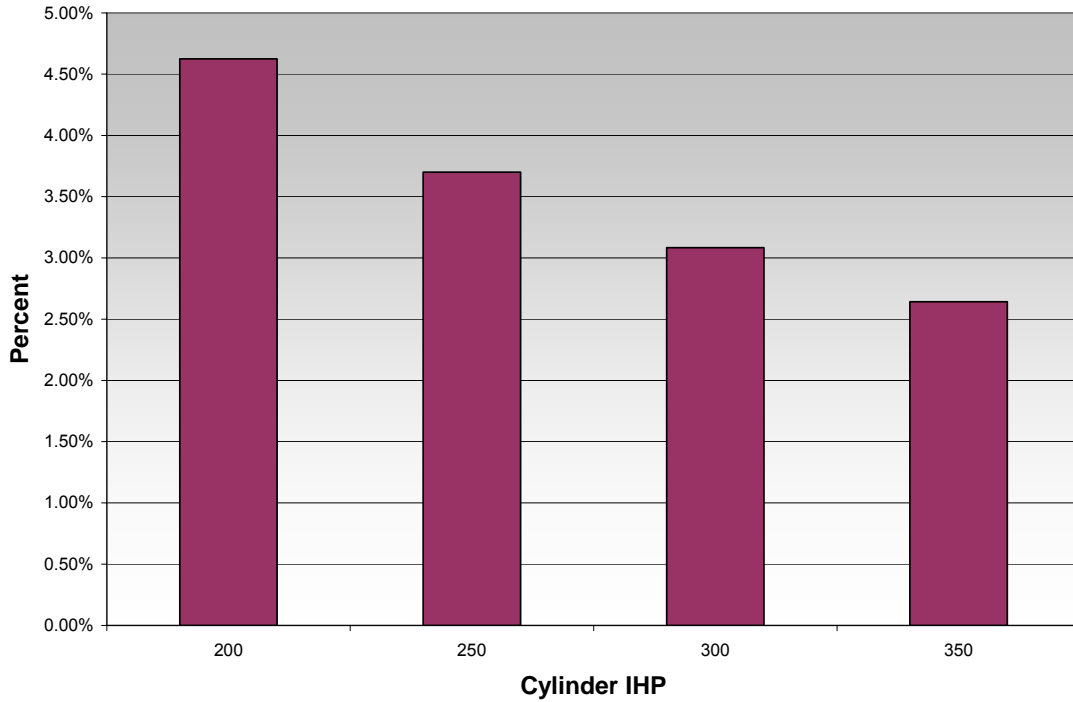


Figure 4-40. Unloaded Frictional Loss as Percent of Compressor Cylinder IHP

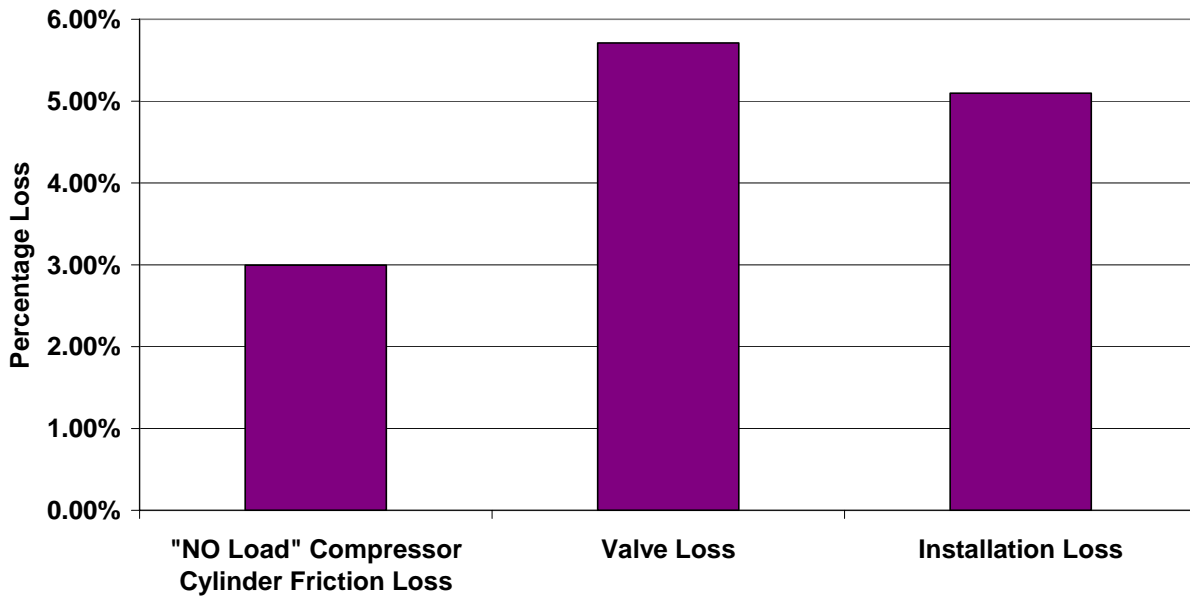


Figure 4-41. Comparison of Inferred Values for Friction, Valves (DIP) and Installation Losses as a Percentage of Indicated Power

4.3.5 MONITORING COMPRESSOR CYLINDER TEMPERATURE RISE

The temperature rise across a compressor cylinder from suction to discharge, if measured accurately in combination with accurate measurement of suction and discharge pressure, can reveal valuable information about the compression process. If the gas composition is known, calculating the ratio between isentropic enthalpy rise from suction conditions to discharge pressure and actual enthalpy rise from suction to discharge conditions provides a close measure of compressor isentropic efficiency. Even if the gas composition is not used, the temperature rise can be mapped as a function of compression ratio and a regression model of this variation developed as a baseline characteristic of the compressor. This model provides an expected value for temperature rise for any ratio, and when compared to the actual temperature rise for that ratio, any repeated and significant differences (above two or three standard error values) indicate deterioration in compressor performance—most likely attributable to valve leakage. Thus, temperature rise monitoring as a function of ratio represents a simple and effective condition monitoring technique which, if deployed and used, will help maintain the pipeline compression system near its optimum capacity and efficiency. Permanently installed temperature and pressure sensors, which are well calibrated and regularly calibrated, will make such monitoring most effective. Discharge temperature sensors on each nozzle are the most discriminating and allow the deterioration to be tracked to a particular cylinder. In fact, simply comparing temperature rise for each cylinder against other cylinders can reveal a potential deterioration if one cylinder reflects substantially higher temperature rise than the others.

The project has developed data showing noticeably different temperature rise across different cylinders. Figure 4-42 presents data from installed instrumentation on an HBA-6T. It shows temperature rise as a function of compression ratio for the three compressor cylinders on this unit and the trend lines representing the regression models for these three cylinders. One cylinder shows higher temperature rise than the other two, by over 1 degree. As a simple estimate, one-degree excess temperature rise out of 45 indicates this cylinder's efficiency could be 2% lower than the others.

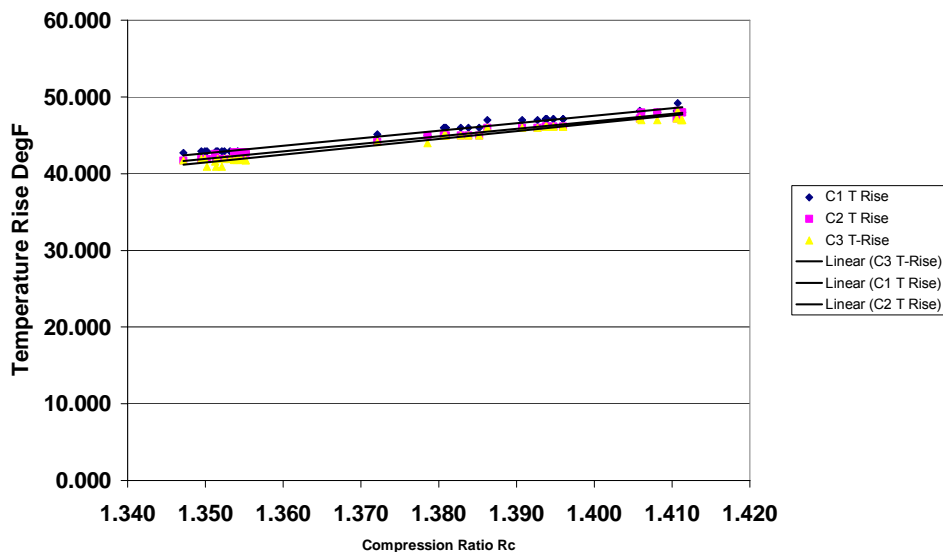


Figure 4-42. Temperature Rise versus Ratio for 3 Cylinders on a GMW10

Figure 4-43 shows the consistency of averaged cylinder discharge nozzle temperature and header temperature, by plotting one against the other. The data suggests at most 0.25-degree temperature drop between nozzles and header. The significance of this is to provide some support for the use of pressure measured in the header or in the laterals in combination with temperatures measured in the nozzles (right outside the cylinders); the gas is flowing sufficiently fast that it loses very little temperature between nozzles and header. However, it is likely to incur some pressure drop in flowing from nozzles to where it enters the headers, as result of installation losses.

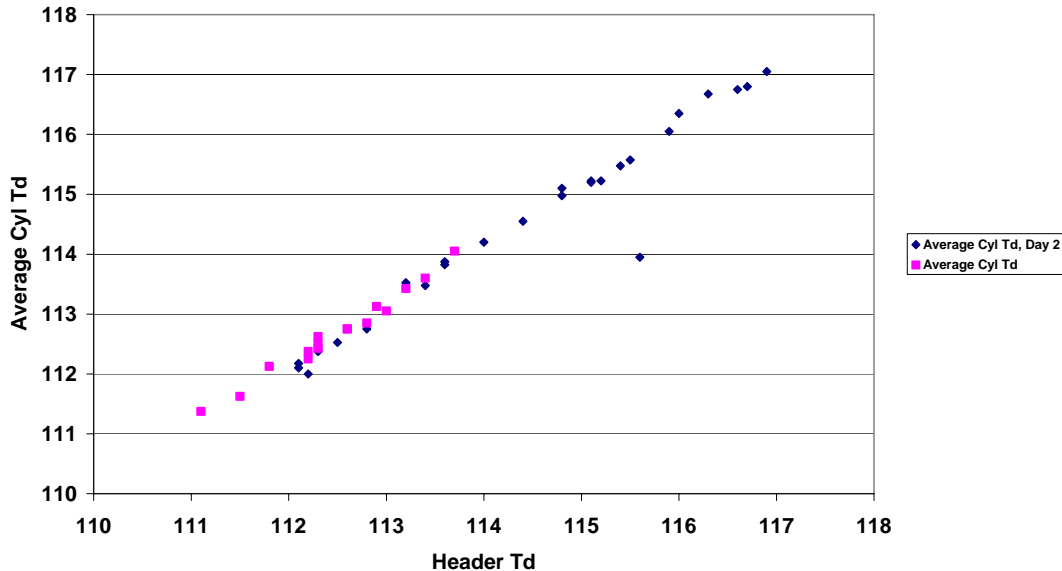
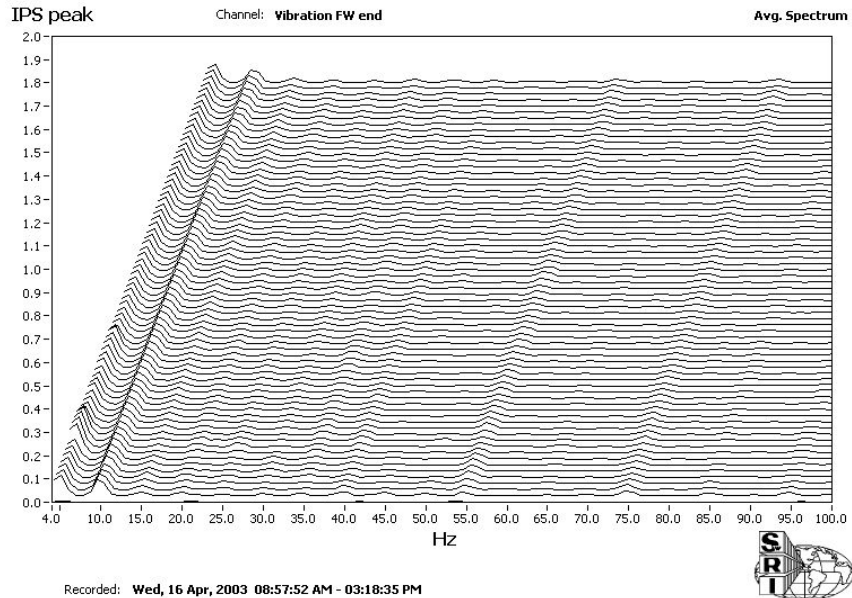


Figure 4-43. Average Cylinder Td versus Header Td; Days 1 and 2

4.3.6 MONITORING FRAME VIBRATION

Compressor frame lateral vibration was monitored during all of the six early tests of this project as a potential basis for detecting severity of loading. Figure 4-44 shows a frequency spectrum in waterfall format during a day’s testing in which a number of balancing and operational changes were made; the frame vibration reflects no significant changes, and based on this observation, it appears unlikely that frame vibration would provide a discriminating means of identifying load severity. A contributory factor for this observation is that frame lateral vibration is most strongly influenced by unbalanced inertia loads (reciprocating and rotating). These would change only if something like a counterweight was lost or a compressor rod broke.

Frame vibration remains a valuable quantity for detecting major events such as these. It has also been shown by Smalley, Mandke, et al. [7] that frame vibration at the bearing centerline is a good indicator of mounting integrity. The data set in this report showed foundations in good condition with bearing centerline vibrations below 7 mils (175 microns) and deteriorated foundations with frame vibrations of twice this level or more (14+ mils; 350+ microns).



**Figure 4-44. Vibration Bearing Centerline (Throw 1);
(Kinder Station (El Paso Station 823); April 2003)**

4.3.7 MONITORING INSTANTANEOUS ROTATIONAL VELOCITY

Early tests indicated that the peak-to-peak amplitude of instantaneous rotational velocity (IRV as described in Section 3 of the report) was also limited as a discriminating indicator of load severity. However, Figure 4-45 (which presents revolution by revolution variation in power cylinder power), in combination with Figure 4-46 (which presents the time variation of IRV), shows the time series variation of IRV responding directly to a power cylinder misfire. As a basis for detecting anomalies in loading severity, the time series IRV would require substantial process and detection logic, but this data shows this diagnostic potential clearly exists.

4.3.8 ISOLATING INSTALLATION LOSSES

Flow resistance losses occur at compressor valves, in the cylinder passages, at nozzle orifices, at line orifices, and at contractions or expansion in the piping. The losses at orifices and piping expansion/contractions are referred to as installation losses. The project demonstrated the use of pressure measurement in cylinder, nozzle, and lateral to distinguish installation pressure drop losses from cylinder pressure drop (resistance) losses. Figure 4-47 shows variation of pressure as a function of crank angle in the cylinder, at the nozzle transducer (normally located inboard of the nozzle orifice), and at a transducer in the lateral for an HBA-6. With carefully matched and calibrated transducers, the PV area difference between cylinder and nozzle pressure provides a good measurement of cylinder losses, and the PV area difference between nozzle and lateral pressures provides a good measure of installation losses. Figure 4-48 shows a pressure transducer installed in the lateral for a TCVC10. Figure 4-49 shows Cylinder 3 pressure, nozzle pressure, and lateral pressure as a function of crank angle for a TCVC10. Again, the reduction in peak pressure along the flow path is clear and the potential for using this data to calculate effective losses in cylinder and installation is demonstrated.

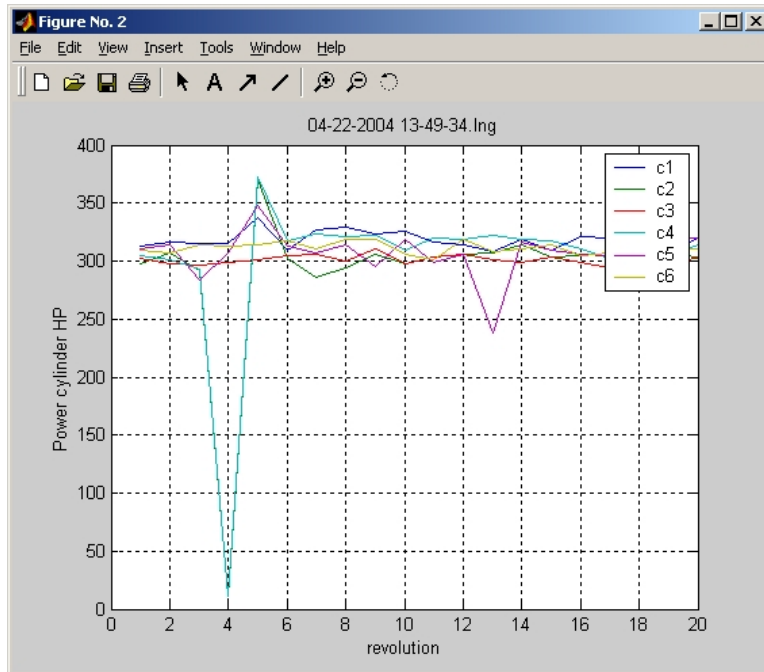


Figure 4-45. Engine Cylinder Power Over 20 Revolutions

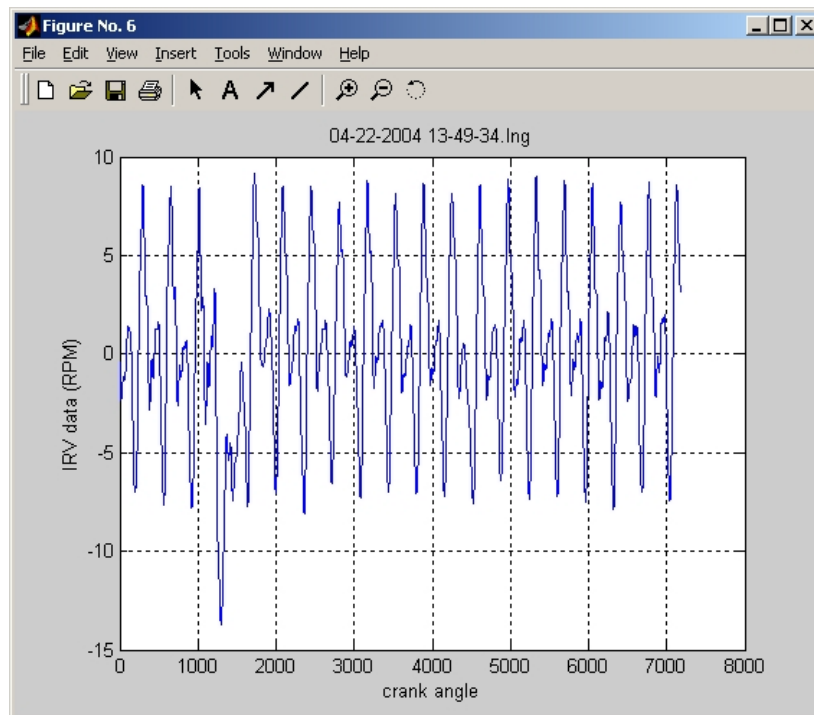


Figure 4-46. Instantaneous Rotational Velocity, as a Function of Crank Angle Over 20 Revolutions



Figure 4-47. Heated Pressure Sensor Installed on Suction Nozzle; Dresser-Rand TCVC10 (Dominion Groveport Station; Unit 1; April 20, 2005)



Figure 4-48. Heated Pressure Sensor (Suction Lateral); Dresser-Rand TCVC10 (Dominion Groveport Station; Unit 1; April 20, 2005)

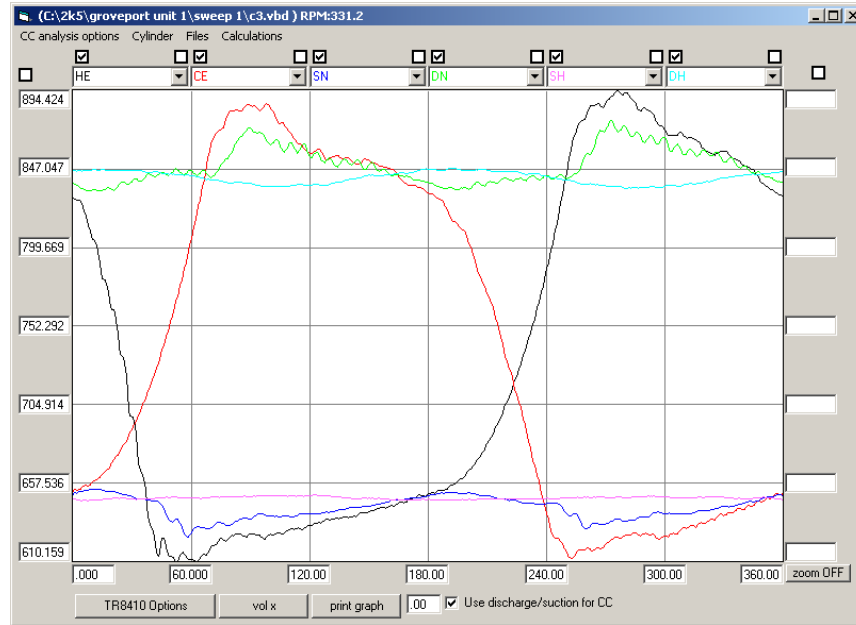


Figure 4-49. Pressure as a Function of Crank Angle; Cylinder 3 Head End, Crank End, Nozzles, and Laterals; Dresser-Rand TCVC10; 330 RPM Operation (Dominion Groveport Station; Unit 1; April 20, 2005)

For tests on this project, a coarse observation is that installation losses are comparable to the cylinder losses.

Enthalpy based efficiency data reflects the combination of cylinder and installation losses and helps provide confirmation of the sum of cylinder and installation losses.

4.3.9 MONITORING CRANK STRAIN

The Strain Data Capture Module (SDCM) is a well-established measurement method, which had established its value in numerous integrity evaluations prior to this project. The SDCM was used on most of the engine/compressor tests under this project. It continued to demonstrate its value and reflected the influence of balancing in reducing crankshaft dynamic strain and the influence of timing changes on crankshaft on strain.

Figure 4-50 shows the variation of the first eight orders as a function of time from the start of SDCM installation on a GMW10. This figure demonstrates the ability of the SDCM to characterize crank strain. First and second orders tend to dominate and are very similar to each other during this test.

4.4 NEEDS (TECHNOLOGY, DATA, METHODS) OF INTEGRAL ENGINE/COMPRESSORS

This sub-section summarizes the needs demonstrated or reaffirmed by the tests performed on a number of widely deployed engine/compressor models and discussed in previous sub-sections:

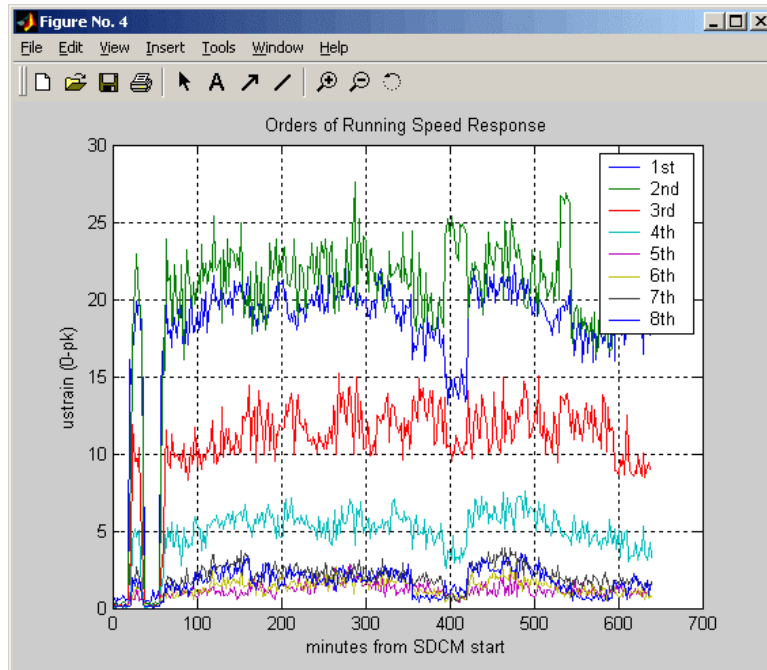


Figure 4-50. Spectral Orders of Crankshaft Dynamic Microstrain Variation; Unit 6; After Modification (Williams' Station 60; Day 2; August 26, 2004)

4.4.1 COMBUSTION BALANCING

The benefits of effective combustion balancing have been shown as a small reduction in heat rate and a reduction in crankshaft strain. It has been further shown that peak firing pressure balancing does not necessarily move the engine operation closer to equal combustion across the power cylinders and that a more desirable target is to equalize the air/fuel ratio. The two alternatives evaluated under this project (Standard Deviation Balancing and Combustion Pressure Ratio [CPR] balancing) both seek to equalize equivalence ratio across the cylinders. CPR balancing proved very easy and effective to implement manually; it was also demonstrated in an automatic balancing installation. A further benefit of equalizing air/fuel ratio is to maximize margins between nominal operation and the extremes, which can lead to a misfire or to detonation. Figure 4-51 plots spark timing against fuel/air equivalence ratio. It emphasizes how reducing the spread in equivalence ratio maximizes the minimum vertical margin to knock and maximize the horizontal margin to the lean limit (misfire), providing maximum flexibility of operation. Peak firing pressure balancing on engines with wide variation in air supplied can lead to detonation.

4.4.2 BALANCED AIR TO EACH POWER CYLINDER

The need was shown on this project to equalize the air supplied to each cylinder and to understand the causes of air imbalance. A leading candidate cause is dynamic pressure and density variation over space and time in the air and exhaust manifolds documented clearly on this project. Other candidates are geometrical differences between the cylinders (e.g., in flow passages and clearance).

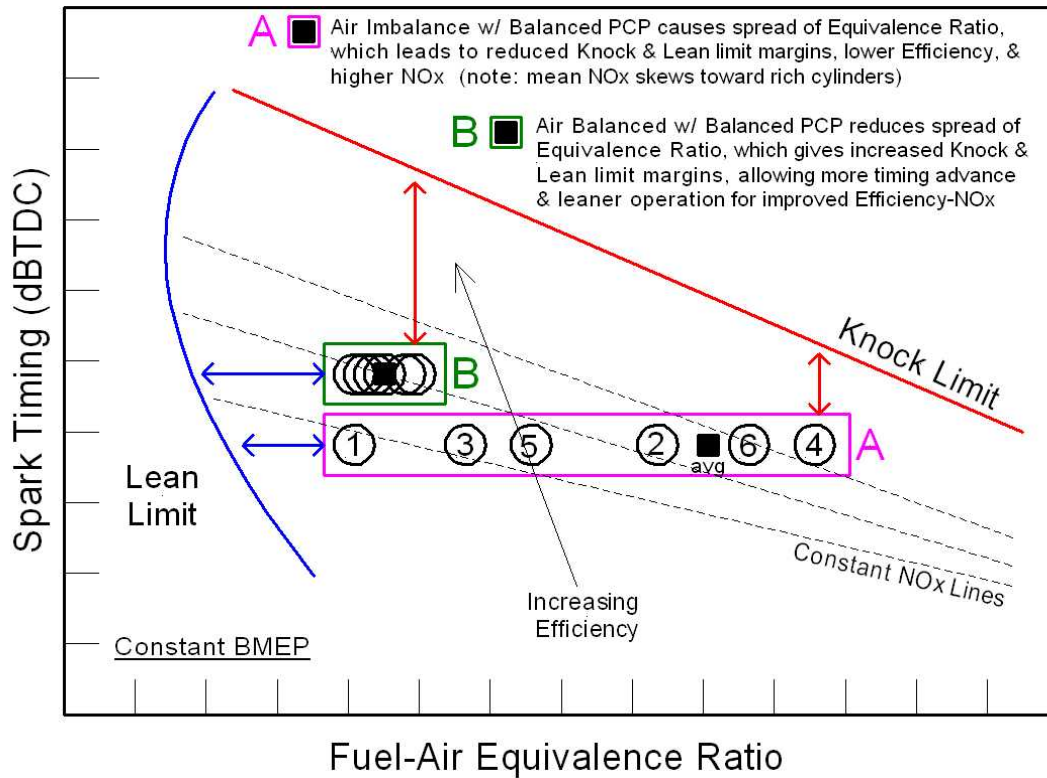


Figure 4-51. Typical Lean-Burn Spark-Ignited Gas Engine Operating Boundaries

4.4.3 ACCURATE MONITORING OF POWER AND TORQUE

As previously discussed, the appropriate operating philosophy to minimize fuel consumption while avoiding overload is to keep the engine loaded to 100%. If the basis used by the station for loading yields load values higher than actual loads, then the engine will be underloaded and fuel consumption will be excessive. If the basis used by the station yields load values lower than actual loads, then the engine will be overloaded with the potential for damage and excessive maintenance costs.

During the project, several comparisons were made between brake horsepower inferred from indicated compressor cylinder horsepower and the power values being used by the station to load the engine by load step adjustment. Figure 4-52 shows one such comparison; here the station inferred load is consistently low by 7% or 8%, with the potential for overload.

Figure 4-53 shows another comparison. Here the agreement between the station and the indicated power is close, indicating the likelihood of accurate loading with minimized fuel consumption and minimized risk of damage. It is reported that the basis for load inferred by the station is an extensive test program to calibrate the compression model used. Thus, it is demonstrably possible to load an engine accurately. However, it requires a substantial investment in compressor performance testing. It should also be recognized that the performance testing is usually performed with the compressor cylinders and valves in good condition. Any leaks, which develop will not be reflected in the calibrated model and could lead to high or low uncertainty in the engine load.

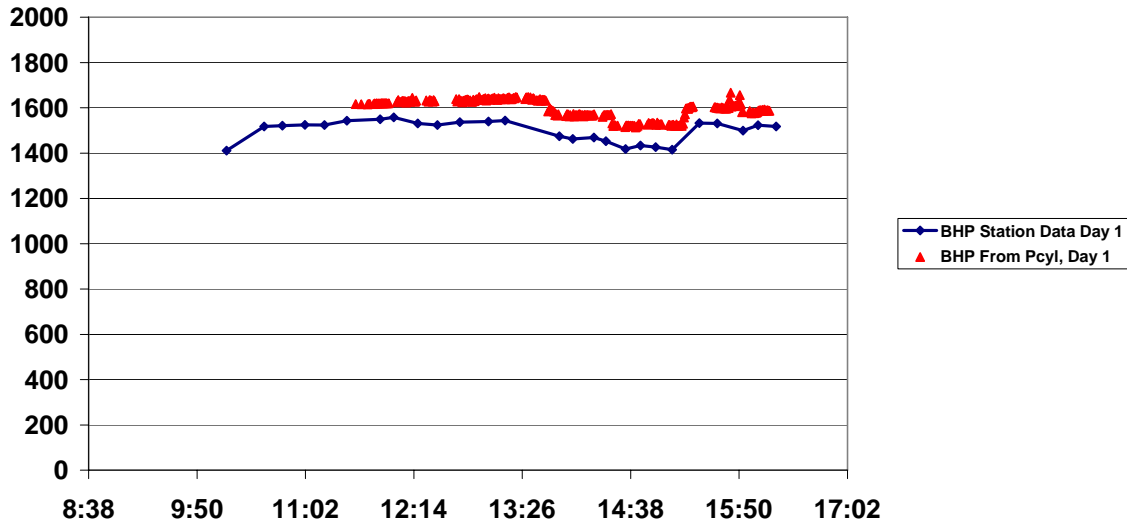


Figure 4-52. Comparison of Station BHP to BHP from Cylinder Pressure (Using 0.95 Mechanical Efficiency)

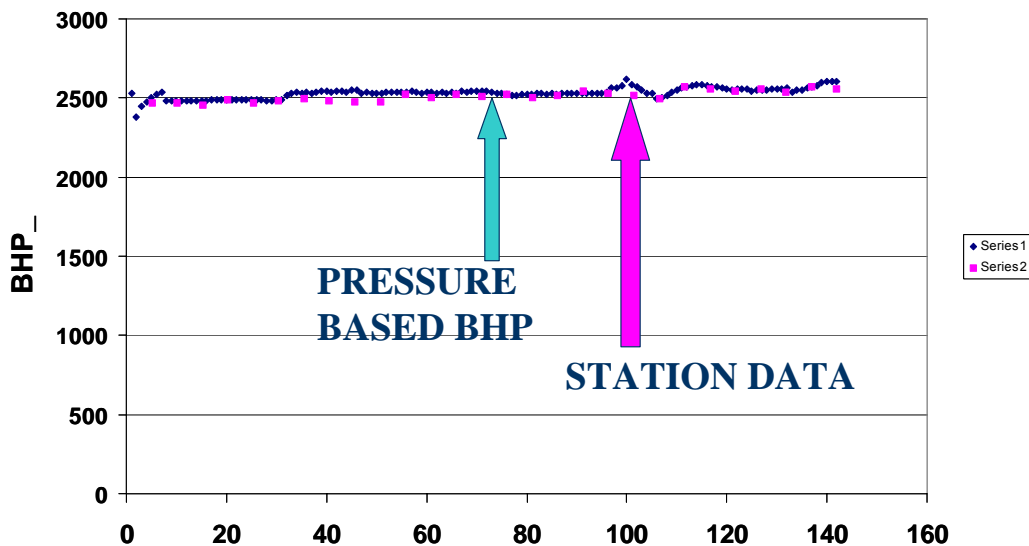


Figure 4-53. Pressure-Based BHP versus Station Data

This discussion and data indicate the need for and value of a method to monitor engine load directly, accurately, reliably, and cost-effectively. The Rod Load Monitor has been shown on this project to be a viable candidate for this purpose.

4.4.4 UNIT THROUGHPUT MONITORING AND MEASUREMENT

The limited ability to directly measure capacity (throughput) for reciprocating compressors represents a major technological limitation. The primary objective of pipeline compressors is to flow gas, yet this essential item of performance cannot be directly measured.

Thus, the ability to measure flow down to the unit level is a major need of the pipeline industry. The following are options deserving of further pursuit, but none have established themselves as state-of-the-art techniques in the pipeline industry.

There has been some success in the past with the use of ultrasonic flow measurement if the signal processing is modified to allow each ultrasound velocity perturbation at say 1,000 Hz to be recorded and integrated for flow rather than averaged. An in-line ultrasonic meter with non-standard signal processing was used with success for measuring flow through a UTC integral engine/compressor as documented by Smalley [8].

A strap on ultrasonic meter was evaluated during one test under this project, but encountered unmanageable noise problems as configured at the test site. It is believed these noise problems could be overcome with appropriate filtering and signal processing, but this could not be pursued under the present project.

Smalley, Harris, et al. [9] have documented a method of measuring flow through a reciprocating compressor, which uses a tracer gas injected into the inlet at a known rate and a means to measure tracer gas concentration at exit. This measurement technique compared closely with an enhanced inferential method, which accounted for suction gas heating and real gas properties in its interpretation of measured cylinder pressure data.

Thus, tracer gas measurement is promising for performance testing applications, but its potential as a monitoring method is less clear. It requires an accurate gas chromatograph to measure tracer concentration in the compressor discharge lateral, and the issue of tracer gas being injected up and down the line may complicate measuring the effect of injection upstream of one unit on concentration just downstream of that unit.

Station flow measurement well downstream of the compressors will give reasonably accurate flow for a single unit if only that unit is running.

The use of an insertion turbine meter, which is light enough to respond to all significant pulsation frequencies, is a potential option.

If horsepower is accurately measured and if temperature rise is accurately measured and a good gas composition is available, then the power divided by the enthalpy rise across the unit yields mass flow.

4.4.5 PROTECTION AGAINST THE DAMAGE OF DETONATION

Unchecked detonation leads to severe engine damage, such as a burnt up cylinder liner, burnt up valves, or a failed bearing. If engines operate significant periods of time unattended, an operating strategy, which essentially guarantees no detonation, becomes essential. This acts as a deterrent against strategies, which improve performance by bringing that engine closer to a detonation boundary, particularly on engines, which exhibit wide cycle-to-cycle variability. Advanced timing has been shown to reduce heat rate but to also carry with it a penalty in terms of increased likelihood of detonation. Likewise, it has been shown that retarding timing reduces the chance of detonation

The preceding paragraph emphasizes the need for a reliable detonation detector, coupled with a conditional control strategy, which can rapidly and reliably move the engine away from a condition of detonation by retarding timing and/or leaning the fuel/air mixture. A method for

closed loop control of equivalence ratio will be subsequently discussed below and represents a means to implement controlled leaning of the mixture as one means of detonation protection.

4.4.6 LOW LOSS PULSATION CONTROL

As previously discussed, devices and methods for controlling pulsations include orifices, in-line filters, side branch resonators, and selective location of junctions within bottles. Of these options, orifices typically incur the highest loss. While filters incur expansion/contraction losses at choke tube exit and inlet, these are typically significantly lower than orifice losses. Figure 4-54 emphasizes the losses at orifices for the TCVC10 compressor tested under this project. With significant flow resistance at all eight orifices including nozzle and line orifices, the total loss from suction and discharge is about 480 horsepower for the pulsation control system on this compressor—about 10% of the engine’s nominal 5,000 HP, and a high price for pulsation control which has not proven very effective.

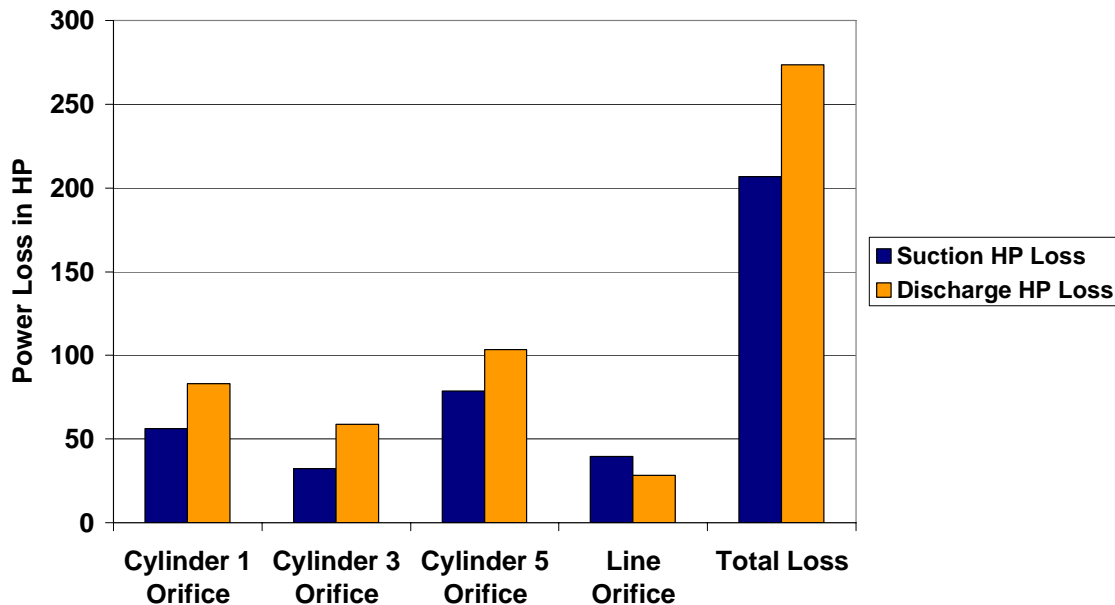


Figure 4-54. Predicted Power Losses at Pulsation Control Orifices TCVC10 Compressor

The need clearly exists for pulsation control options, which avoid the need to install orifices, together with accurate tools to predict system pulsations and losses. The combination of in-line filters and side branch resonators will be discussed and illustrated later in this section, and the ability to predict their influence will be demonstrated.

4.4.7 CAPACITY AND HORSEPOWER RECOVERY ON LOW EFFICIENCY COMPRESSORS

Many compressors installed in the 1950s, 1960s, and 1970s date from an era when regulation of interstate natural gas transportation made pursuit of high efficiency and optimum capacity less important than today. While none of the units tested under this project has isentropic efficiencies as low as some in the GMRC survey of the 1990s, some exhibit significant room for improvement; since the project sample is also smaller than in the GMRC survey, there

may still be an appreciable number of compressors with yet lower efficiency than seen in this project.

Every percentage point in compressor efficiency represents at least one percentage point increase in capacity. At pipeline bottlenecks, the potential to increase compressor thermal efficiency by modification rather than by replacement offers a cost-effective option for gaining capacity with no change in installed horsepower. In addition, keeping the efficiency as close as possible to its leak free value by effective condition monitoring helps ensure the potential capacity is always available.

4.4.8 REFINED KNOWLEDGE OF MECHANICAL LOSSES

As discussed at several points in the preceding sub-sections, a significant uncertainty exists in the mechanical losses and associated efficiency of power transmission between the crankshaft and the compressor piston face. This uncertainty affects the ability to accurately determine brake horsepower and brake fuel energy consumption (heat rate) and leaves the industry without targets or benchmarks for improvement in this area of loss. In summary, the need remains for the following:

- Effective methods to measure mechanical loss in bearings, packing, rings, and rider bands.
- More comprehensive working models of mechanical efficiency for use in estimating BHP.
- Usable models of specific loss mechanisms for guidance in loss reduction efforts.
- Deployed effective methods of measuring brake horsepower and torque.
- Demonstrated and deployed technologies for reducing mechanical losses.

The RLM technology described in this section has promise for addressing several of these needs, including measurement of BHP and for measuring mechanical losses. The Free Floating Piston and oil temperature control previously discussed are examples of options to be evaluated for mechanical loss reduction, together with bearing redesign and alternative operating strategies, which may be revealed by mechanical loss testing and modeling under different conditions.

4.5 TECHNOLOGIES

4.5.1 STANDARD DEVIATION BALANCING

This technology (Raymer [10]) has the objective of finding the combination of fuel supply to each cylinder, which achieves combustion equality (i.e., equal equivalence ratio) in each cylinder of a two-cycle slow speed natural gas engine. It uses a surrogate for equivalence ratio, which is the standard deviation in peak firing pressure for cycle-to-cycle variation. The basis for this surrogate is that rich cylinders tend to combust more consistently and lean cylinders tend to combust with more variance. Adjustment to cylinder fuel is made to equalize the standard deviation in peak firing pressure. Specifically, fuel is reduced to the cylinder with the lowest standard deviation or increased to the cylinder with the highest standard deviation, and this step is repeated until the standard deviations are as equal as possible. The measure of

equality used is the coefficient of variation (standard deviation/mean) across the cylinders of the standard deviation of cycle-to-cycle variation for each cylinder, with a target of 10% or below.

Figure 4-55 shows the results from tests of standard deviation balancing for an HBA-6T at El Paso’s Kinder Station 823. It shows that as standard deviation balancing was implemented, the time between high peaks (over 70 microstrains) in crank strain increased substantially to over 70 minutes. This benefit may be compared to the reduction observed in peak-to-peak crankshaft strain in balancing tests already discussed in this report section.

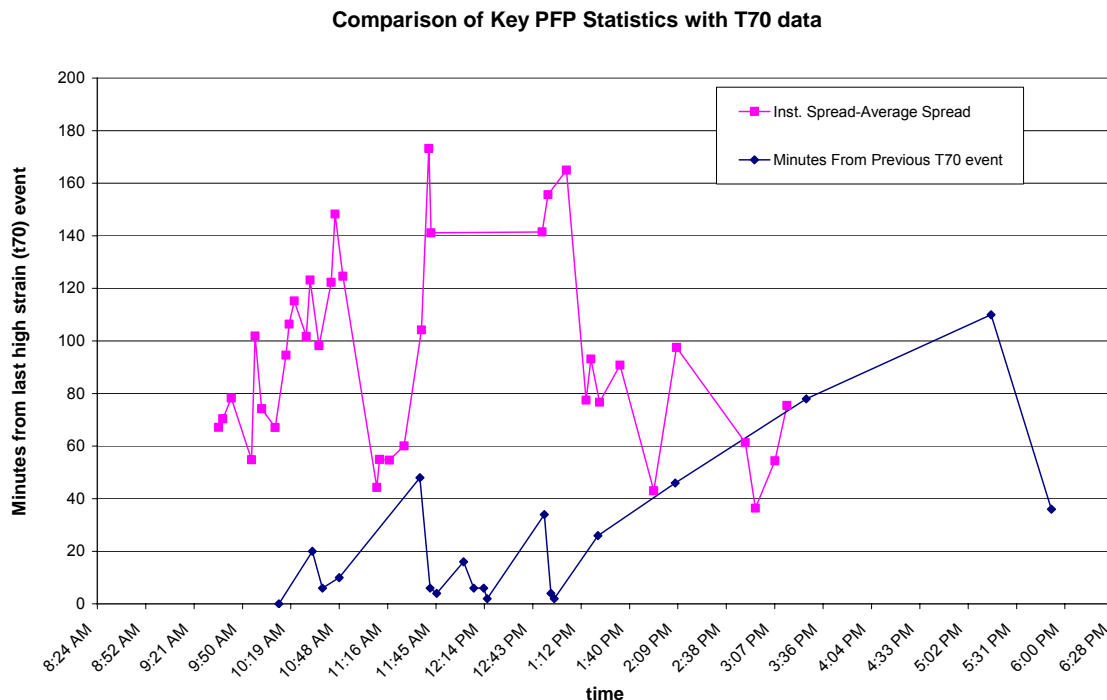


Figure 4-55. Comparison of Key PFP Statistics (Instantaneous Speed – Average Spread); and Time from Last 70+ Microstrain Event; HBA-6T; Test #1; (Kinder Station (El Paso Station 823); April 2003)

Standard deviation balancing has seen limited testing under the project. This testing demonstrated an encouraging influence on peak-to-peak crankshaft strain variation.

4.5.2 COMBUSTION PRESSURE RATIO BALANCING

Following the firsts tests on an HBA-6T, which revealed significant differences between compression pressure ratio, combustion simulation analysis was undertaken to help clarify how air imbalance attributable to compression pressure variation might impact balancing, and whether alternatives to peak pressure balancing might be devised, which avoided “fighting” the low compression ratio in some cylinders by making these cylinders overly rich.

A spread in air manifold pressure was postulated across the cylinders, which resulted in a 10% variation in compression pressure across the cylinders, qualitatively similar to that observed. A random variation in fuel supply was postulated, which led to Figure 4-56, which compares pressure as a function of crank angle for six cylinders with a range of compression

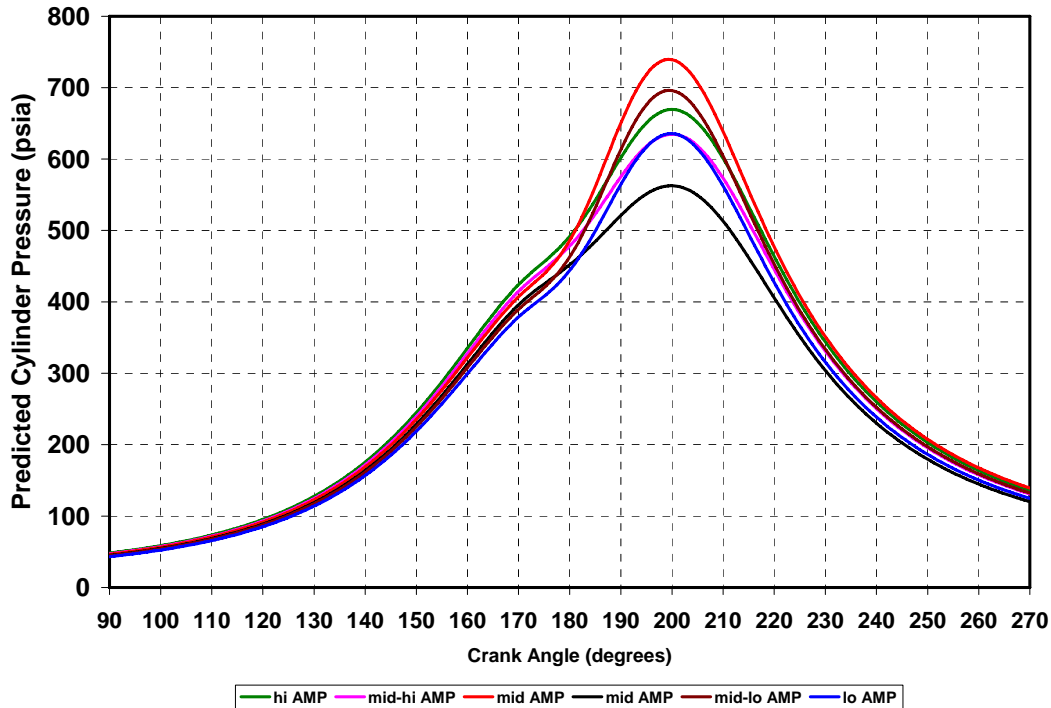


Figure 4-56. Unbalanced Engine Simulation – Spread in Compression Pressure Induced by Even Increment Spread in AMP – 15% Random Spread in A/F Ratio

pressures and a distribution in peak firing pressure, which differs in relative levels from the distribution in compression pressure. Figure 4-57 is a bar-graph, which compares for six cylinders the air/fuel ratio resulting from two different balancing strategies, each starting with the air/fuel ratio and compression pressures for Figure 4-56. One set of air/fuel ratios results from peak firing pressure balancing and one from equalizing the ratio of peak firing pressure to compression pressure. It is clear in this simulation that combustion pressure ratio balancing equalizes air/fuel ratio, and that peak firing pressure balancing has to bias the air/fuel ratios, because of air imbalance.

Figure 4-58 and Figure 4-59 compare combustion pressure ratio (CPR) before and after combustion pressure ratio balancing on an unmodified GMW10 engine at Williams Station 60. Figure 4-58 shows variation in CPR from 3.10 to 3.37 before CPR balancing, a spread of over 8%. Figure 4-59 shows variation in CPR from 2.97 to 3.08 after CPR balancing—a spread of about 3.5%. A similar balancing process was performed a number of times on different engines, and typically took less than 30 minutes and achieved a similar spread in CPR. As implemented, CPR is calculated each cycle for each cylinder and each cylinder’s CPR value is averaged over a large number of cycles. It was found that averaging over 100 cycles led to a more consistent data set from which to make balancing decisions than averaging over 50 cycles.

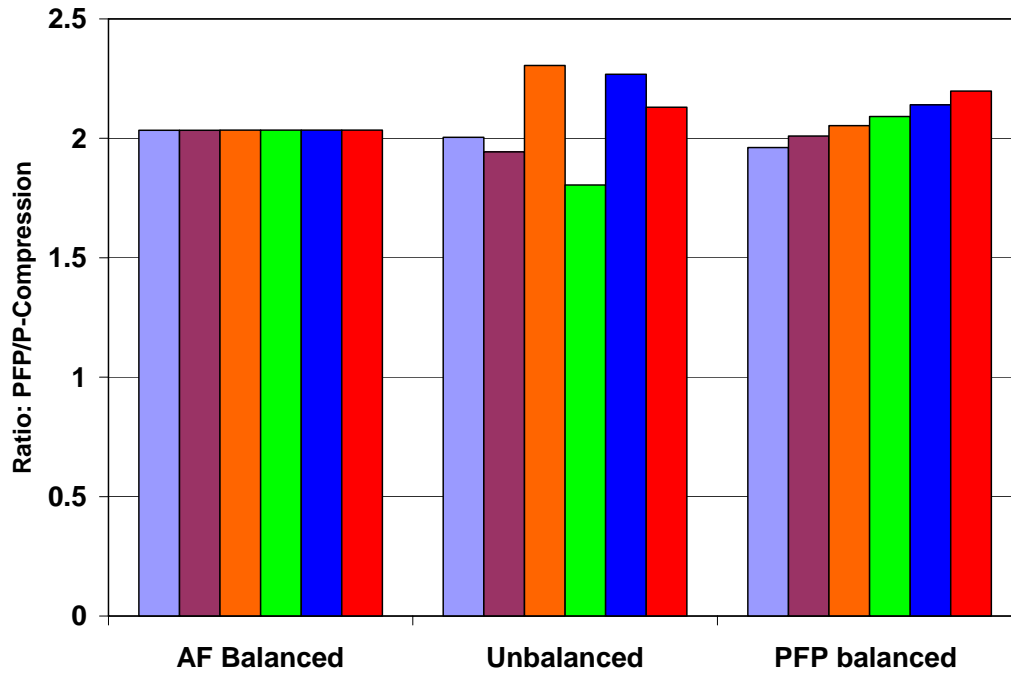


Figure 4-57. Ratio of PFP to Compression Pressure for Three Different Balancing Situations

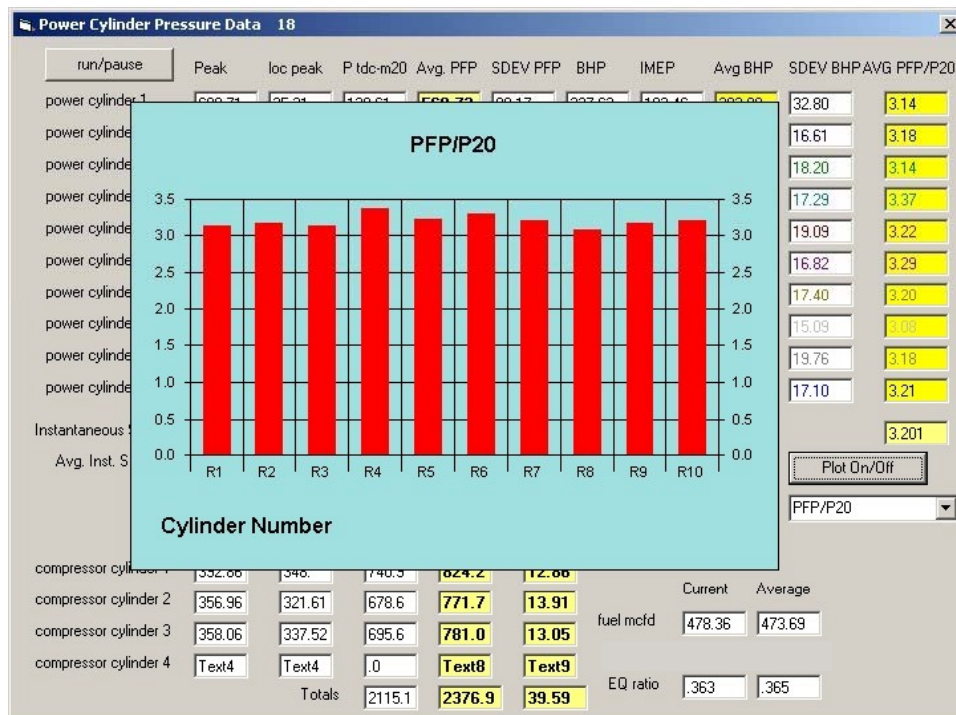


Figure 4-58. Cylinder-to-Cylinder Variation in Combustion Pressure Ratio (CPR); Day 1 (Williams' Station 60; February 2004)

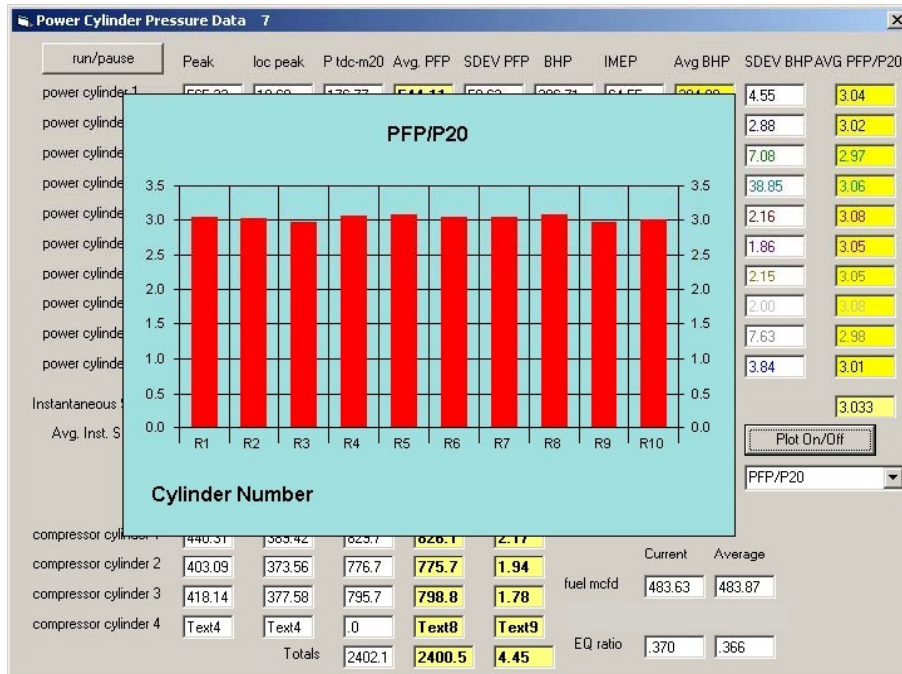


Figure 4-59. Cylinder-to-Cylinder Variation in Combustion Pressure Ratio after CPR Balancing (Williams' Station 60; February 2004)

The small benefits of CPR balancing in heat rate reduction and the more distinct benefits in crank strain reduction have been demonstrated in several tests.

From a theoretical point of view, CPR balancing if used instead of peak firing pressure balancing should naturally help to account for differences in compression pressure, which result from cylinder-to-cylinder differences in the amount of air which flows through the inlet ports and is trapped at port closure. It will also help to avoid compensation for low compression pressure by the addition of excess fuel to achieve equalized peak firing pressure, even if some of the compression pressure differences are attributable to differences in cylinder and piston geometry, clearance, and kinematics.

In summary, CPR balancing is a patented method, which is easy and effective to apply. It has been demonstrated both for manual balancing and as an algorithm in an automated balancing system. If any cylinder-to-cylinder variation in trapped air exists, it should be better than peak firing pressure in equalizing air/fuel ratio and should be equivalent to it if there is no inequality in trapped air. It does require a balance analyzer, which can determine cylinder pressure as a function of crank angle.

For these reasons, CPR balancing should be seriously considered as an alternative to peak firing pressure balancing.

4.5.3 CLOSED LOOP WASTE-GATE CONTROL

The feasibility of controlling global air/fuel ratio by direct application of an off-the-shelf exhaust gas oxygen sensor (UEGO) and an industrial controller has been demonstrated. The approach was simple and had the clear effect of maintaining the global equivalence ratio constant for an HBA-6T under conditions of change, which otherwise had a demonstrable influence on

global equivalence ratio. Figure 4-60 shows the main components required for this demonstration—the waste-gate actuator, the sensor in the exhaust stack, the industrial controller, and the connection from the controller to the gas pneumatic system, which controls the waste-gate in open loop. Figure 4-61 compares the variation of equivalence ratio in open loop and closed loop conditions as a function of speed. Figure 4-62 shows the distinct difference in cycle-to-cycle standard deviation, also as a function of speed. Clearly, the closed loop control reduces the cycle-to-cycle variability.



Figure 4-60. Element of Waste-Gate Control for Equivalence Ratio; HBA-6T at Kinder Station (El Paso Station 823); April 2004

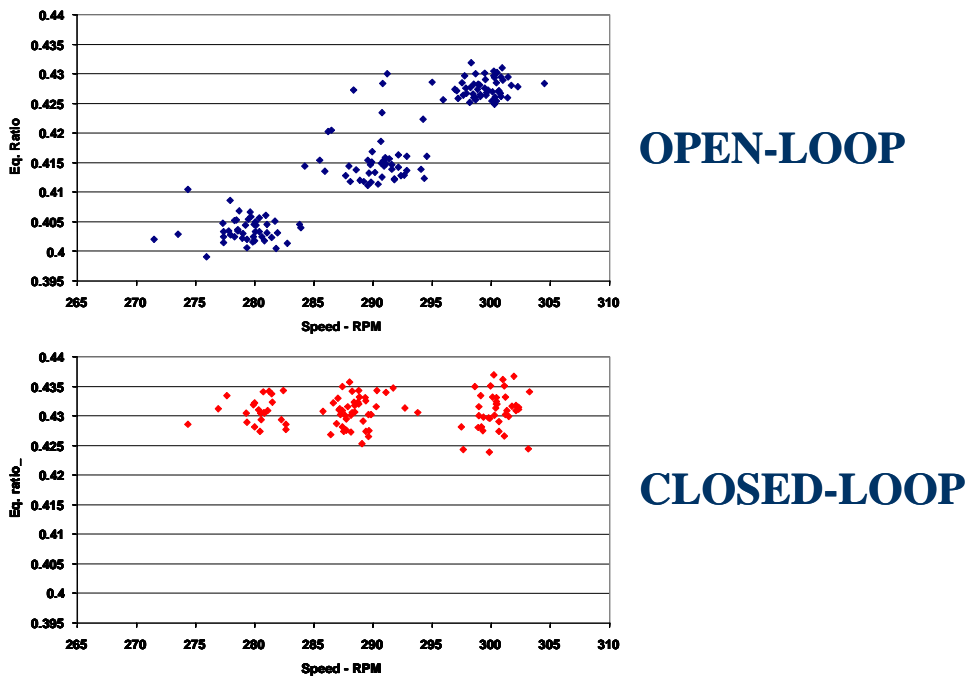


Figure 4-61. Equivalence Ratio versus Speed; Comparison of Open-Loop and Closed-Loop Control (Kinder Station (El Paso Station 823); April 2004)

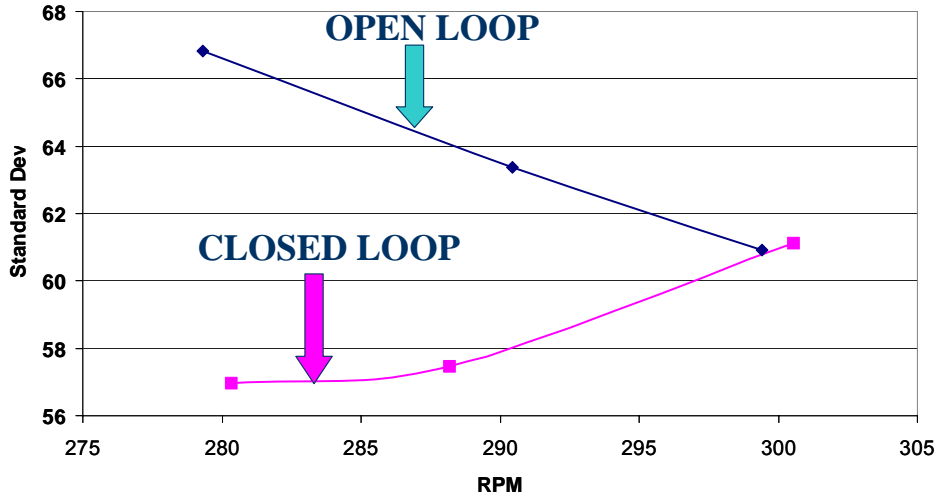


Figure 4-62. Mean Cylinder Cycle-to-Cycle Standard Deviation versus Speed; Comparison of Open-Loop and Closed-Loop Control of Waste-Gate (Kinder Station (El Paso Station 823); April 2004)

This test was strictly one of feasibility demonstration; it does not seek to optimize any particular performance attribute, but options clearly exist to maintain a richer or a leaner global equivalence ratio according to a desired operating strategy.

This stops short of controlling trapped equivalence ratio but is also simpler than methods, which seek such control. This test also demonstrated feasibility in use of a UEGO sensor for control in preparation for similar control of fuel rate in a four-stroke carbureted engine.

The use of a detonation detector in conjunction with conditionally applied controls to reduce the potential for detonation has been discussed. Closed loop control of global equivalence ratio, coupled with timing control, offers a powerful and flexible method of achieving this conditional reduction of detonation prevalence in response to the development of detonation as ambient and operating conditions change.

4.5.4 CLOSED LOOP FUEL RATE CONTROL FOR CARBURETED FOUR-STROKE ENGINES

Figure 4-63 shows installation of the piping modification, which enabled the closed loop control of fuel rate on a KVG103, which is targeted for catalyst installation to reduce NO_x and HAPS. Achieving peak efficiency and reliability of the catalyst requires precise control of the air/fuel ratio. Commercial systems are available to accomplish this precise control. Based on an offer of assistance by Compliance Controls Corporation to make a demonstration system available to the project and to provide some on-site assistance, it was decided to include a test of this commercially available technology within the test program using the Compliance Controls MEC-L system. This system uses a UEGO sensor in the exhaust stack and allows the flexibility of tuned/optimized control ranging from stoichiometric over a range to lean equivalence ratio.

Expert pipeline welders prefabricated a replacement yoke, then cut out a section of the header, and welded this yoke in its place. This yoke provides two fuel paths to the carburetors—one via a 2-inch ball valve, which could be opened or closed, and one via a 75-mm Flo-Tech control valve modulated by the signal from the MEC-L controller. This parallel path was utilized only because a 100-mm Flo-Tech, which would be the correct size to achieve the fuel

75mm FloTech control valve w/ parallel 2" ball valve



Figure 4-63. MEC-L Flo-Tech Control Valve

flow requirement with the available pressure setting, was not available for demonstration testing. During the closed loop test, the ball valve was partially open to allow some fuel flow and allow the control valve to stay within an operable range. At the end of the test, the control valve could be removed—allowing continued normal operation through one or both legs of the yoke.

Figure 4-64 shows the MEC-L controller, the sensors (MAP, MAT, RPM, UEGO, and EGT), and the connections to the control module. Figure 4-65 demonstrates that the controller works as desired. The two “strip chart” records presented here show the variation of O_2 and NO_x during unloading of the unit. In the upper chart, operation is in open loop without manual adjustment. The O_2 drops with reduced load, indicating a richer mixture under reduced load, while NO_x stays constant. The lower chart shows operation in closed loop with automatic fuel rate adjustment. Here the O_2 stays constant with reduced load indicating the equivalence ratio has been kept steady by the controller; however, the NO_x drops. This result confirmed the effectiveness of available technology for fuel rate control as this station implements plans to install a catalyst for emissions reduction.

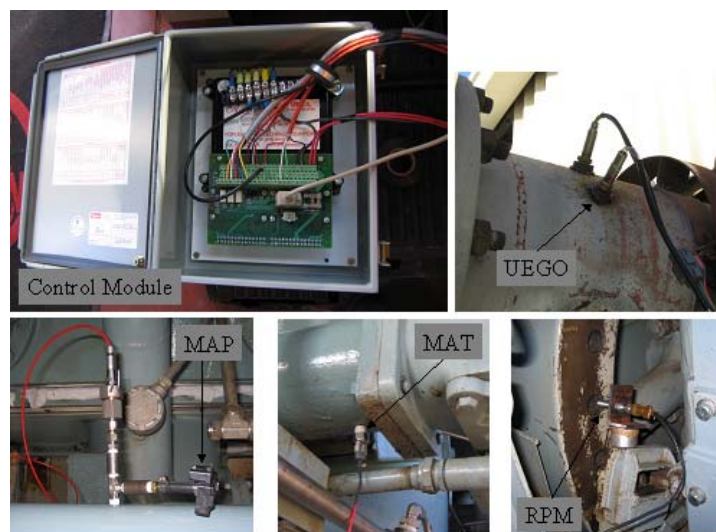


Figure 4-64. MEC-L Controller and Sensors

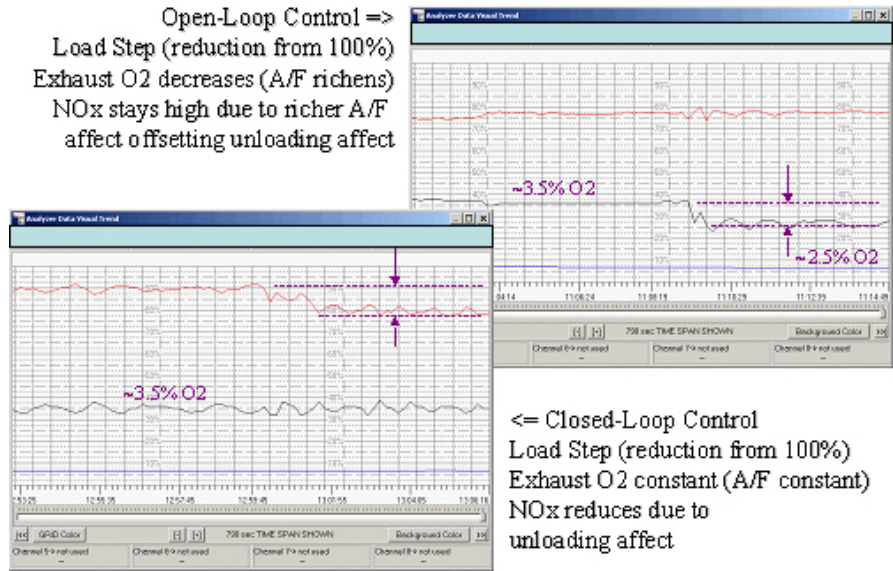


Figure 4-65. Simple Test of Closed-Loop

Adding closed loop fuel/air ratio control would benefit operation of this KVG, whether or not a catalyst is added. Without such control, the fuel/air ratio must be manually adjusted after any load change based on manifold vacuum with the goal of maintaining a consistent lean operation. With the MEC-L or similar system, a specified degree of lean operation could be established and maintained without further manual intervention. Since the manifold vacuum is only an indirect measure, control using the UEGO sensor would be more consistent and effective and could be optimized for different goals, such as emissions control or heat rate control.

4.5.5 ROD LOAD MONITOR

Figure 4-66 shows the GMRC Rod Load Monitor (RLM) installed on the crosshead of an HBA-6T. The RLM has a generator whose motion past a fixed magnet array powers the strain gages and RF transmitter. The stationary receiver is a horizontal “rod” oriented parallel to

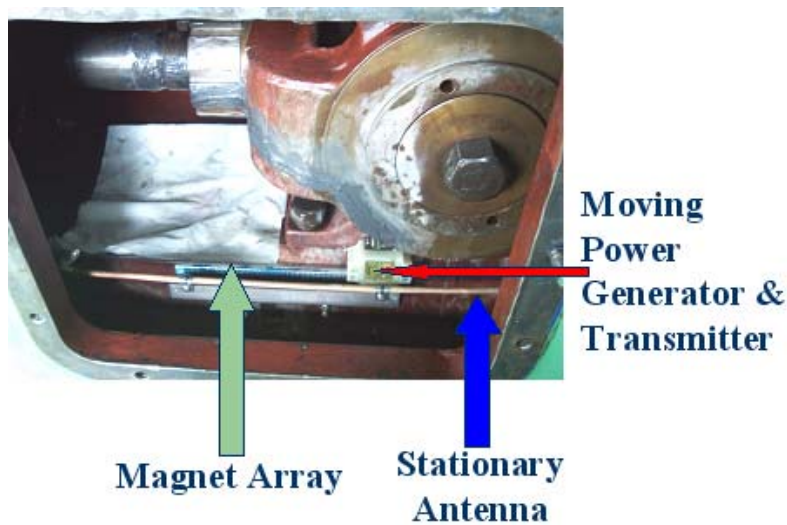


Figure 4-66. Self-Powered Rod Load Monitor (RLM)

crosshead's direction of motion so it maintains a constant normal separation from the transmitter over the full extent of the transmitter's horizontal motion. Two strain gages arrayed on either side of the piston rod, and appropriately bridged, cancel any bending in the horizontal plane and provide a signal proportional to axial tension and compression of the rod as it drives the piston. Installation methodology has been refined and validated during the project to achieve the appropriate length of magnet array and clearance between the array and the generator and so to provide adequate power.

In this configuration, the RLM is designed for permanent installation as a monitoring device. In short-term testing applications, the self-powering feature is not needed and can be replaced by a battery, which simplifies installation and field adjustment. The RLM was used this way for several of the tests under the project. After some refinements early in the project, the consistency and accuracy of the RLM output have been demonstrated by comparison of power determined from the RLM against compressor piston face power determined from cylinder pressure measurement.

Figure 4-67 shows such comparison on a GMW10. Here the maximum difference between RLM and piston face power is about 10 horsepower. Figure 4-68 presents the same data as a percentage difference between the two power values, and shows a maximum difference of about 1.6%.

The potential value of the RLM where deployed as a permanent monitoring device is to make available an accurate value for load on the engine. The RLM power value involves much less inference than a power value calculated from operating conditions, and cylinder clearance information, for the prevailing load step. It is possible, with substantial, unit specific, testing, to calibrate such calculation methods, but the RLM eliminates the need for such testing and remains accurate even when valve leaks develop, or new valves with different flow resistance are installed. The potential for 0.6% heat rate increase for each percentage point reduction in load and the increased risk of damage with overload makes clear the value to operational efficiency and reliability of maintaining load neither below nor above 100%. The RLM where deployed can ensure 100% loading.

There remains a need for a demonstration project where load on the engine is adjusted up and down through the load step setting on the basis of measured rod load power or torque.

The RLM has also demonstrated its value for short-term testing—for example, in isolating mechanical losses in rider bands, rings, and packing. This application needs to be refined and used in a program of mechanical loss identification and reduction.

4.5.6 STRAIN DATA CAPTURE MODULE

The Strain Data Capture Module (SDCM) was first developed on an SwRI internal research project and was first demonstrated and applied on an earlier GMRC research project. Thus, it was available technology at the start of this project and had already been applied on a number of different compressors. This project provided five more demonstrations of its reliable capabilities as a sensor for engine and compressor crankshaft integrity testing, and quantified in several tests how changes in ignition timing and in the state of balance directly influence peak-to-peak crank strain variation (see Figure 4-25 for example).

As used in these multi-day tests, the memory capacity of the current generation SDCM required daily downloading of data, and time consuming safety checks, lockouts, and permits,

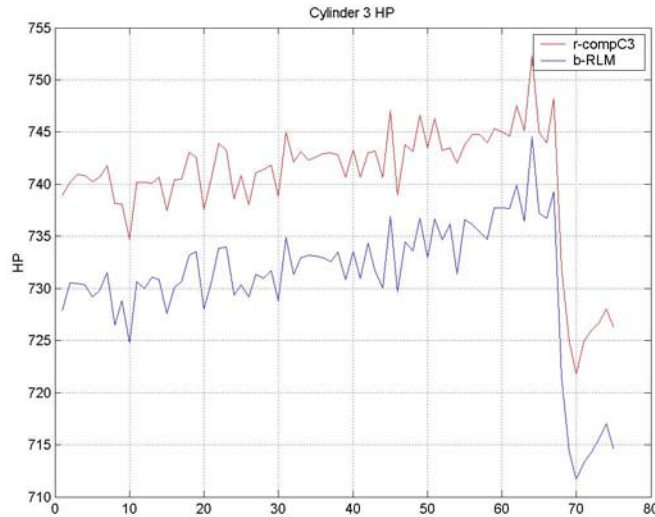


Figure 4-67. Comparison of Horsepower Based on the Rod Load Monitor and on Cylinder Pressure; Unit 6; After Modification (Williams’ Station 60; Day 1; August 25, 2004)

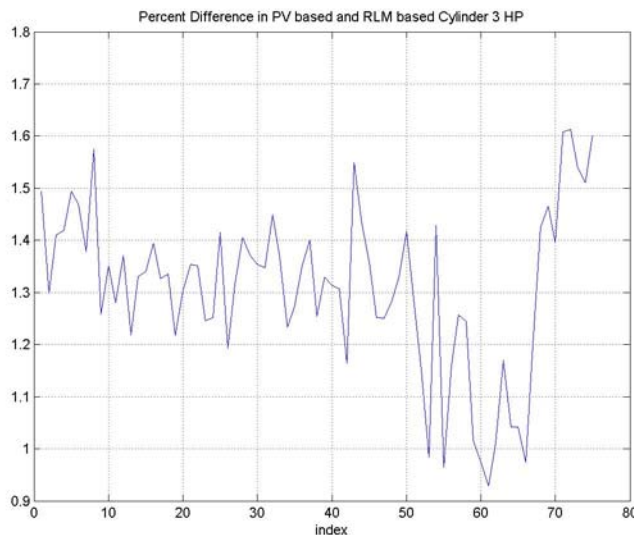


Figure 4-68. Percentage Difference Between Horsepower Based on Rod Load Monitor and on Cylinder Pressure; Unit 6; After Modification (Williams’ Station 60; Day 1; August 25, 2004)

associated with the necessary crankcase cover removal. Extending its memory to allow uninhibited multi-day testing would avoid these delays and a next generation SDCM has now been developed with this refinement. If the SDCM were to be used for continuous monitoring, a self-powering version with telemetry would be needed.

4.5.7 HIGH PRESSURE FUEL INJECTION

This technology has been developed to allow fuel gas injection at a much higher pressure than in the original design of these engines. This should produce better mixing of fuel and air in lean mixtures. Under the project, a pair of tests was undertaken to evaluate the benefits of high-

pressure fuel injection on a specific GMW10 at Williams Station 60. The first test was performed on the engine prior to any modification, and the second test was performed after the high-pressure fuel system had been installed by Enginuity in combination with a turbocharger.

Figure 4-69 shows one bank of power cylinders with the high-pressure fuel injection installed. The various lines to be seen are for the high-pressure fuel and for the hydraulics, which activate the high-pressure fuel valve. Visible also is the power cylinder transducer installed as part of the system and used for automatic balancing of the power cylinders. Figure 4-70 shows the turbocharger installed as part of the modification.



Figure 4-69. High-Pressure Fuel Injection System Installed on a GMW10 (Williams' Station 60)



Figure 4-70. Turbocharger Installed as Part of a Modification on a GMW10 (Williams' Station 60)

Figure 4-71 presents the changes in heat rate, system thermal efficiency, and normalized NO_x, measured by the two tests for four different conditions.

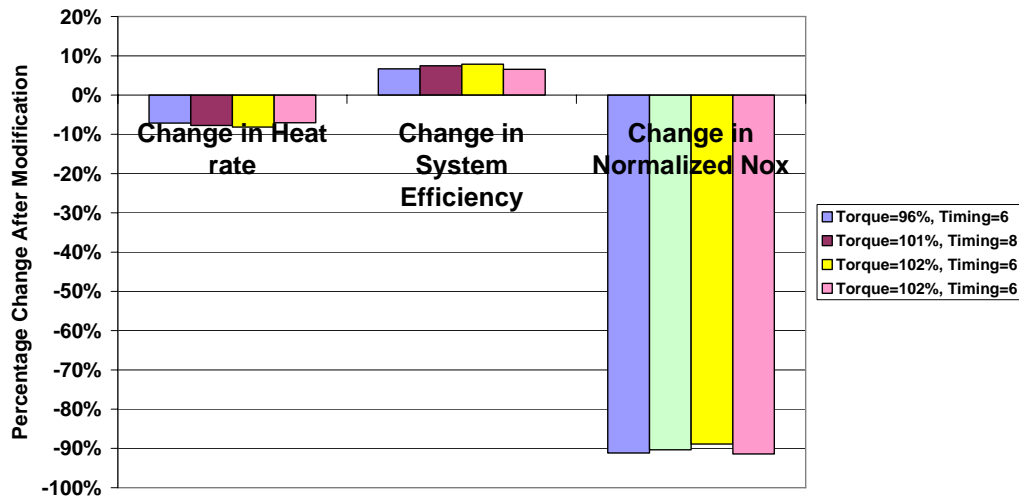


Figure 4-71. Evaluation of Adding High Pressure Fuel and Turbo to a GMW10

As a result of adding high pressure fuel and a turbocharger to this GMW10, these tests document that heat rate reduced by about 7%; system thermal efficiency increased by about 7%; and NO_x fell by about 90%.

4.5.8 DETONATION DETECTOR

Data was acquired during three tests from a detonation detector made available to the project by Metrix. This device, mounted on a power cylinder as in Figure 4-72, monitors acceleration and provides a voltage output proportional to the frequency with which acceleration exceeds a pre-set threshold.



Figure 4-72. Detonation Detector Mounted on Power Cylinder 7 on a KVG103

During the first test on an unmodified GMW10, as shown in Figure 4-73, the output was at 2.5 volts or below during operation with 6 degrees timing. When timing was advanced to 8 degrees, the voltage output jumped to between 4 and 5 volts, and at the same time audible and repeated knocking was observed on Cylinder 4L (on which the device was mounted). Changing the timing back to 6 degrees immediately dropped the output voltage below 2 volts and the audible knock went away.

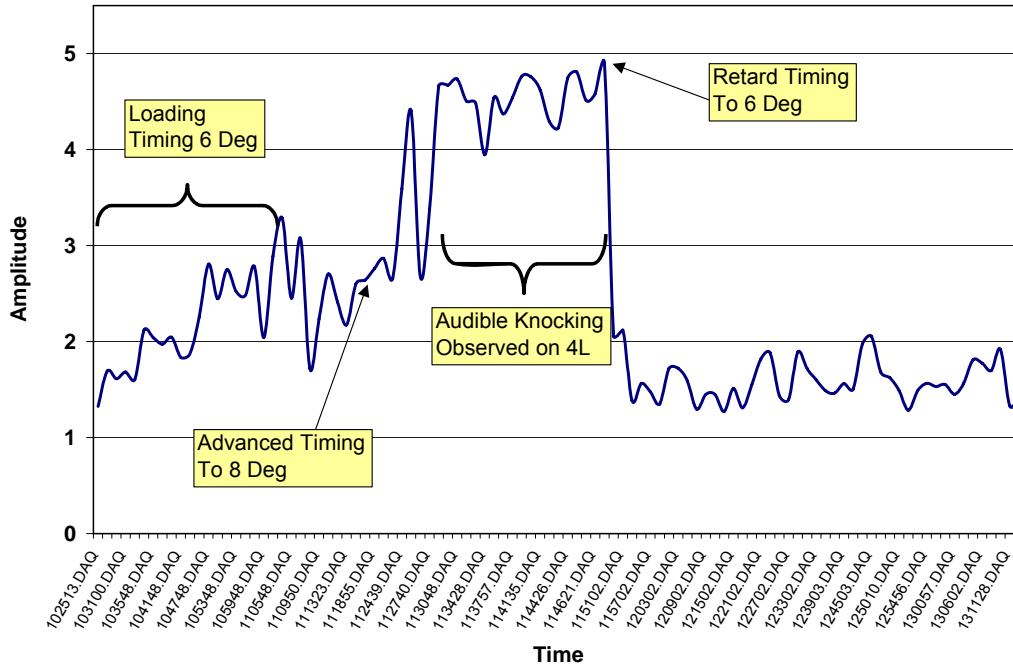


Figure 4-73. Knock Detector Output (Williams' Station 60)

During the second test, a more gradual change in conditions was imposed on an HBA-6T. Starting with the engine timing at 10 degrees and equivalence ratio at 0.43, timing was advanced to 12 degrees and the airflow was gradually reduced causing the equivalence ratio to increase from 0.43 to 0.46. These changes will tend to increase the likelihood of detonation. As a direct result of this gradual increase in equivalence ratio, Figure 4-74 shows the detonation detector output increased from an average of about 1.75 volts to an average of almost three volts. An occasional knock was observable during the period of richest fuel. Reduction of equivalence ratio back to 0.43 and retarding timing to 10 degrees caused the detonation detector output to drop to about 2 volts.

Figure 4-75 and Figure 4-76 present a direct correlation between cylinder pressure and detonation detector output during the first day of tests on a GMW10 after modification for high-pressure fuel. In the first half hour of testing just after startup and loading, the unit was found to be detonating unacceptably. Fuel adjustments were made and after about half an hour, the detonation was corrected and performance testing could start. Figure 4-75 shows peak firing pressure in Cylinder 4L during these 30 minutes of detonation to be close to 700 PSI, which is 125 to 150 PSI above the peak pressure after the detonation was stopped. This peak firing pressure is averaged, so the highest excursions were undoubtedly higher than 700 PSI.

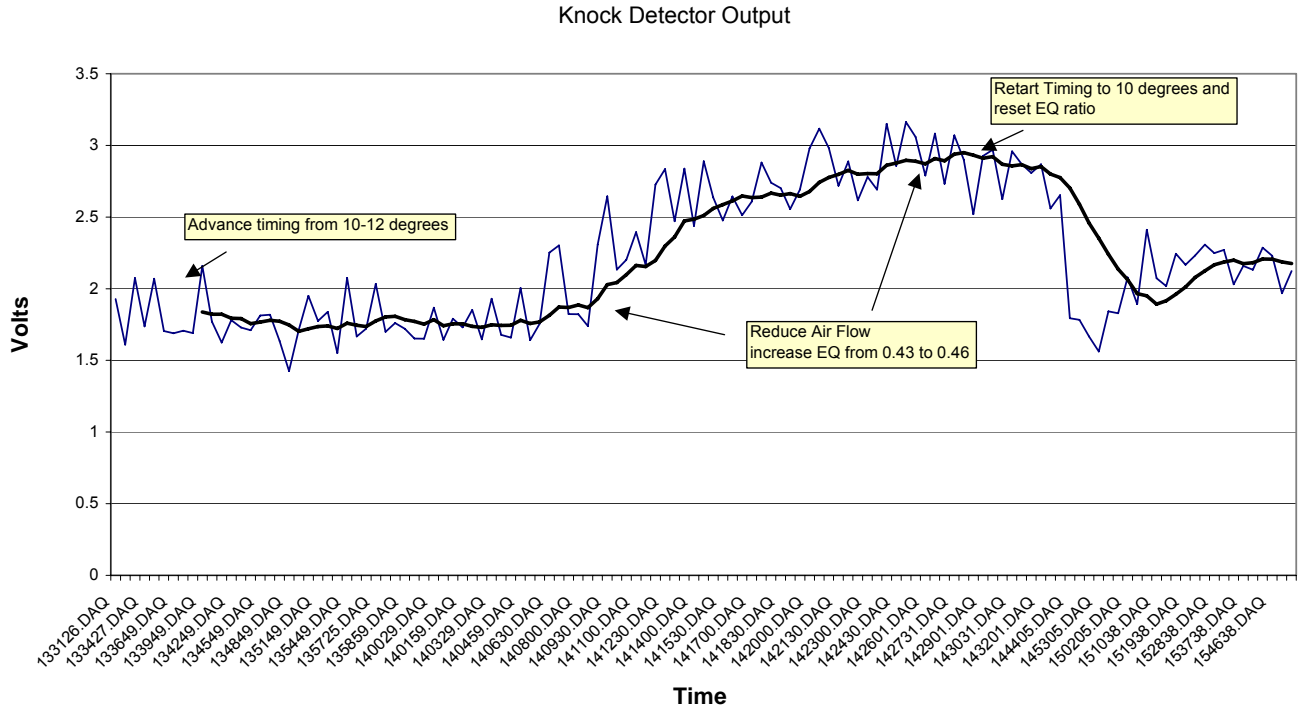


Figure 4-74. Knock Detector Output (Kinder Station (El Paso Station 823))

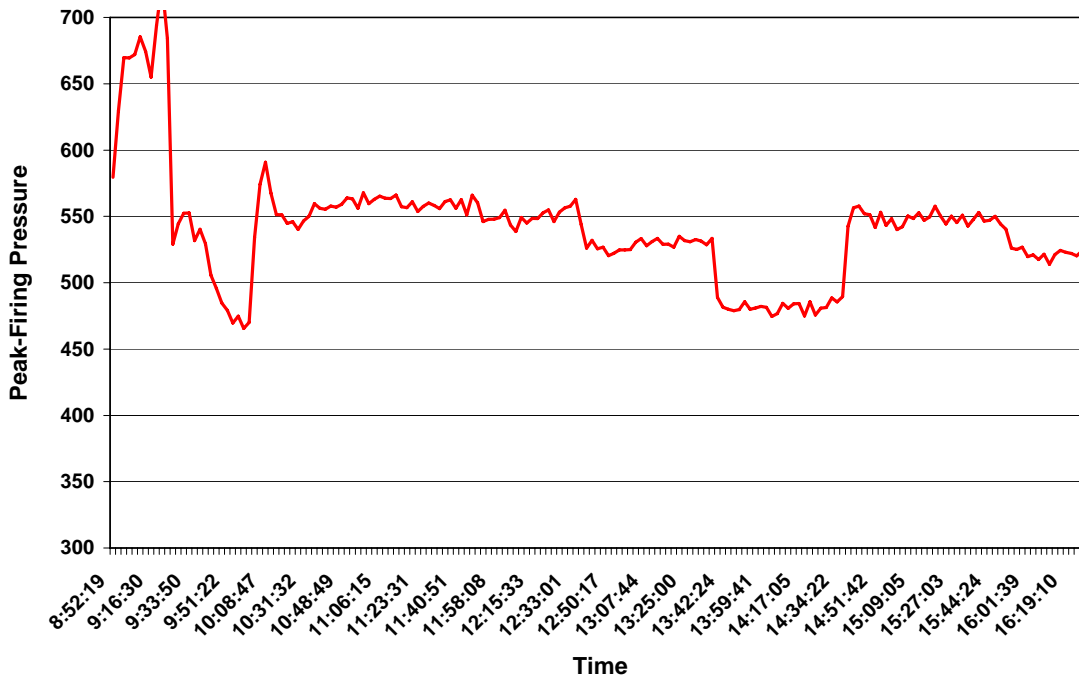


Figure 4-75. Power Cylinder 4 (Left); Average Peak Firing Pressure; Unit 6; After Modification (Williams' Station 60; Day 1; August 25, 2004)



Figure 4-77. Photograph of TCVC 10 as Tested Showing Compressor Cylinders, Suction Bottle, and Suction Piping

every discharge nozzle, at the joint between suction lateral and suction bottle, and at the joint between discharge lateral and the discharge bottle. The combined power loss associated with the orifices is predicted to be 480 horsepower, 10% of rated power for this engine! The lack of filtering limits the ability to control pulsations and shaking forces.

Keeping pulsations under control without excessive power loss maintains engine/compressor integrity, but requires reliable predictive tools and availability of pulsation control options, which will minimize associated power loss.

GMRC and SwRI have developed powerful digital technology to predict pulsations (Interactive Pulsation Prediction Software–IPPS). This technology accurately models cylinder-piping interaction; dynamically varying valve flow drives pulsations throughout the piping, while the pulsations just outside the cylinder dynamically influence the pressure differential across the valves and the resulting valve flow.

Figure 4-78 provides confirmatory evidence of this pulsation software’s ability to guide design for pulsation reduction. It compares pulsations in nozzles and laterals before and after changes to the compressor piping of an HBA-6 obtained from tests at Duke Energy’s Bedford station. The highest measured nozzle pulsations have dropped from over 5% of line pressure to below 2% of line pressure as a result of adding a suction side branch absorber and suction nozzle orifices. Similar pulsation reduction was predicted. Retrofit solutions, which would avoid any use of orifices, were not cost-effective at this station. The data of Figure 4-78 helps build confidence in the design analysis capability of the IPPS software.

Unbalanced Shaking Forces

Project Title IPPS Digital Analysis

Company Dominion Transmission

Project 18.06223.01.306

Site Groveport

Test Test 1

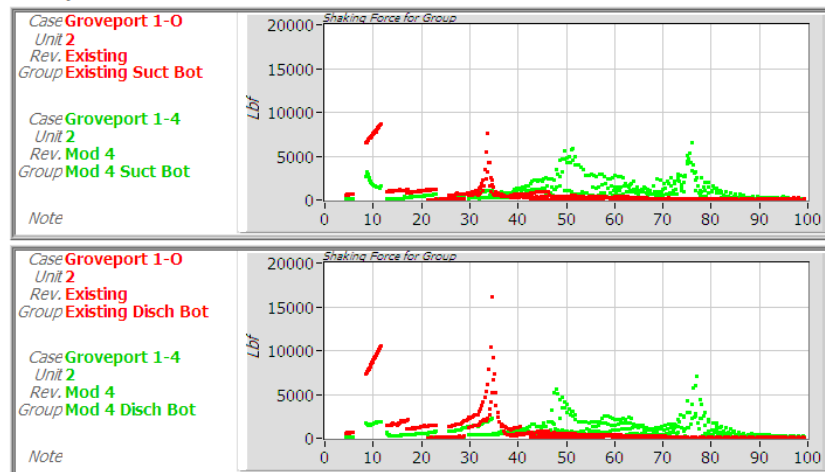


Figure 4-80. Comparison of Predicted Shaking Forces – Suction and Discharge Bottles

data points). Clearly, the highest shaking forces are cut in half from 15,000 lbs to 7,500 lbs. Of equal importance, the new design has no orifices and so cuts predicted power loss in the pulsation control system from 480 horsepower to 44 horsepower.

4.5.10 SIDE BRANCH ABSORBERS FOR PULSATION CONTROL

A major contributor to the predicted and measured pulsation control in the HBA-6 and the TCVC10 discussed above is the use of Side Branch Absorbers (SBA). The SBA is a device, which can be combined with other devices, providing the designer with powerful tools for pulsation control and manipulation, which can often remove the need for orifices and their attendant power loss.

The side branch absorber is a dead-ended device consisting most often of a choke and a volume. No net flow occurs into or through the dead-ended SBA. Figure 4-81 presents a schematic of the SBA added to the HBA-6 discussed above. Figure 4-82 presents a photograph of the same suction SBA after installation.

The role of the SBA is to add an acoustic natural frequency to the system characteristics. The SBA is sized so that, analyzed by itself as a standalone choke-volume system, its own single natural frequency matches a problem natural frequency which is known to be resonant in the existing system. When this SBA is attached into the existing system, the modified system is found to have no natural frequency where there used to be a problem, but it has one natural frequency below and one above the previous problem frequency. The amount of separation between these two new frequencies is a function of the overall size of the SBA. For the HBA-6, the SBA moved a natural frequency which lay close to one times the compressor's fundamental operating frequency (5 Hz) to frequencies sufficiently below and sufficiently above 5 Hz that they were not excited under single-acting conditions. This change eliminated the strong beating phenomenon observed on this compressor when the original natural frequency was excited under single-acting conditions.

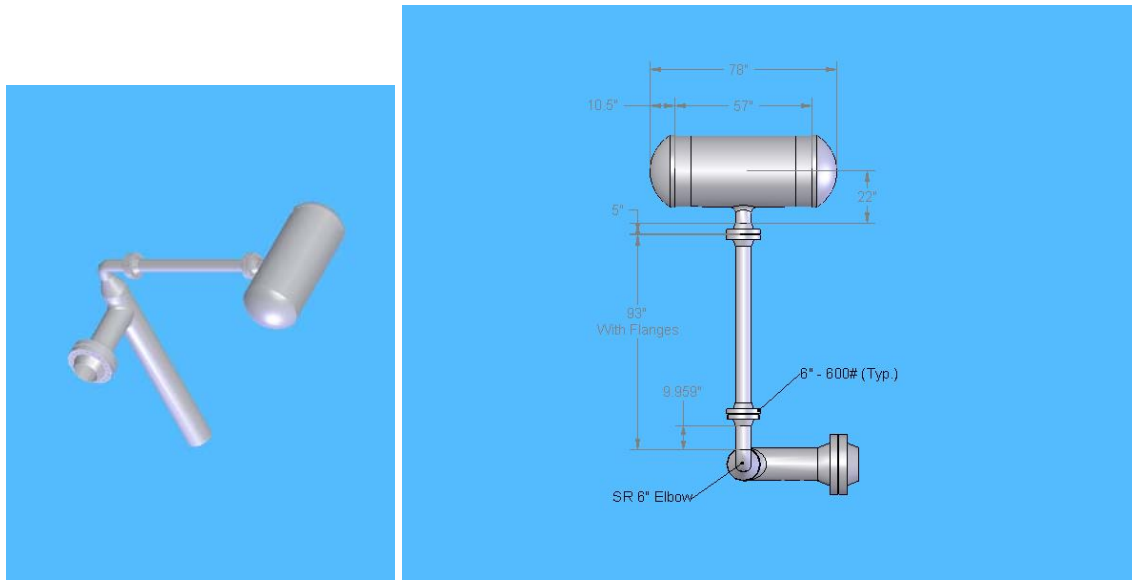


Figure 4-81. Schematic of Side Branch Absorber to be Connected to Suction Lateral Line



Figure 4-82. Suction Side Branch Absorber (SBA)

4.5.11 IN-LINE FILTER BOTTLES

Equally valuable as a pulsation control tool is the in-line filter. Increasingly, such filtration is being accomplished for both suction and discharge by extending the length of each bottle beyond that needed to cover the compressor cylinders to provide a “common chamber” not connected directly to any cylinder nozzle. This common chamber is connected into the system by choke tubes, which connect it to the chambers, into or out of which flow from nozzles occurs. Figure 4-83 shows the new suction and discharge bottles designed for the TCVC10 pictured in Figure 4-77, which combined with the SBAs on suction and discharge for this compressor

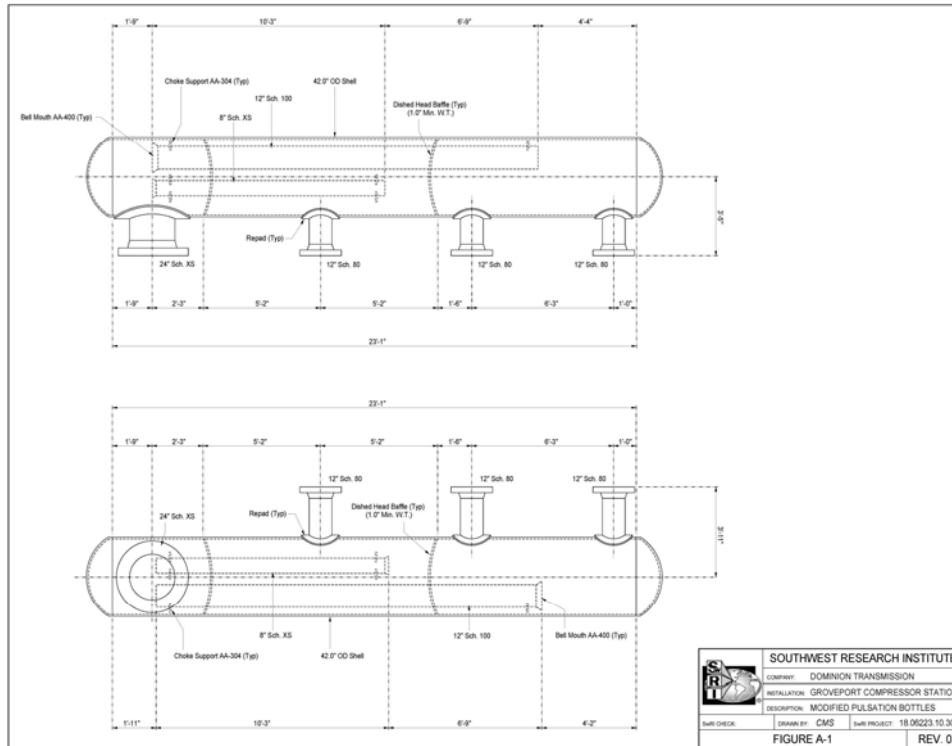


Figure 4-83. Schematic of Redesigned Bottles

system allow all orifices to be removed. These bottles each have a common chamber to the left of the figure. The suction and discharge laterals each connect into the common chamber. The chambers for the cylinders have choke tubes, which carry flow to or from the common chamber and which, in combination with the chamber volumes, creates effective acoustic filters.

The combined SBA and in-line filter system achieve the pulsation control illustrated in the predicted shaking forces of Figure 4-80. The new pulsation control system for the TCVC10 has yet to be installed and tested.

Assuming as expected the predicted 446 horsepower loss reduction is accomplished in practice, it can be viewed as “Horsepower Recovery” guided by the IPPS pulsation control design software. For the cost of new pulsation bottles and some piping changes, 446 horsepower will have been added to each of the three units at the station—a total of 1,338 horsepower “recovered” and made available for useful compression in the pipeline system with no addition of engine horsepower.

5. RESULTS AND DISCUSSION: AIR BALANCE STUDY

5.1 ENGINE MEASUREMENT, TESTING, AND SIMULATION

5.1.1 THE GMVH-6 ENGINE

The GMVH-6 integral compressor engine is a turbocharged two-stroke engine. This engine is loop scavenged, Schnurle type, with inlet and exhaust ports fixed in the cylinder liner. Port opening and closing is, therefore, governed by piston motion. A cross-sectional view of the GMVH engine is provided in Figure 5-1. The power cylinders are arranged in a Vee, with the compressor cylinders horizontal to the crankshaft centerline. The compressors are integrated into the engine design and driven by the master connecting rod. The power cylinder pistons are connected to the slave rods in an articulated rod configuration. Rotations of the slave rod hinge pins are elliptical rather than circular (as with traditional slider-crank configurations in typical engines). Figure 5-2 shows the articulating motion of the hinge pins. The resulting piston motions differ slightly between left and right banks, as shown in Figure 5-3, creating slight differences in port timings. The exhaust port timings based on nominal dimensions are shown in Figure 5-4. Due to articulation and the different piston motion between banks, the nominal exhaust port closing (EPC) timing varies between banks by 6.5 crank angle degrees. However, the exhaust port opening (EPO) timings vary between banks by only 1.5 crank angle degrees. The intake port timings based on nominal dimensions are shown in Figure 5-5. The variance between banks on the intake port closing (IPC) and intake port opening (IPO) timings is 7.5 and 3.0 crank angle degrees, respectively.

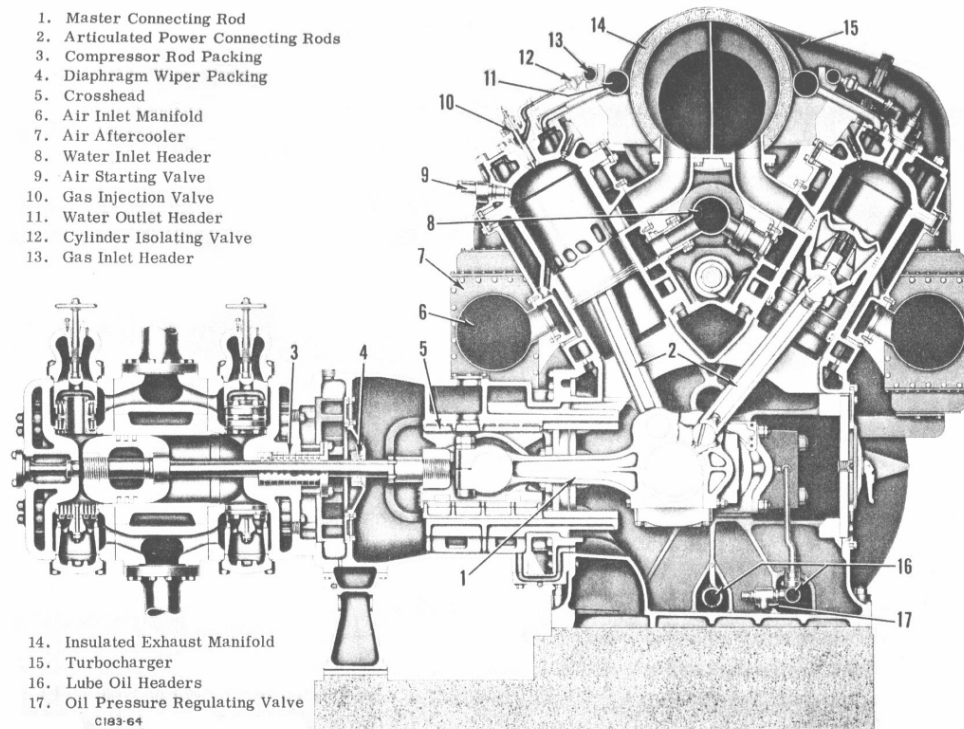


Figure 5-1. Cross-Section of a Cooper-Bessemer GMVH Integral Compressor Engine

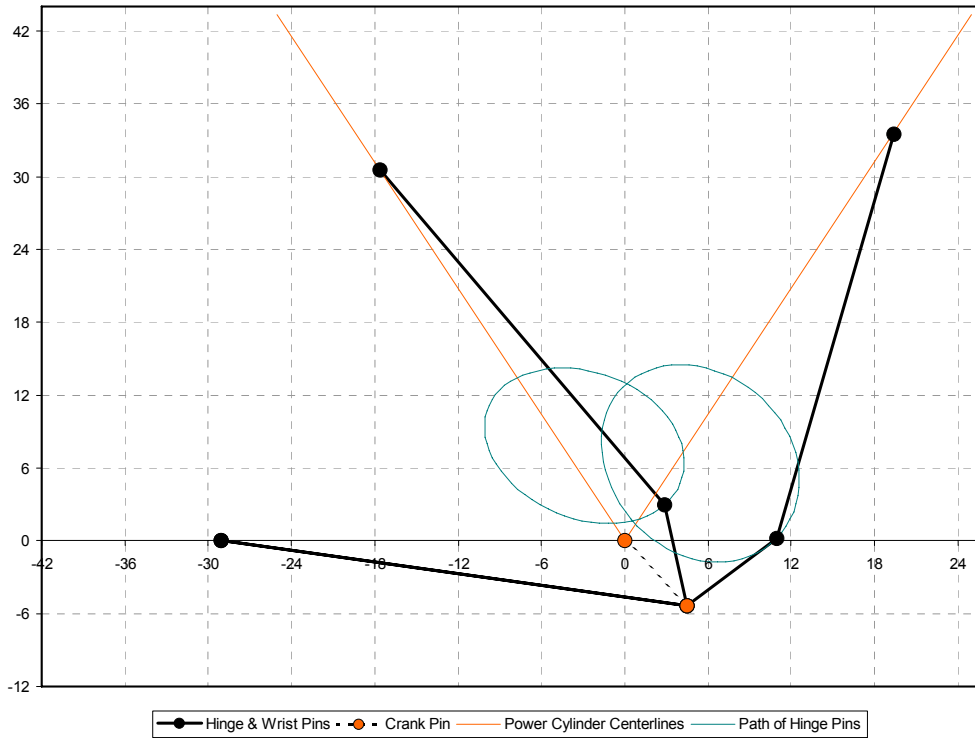


Figure 5-2. Kinematic Model Illustration of GMVH-6 Articulation

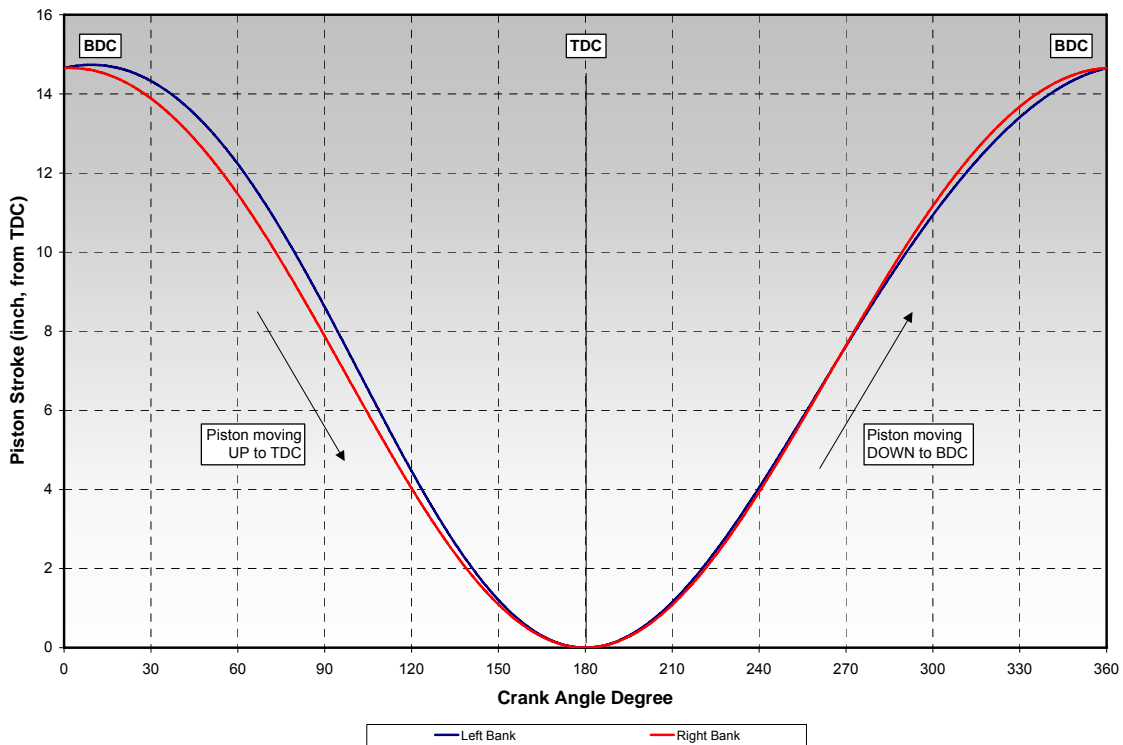


Figure 5-3. Kinematic Model Results of Left and Right Bank Piston Travel versus Crank Angle Degree

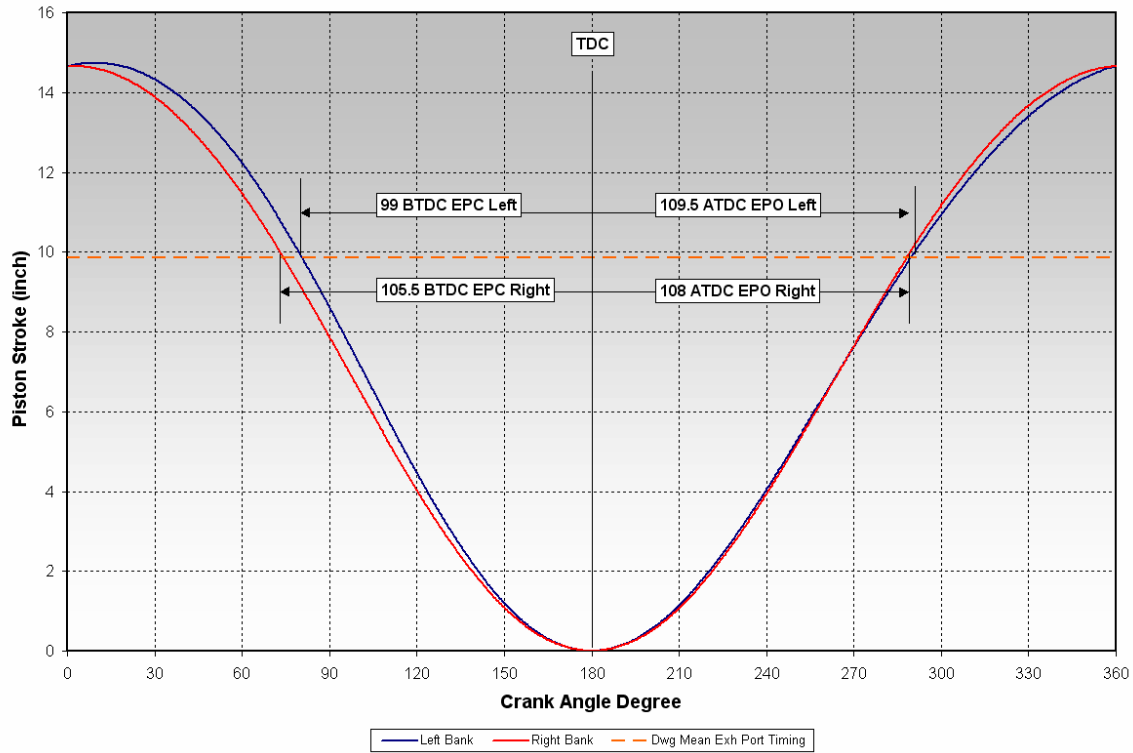


Figure 5-4. Nominal Exhaust Port Timings for Left and Right Banks

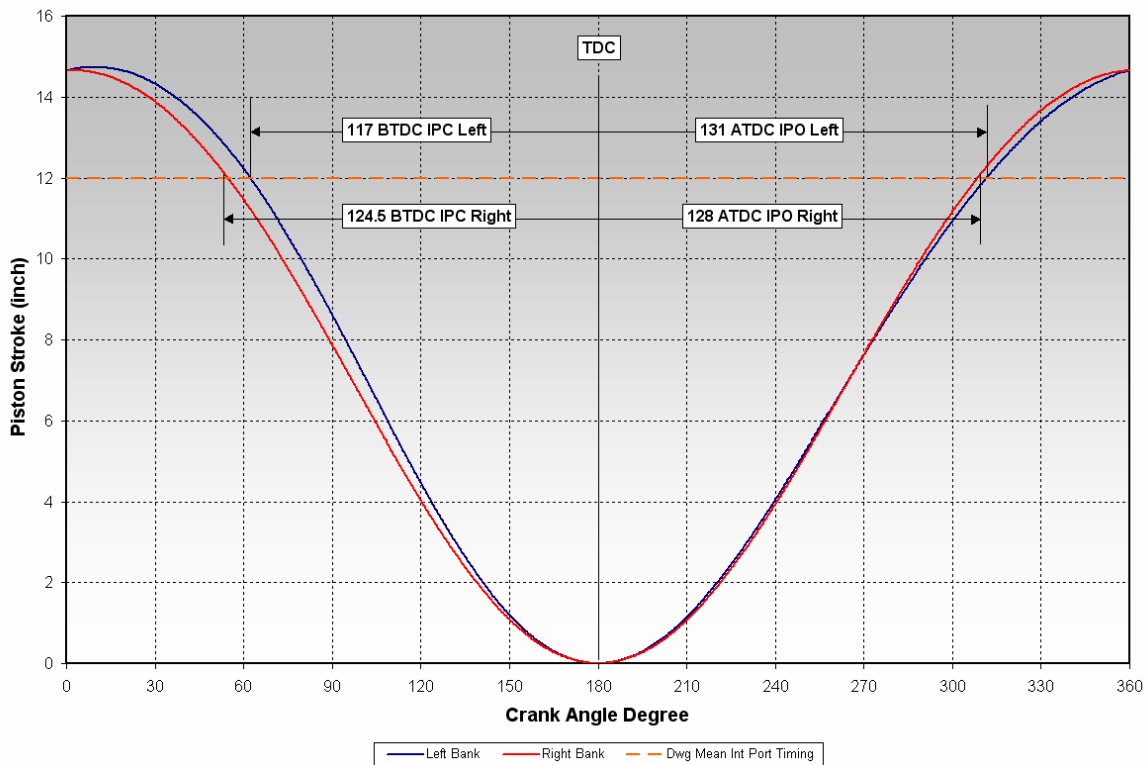


Figure 5-5. Nominal Intake Port Timings for Left and Right Banks

A two-stroke engine does not have the exhaust stroke to “push” the residual combustion gases out of the cylinder into the exhaust system. In the GMVH design, the exhaust port opens early in the expansion, or power, stroke and a portion of the residual gases “blows down” into the exhaust due to the high-pressure differential. After a few more crank angles in the expansion stroke, the intake ports open and pressurized fresh air enters the cylinder. The intake ports are also opened early, before bottom dead center (BDC), allowing fresh air to begin scavenging the remaining residual gases out of the cylinder into the exhaust system. The air motion is, by design, directed upward toward the cylinder head to both effectively scavenge residual from the whole cylinder volume and prevent excess short-circuiting of fresh air straight through the cylinder into the exhaust. This air motion makes a “looping” path from the intake ports to the exhaust ports, thus, the loop-scavenged term. The scavenging event continues past BDC of the piston travel and into the compression stroke. Earlier opening of the exhaust port for blowdown also gives later closing of the exhaust port due to being cast into the cylinder. Therefore, some cylinder contents are pushed into the exhaust system by the piston in the time between IPC and EPC. Figure 5-6 shows the scavenging events on a plot of cylinder pressure versus crank angle degree (P-T). Figure 5-7 shows the scavenging events on a logarithmic plot of cylinder pressure versus cylinder volume (logP-logV).

The scavenging process is quite complex. It is dependent on dynamic pressure differentials between the inlet, cylinder, and exhaust. Scavenging residual combustion gases with fresh air undoubtedly creates some pure displacement and some mixing of the gases, as well as some short-circuiting of the fresh inlet air to the exhaust. Many mathematical models have been developed to quantify this highly dynamic process that ranges from simple zero-dimensional to complex multi-dimensional [11-15]. Pulsations in the manifolds, due to design and/or unsteady combustion, could affect the dynamic pressures during scavenging and likely create deviations in flow between cycles and cylinders. All the factors that affect airflow and cylinder scavenging, in turn, affect the trapped air/fuel ratio, combustion rate, and emissions.

An additional aspect of integral compressor engines, especially the two-stroke designs, is that they feature direct in-cylinder fuel admission to prevent scavenging of raw fuel into the exhaust. This direct fuel admission is performed in originally equipped engines with cam-actuated poppet valves in each cylinder that have a fixed duration tied to crankshaft speed. Individual balance valves are installed in the jumper lines to each cylinder, which are manually adjustable to provide some fuel compensation to individual cylinders to balance combustion pressures across the engine. A governor typically modulates the main fuel header pressure to maintain the engine speed set point. In engines equipped with modern electronic fuel injection, the cylinder combustion pressure balancing and speed governing are accomplished by the electronic control module via modulation of the injection duration. The goal of the fuel admission system design is to create a homogeneous mixture of fuel and air in the cylinder by the time ignition occurs near top dead center (TDC). However, similar to the scavenging process, there is undoubtedly some stratification of fuel and air within the cylinder volume and the resulting mixture is not completely uniform. Fuel valve opening (FVO) and closing (FVC) timings for the GMVH are shown in Figure 5-6 and Figure 5-7, along with the scavenging events.

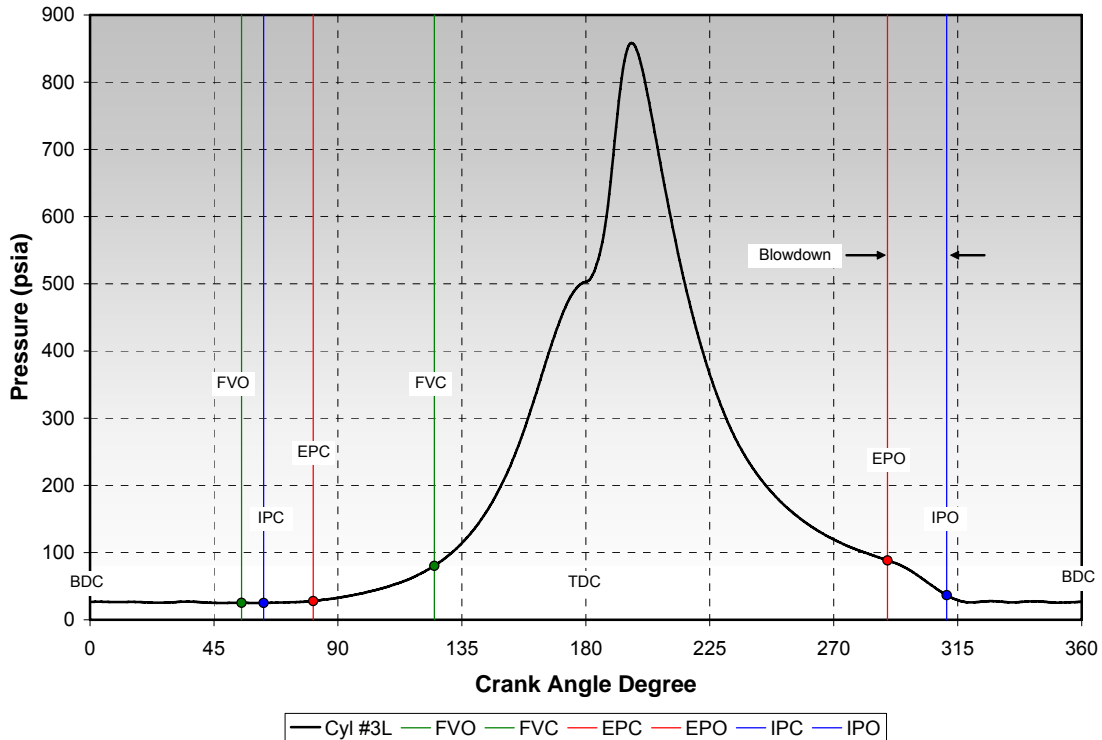


Figure 5-6. GMVH Cylinder Pressure versus Crank Angle – Scavenging and Fuel Admission Events Noted

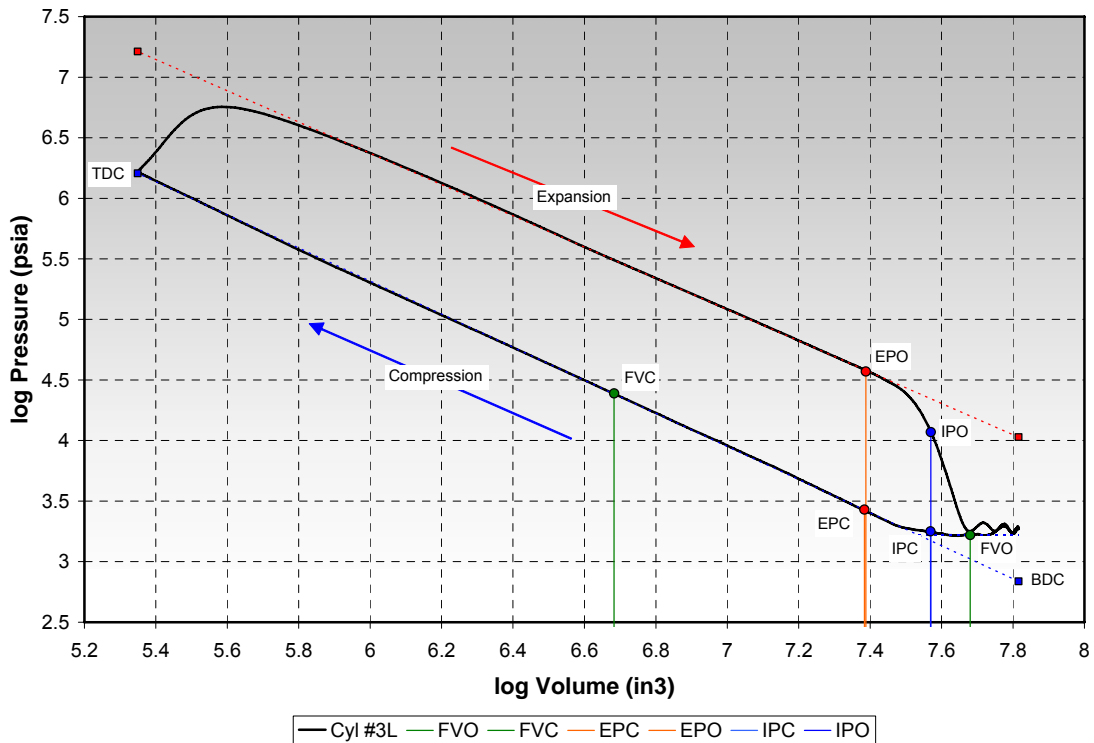


Figure 5-7. GMVH Cylinder Pressure versus Cylinder Volume on Logarithmic Scale – Scavenging and Fuel Admission Events Noted

The intake and exhaust manifolds on the GMVH-6 engine are comprised of tubular logs with rectangular runners branching to each cylinder. The exhaust manifold features one log, which is located within the Vee of the cylinders. The rectangular exhaust runners curve from the cylinder flanged at 30 degrees from vertical to horizontal flanges at the bottom of the manifold log. Inside the exhaust manifold log, there are vertical plates between each pair of cylinders that provide stiffening to the manifold and likely prevent the blowdown pulse from one cylinder directly interfering with the adjacent cylinder. A gap exists between these plates at the expansion joints between cylinder pairs.

The intake system features tubular log manifolds on the outside of each bank of cylinders. The rectangular intake runners are straight from the manifold log to the cylinder flange. Since there are two intake manifolds for each bank, the turbocharger compressor has two outlets feeding through separate intercoolers to each bank manifold. A simple schematic of the intake and exhaust systems, as well as the cylinder arrangement and fuel system, is provided in Figure 5-8.

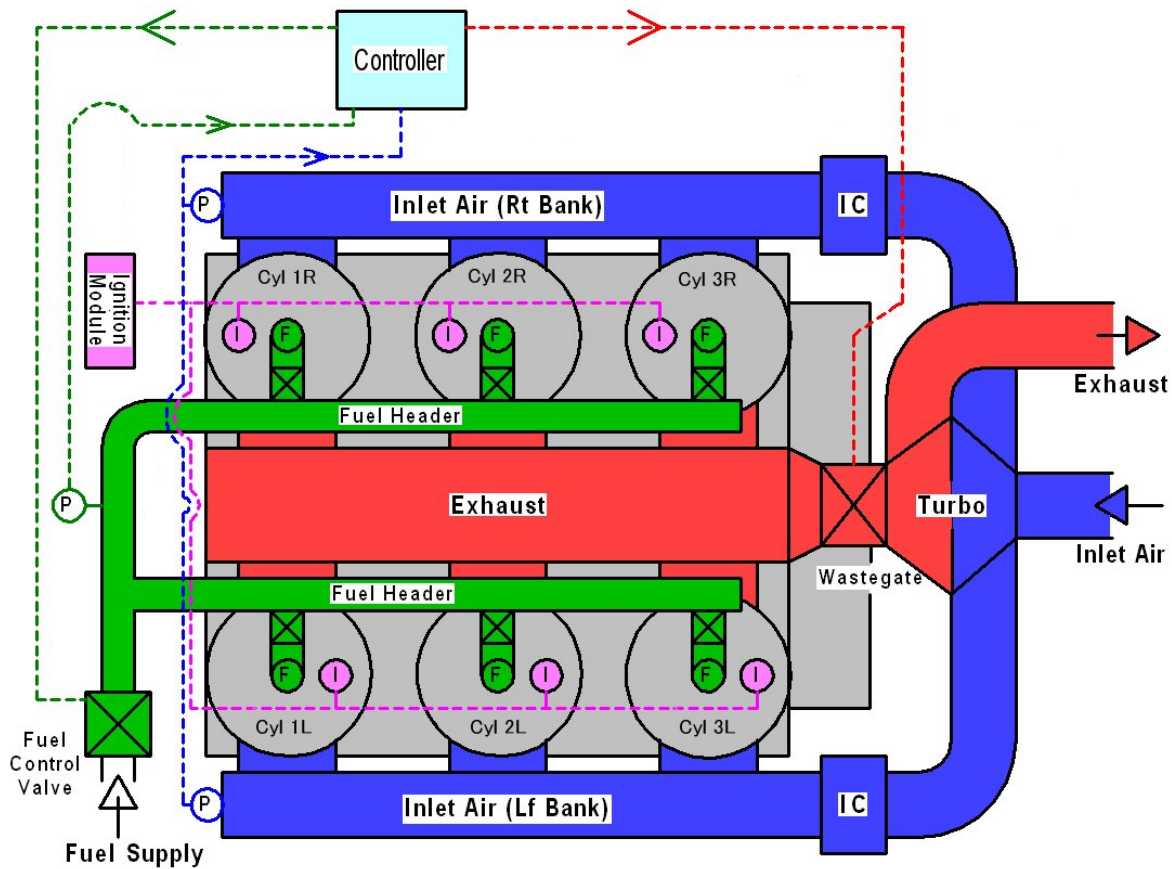


Figure 5-8. Top-View Schematic of GMVH-6 Engine

5.1.2 GMVH-6 BASELINE TESTING

Baseline testing of the GMVH-6 engine involved operation in both open chamber and pre-chamber configurations. The engine was tested over engine speeds of 231, 264, 297, and 330 rpm. Engine load was also varied from 70, 85, 90, and 100 percent of rated. Within this map of engine speed and load, the air/fuel ratio and spark timing was varied. In analyzing the data, the spread of compression pressures was seen to remain very consistent regardless of the operating condition. This consistency is shown in Figure 5-9, where the pressure at 20 degrees before top dead center (TDC) for all cylinders at all operating conditions tested is plotted versus air manifold pressure. All data obtained on the GMVH-6 prior to disassembly indicated that the low cylinder (pressure at 20 degrees BTDC) is always Cylinder 3L and the high cylinder (pressure at 20 degrees BTDC) is always 2R.

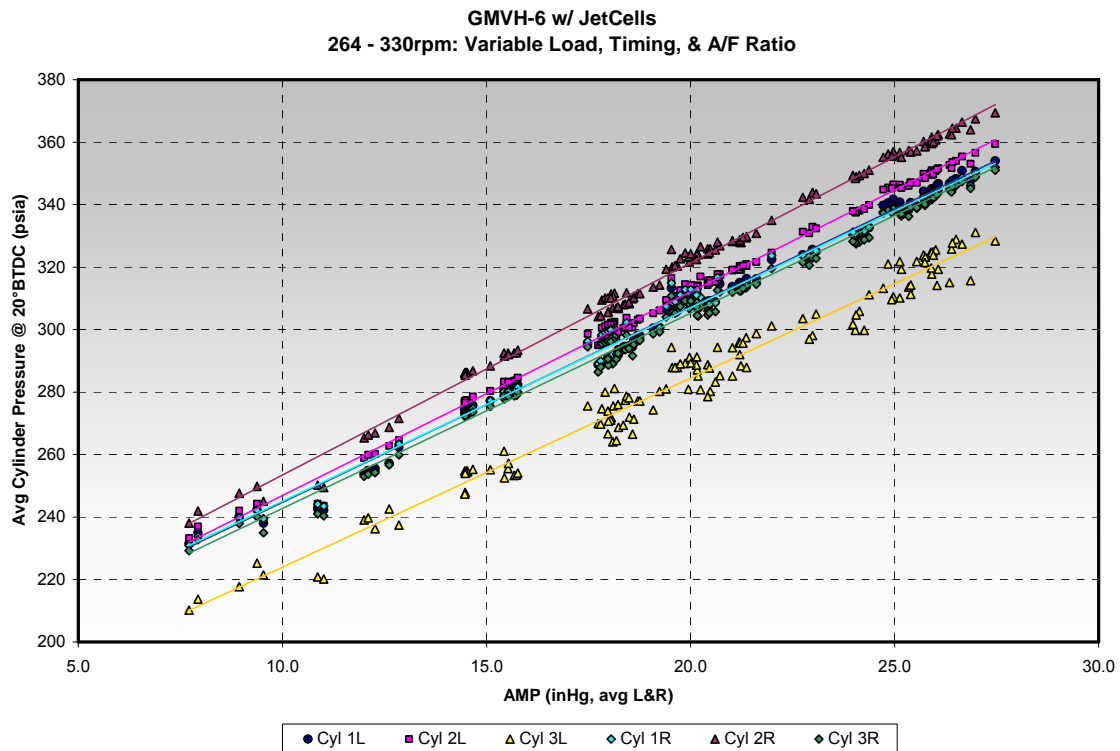


Figure 5-9. Comparison of Cylinder-to-Cylinder Compression Pressure (20 Degrees BTDC) at All Operating Conditions

Engine test data was acquired for comparison of performance and emissions, simulation validation, and analytical purposes. For comparison purposes, the fuel efficiency and NO_x emissions versus various operating conditions were documented. The fuel efficiency was quantified in terms of Brake Specific Energy Consumption (BSEC) in units of BTU/bhp-hr. NO_x emissions were quantified in both parts per million (ppm) concentration and brake specific (g/bhp-hr). The efficiency trends for the open chamber tests are shown in Figure 5-10 and Figure 5-11, where BSEC is plotted versus engine speed and load, respectively, at a constant 4 g/bhp-hr NO_x. This data shows peak efficiency occurs at the rated speed and load.

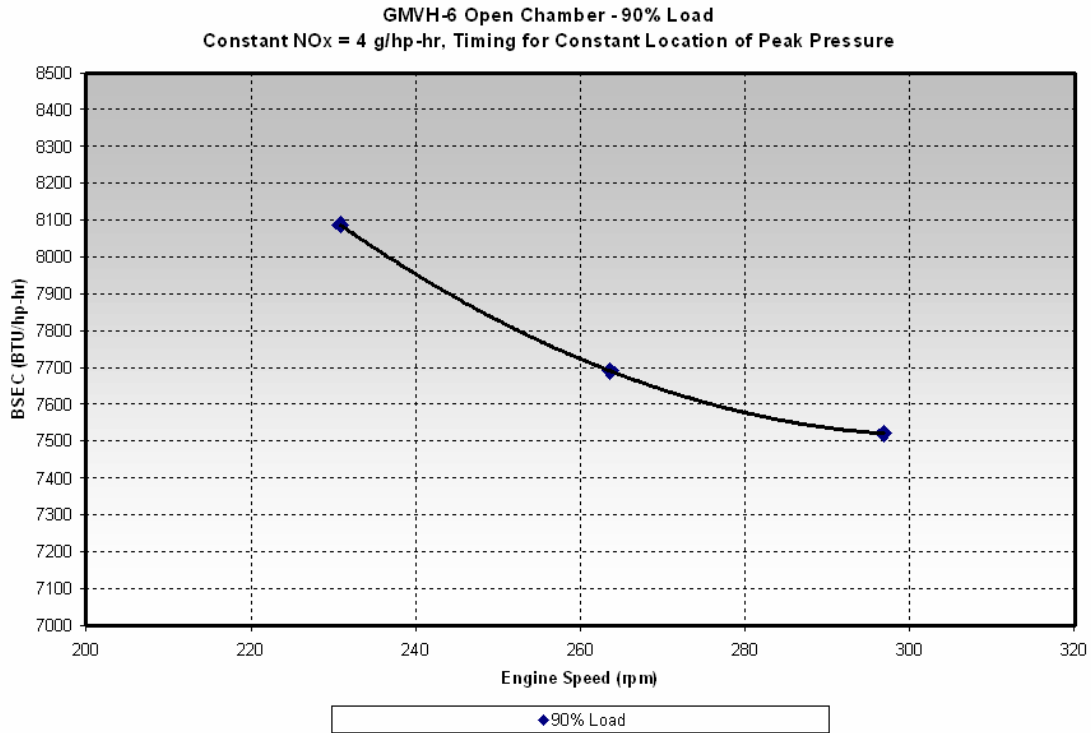


Figure 5-10. Open Chamber Fuel Efficiency versus Engine Speed at Constant NO_x

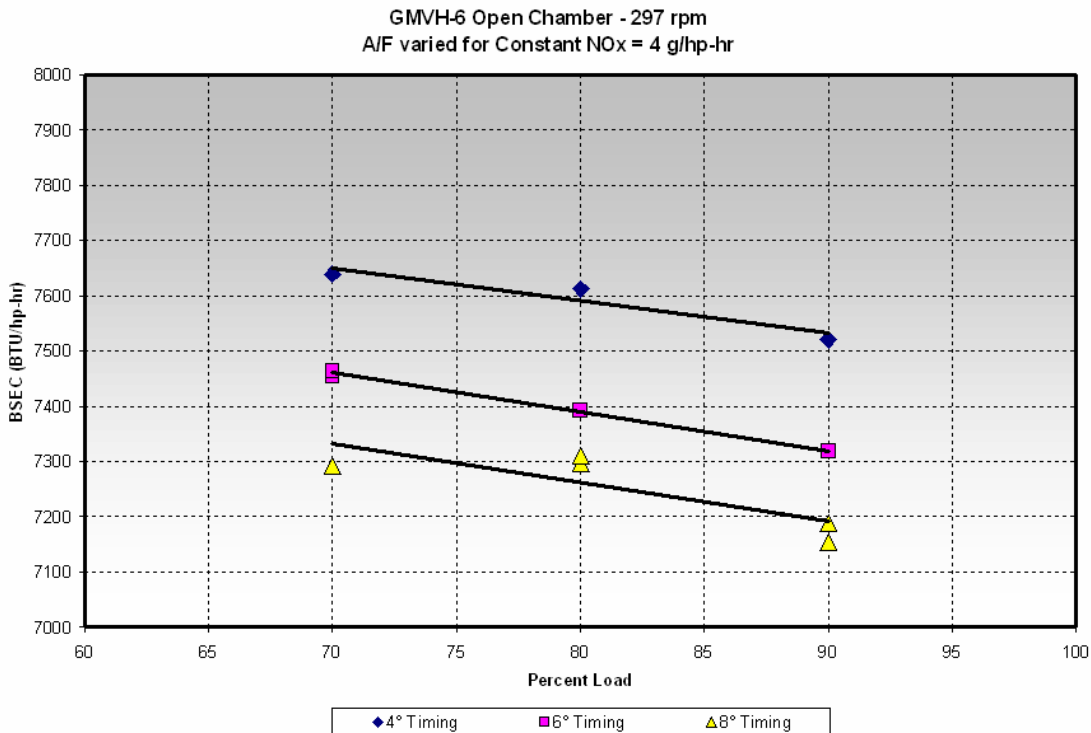


Figure 5-11. Open Chamber Fuel Efficiency versus Engine Load and Ignition Timing at Constant NO_x

Efficiency data for the prechamber configuration is provided in Figure 5-12, and again shows peak efficiency at maximum load and rated engine speed. A comparison of the NO_x-Efficiency trade-off for both prechamber and open chamber is provided in Figure 5-13 and includes additional data acquired on the GMVH-6 engine. This plot shows the typical “knee” in the curves where NO_x emissions increase rapidly beyond the optimum trade-off point with improving efficiency and also shows the improved relationship with the prechamber configuration over the open chamber configuration. The prechamber configuration, with its improved ignition capability, provides better efficiency and lower NO_x emissions. This NO_x-efficiency improvement with prechambers is due to more stable combustion at leaner air/fuel ratios and faster burn rates. The improved combustion with prechambers is illustrated further in Figure 5-14 through Figure 5-16 for the same operating condition of 330 RPM, 100% load, and 2 g/bhp-hr NO_x. Average cylinder pressure for Cylinder 1L from both open chamber and prechamber tests is plotted in Figure 5-14. A higher compression pressure for the open chamber run can be seen and is due to the need for higher boost to operate at the same speed, load, and NO_x emissions level. The heat release rate and cumulative heat release for the prechamber and open chamber tests are shown in Figure 5-15 and Figure 5-16, where the faster burn rate can be seen for the prechamber combustion.

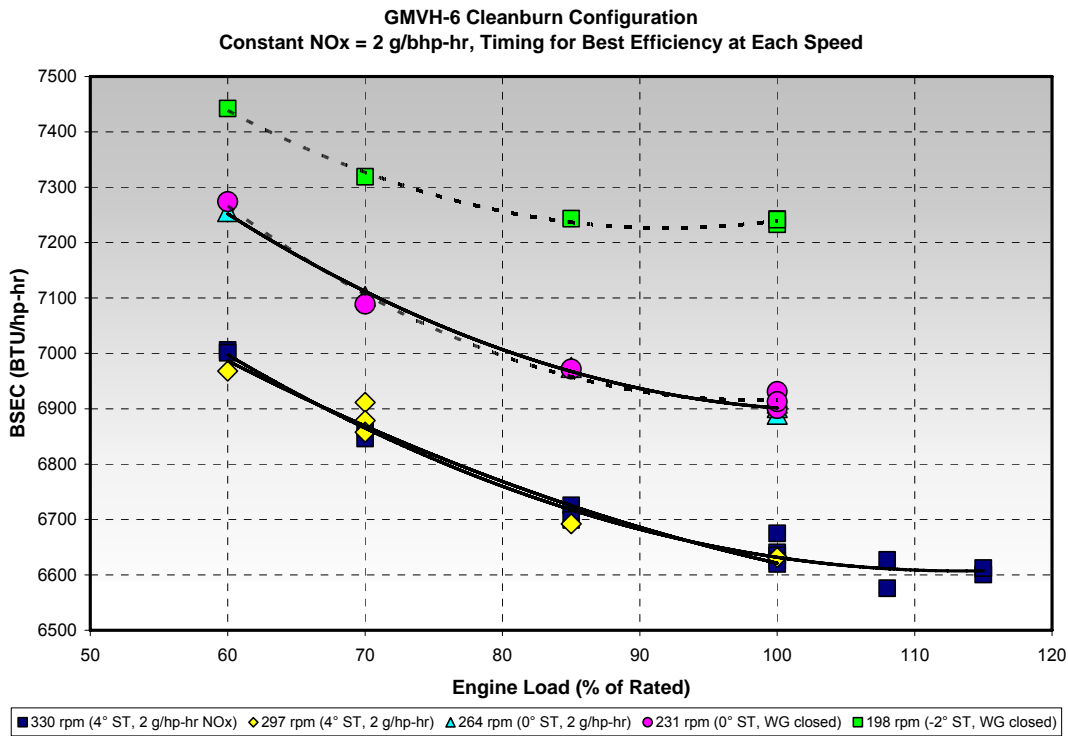


Figure 5-12. Prechamber Fuel Efficiency versus Engine Load, Speed, and Ignition Timing at Constant NO_x

**GMVH-6
Comparison of NO_x-Efficiency Trade-Off**

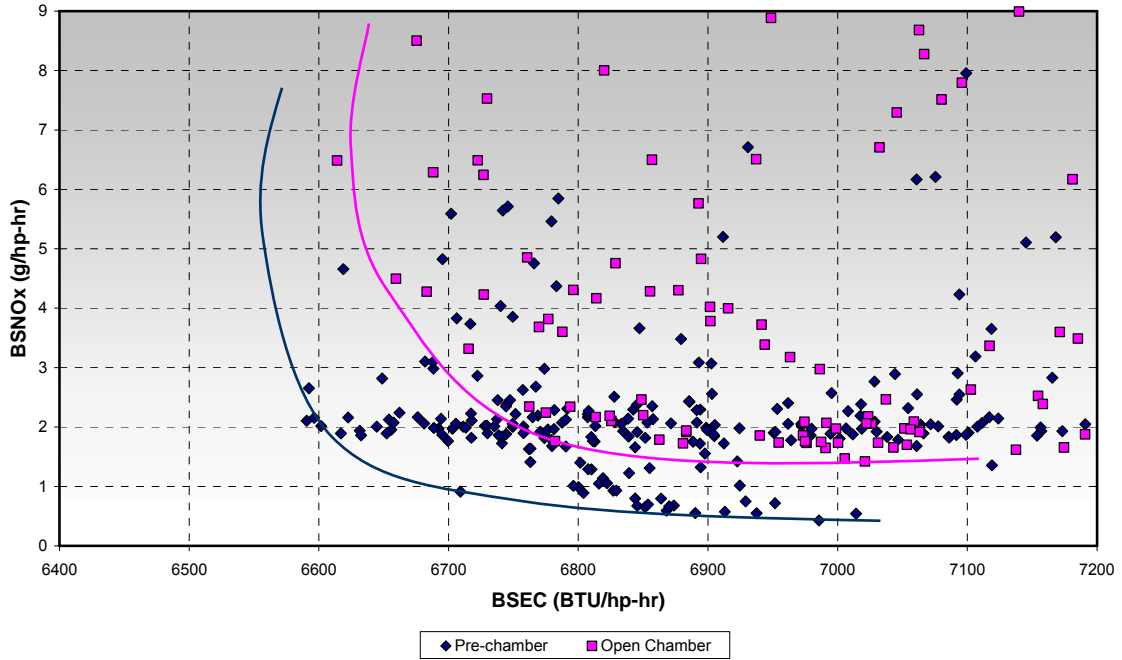


Figure 5-13. Prechamber and Open Chamber NO_x – Efficiency Trade-Off

**GMVH-6 - Cylinder 1L
330rpm - 100% Load - 2 g/bhp-hr NO_x**

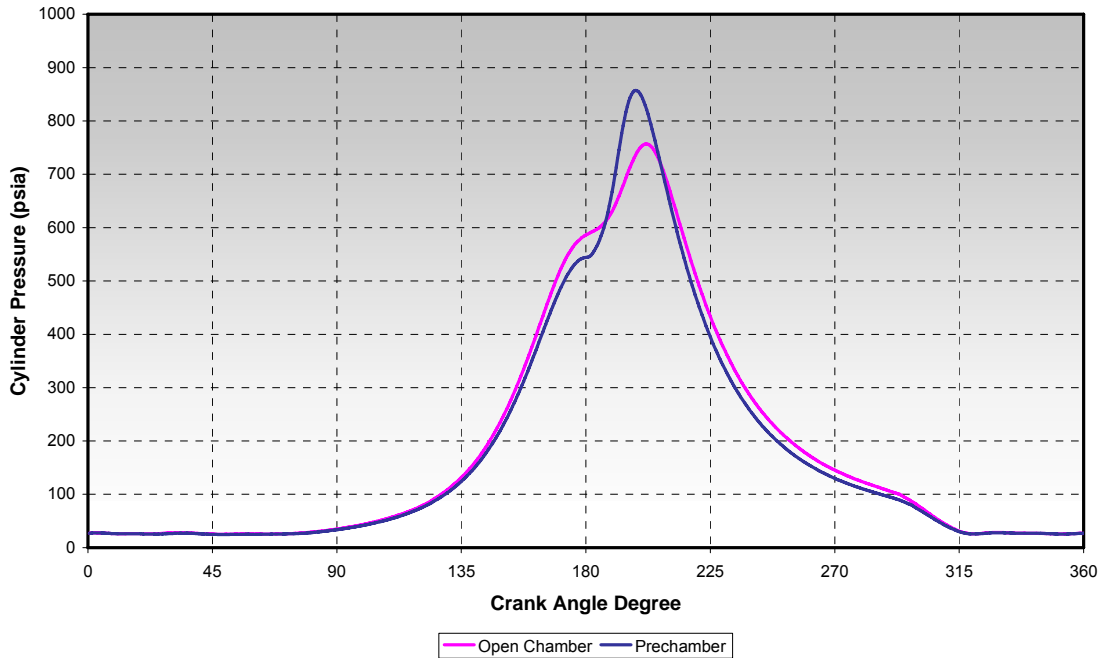


Figure 5-14. Cylinder 1L Pressure Comparison for Prechamber and Open Chamber

GMVH-6 - Cylinder 1L
 330rpm - 100% Load - 2 g/bhp-hr NOx

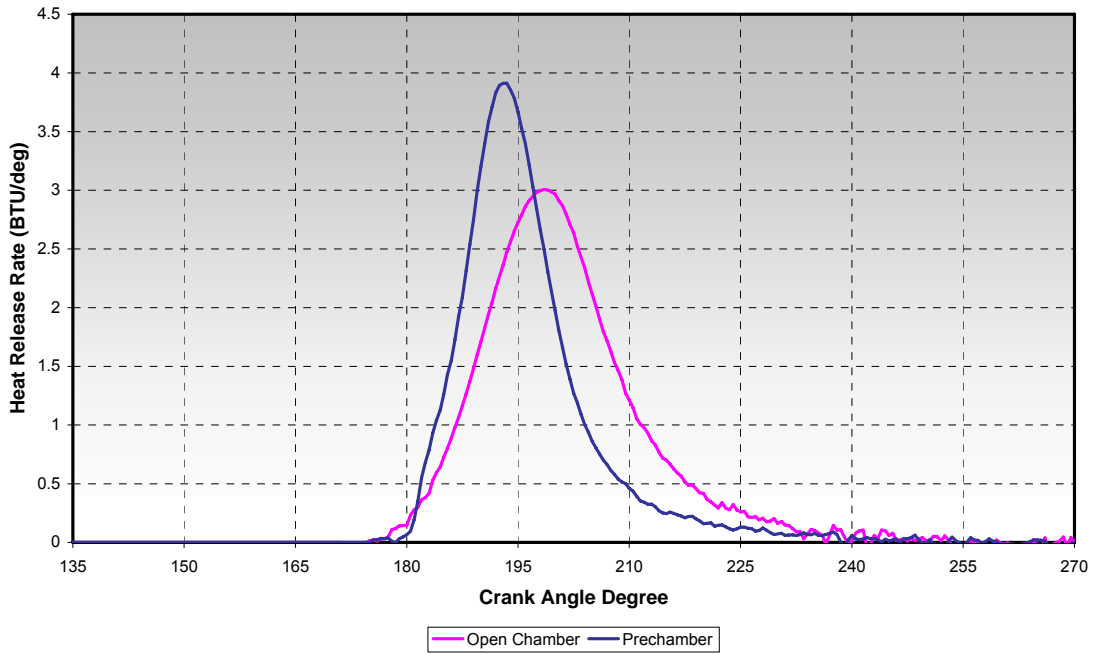


Figure 5-15. Cylinder 1L Apparent Heat Release Rate Comparison for Prechamber and Open Chamber

GMVH-6 - Cylinder 1L
 330rpm - 100% Load - 2 g/bhp-hr NOx

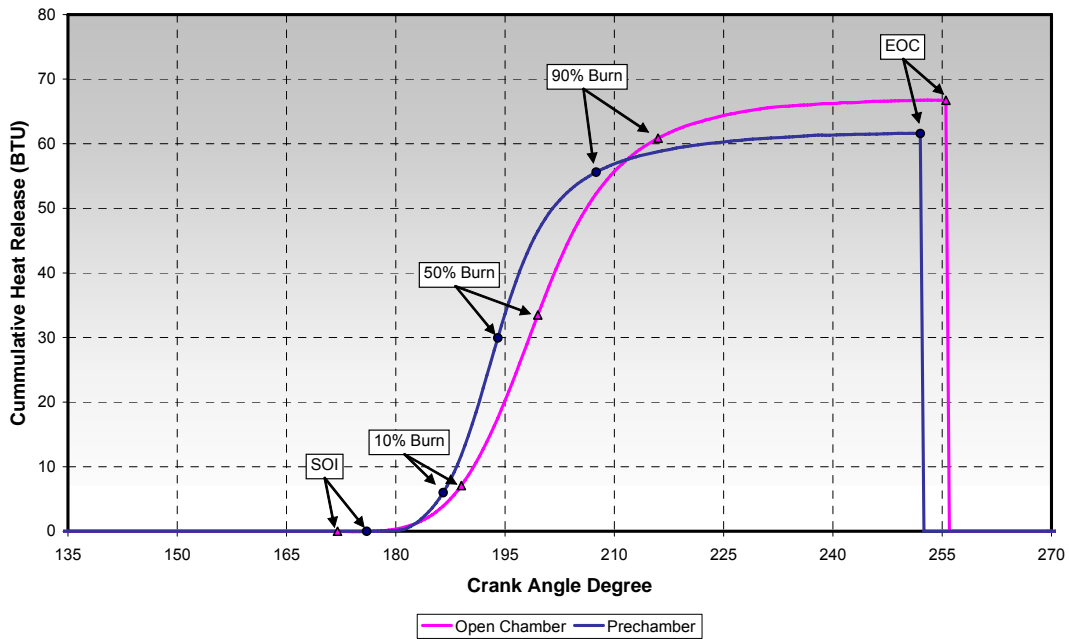


Figure 5-16. Cylinder 1L Cumulative Heat Release Comparison for Prechamber and Open Chamber

Test data for simulation validation included time-averaged performance parameters and dynamic trace data for each cylinder. Performance parameters included both global and individual cylinder variables. This data, from select runs, was used to tune the model and compare simulation results. Test data for analytical purposes was trended, as in the previous graphs above, and analyzed to investigate factors, such as intake and exhaust pulsations. Further discussions on these efforts are provided in appropriate sections below.

5.1.3 GEOMETRIC ANALYSIS

At the beginning of the project, mean dimensions of cylinder components (from drawings provided by Cooper) were used in data analysis and in the construction of the simulation model. Several assumptions for dimensions and complex volumes were used in the model where drawings were either difficult to interpret or were not obtained. Initial simulations with these values and geometry yielded less than satisfactory results. These initial simulations predicted mass airflow closely, but did not accurately predict the amplitude and phasing of pulsations in the inlet and exhaust manifolds. It was believed that the inaccurate manifold dynamic predictions were due to the use of inaccurate discharge coefficients and inaccurate representations of the complicated cylinder plenum geometry that could not be measured externally. It was also believed that the selection of mean values might have also contributed to the erroneous simulation results. Based on these issues, the engine was disassembled so that actual measurements could be obtained. In doing so, it could also determine if any geometric variances were contributing significantly and directly to the compression pressure spread. As mentioned previously, it is well known that geometric factors (such as compression ratio and port geometry) can affect compression pressures and must be quantified prior to any manifold redesign.

The GMVH-6 engine was disassembled and all pistons and connecting rods were removed. Three of the six cylinders were left installed on the base, while the other three cylinders were removed for flow testing. Several measurements were taken on each cylinder's components as listed in Table 3-4. From these measurements, the following parameters were obtained:

- Base and cylinder air chest geometry – individual cylinder airbox volume.
- Intake and exhaust manifolds – internal dimensions and geometry, specifically at junctions and transitions in each manifold.
- Mechanical and effective compression ratio – individual cylinder clearance volume (head, piston, crevices), TDC piston height, stroke, and exhaust port timings.
- Port flow – port dimensions and area, shape, timings, angles, lip radius, and volumes for each port in each cylinder.
- Fuel valve lift profile – individual fuel valve travel versus crank angle.

Two important observations were made during disassembly. The first critical observation was that the “air chest” cast into the base was open and communicating with the inlet air system. The second critical observation was that one of the six cylinders had a different casting number and different geometry of the inlet and exhaust ports.

5.1.3.1 Base Air Chest

The base air chest was initially believed to be blocked off by gaskets, since it serves no purpose in breathing with separate intake manifolds, as is the case with the turbocharged version of the GMV. The base air chest was the original inlet air path with earlier versions of the GMV engine that were piston scavenged. The base air chest was, however, found to be open and connecting the airboxes from each cylinder to a common volume, thus, acting like a large accumulator. This explained immediately why the initial simulations showed significantly higher inlet manifold pressure pulsations than were measured. The discovery of the base plenum being active and connected to the inlet system was a very important finding, as accurate simulation would have never been achieved without this feature being incorporated into the model.

The size and shape of the air chest volume was unknown during initial modeling of the engine. After discovering that the base plenum had been connected, base drawings were requested from Cooper. To accurately reflect the base air chest in the simulation model, several physical measurements were made and the base drawing consulted for hidden geometry. A CAD model, depicted in Figure 5-17, was then generated from the measurements to calculate the air volume and to allow for visual investigation on the proper method to simulate the flow paths. A total volume of 65,106 in³ was derived from this CAD model. A photograph of the GMVH base with cylinders removed is shown in Figure 5-18 where arrows highlight the air chest ports.

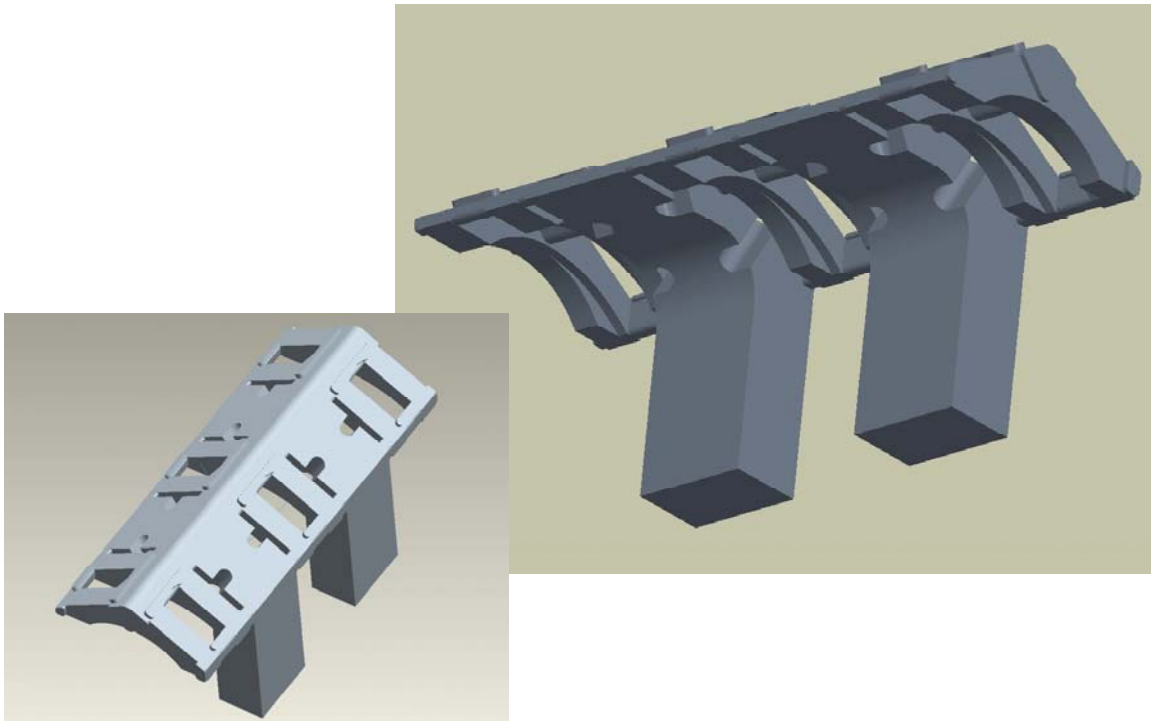


Figure 5-17. CAD Model of Base Air Chest (air volume shown as solid)

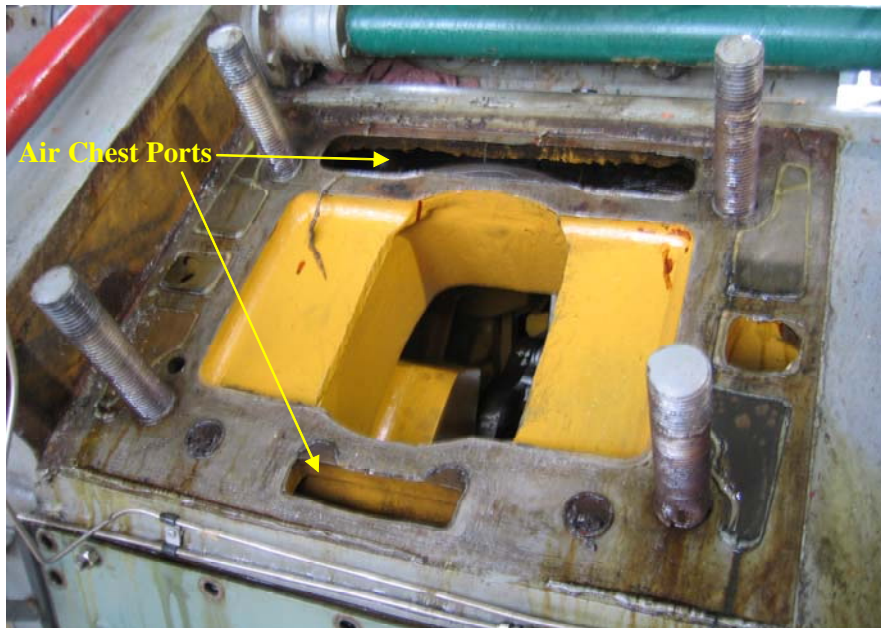


Figure 5-18. Photograph of GMVH Base with Cylinder Removed – Air Chest Ports Highlighted

5.1.3.2 Cylinder Castings and Port Shape

Further investigation on the disassembled engine showed that Cylinder 1R had a different casting number than the other six cylinders. The exhaust port shape for Cylinder 1R was different from the other cylinders and matched Shape No. 3 shown in Figure 5-19. All other cylinders matched Shape No. 1 in Figure 5-19. The drawings in Figure 5-19 are an excerpt from the original OEM drawing showing allowable port shapes. Although Cylinder 1R did not appear to be a problem in terms of compression pressure, this different port shape yielded different flow characteristics and, therefore, was replaced during reassembly with a cylinder that had a matching casting number and exhaust port shape. Cylinder port airflow testing (described below) was initially to be performed on only Cylinders 1L and 3L; however, the mismatched Cylinder 1R was added to the test matrix to provide insight to the effect of port shape on flow characteristics.

5.1.3.3 Cylinder Inlet Airbox

The cylinder inlet volume (“airbox” within each cylinder casting) is another critical parameter for accurate simulation of the fluid dynamics in the engine. The cylinder inlet airbox is the volume between the intake manifold flange, base air chest ports, and inlet ports to the combustion chamber. Drawings provided by Cooper were of a 1950’s vintage and hand drawn. The true geometry of the cylinder inlet air plenum was difficult to distinguish by the dotted lines and a few cross-sectional views. Therefore, initial estimates of the inlet volume were incorrect due to misinterpretation of the drawing. Once apart, the cylinder inlet volume was physically measured by filling the airbox with metered water. This required sealing the ports (at the cylinder wall) and base openings. The inlet port runners were, therefore, included in these volume measurements. A difference was measured between the two different casting number cylinders installed on this engine, with Cylinder 1R having approximately 4.3% smaller volume. The results of measurements on the three removed cylinders are shown in Figure 5-20.

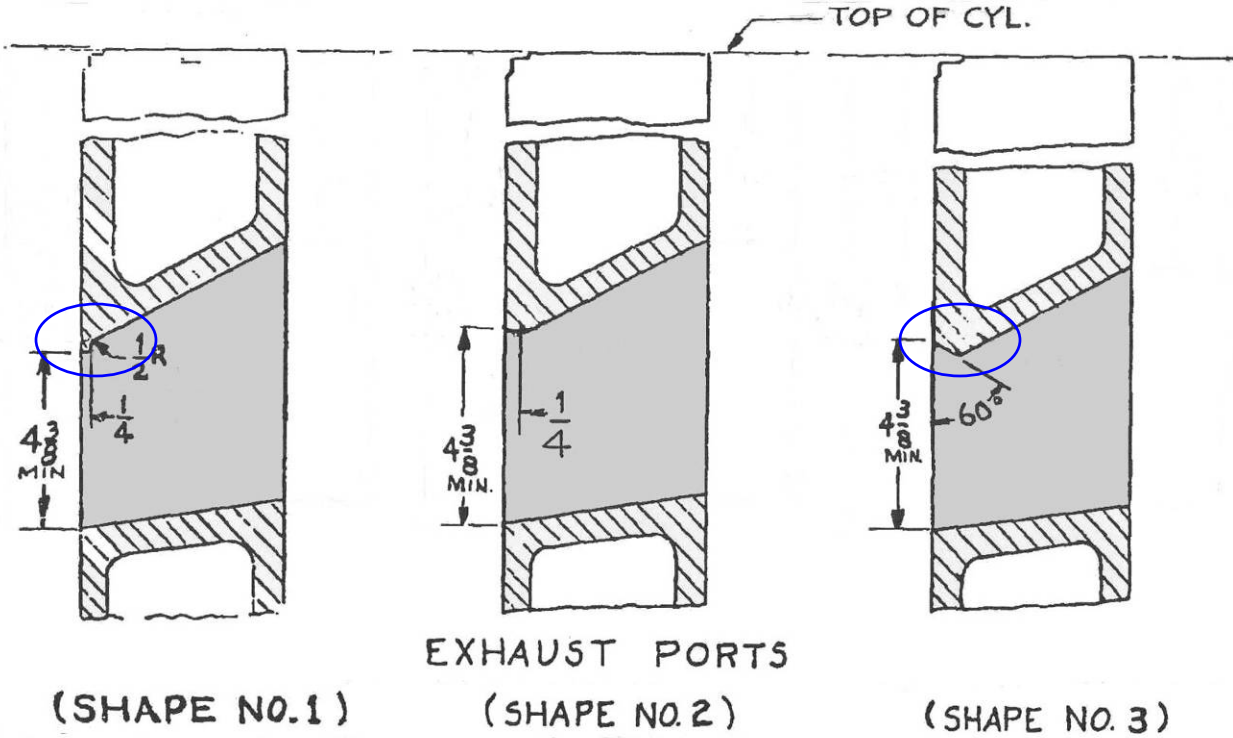


Figure 5-19. Exhaust Port Shapes

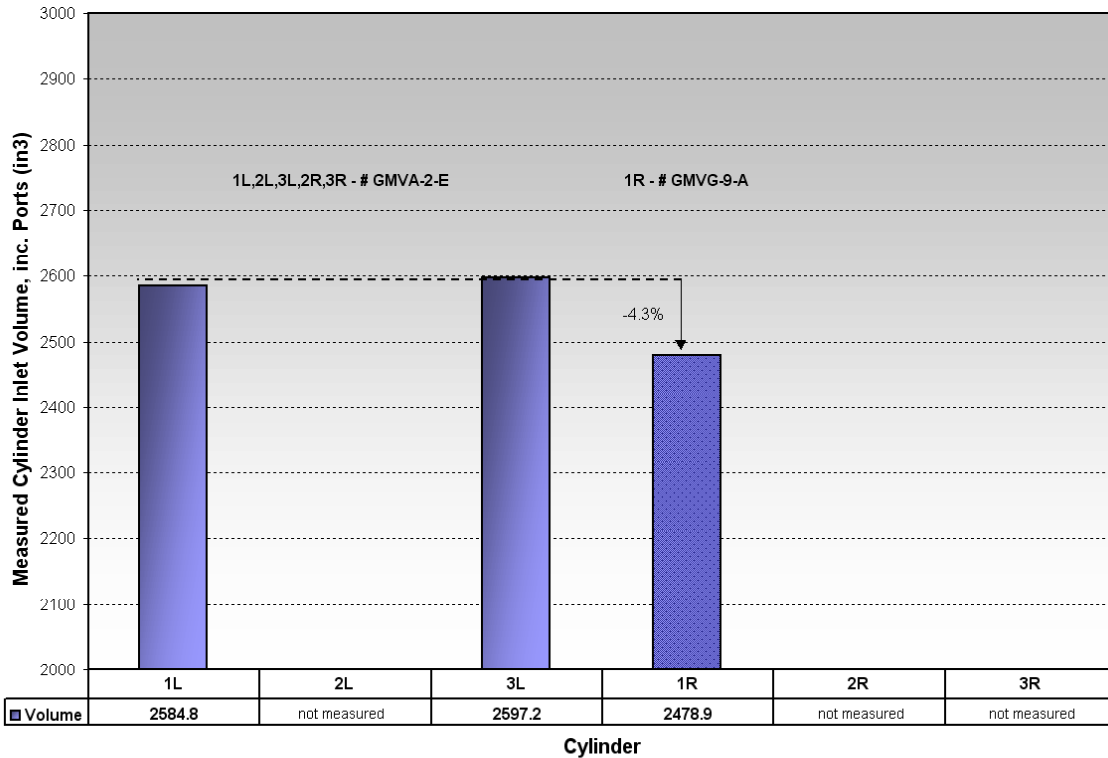


Figure 5-20. Cylinder Inlet Volume Measurements

5.1.3.4 Inlet and Exhaust System

In addition to deriving the base air chest and cylinder airbox volumes, measurements were made on both the intake and the exhaust manifolds with the engine disassembled to capture the internal geometry in detail for an improved model. It was felt critical that every junction and transition be represented in the model for accurate simulation. Several images to help illustrate the complex geometries of the inlet and exhaust systems are provided in Figure 5-21 through Figure 5-24. The first image, Figure 5-21, is the cross-section schematic of the GMVH with the inlet air paths colored in blue and the exhaust paths colored in red. Photographs of the external geometry of the inlet air system are shown in Figure 5-22. Photographs of the external geometry of the exhaust system are shown in Figure 5-23. Internal geometry of the exhaust system (one section) is shown in photographs in Figure 5-24.

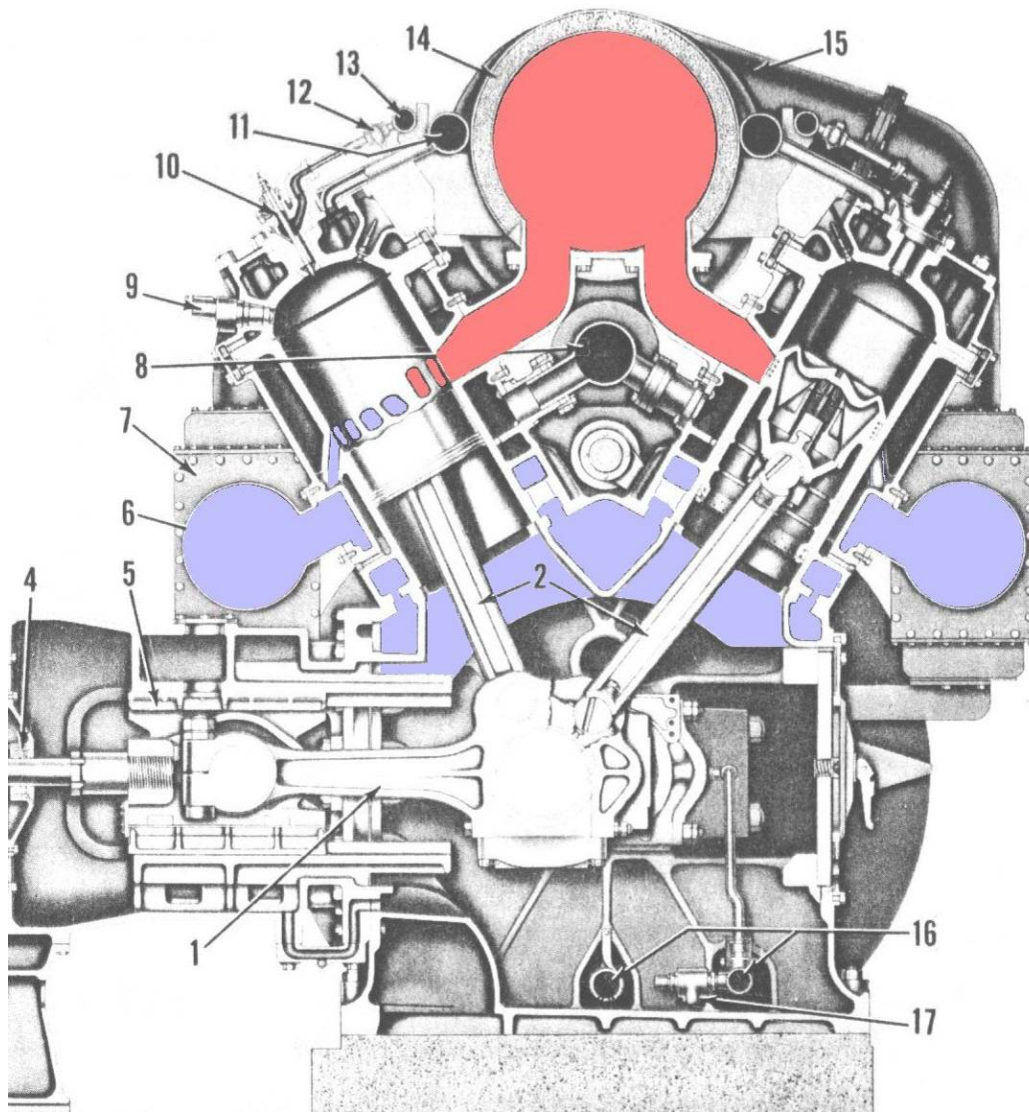


Figure 5-21. GMVH Cross-Section with Inlet (blue) and Exhaust (red) Highlights

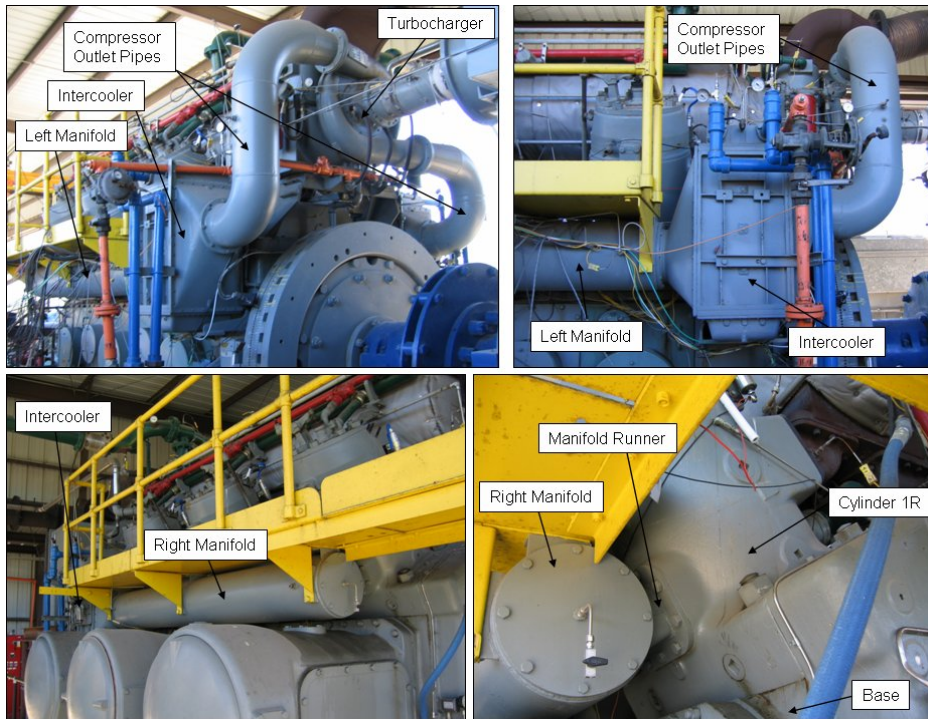


Figure 5-22. Photographs of External Inlet Air System

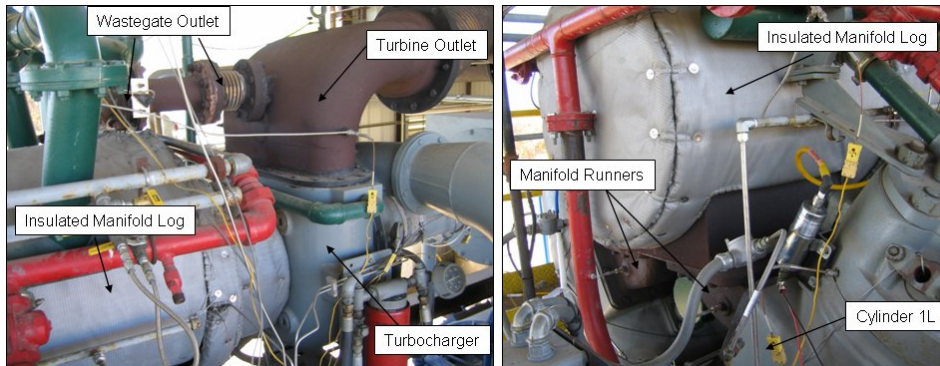


Figure 5-23. Photographs of External Exhaust System



Figure 5-24. Photographs of Internal Geometry of Exhaust Manifold

5.1.3.5 Piston Stroke

One of the first measurements to be taken on all cylinders was the piston stroke as a function of crank angle degree to determine if there were any variations in crankshaft throws. The piston travel profile resulting from the articulation is slightly different between the left and right banks, as discussed previously. Measurements of each piston stroke are shown with the calculated motion in Figure 5-25 and Figure 5-26 for left and right banks, respectively. The measurements were made by barring the engine, so only the up-stroke and crossover of TDC and BDC was measured. Measurements of the down-stroke were not taken, as they would be skewed by any slack in the bearings due to pulling the piston down against ring friction. As can be seen in Figure 5-25 and Figure 5-26, negligible variations were observed between cylinders, and the results tracked the calculated motion very well. The left bank variation in TDC to BDC stroke was only 0.019” out of a mean stroke of 14.737” and right bank variation was only 0.011” out of a mean stroke of 14.660”. Furthermore, the mean stroke values for left and right banks were within 0.004” from the kinematic model calculations. Individual measured and drawing mean piston stroke values are provided on Figure 5-27 for comparison.

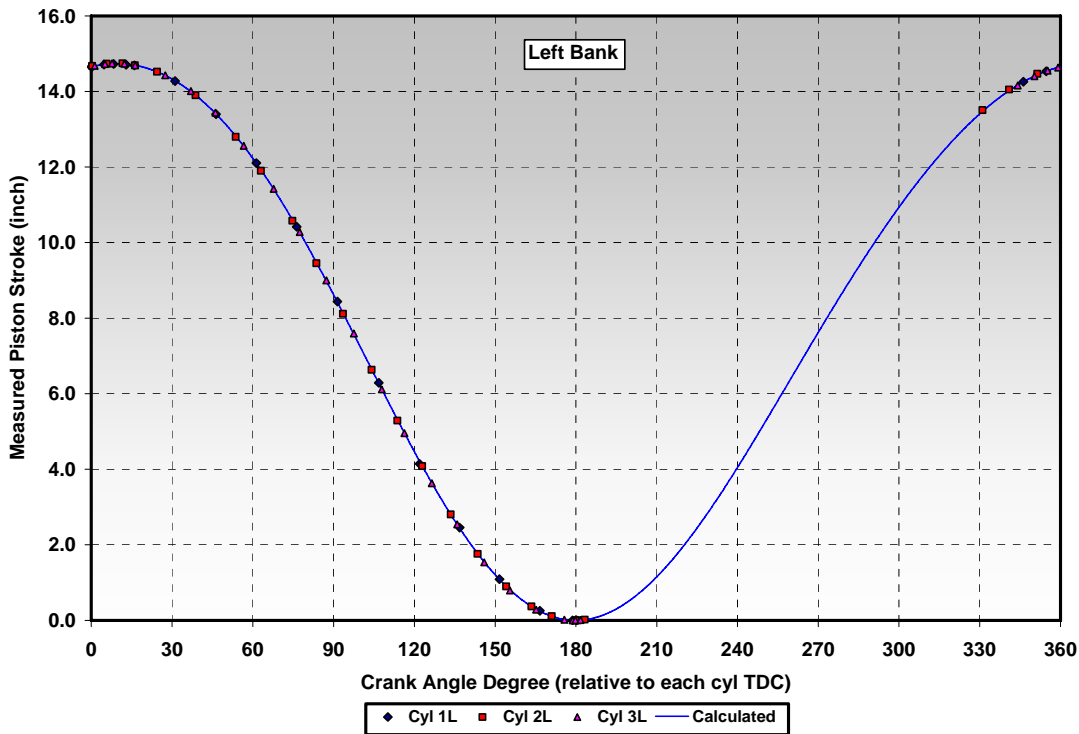


Figure 5-25. Measured Left Bank Piston Motions versus Calculated Motion

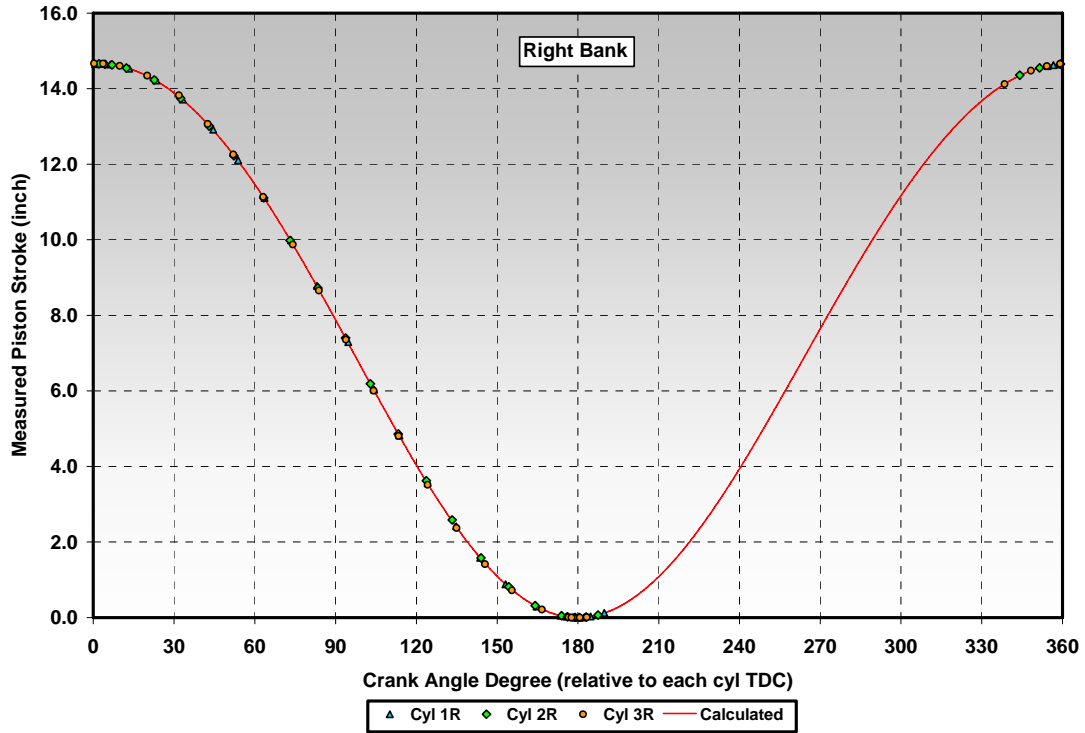


Figure 5-26. Measured Right Bank Piston Motions versus Calculated Motion

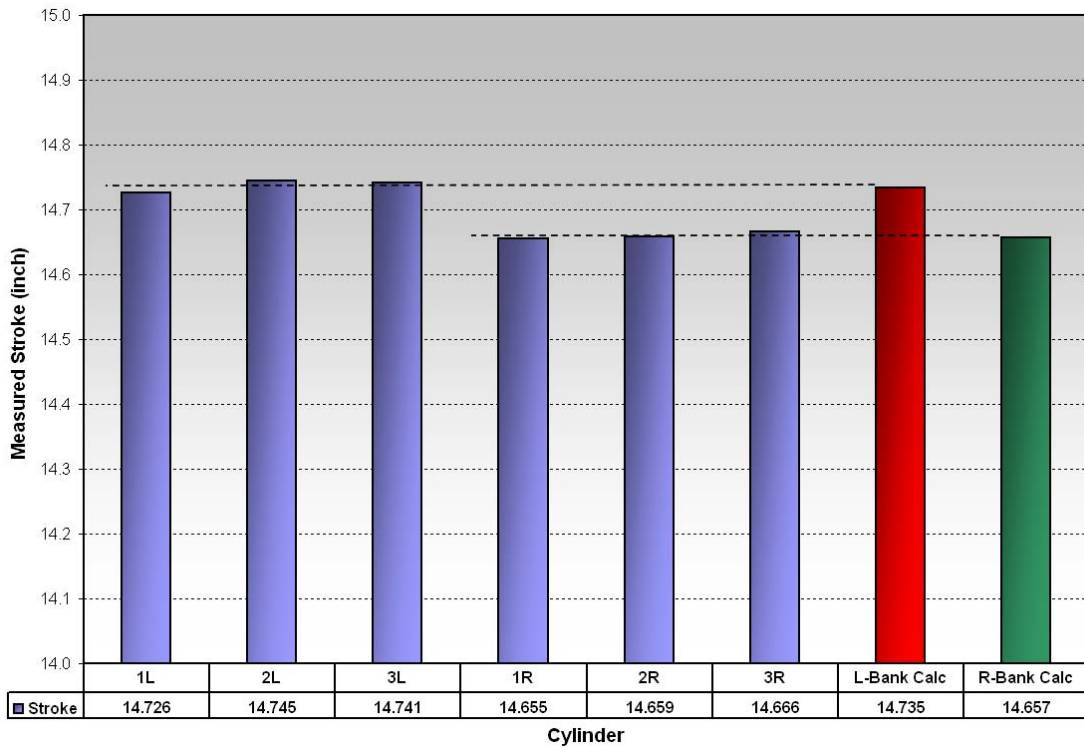


Figure 5-27. Measured Piston Stroke per Cylinder Compared to Drawing Mean Values

5.1.3.6 Compression Ratio

Once the stroke was measured, several measurements on each cylinder were combined to calculate the compression ratio. Each cylinder bore was measured and found to be consistent between cylinders within ± 0.003 inch. Each cylinder head was measured for the combustion chamber volume, in which the values ranged ± 3.7 in³ or within 1 percent. Each piston crown was also measured to calculate the volume displaced in the combustion chamber at TDC. Resulting calculations of TDC clearance volumes showed a maximum variation between cylinders of 3.4 percent. The exhaust port heights were then measured to determine the effective strokes and resulting effective compression ratios. The effective stroke was determined by measuring the piston travel from TDC to the point where the piston edge crossed the top of the highest exhaust port. There was some discussion that the effective stroke should be calculated using the point where the top ring passes the highest exhaust port. However, later flow testing of the cylinders showed minimal flow during the travel from top ring to piston edge crossing. Figure 5-28 shows the measured exhaust port heights (top of port to top of cylinder) and Figure 5-29 shows the effective compression ratio for each cylinder. As can be seen in Figure 5-28, Cylinder 3L had two of the five ports significantly lower than the mean and Cylinder 2R had one. It should be noted that a smaller value represents a shorter distance from the top of the cylinder, resulting in earlier openings and later closings. Figure 5-29 shows the effective compression ratio for each cylinder, as well as the calculated TDC clearances. These calculated effective compression ratio values indicated a spread of 0.3 points out of a mean of 7.7:1. Note that Cylinder 2R had the lowest effective compression ratio, Cylinder 3L had the next lowest, and Cylinder 1L had the highest. The spread of 0.3 points in effective compression ratio was initially thought to be reasonably low, since a spread of >0.8 points was calculated to be required to match the measured spread in compression pressures (assuming compression ratio

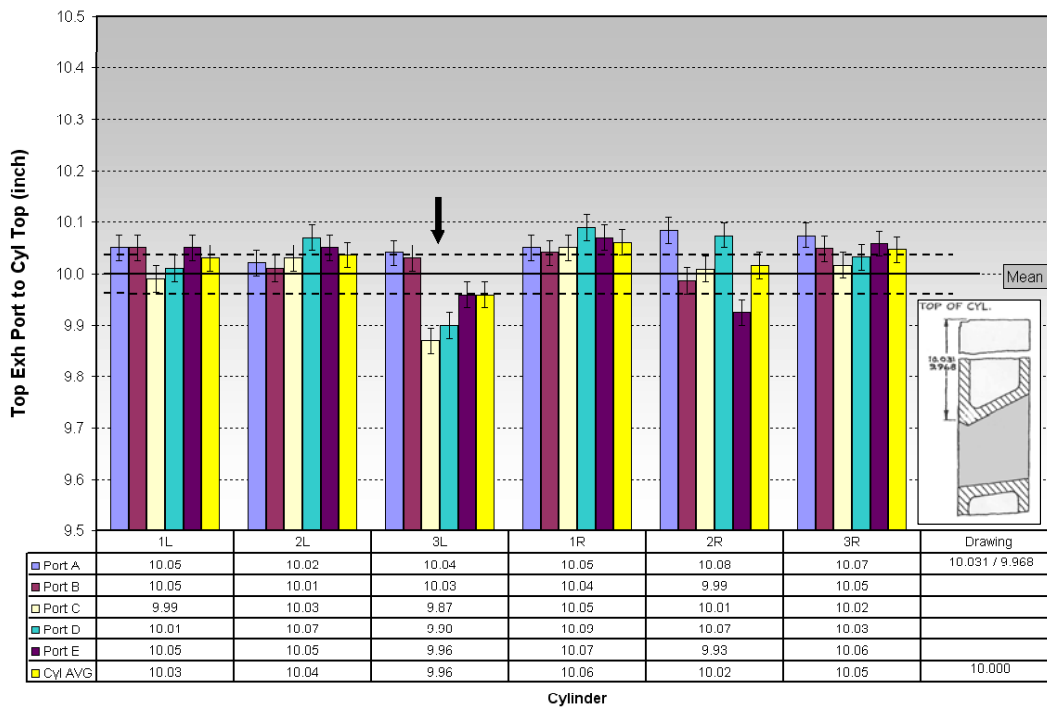


Figure 5-28. Measured Distances from Cylinder Top to Exhaust Port Top

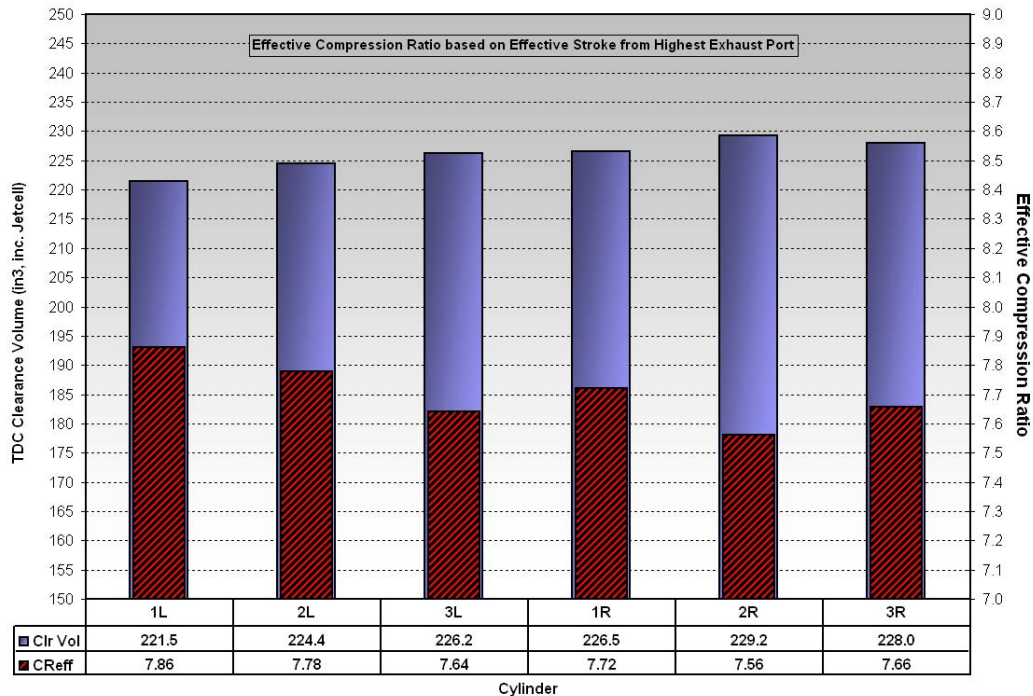


Figure 5-29. Calculated TDC Clearance Volumes and Effective Compression Ratios for Each Cylinder

alone caused the spread). The disconcerting result of this analysis was that Cylinder 2R has consistently yielded the highest compression pressure but has the lowest effective compression ratio. However, the low effective compression ratio for 3L does trend with it having a low compression pressure.

5.1.3.7 Port Geometry

The next factor to be investigated was port flow geometry. The geometric parameters involved with port flow include the port timings, port area, and port shape. The exhaust port opening and closing timings (based on top edge distance to cylinder top and piston edge crossing) are shown in Figure 5-30 and Figure 5-31, respectively. The effect on exhaust timings due to the two out-of-specification ports on Cylinders 3L and 2R can be seen in these figures. The bank-to-bank differences are due to the non-symmetrical piston motions from articulation (see Figure 5-4). Earlier exhaust opening and later closing not only lowers the effective compression ratio but also affects airflow by allowing earlier blowdown and later trapping of cylinder mass.

The exhaust port areas were calculated from the height, width, and corner radius measurements. The measured areas include the “open” areas at the cylinder wall surface facing the combustion chamber. The five cylinders that had the same casting number were very consistent in exhaust port open area. Cylinder 1R, which had the different casting number, had significantly smaller exhaust port open areas, which were approximately 8% less than the other cylinder’s exhaust ports. Calculated values of exhaust port open area for each cylinder and each port are shown in Figure 5-32.

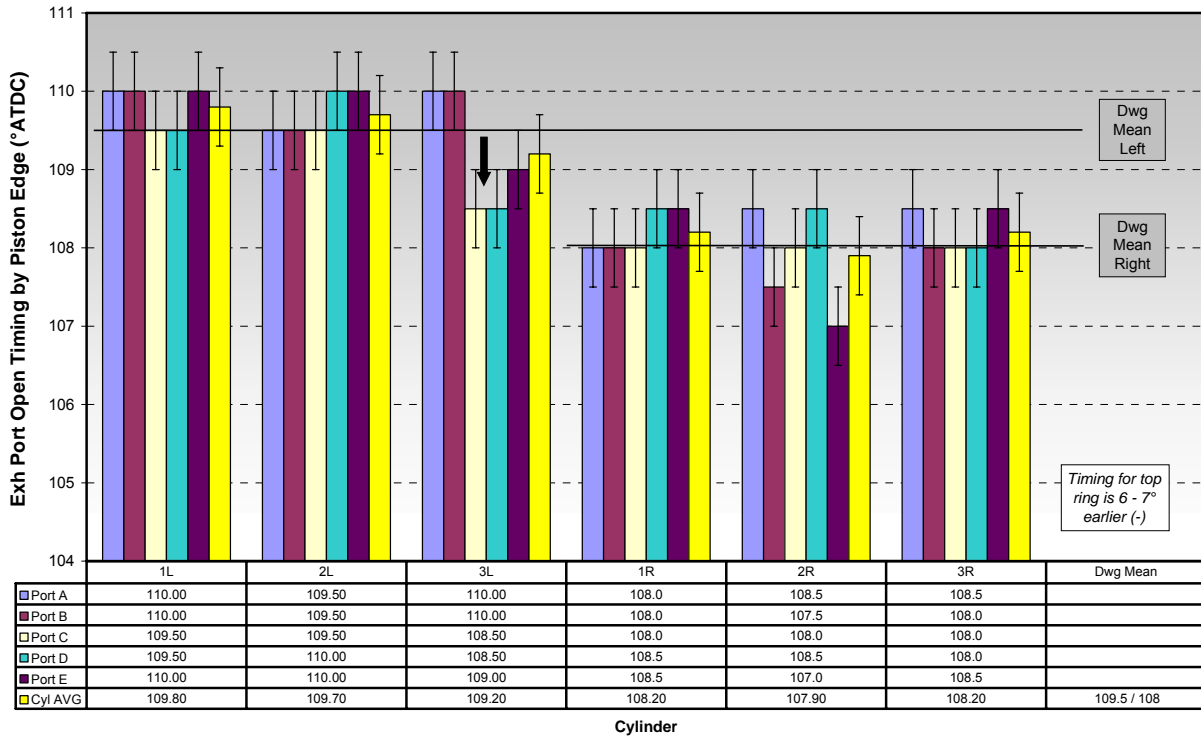


Figure 5-30. Calculated Exhaust Port Opening Timings for Each Cylinder

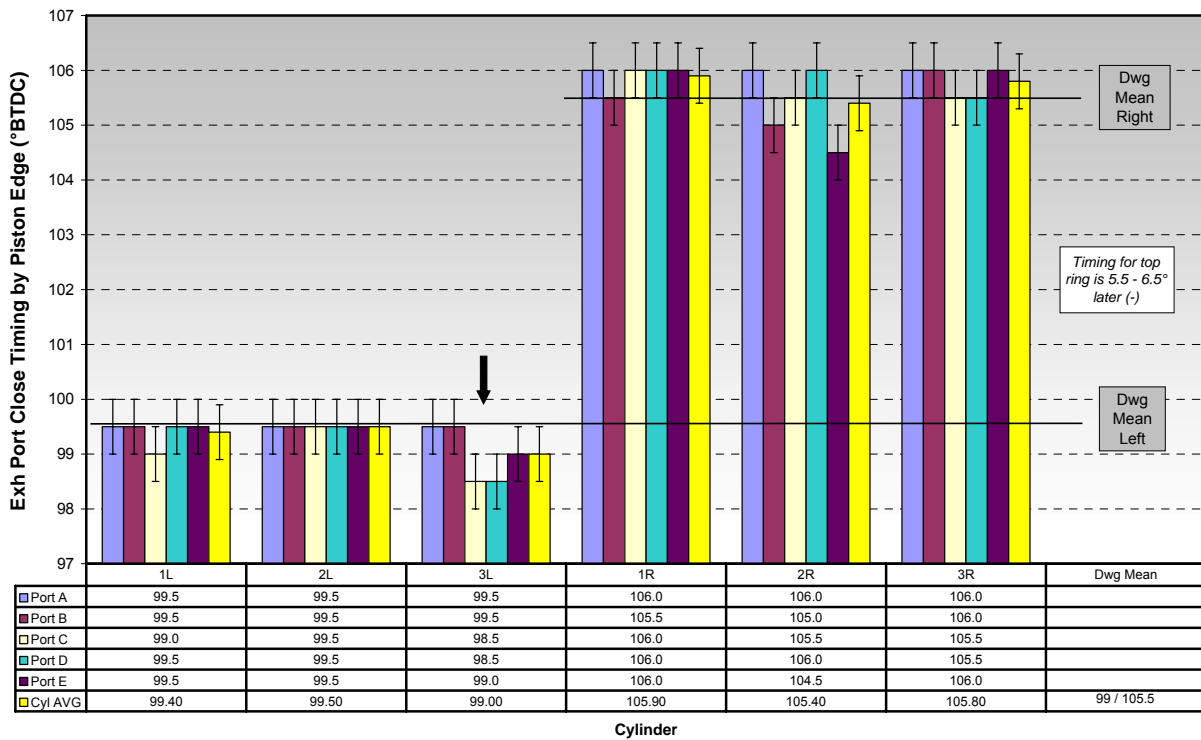


Figure 5-31. Calculated Exhaust Port Closing Timings for Each Cylinder

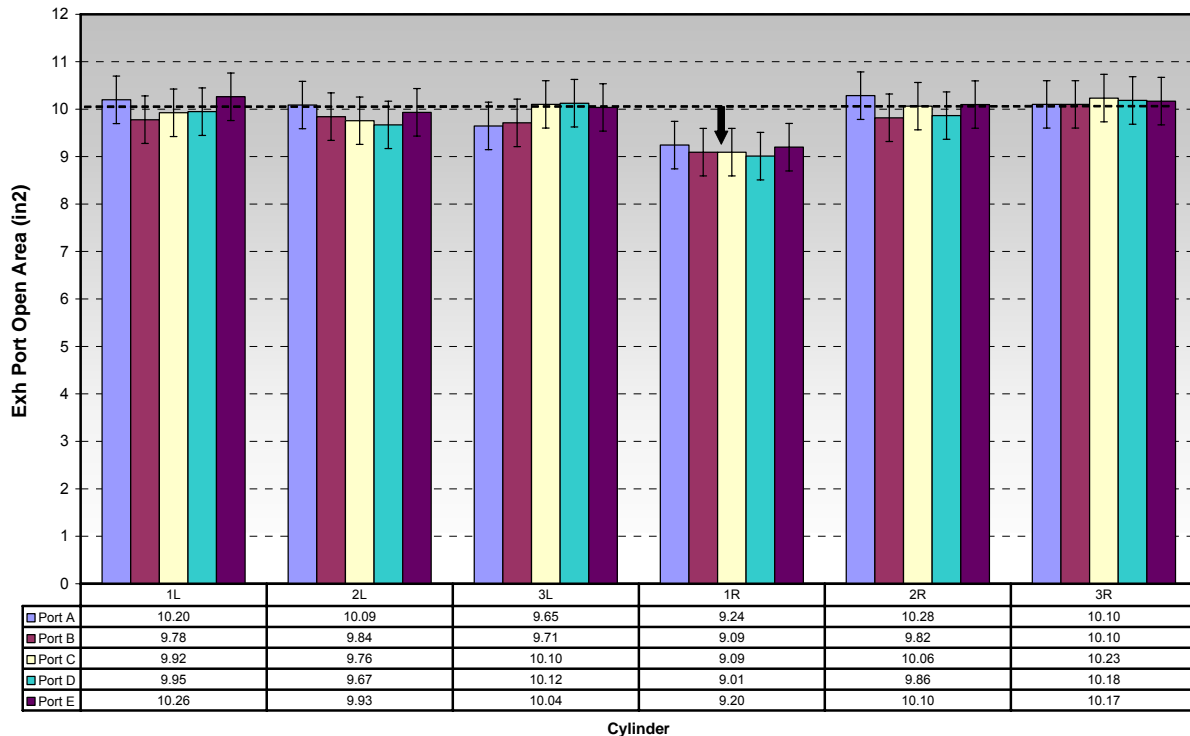


Figure 5-32. Calculated Exhaust Port Areas for Each Cylinder

Intake port opening and closing timings are shown in Figure 5-33 and Figure 5-34, respectively. In these figures, the timings for Cylinder 1R are shown to deviate from the other cylinders, which is due to the top port edges being on the low side (later opening and later closing). The bank-to-bank differences are due to the non-symmetrical piston motions from articulation (see Figure 5-5). The calculated intake port open areas are shown in Figure 5-35. The difference in area between ports on a given cylinder is due to pairs of the eight ports having different skew angles as shown in Figure 5-36. Comparing the data in Figure 5-35, Cylinder 1R is again shown to differ from the other cylinder's values. Thus, the different casting cylinder originally installed on 1R has differences in both the exhaust and intake ports. The five cylinders with the same casting number were consistent in terms of the intake port dimensions acquired. The intake ports enter the cylinder from the airbox at an angle of nominally 30 degrees from vertical, as shown in Figure 5-36. The actual angles for each intake port were also measured, and Cylinder 3L had an average angle variance of 3.8% lower than the nominal value.

5.1.3.8 Fuel Valve Travel

The last significant geometric measurement made was the fuel valve travel. This was done because several questions arose during early engine testing regarding the actual fuel valve timing and duration, as well as possible variations in the fuel admission. Fuel valve travel was measured as a function of crankshaft angle degree. Results of the measurements on each cylinder's fuel valve are shown in Figure 5-37. The data show very consistent fuel valve lift profiles, with only a slight reduction in duration for Cylinders 3L and 3R (same cam lobe) of one degree. These measurements were made after reassembly of the engine.

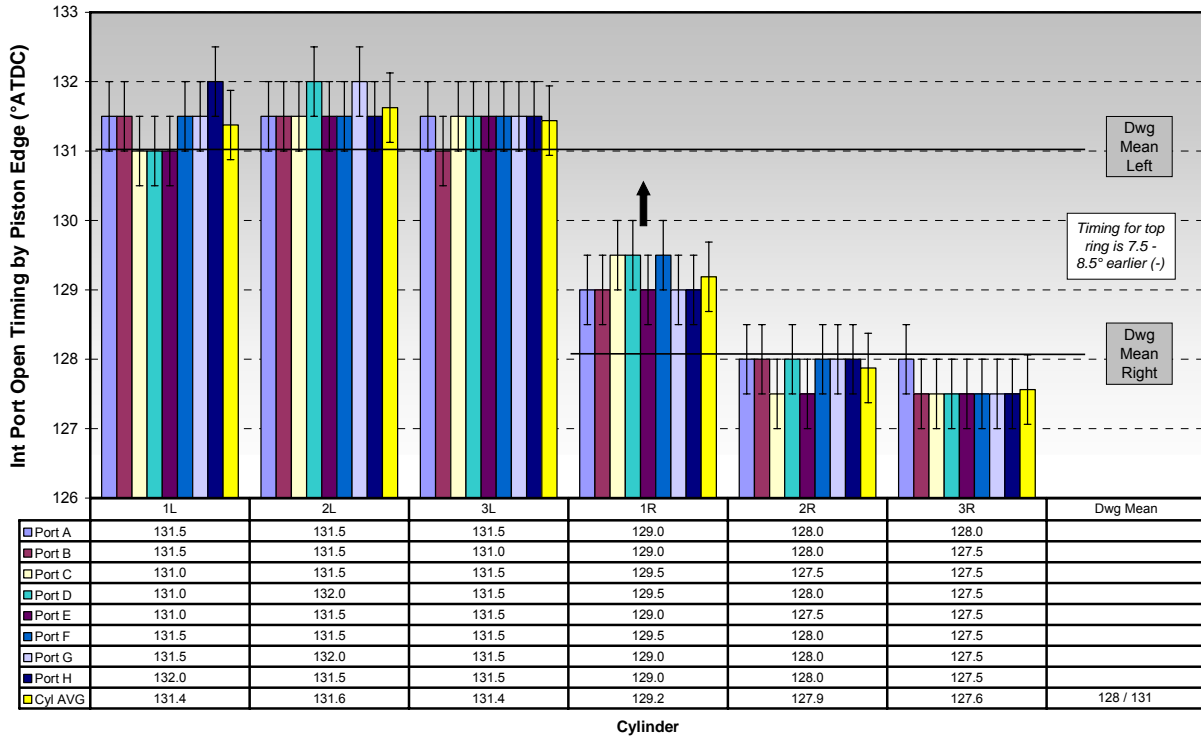


Figure 5-33. Calculated Intake Port Open Timings for Each Cylinder

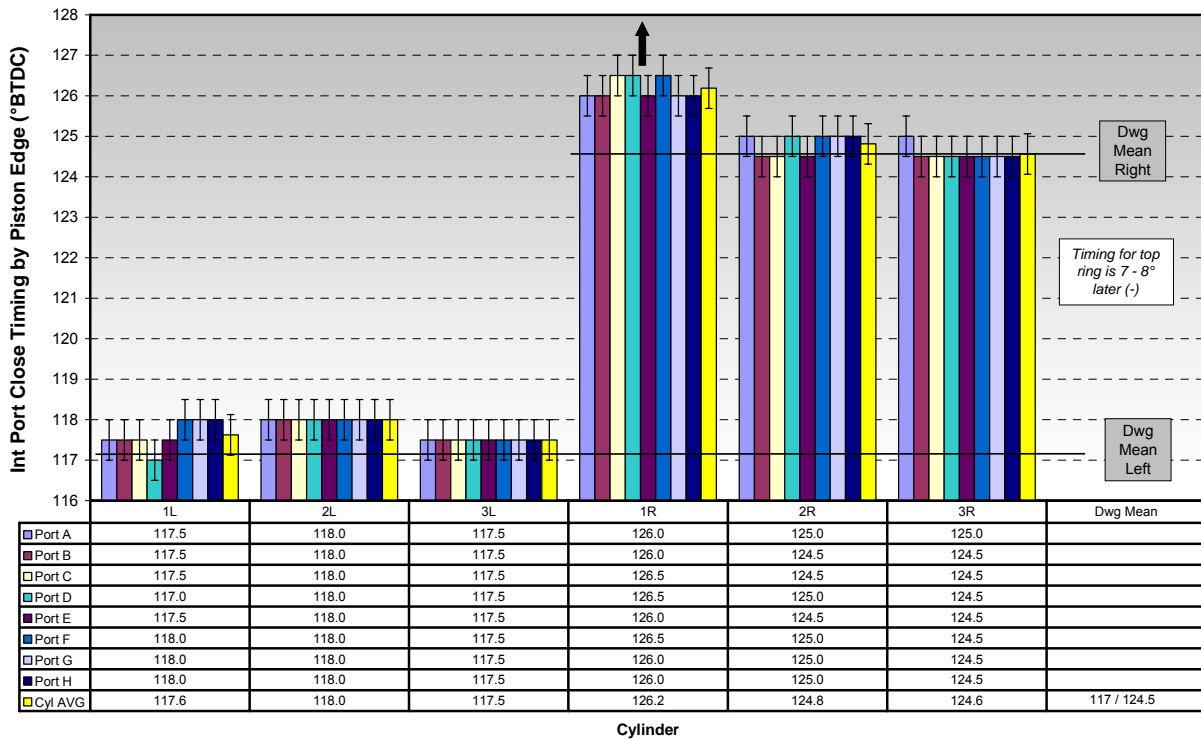


Figure 5-34. Calculated Intake Port Closing Timings for Each Cylinder

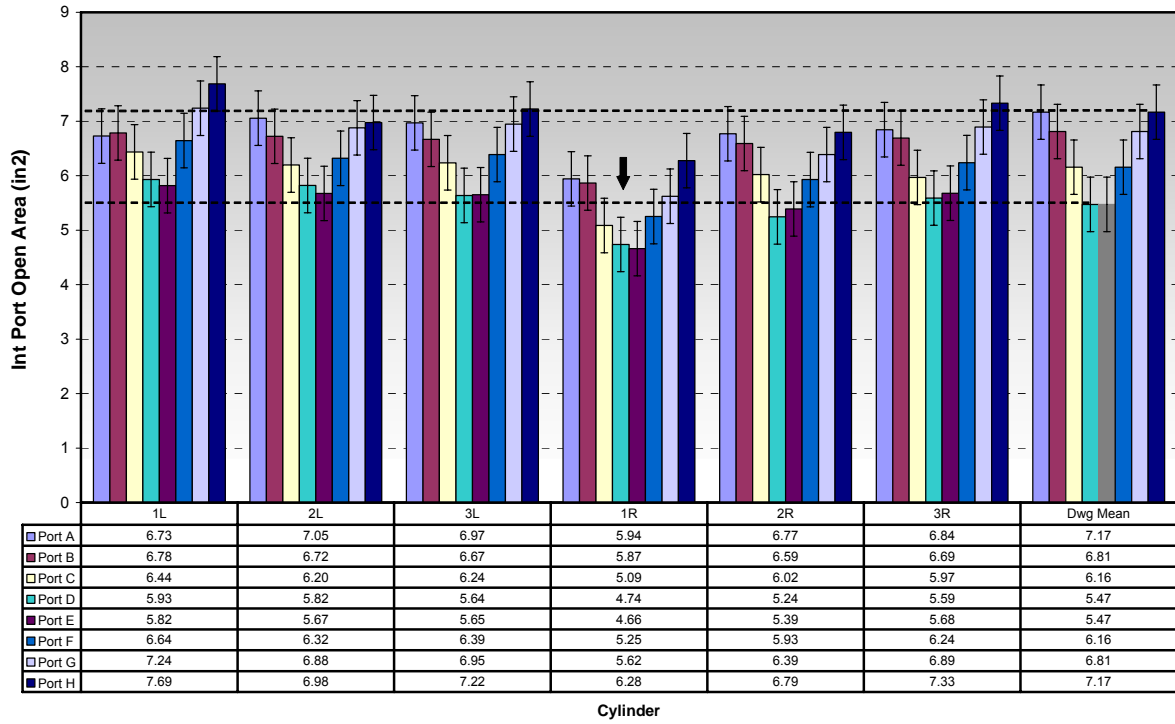


Figure 5-35. Calculated Intake Port Areas for Each Cylinder

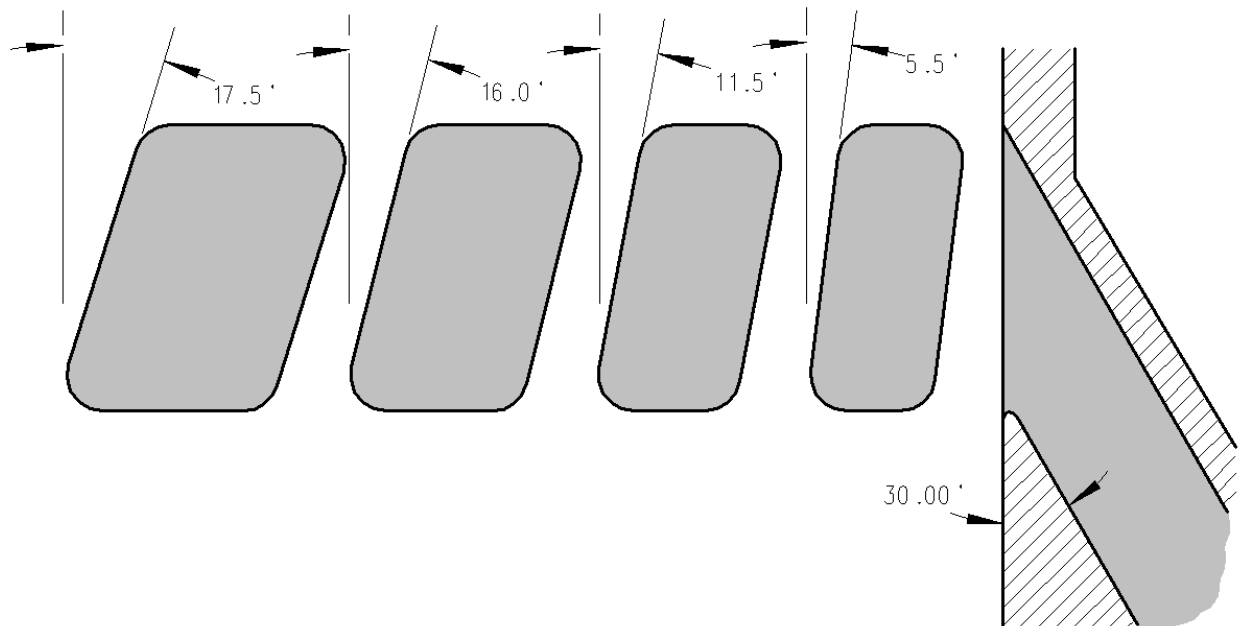


Figure 5-36. Schematic of Intake Port Geometry

GMVH-6 Fuel Valve Travel

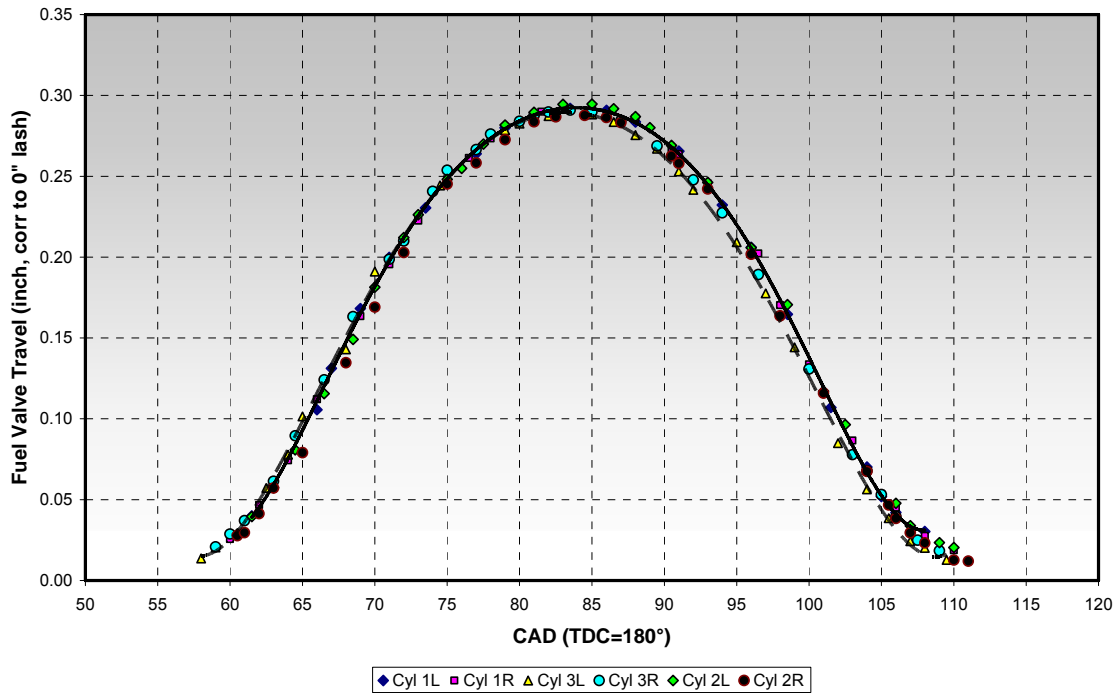


Figure 5-37. Measured Fuel Valve Travel

5.1.4 PORT FLOW TESTING

Flow testing was desired to obtain accurate discharge coefficient data for modeling and secondly to determine the variation between cylinders due to geometry of the ports. Cylinders 1L and 3L, representing a high and low compression pressure on a given bank, were removed from the base and flow tested. Cylinder 1R had a different exhaust port shape, as discussed above, and was removed to be flow tested as well. The testing involved flows of both the inlet and exhaust ports at various piston heights and pressures. The compressed air supply was limited in capacity, so only half of the area ratio range was achieved in most tests. Data was acquired from the various sensors at a rate of 5 Hz to allow a significant number of samples to be acquired in a short period of time. The dynamic measurements were reviewed at each test point to ensure stable operation. The data were averaged and the total airflow and discharge coefficient was calculated for each condition.

Several measurements on each set of ports (intake or exhaust) for each cylinder were taken at different pressure ratios and port openings. The test stand allowed for setting piston height to set a prescribed opening area and adjustments to the compressed air outlet regulator and control valve allowed for prescribed pressure ratios. The two different size flow nozzles were used for high and low flows, and installed in the meter run to measure the airflow. Two nozzle sizes were needed to either keep from choking across the nozzle or keep the delta-pressure in a good measurable range over the flow range tested. Since the air supply was from a compressed air storage facility, the time for conducting this testing was longer than planned due to time required to recharge the tanks between runs. The airflow capacity of the system was also

insufficient for normal testing at the larger port openings, although a few quick measurements at the lowest pressure ratio were acquired at full opening to ensure the extrapolation at other pressure ratios was accurate. In addition, the extensive test range at mid to low port openings gave further confidence in the extrapolations.

Cylinder 1L was the first tested and extensively mapped. Cylinder 3L was only tested at select points to give necessary indication of flow and discharge coefficient variances and to reduce total test time. Cylinder 1R was tested more extensively than 3L, due to the more significant geometric differences, although a few conditions were eliminated for time reduction. The raw (as-measured) data for Cylinder 1L intake are given in Figure 5-38 and Figure 5-39. Figure 5-38 shows the mass flow versus piston location from BDC for several pressure ratios. In this figure, the flow at higher piston positions is very low because the piston edge is above the port, but the top ring is below, and flow is through the crevice area. As the piston edge uncovers the ports, the flow then increases linearly with reducing piston location or increasing port opening by the piston edge. The increasing flow with pressure ratio is clearly present. Figure 5-39 shows the mass flow versus plenum pressure, which is the pressure upstream of the ports, for several piston positions. The flow is shown in this figure to increase rapidly at first with increasing pressure (pressure ratio) and taper off as pressure increase continues.

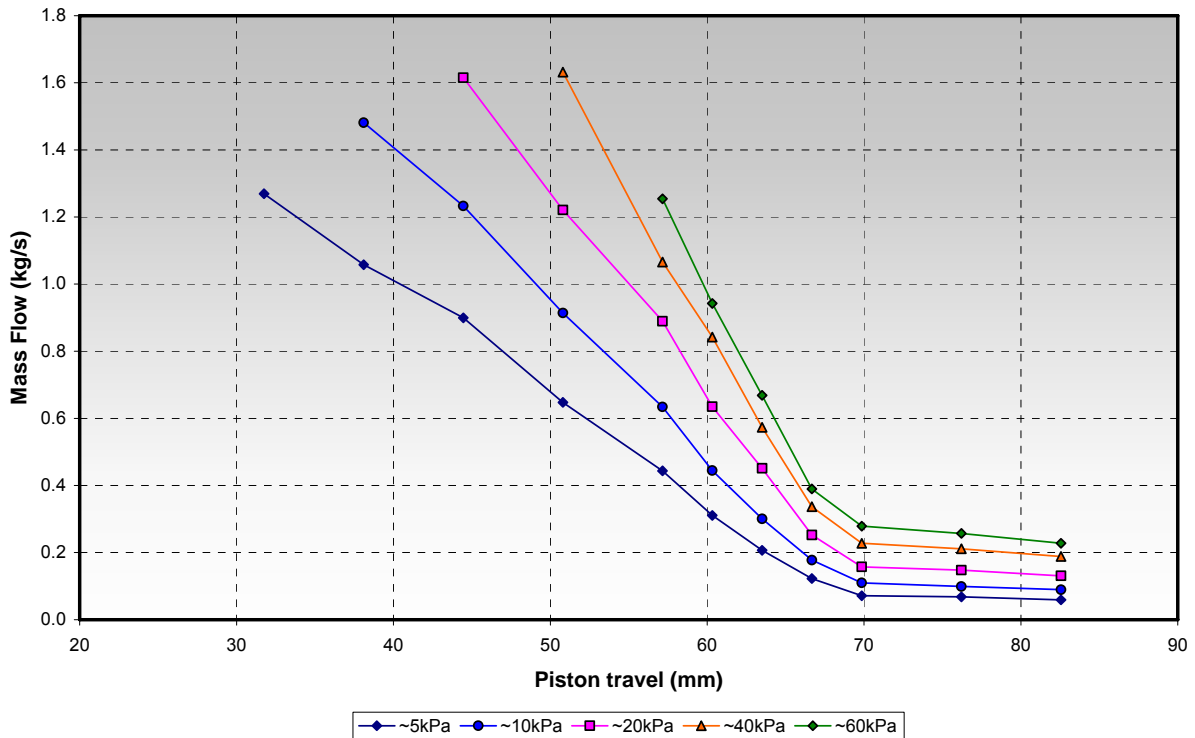


Figure 5-38. Cylinder 1L Intake – Mass Flow versus Piston Travel from BDC

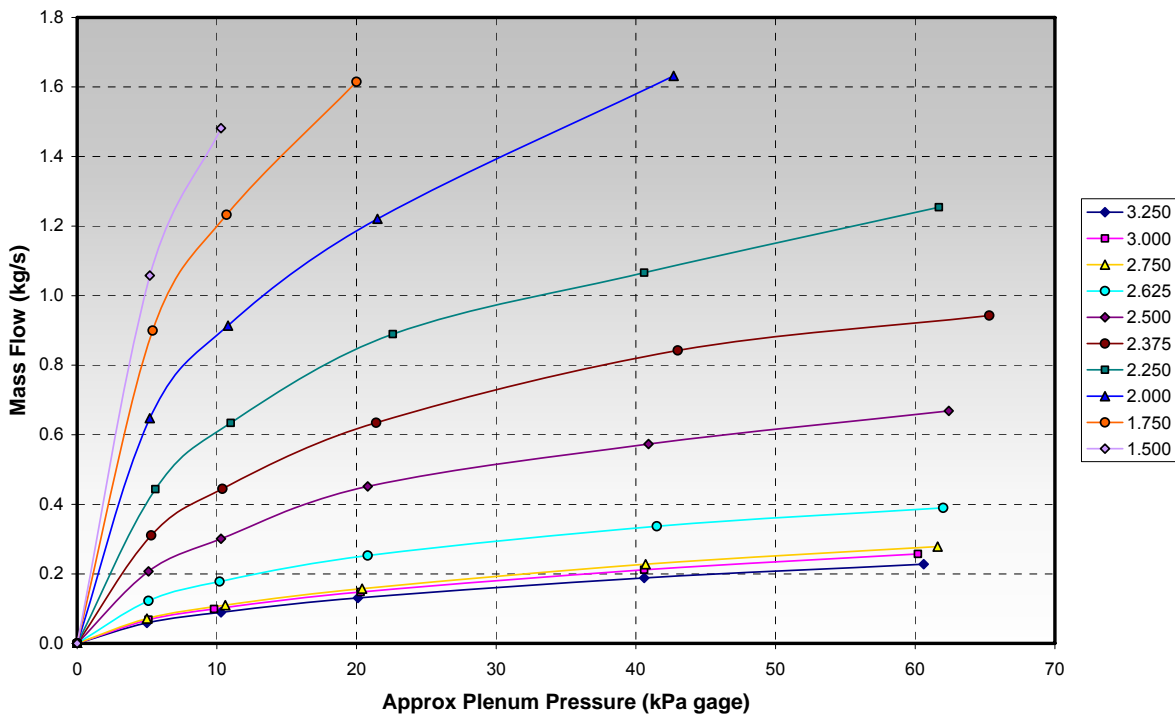


Figure 5-39. Cylinder 1L Intake – Mass Flow versus Plenum Pressure

The raw (as-measured) data for Cylinder 1L exhaust are given in Figure 5-40 and Figure 5-41. Figure 5-40 shows the mass flow versus piston location from BDC for several pressure ratios. In this figure, the flow at higher piston positions is again very low because the piston edge is above the port, but the top ring is below, and flow is through the crevice area. Fewer points were acquired on the exhaust with the piston edge above the port top since the trend was documented with the limited data taken at these positions. As the piston edge uncovers the ports, the flow then increases linearly with reducing piston location as similarly seen with the intake test data. Again, the increasing flow with pressure ratio is clearly present. Figure 5-41 shows the mass flow versus plenum pressure for several piston positions. The flow is shown in this figure to increase similarly as with the intake tests with increasing pressure.

The geometric analysis showed that there is some variation between ports and between cylinders. Therefore, it is important to view the measured data in terms of actual pressure and area ratios. The area ratio is based on the open area (vertical exposed area at port edge in cylinder). The pressure ratio is the ratio of pressure across the ports (upstream/downstream). A comparison of the intake mass flow versus area ratio is shown in Figure 5-42, for the three tested cylinders at a pressure ratio of 1.05. This figure shows that both Cylinders 3L and 1R have lower mass flow versus area ratio relationships than Cylinder 1L. The Cylinders 1L and 3L shared similar dimensions pertaining to the inlet plenum and ports, so the cause for reduced flow for 3L is unclear at this time. Cylinder 1R has several differences in plenum volume and port areas (height-width relationship), which likely explains its reduced flow.

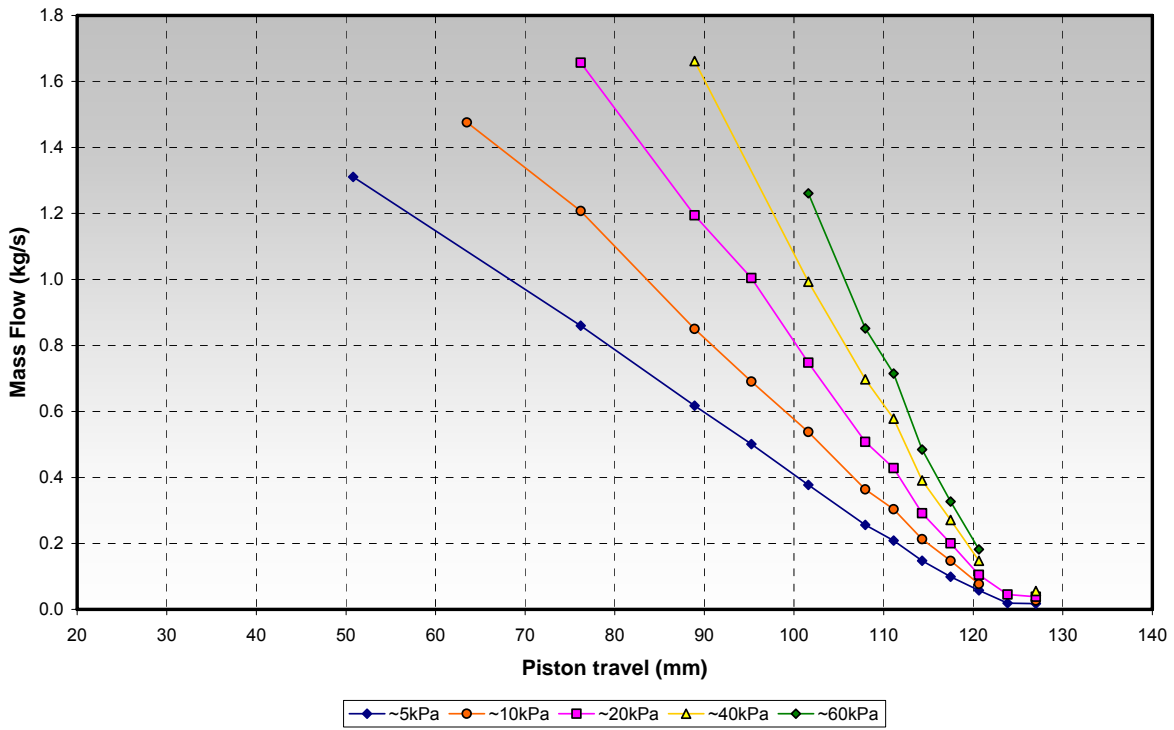


Figure 5-40. Cylinder 1L Exhaust – Mass Flow versus Piston Travel from BDC

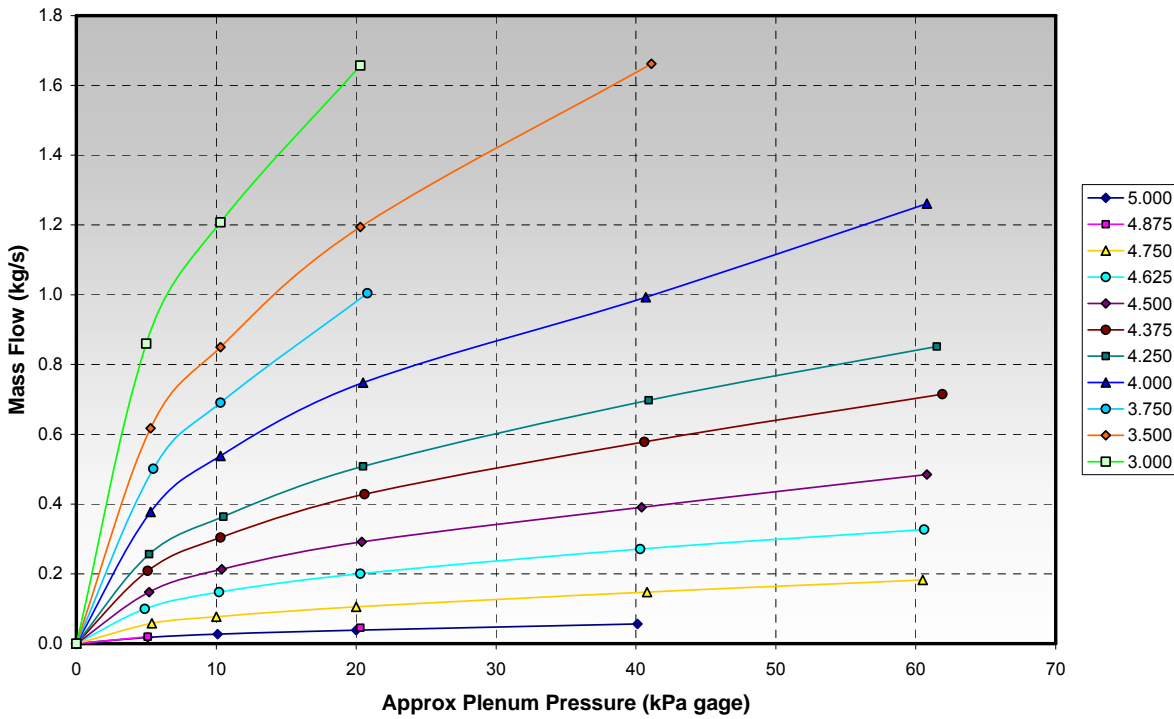


Figure 5-41. Cylinder 1L Exhaust – Mass Flow versus Plenum Pressure

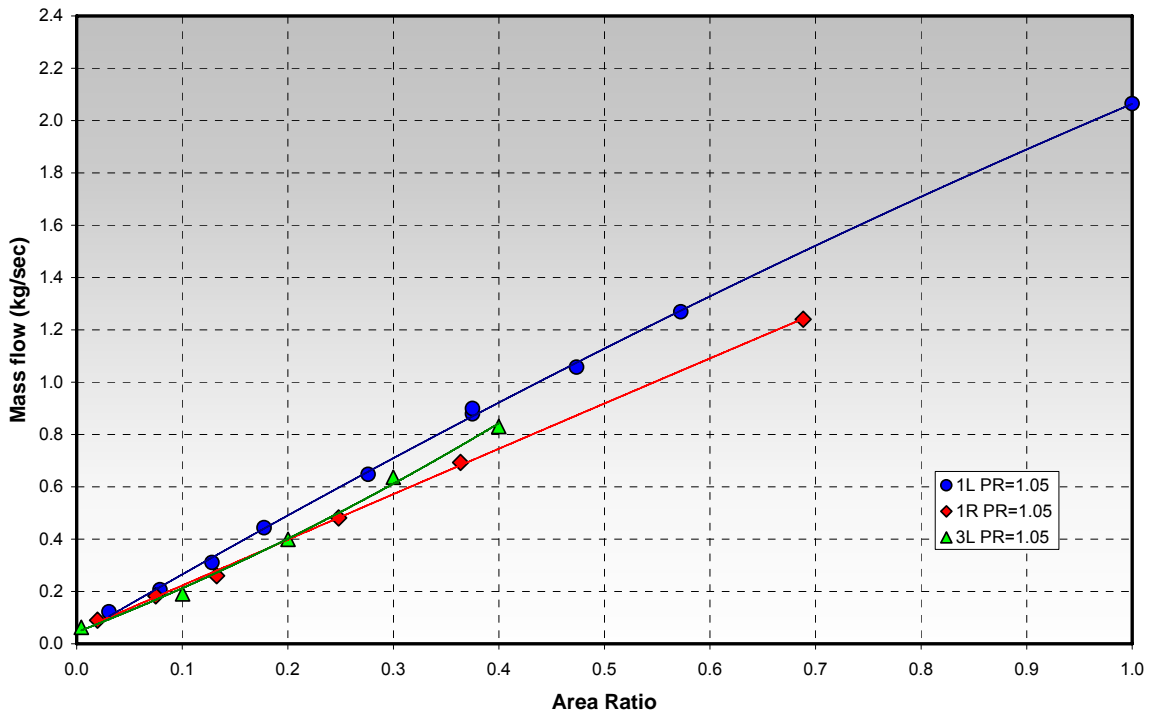


Figure 5-42. Comparison of Intake Mass Flow versus Area Ratio (Pressure Ratio=1.05)

A comparison of the exhaust mass flow versus area ratio is shown in Figure 5-43, for the three tested cylinders at a pressure ratio of 1.05. This figure shows that both Cylinders 1L and 3L have similar flow characteristics. Cylinder 1R has a lower mass flow than Cylinders 1L and 3L. Although Cylinder 1R has a lower total port area, the port timings and widths were similar and should flow similarly at part openings. However, the shapes of the exhaust ports in Cylinder 1R are different and is likely the reason for its reduced flow. This is more apparent in the discharge coefficient calculations.

The data was further reduced to discharge coefficients versus area ratio and pressure ratio. The discharge coefficient was determined from isentropic flow equations with compensation for the moisture content in the air. The intake port areas were based on the projected open area perpendicular to the top wall, rather than the vertical open area on the cylinder surface. The intake ports and the piston crown have the same angle, so the projected area is more appropriate to use. This projected area is illustrated in Figure 5-44. The exhaust port's top wall angle is somewhat of an opposite angle than the piston crown as shown in Figure 5-45, thus, the vertical open area parallel to the cylinder wall was used in exhaust discharge calculations. The resulting discharge coefficients were calculated for the area ratios and pressure ratios that could be tested within the limits of the flow test rig.

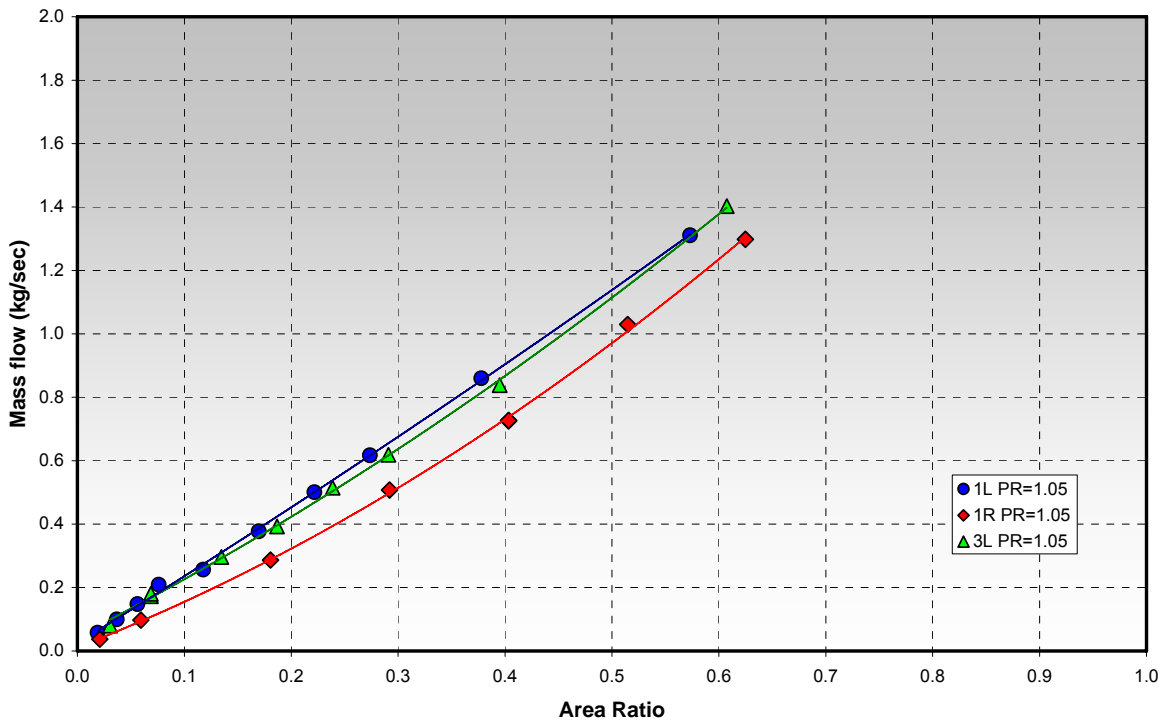


Figure 5-43. Comparison of Exhaust Mass Flow versus Area Ratio (Pressure Ratio=1.05)

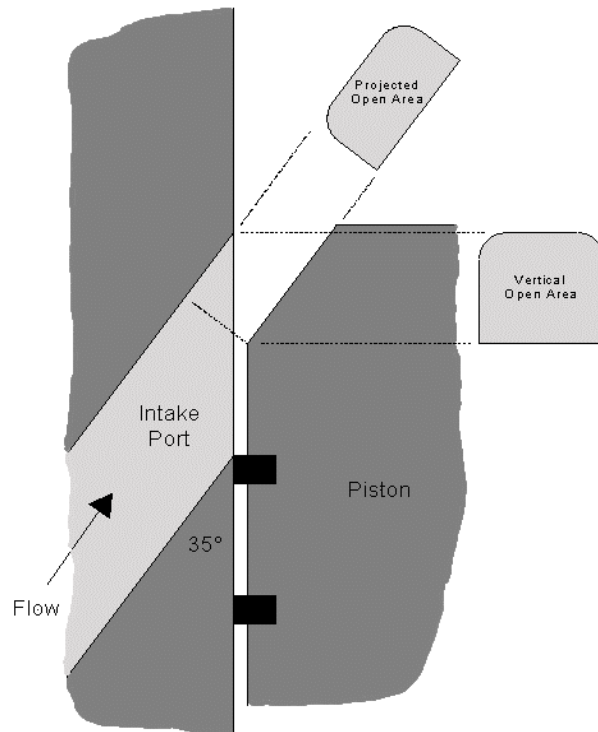


Figure 5-44. Intake Port Flow Area Schematic

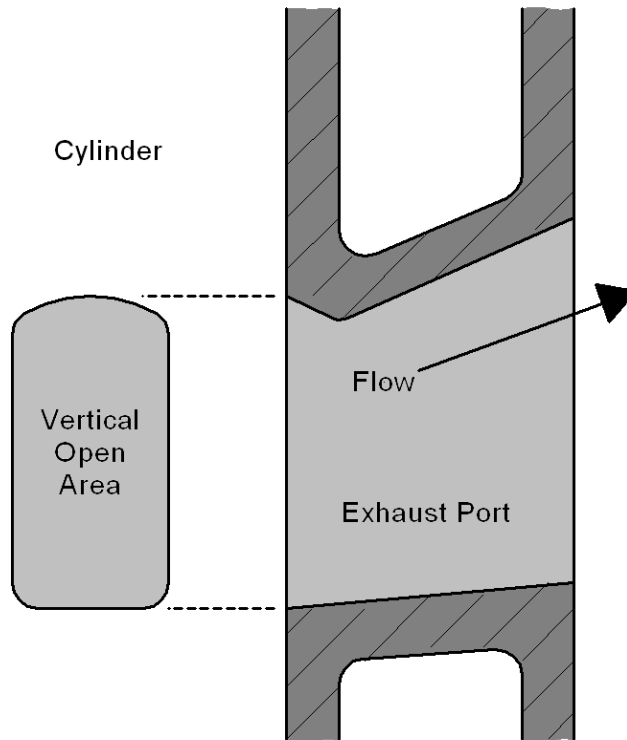


Figure 5-45. Exhaust Port Flow Area Schematic

The discharge coefficient versus area ratio for Cylinder 1L intake at various pressure ratios is given in Figure 5-46. A decreasing trend of discharge coefficient versus pressure ratio can be seen in this figure. The discharge coefficient versus area ratio for Cylinder 1L exhaust at various pressure ratios is given in Figure 5-47. No trend with pressure ratio is exhibited in the exhaust port data. Comparisons of the intake discharge coefficients for the tested cylinders at pressure ratios of 1.05 and 1.2 are given in Figure 5-48 and Figure 5-49, respectively. Similar trends can be seen under both pressure conditions, with an increased discharge coefficient for Cylinder 1R and reduced values for Cylinder 3L at low area ratios. Comparison of the exhaust discharge coefficients at pressure ratios of 1.05 and 1.2 are given in Figure 5-50 and Figure 5-51, respectively. Similar trends can be seen in both figures, with Cylinders 1L and 3L matching and Cylinder 1R having a more significant reduction in discharge coefficient at low area ratios. This significantly different trend for Cylinder 1R is presumed to be caused by the different shape of the top of the exhaust port runners.

These values and trends closely follow values and trends presented in the literature [11-13]. The flow test rig data was added to the computational model to generate a map of discharge coefficients versus area ratio and pressure ratio. Figure 5-52 and Figure 5-53 show the full map of discharge coefficients for the exhaust and intake ports on Cylinder 1L, respectively.

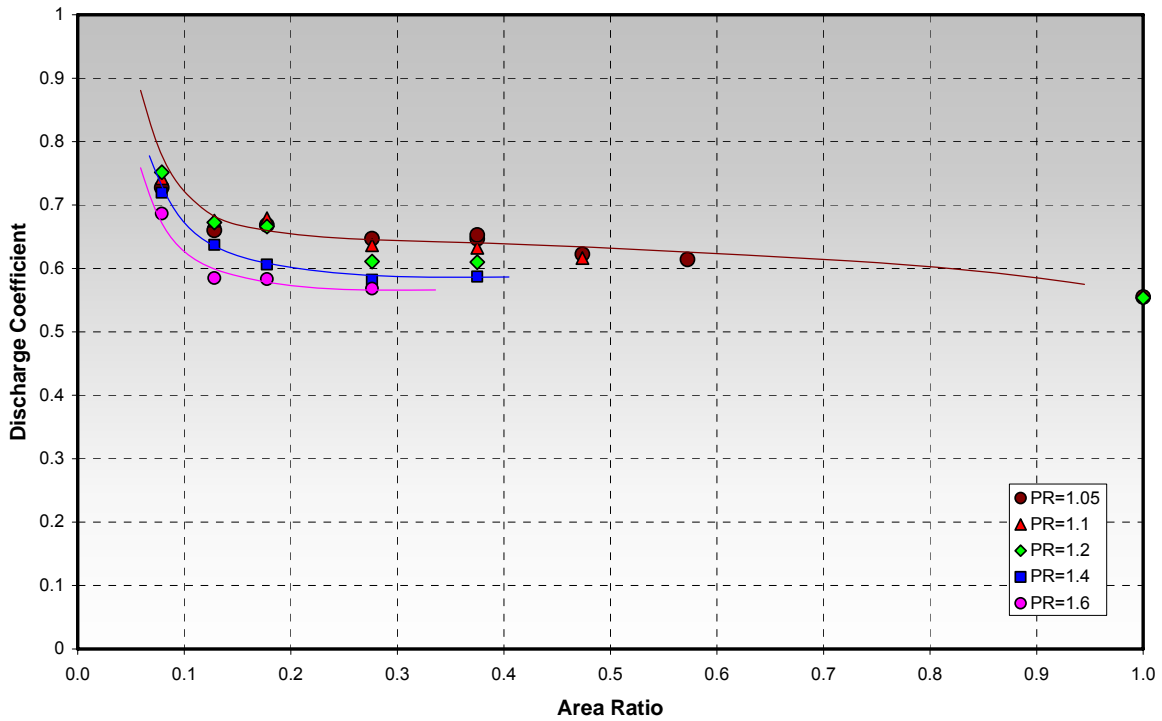


Figure 5-46. Cylinder 1L Intake Discharge Coefficient versus Area Ratio at Tested Pressure Ratios

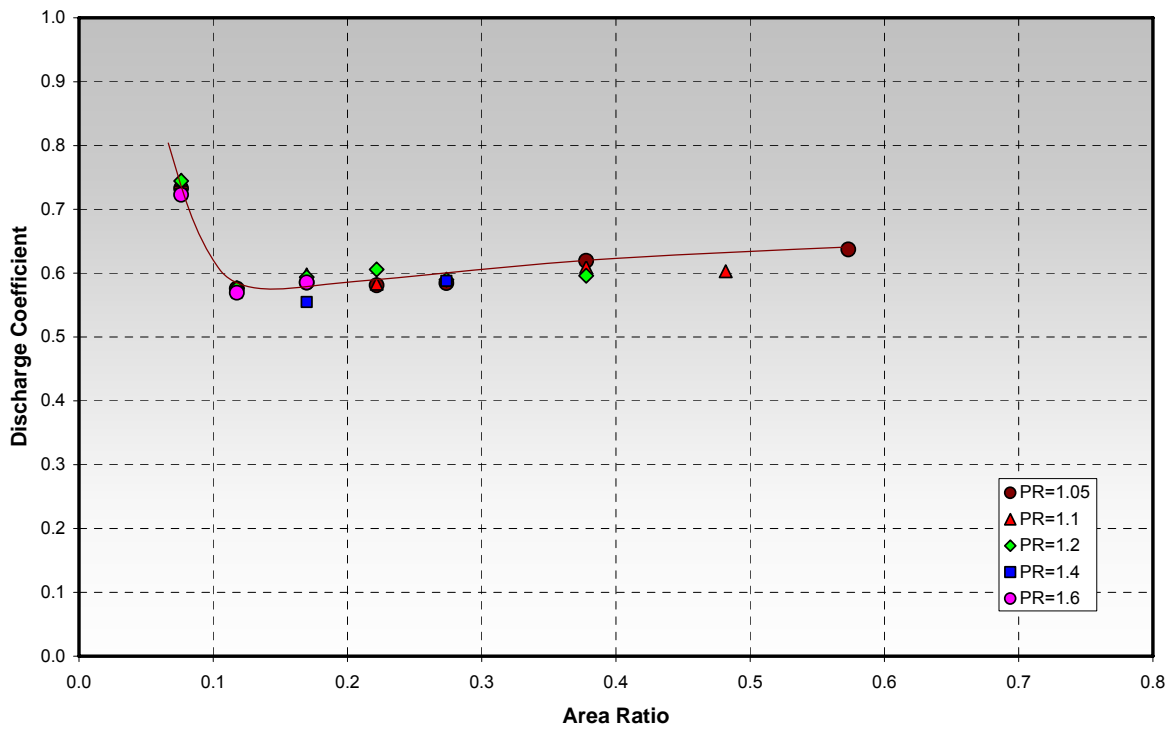


Figure 5-47. Cylinder 1L Exhaust Discharge Coefficient versus Area Ratio at Tested Pressure Ratios

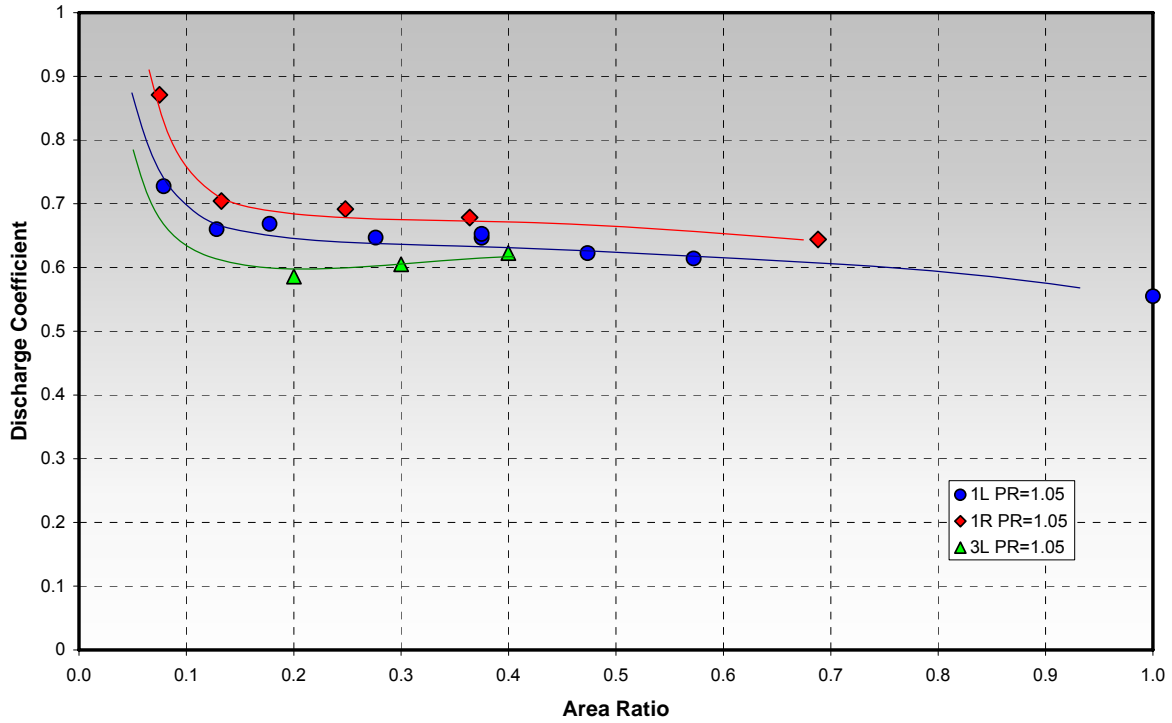


Figure 5-48. Intake Discharge Coefficient versus Area Ratio for Tested Cylinders (Pressure Ratio=1.05)

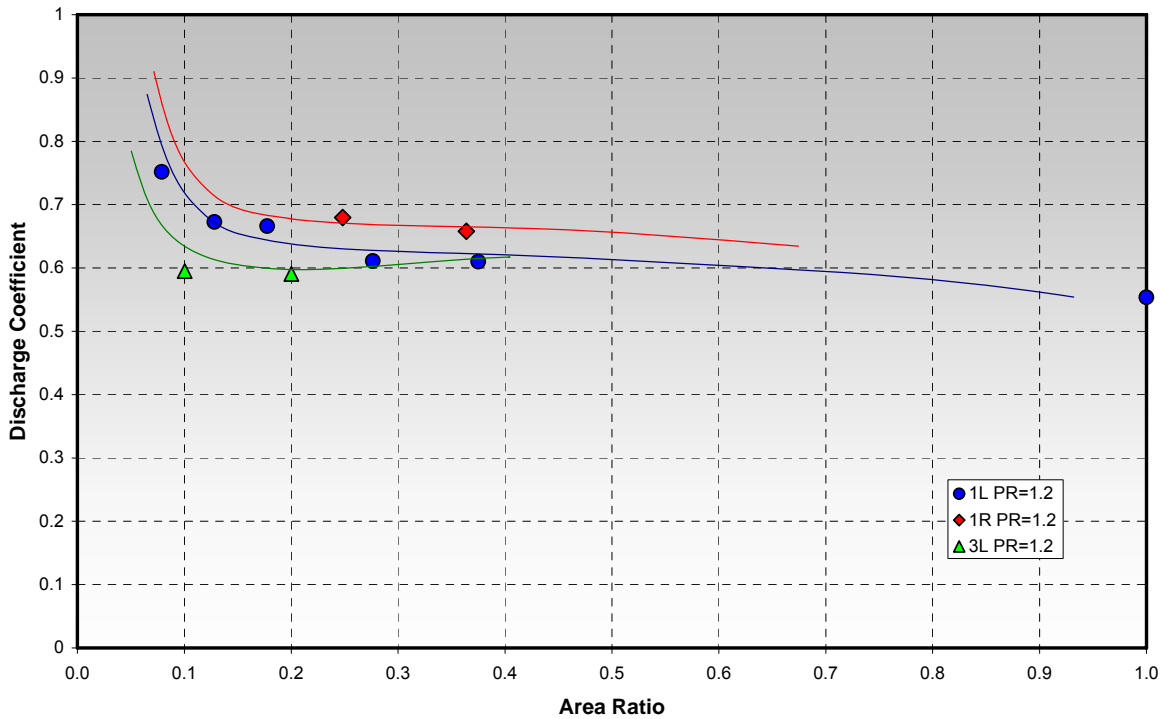


Figure 5-49. Intake Discharge Coefficient versus Area Ratio for Tested Cylinders (Pressure Ratio=1.2)

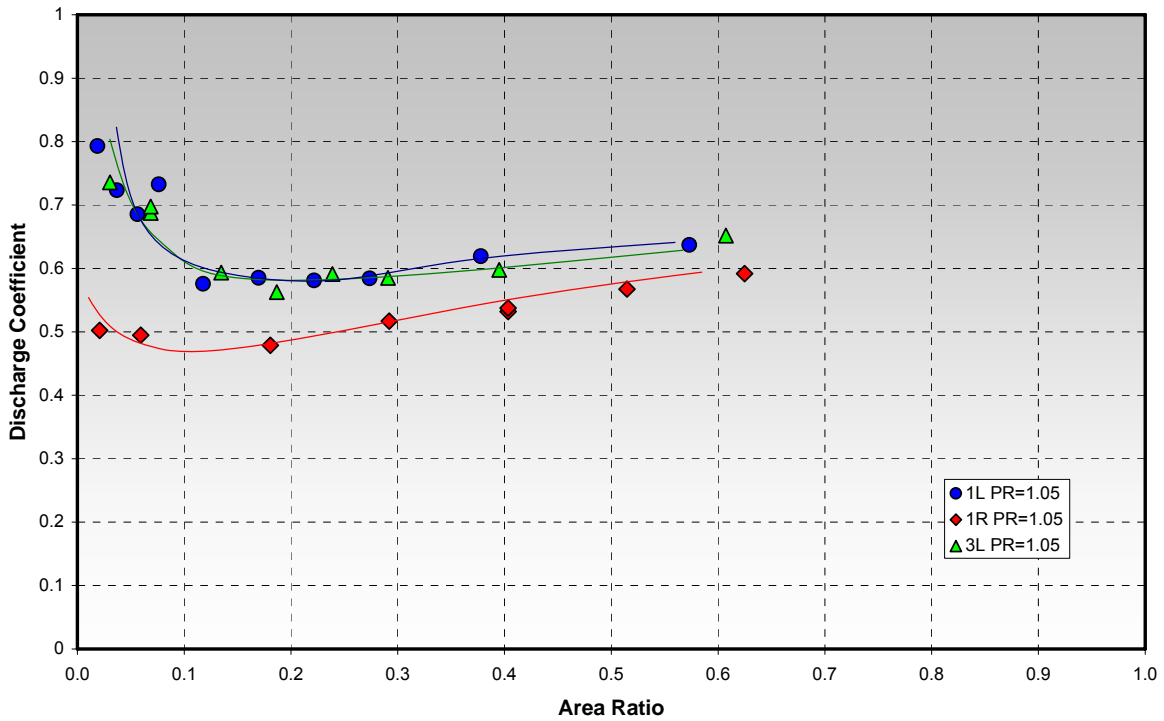


Figure 5-50. Exhaust Discharge Coefficient versus Area Ratio for Tested Cylinders (Pressure Ratio=1.05)

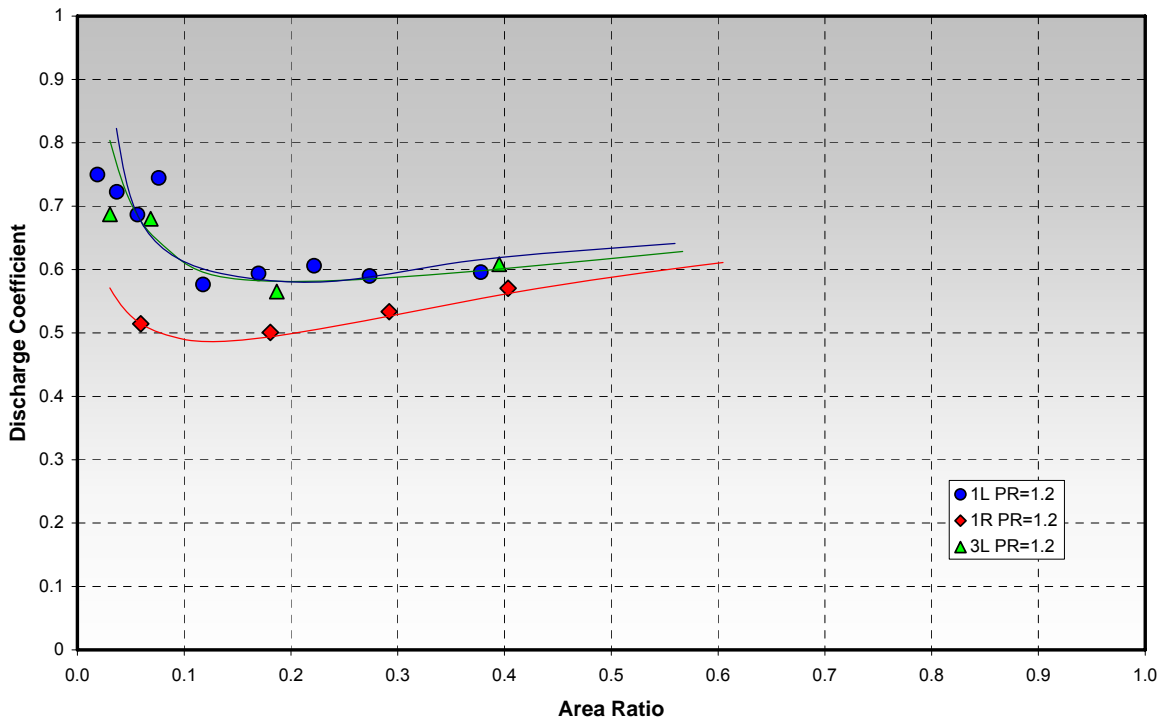


Figure 5-51. Exhaust Discharge Coefficient versus Area Ratio for Tested Cylinders (Pressure Ratio=1.2)

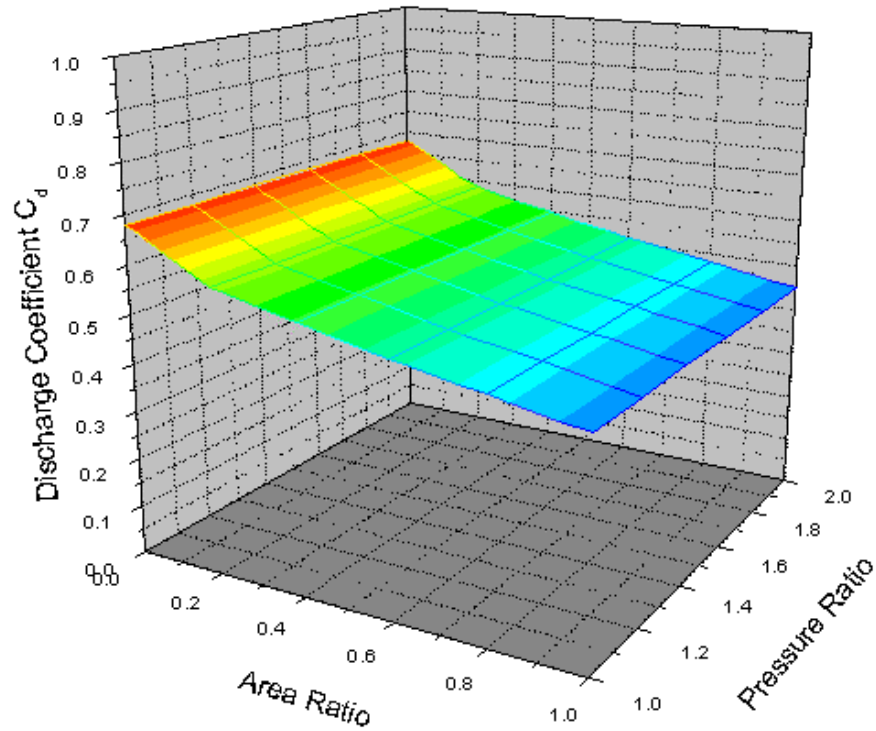


Figure 5-52. Model Generated Exhaust Discharge Coefficients

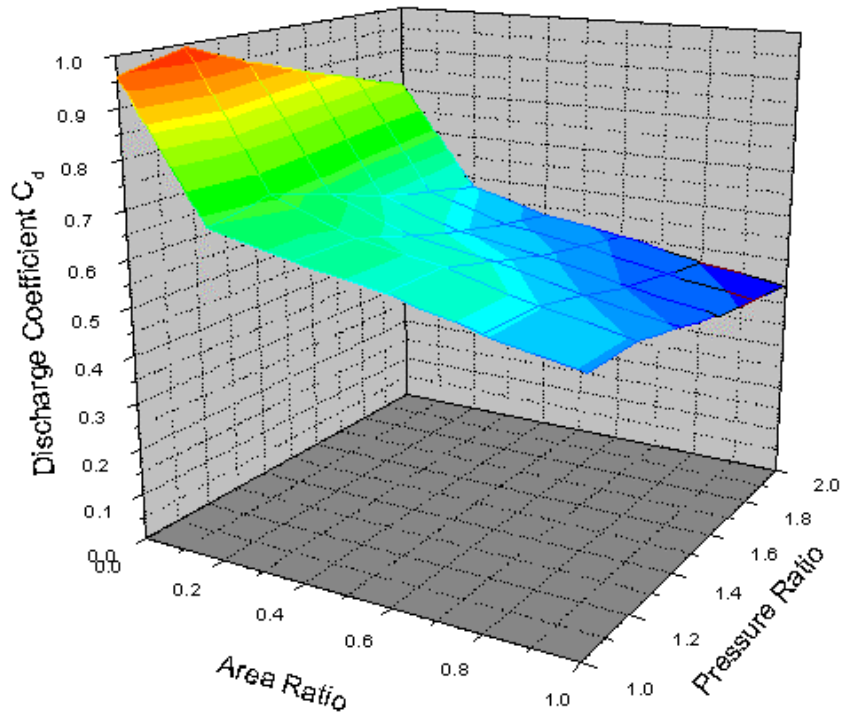


Figure 5-53. Model Generated Intake Discharge Coefficients

5.1.5 COMPUTATIONAL MODELING

Computational modeling was conducted first to help quantify the causes of the compression pressure differences between the cylinders and second to provide a tool for conceptual manifold design. The computational modeling was performed with software purchased on this project from Optimum Power Technology. The particular software package is titled Automated Design with Virtual 2-Stroke[®]. This software is written specifically for modeling of two-stroke engines and is a one-dimensional cycle-simulation model that focuses on the fluid dynamics in an internal combustion engine. Prior to conducting simulations of the GMVH engine, a significant effort was expended with workstation configuration, new software training, and working with Optimum Power Technology to get needed revisions for large-bore integral engine simulation (i.e., addition of direct fuel admission feature).

A model of the GMVH was initially configured with mean dimensions derived from drawings provided by Cooper Compression as well as external physical measurements made on the engine. Data was also provided by Cooper Compression to develop compressor and turbine maps for the turbocharger model installed on this engine. Later in the project, the dimensional data acquired during disassembly was used to refine the model in which several assumptions and nominal values had been initially programmed. It was not until detailed geometry, derived during engine disassembly, was incorporated into the model that satisfactory simulation of the engine was achieved.

5.1.5.1 Model Validation

The model validation was a difficult yet significant task. The model must accurately simulate the dynamic flows, pressures, and temperatures of the real engine so that a realistic manifold design can be performed. To construct a detailed model of the GMVH-6 engine from scratch, several items were required to be defined for construction. These items were as follows:

- Turbocharger compressor and turbine maps
- All inlet air system components – pipes, intercoolers, junctions, and transitions
- All exhaust system components – pipes, waste-gate, junctions, and transitions
- Port geometry, discharge coefficient, and timings
- Scavenging – efficiency versus scavenging ratio
- Cylinder volume and piston motion
- Fuel admission – timing, rate, and total mass per cycle
- Combustion – timing and rate of heat release
- Heat transfer – coefficients for cylinders, block, and manifolds
- Operating conditions – speed, percent waste-gate, and ambient conditions

Once the model was constructed, several iterations were performed to compare simulation results to measured parameters. Several parameters in the above list were not known precisely, such as the heat transfer coefficients and required tuning based on comparison to measurements. An extensive effort was expended at this stage of the project attempting to achieve correlation with engine measurements.

As discussed previously, mean drawing dimensions were used in initial model construction, and the base air chest was not known to be an active feature of the inlet air system. Correlation, therefore, could not be achieved to a satisfactory level, and at this time, it was decided to conduct the geometric analysis and port flow testing. Plots showing the best initial simulation results to measured data are provided in Figure 5-54 through Figure 5-56. A comparison of cylinder pressure from one cylinder is provided in Figure 5-54 where discrepancies can be seen in the compression pressure and blowdown regions. Figure 5-55 shows a comparison of the dynamic intake manifold pressure where higher pulsation amplitude was predicted in the simulation and the phasing of pulses does not match measured data. The dynamic exhaust runner pressure comparison is shown in Figure 5-56, which shows slightly higher pulsation amplitude and a lower mean value but better matching of the phasing.

Results of the geometric analysis and port flow testing were analyzed and incorporated into the GMVH-6 model. The base air chest geometry was also added to the model. A second iteration of tuning heat transfer and flow coefficients in various junctions was then performed. Simulation results now matched measurements much closer and to a level felt satisfactory to deem validation complete. A comparison of the cylinder pressure match with revised geometry is shown in Figure 5-57. Comparisons of the inlet and exhaust runner dynamic pressures, as well as cylinder pressure, are shown in Figure 5-58. The simulated inlet and exhaust pressures are shown in Figure 5-58 to now match very well in both amplitude and phasing of the pulsations. Although cylinder pressure looks very well matched in Figure 5-57, the close-up view of cylinder pressure in the range of scavenging pressures shows some discrepancy between the start to finish of the scavenging event. It was believed that this discrepancy was due to thermal shock of the non-water cooled transducers used for cylinder pressure measurement.

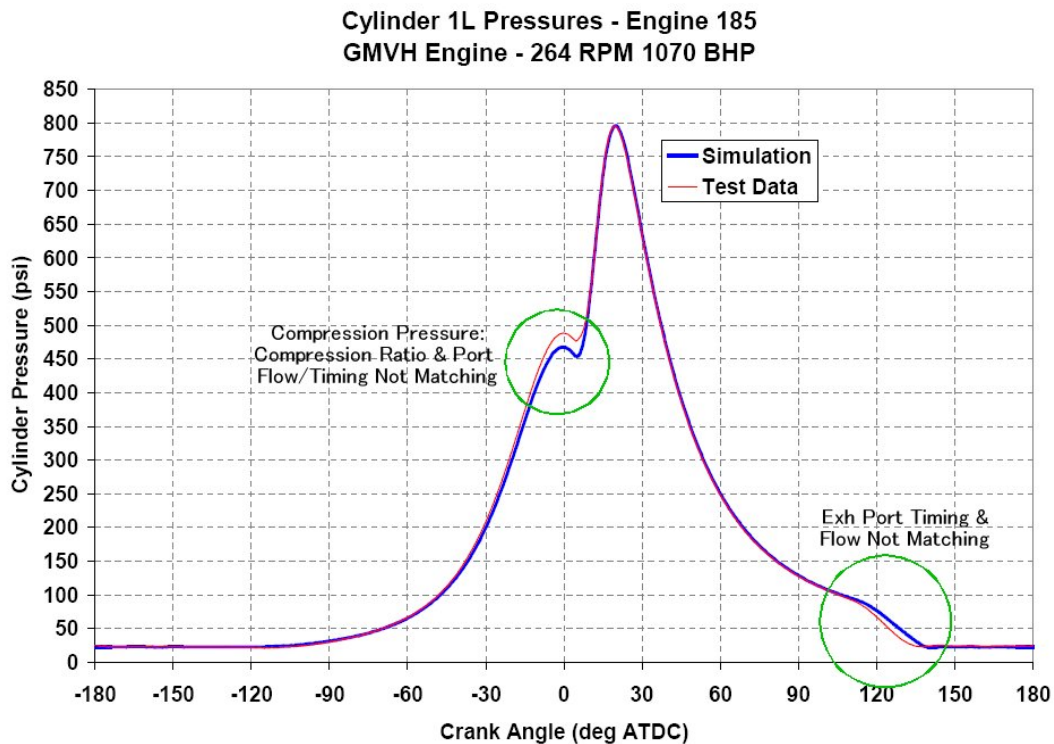


Figure 5-54. Initial Simulation to Measurement Comparison – Cylinder 1L Pressure

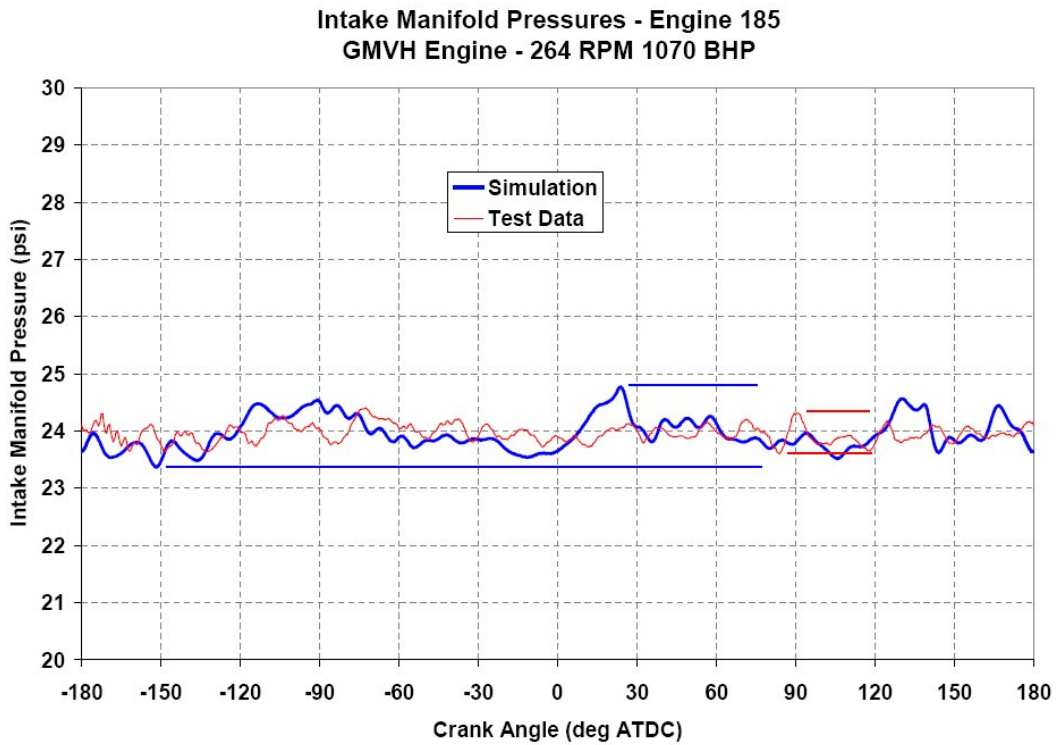


Figure 5-55. Initial Simulation to Measurement Comparison – Intake Manifold Pressure

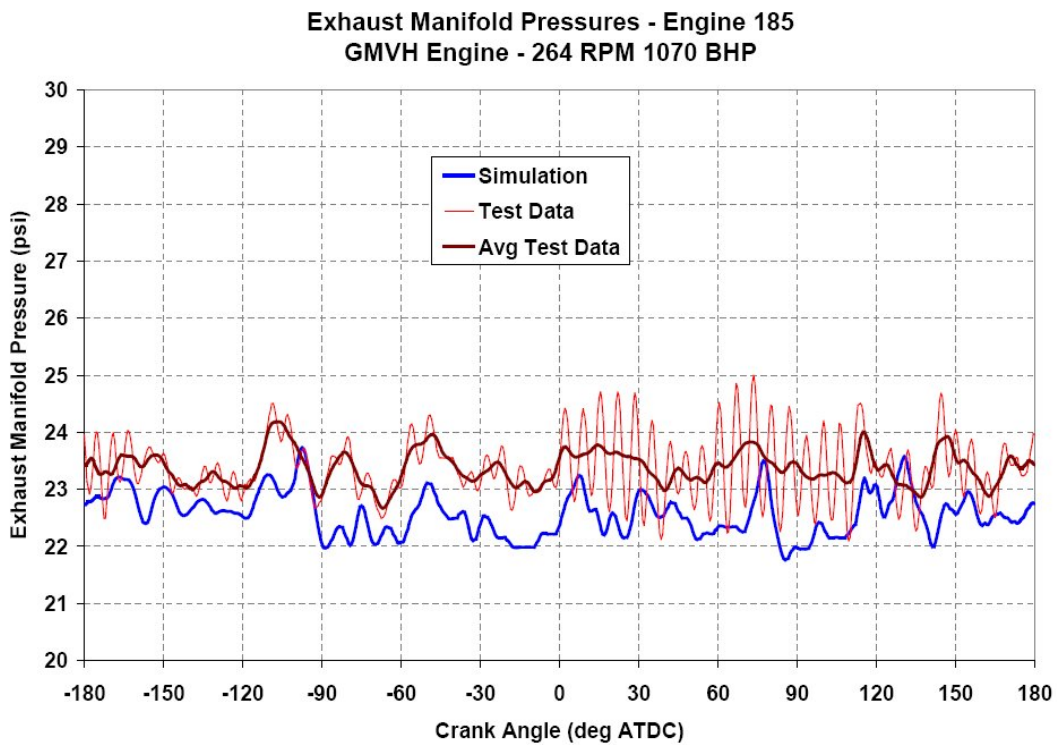


Figure 5-56. Initial Simulation to Measurement Comparison – Exhaust Manifold Pressure

**Cylinder and Manifold Pressures - Run 922
GMVH Engine - 330 RPM 1389 BHP**

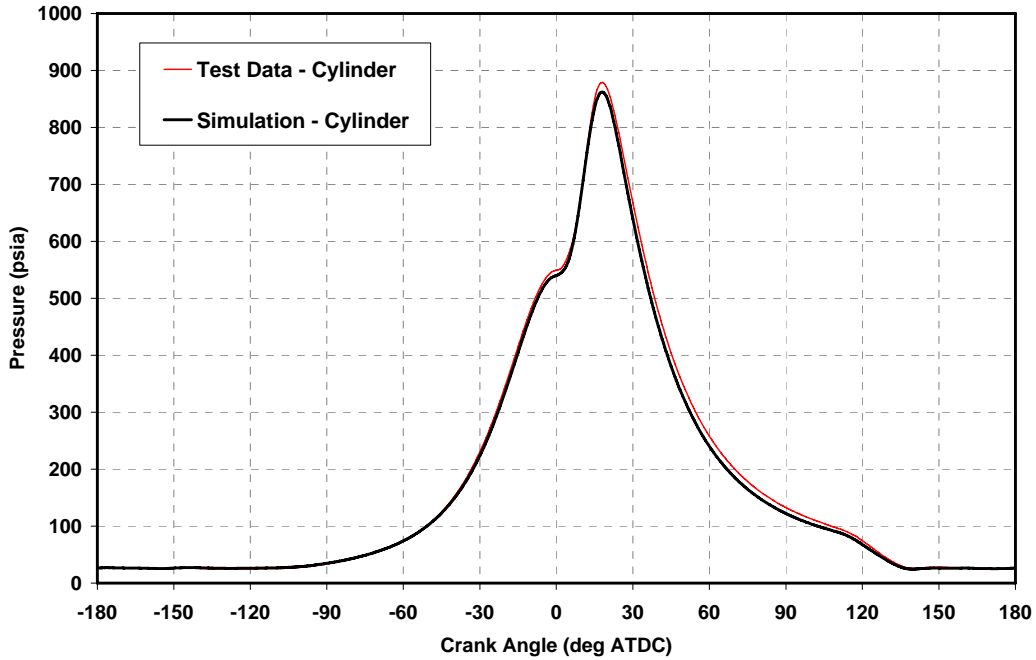


Figure 5-57. Revised Simulation to Measurement Comparison – Cylinder Pressure

**Cylinder and Manifold Pressures - Run 922
GMVH Engine - 330 RPM 1389 BHP**

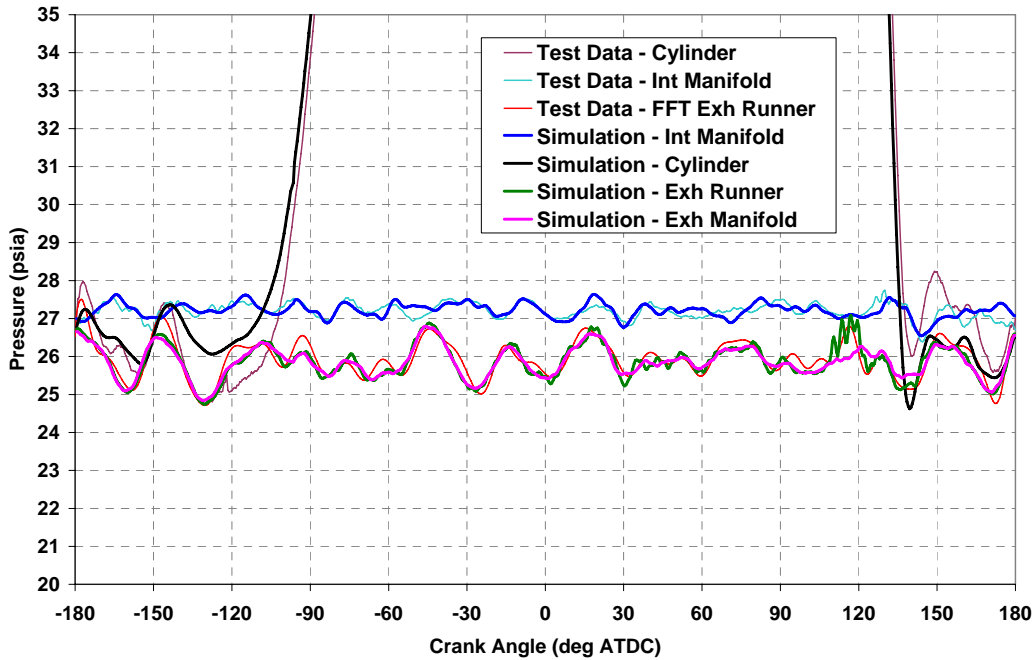


Figure 5-58. Revised Simulation to Measurement Comparison – Inlet, Exhaust, and Cylinder Pressure

5.1.5.2 Identical Cylinder Model

With the model validation achieved, the cylinder dimensional data was averaged to generate a model of the engine with identical cylinders. The identical cylinder model was validated to measurements of Cylinder 1L and used for investigation into manifold design and flow effects without the influence of geometric differences. The premise was that if the identical cylinder model showed similar variations in compression pressure, then the model would provide insight into the causes and could then be used to design manifold solutions. It was reasoned that mean geometric values should be used because the variation in actual geometric values was expected to be random among cylinders in field engines and may range more or less than those measured on the subject GMVH-6. Cylinder geometric variations exist due to manufacturing tolerances and may be more pronounced in field engines due to part mismatch. Therefore, the first analysis sought to investigate manifold effects with identical cylinders in the model to isolate their contribution to imbalance.

The correlation to performance in Cylinder 1L was very good. However, this identical cylinder model did not predict the spread in compression pressures and showed only expected differences from bank-to-bank due to articulation and its effect of port timing. There was no indication from this model that the original manifold designs on the six-cylinder engine, or dynamic flows with these designs, were causing any effect on compression pressure or trapped mass on a given bank. The Cylinder 1L to Cylinder 3L variation in the data was not observed in the simulation. Figure 5-59 shows the compression pressure at TDC from the identical cylinder simulation and corresponding engine measurements. Therefore, the initial conclusion was there is minimal manifold effect on breathing and that the geometric variations were dominating the variations seen in the data.

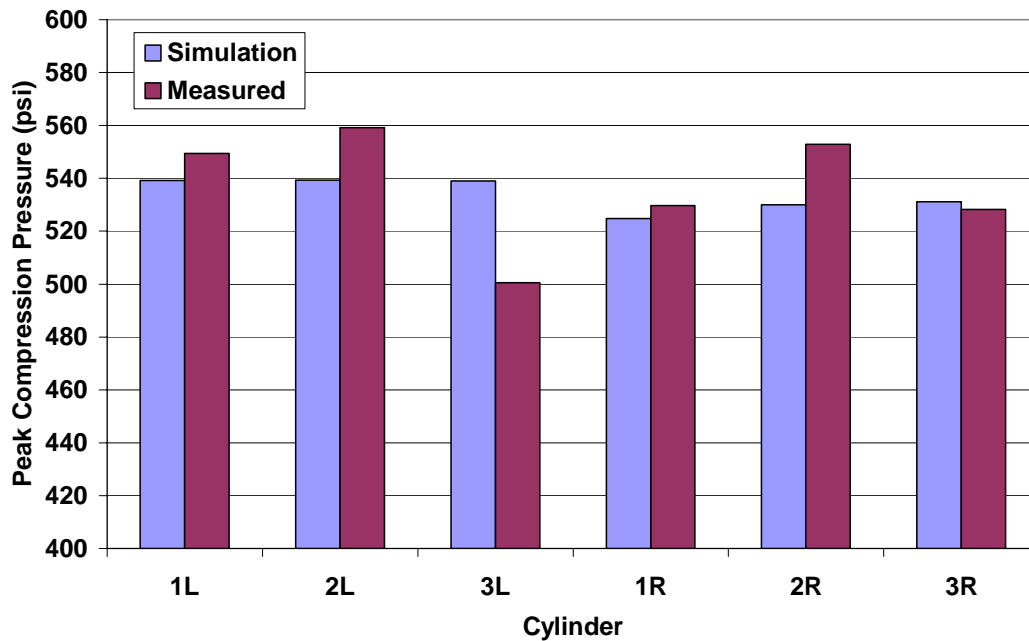


Figure 5-59. Identical Cylinder Simulation to Measurement Comparison – Cylinder Compression Pressure at TDC

5.1.5.3 Geometric Value Sensitivity Study

Recall from Figure 5-9 that a difference of approximately 11% exists between Cylinders 1L and 3L in measured compression pressures. To help quantify the contribution of geometric variation to this spread, a second version of the model was constructed to perform sensitivity studies of the significant geometric factors that may affect imbalance in either flow or compression pressure. The range of values used in the study simulated the minimum-maximum values measured during the geometric analysis.

The first parameters to be swept were intake and exhaust port opening heights (i.e., port timing), and the results are shown in Figure 5-60. The effect on compression pressure due to changes in intake port opening height was negligible. The effect on compression pressure due to changes in exhaust port opening height showed an approximate 2% change. A positive increase of 0.150” in exhaust port opening height represents a 1 to 2 degree later closing of the port, matching the difference from Cylinder 3L. The predicted change in compression pressure was approximately 2% with the full change in exhaust port opening height.

The next set of parameters swept with the model was the intake and exhaust port discharge coefficients. Figure 5-61 shows the results of a $\pm 10\%$ variation from nominal in the discharge coefficients. The predicted change in compression pressure from the minimum to maximum range simulated was approximately 0.6% for the intake and 1.1% for the exhaust. This range of effect was lower than expected with such a large variation in discharge coefficient.

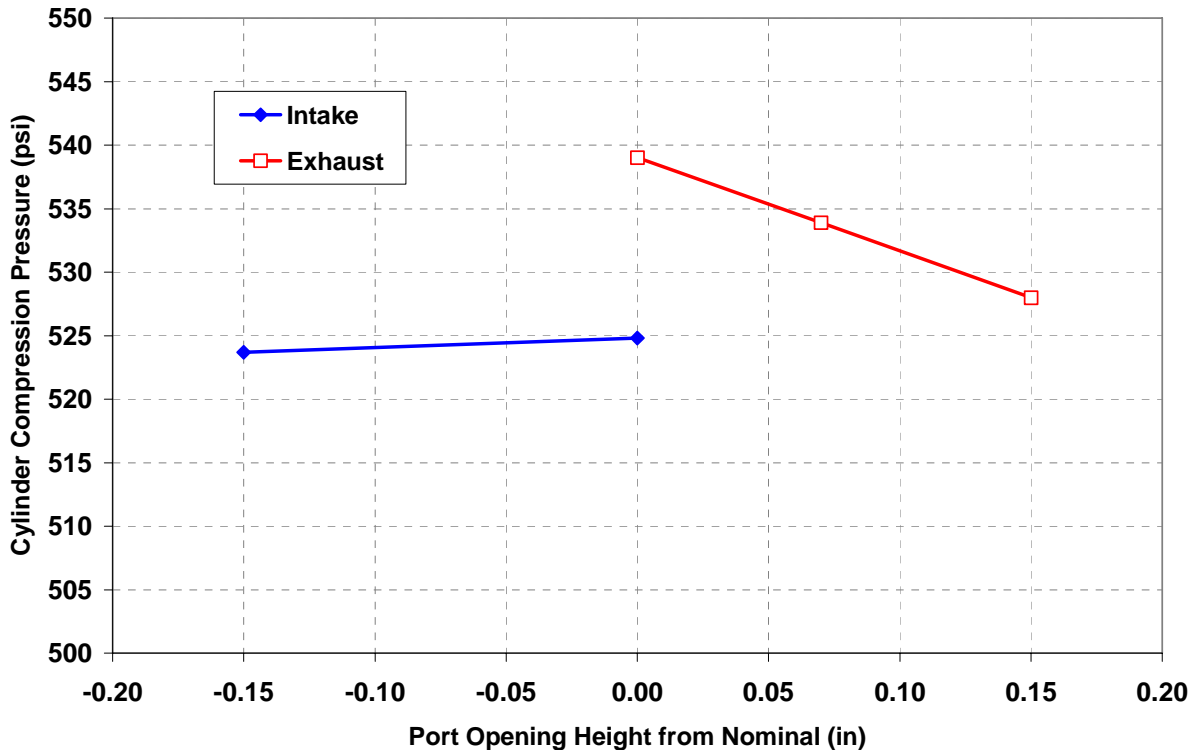


Figure 5-60. Simulation Predictions of Compression Pressure with Variation in Port Opening Height (Timing)

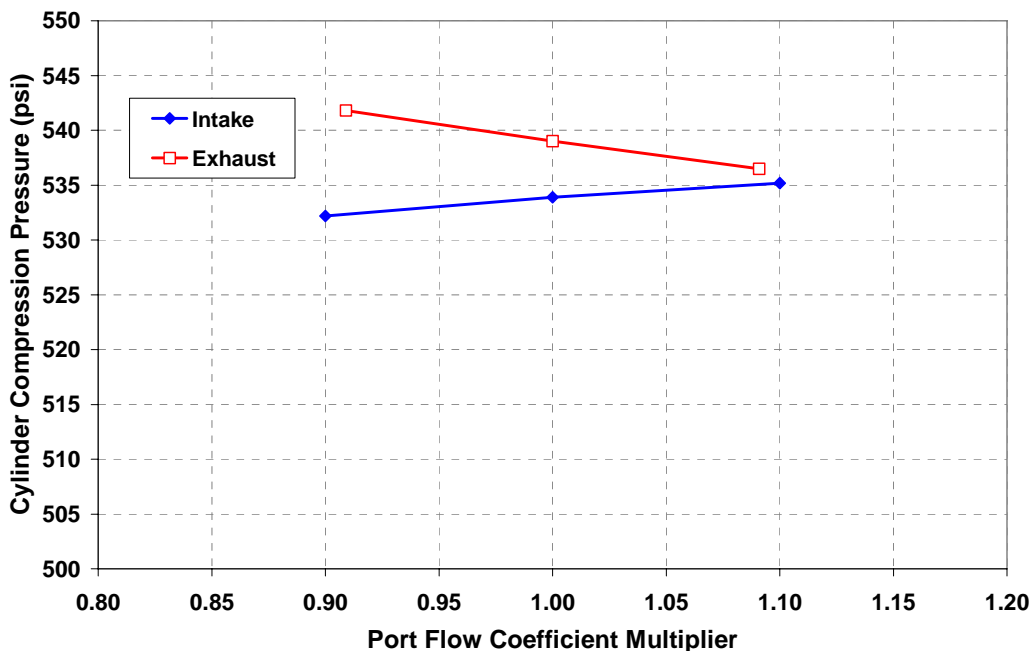


Figure 5-61. Simulation Predictions of Compression Pressure with Variation in Port Discharge Coefficient

The last parameter swept with the model was compression ratio. This was varied by changing the TDC clearance volume. Figure 5-62 shows the mechanical compression ratio (BDC to TDC swept volume) effect on compression pressure. The predicted change to compression pressure for 0.4-point change in compression ratio is 4.3%, which clearly is the dominant effect on compression pressure. This magnitude of change in compression pressure as a function of compression ratio was expected, and given the lesser effects from the previous parameters, this implies that using compression pressure as an indicator for trapped mass is not very accurate.

The results of the model sensitivity study showed that geometric effects do account for a significant portion of the spread seen in the compression pressure. However, a summation of the simulated effects on compression pressure by the geometric variations matching those measured, only accounted for about 6% of the 10% difference between Cylinders 1L and 3L. There is still approximately 4% of 1L-3L compression pressure spread unaccounted for. This discrepancy in accountability and experience with other field engines, where operation and data indicate variations in cylinder-to-cylinder air/fuel ratio, leads to the belief that there is still a breathing issue and likely related to the manifold designs. The Virtual 2-Stoke[®] program is a one-dimensional model, as is most other popular engine simulation models. One-dimensional models are very accurate with flow paths featuring relatively long lengths and small diameters. The GMVH engine, on the other hand, features flow path geometry consisting of large volumes and diameters with relatively short lengths. SwRI engineers suspect that the flow dynamics may not have been predicted accurately in certain regions of the system, and that three-dimensional modeling may be required for complex junctions and/or transitions. The Virtual 2-Stoke[®] program can be coupled to several available three-dimensional software packages. However, time and budget constraints prevented further investigation into this scenario.

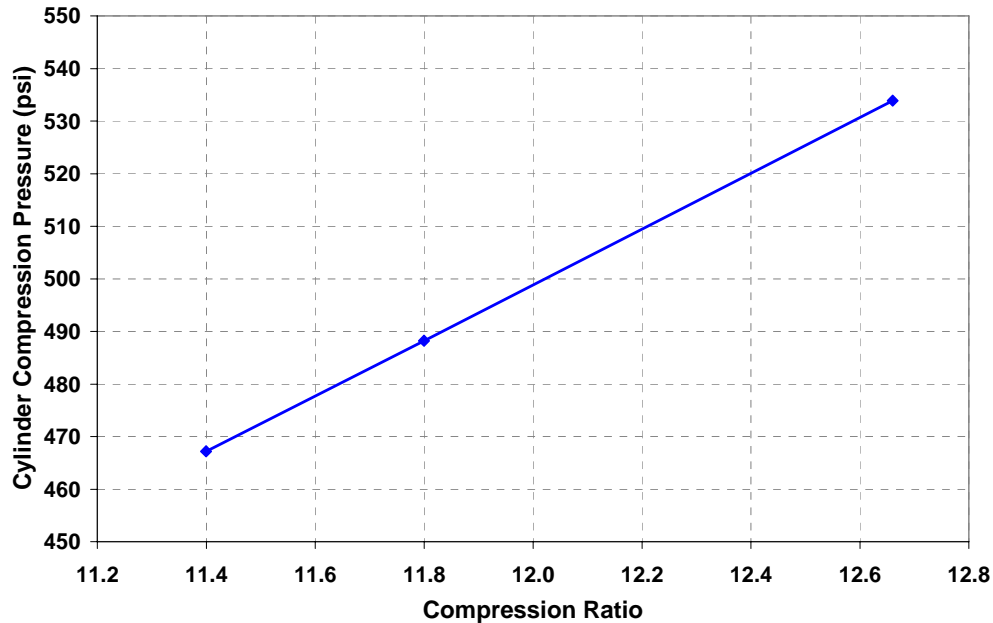


Figure 5-62. Simulation Predictions of Compression Pressure with Variation in Compression Ratio

5.1.6 GMVH-6 COMPONENT SWAP TESTING

Upon completion of the geometric analysis, the engine was re-assembled. Power assemblies (cylinder, piston, rings, and connecting rod) were switched between Cylinders 1L and 3L during reassembly to allow for quantification of the geometric variation effects on compression pressure. Cylinder 3L had the second lowest effective compression ratio and Cylinder 1L had the highest. Cylinder 3L also had two of the five exhaust ports out of specification yielding a slight (1 to 1.5 degree) difference in port timing. In addition, Cylinder 3L showed to have a slightly lower inlet discharge coefficient at low port opening positions. These cylinders were also on the same bank, which would avoid articulation effects complicating the comparison of pre- and post-switch data. As mentioned previously, the different casting number cylinder on 1R was replaced during reassembly with a matching cylinder. This replacement also provided pre- and post-test data to investigate the effects of the low exhaust port discharge coefficient due to differing port shape. Prior analysis has shown that the geometric differences (compression ratio, port timing, and port flow coefficient) could account for as much as 50% to 60% of the difference in measured spread of compression pressure.

The engine was operated over a range of speeds and loads to generate curves similar to those in Figure 5-9. This new data with the swapped power assemblies is shown in Figure 5-63. The compression pressures from Cylinder 1L are lower as expected. However, the compression pressures from Cylinder 3L increased only marginally. To better illustrate the effect on compression pressure from the component swap, compression pressure data from each cylinder at an air manifold pressure of 20 inHg is plotted in Figure 5-64. This plot shows that the compression pressure for Cylinder 1L was reduced by approximately 5%, while the compression pressure for Cylinder 3L increased approximately 1%. The change for Cylinder 1R with the replacement cylinder was less than 1%, as seen in Figure 5-64.

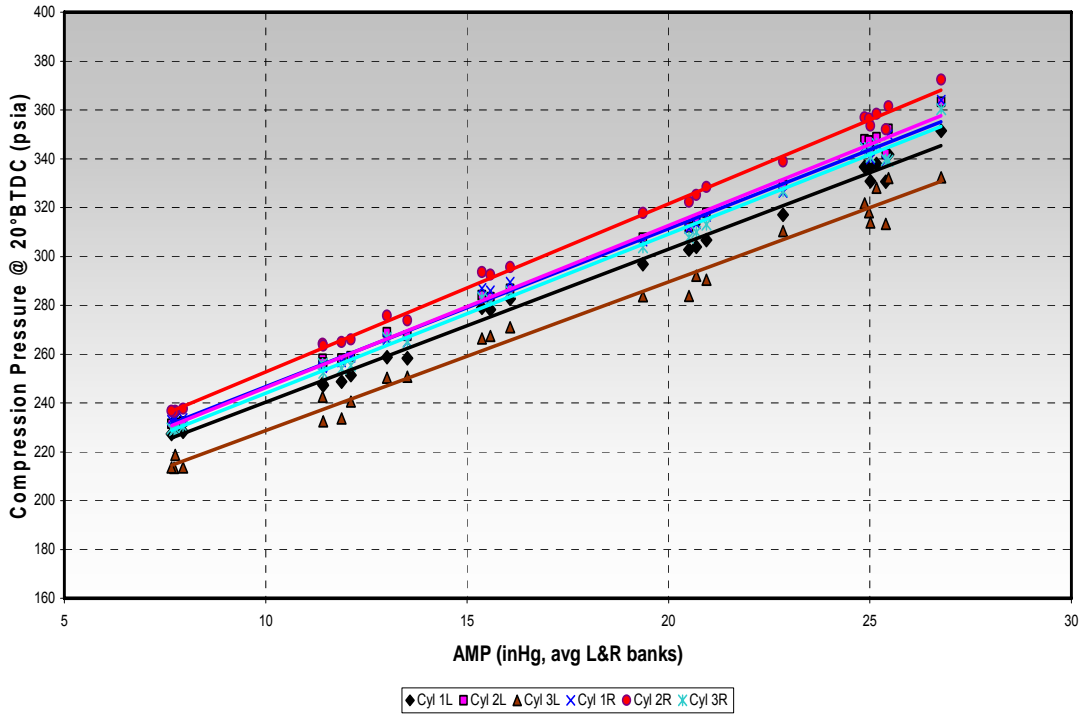


Figure 5-63. 100-Cycle Average Cylinder Pressures at 20 Degrees BTDC versus Air Manifold Pressure – Post Power Assembly Swap

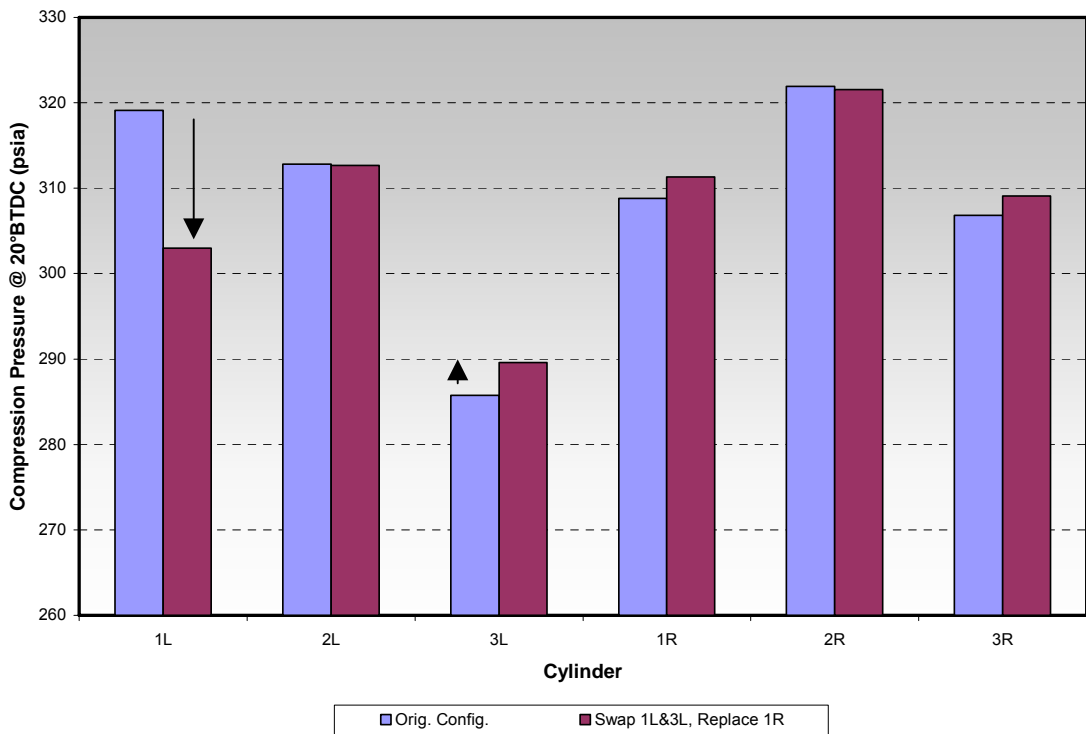


Figure 5-64. Cylinder Pressures at 20 Degrees BTDC for Air Manifold Pressure of 20 inHg – Before and After Power Assembly Swap

The trends are as confusing as they are helpful. The effect on Cylinder 1L was closer to expectations, but the minimal change to Cylinder 3L was not as expected. There is apparently still some phenomenon causing Cylinder 3L to achieve the lower compression pressure. Further investigation of the data was conducted and discussed in subsequent sections of this report.

5.1.7 DETAILED ANALYSIS OF CYLINDER PRESSURE DATA

Several tests were performed to ensure data integrity, and pressure-volume data was analyzed to investigate the causes of the spread in compression pressure. The cylinder pressure measurements taken on the laboratory GMVH-6 were acquired with Kistler 6053 piezo-electric sensors. The cylinder pressure sensors were all flush mounted in the cylinders through plugs modified for insertion through the air start valve ports in the cylinder head. The piezo-electric sensors are not absolute sensors, but instead measure the relative change in pressure. To get the data into absolute pressure, reference absolute pressure sensors were used to “peg” the cylinder pressure data. The reference sensors were installed in each exhaust runner and the exhaust pressure, averaged from BDC + 4 crank angle degrees, became the pegging pressure. This referencing method assumes the cylinder pressure equals the exhaust pressure within this window.

5.1.7.1 Sensor Calibration and Repeatability

Sensors were calibrated frequently, replaced, and switched to ensure accurate readings. The calibration history of the cylinder pressure sensors has shown repeatability within 1% since initial installation. The calibration history of the reference pressure sensors has shown repeatability within 1.5% since initial installation. To ensure that no cylinder specific effects (i.e., installation, thermal, etc.) are skewing the cylinder pressure measurements, the sensors and charge amplifiers were switched between Cylinders 1L and 3L. The data acquired before and after transducer swaps showed results within $\pm 1.5\%$, which fell within calibration repeatability limits. Therefore, cylinder pressure sensor calibration and repeatability could account for as much as 1% to 1.5% of the full-scale pressure, which equates to approximately 5% of the compression pressure spread.

5.1.7.2 Sensor Thermal Shock

The next investigation regarding the cylinder pressure sensors was to determine if the non-cooled 6053 sensors were experiencing significant thermal shock after combustion. Thermal shock is the change in output due to extreme temperature changes that cause variance in the Young’s modulus and resonant frequency of the quartz crystal, and cause expansion/contraction of the diaphragm [17]. Modern piezo-electric sensors are much improved over previous designs in terms of thermal shock. One way to qualify the extent of thermal shock experienced in the GMVH-6 data was to compare the measured data to simulated data. A comparison of the measured (100-cycle average) cylinder pressure from Cylinder 1L to simulation is provided in Figure 5-65. The arrows denote the variation after blowdown and prior to port closure. The variation is negative on the compression side and positive on the expansion side. This variation would, therefore, suggest there is some thermal shock affecting the measured data. Comparison of data from the remaining cylinders showed, fortunately, that the thermal effect was consistent among the cylinders and relative comparisons of measured cylinder data was unaffected.

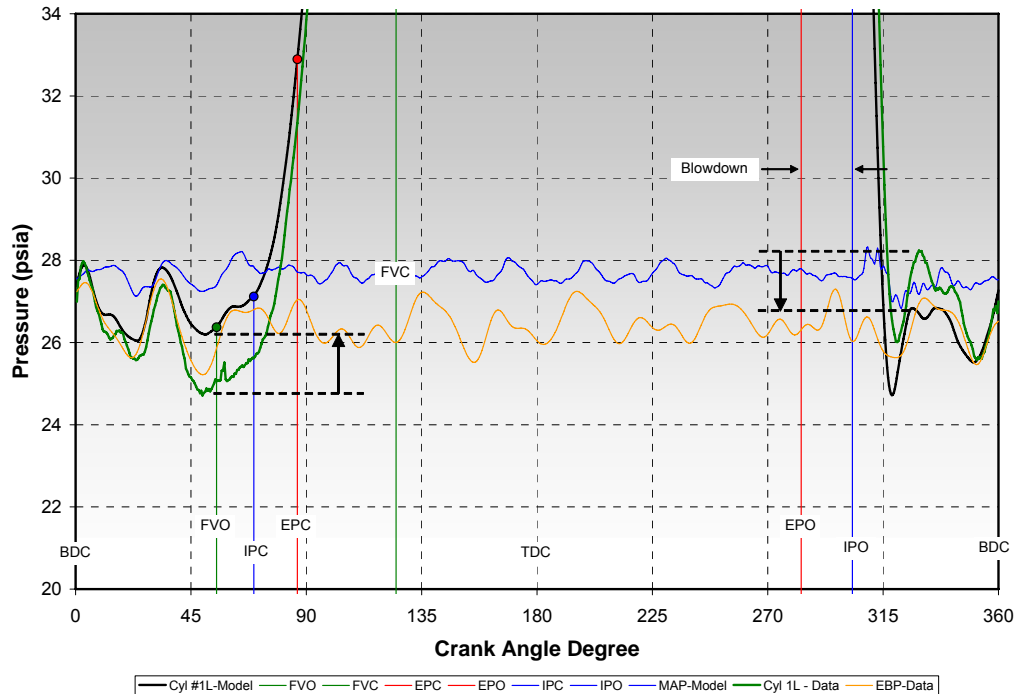


Figure 5-65. Measured and Simulated Cylinder Pressure for Cylinder 1L Showing Effects of Thermal Shock

Since thermal shock has been indicated with the non-cooled sensors used for all of the data acquisition, a brief test with water-cooled Kistler 6061B transducers was conducted. The purpose of this test was to quantify the thermal effect on the 6053 sensors and determine if the pegging procedure was optimum. The 6061B sensor was installed in Cylinder 1L. Since only one 6061B sensor was available at the time of this test, an older 6061 sensor was installed in Cylinder 3L. Both sensors were calibrated with a dead-weight tester prior to installation. The data appeared good during testing. However, post-processing of the data showed a non-linear skew of the pressure-volume relationship, which made this data un-useable. The cause of this skew had been reduced to be either faulty cables or insufficient cooling flow. Unfortunately, correction of the problem and retesting could not be performed within the project schedule. Further testing will be conducted in follow-on projects.

5.1.7.3 Analysis of Pressure Data

The metric used initially to indicate an air balance problem was the spread in compression pressure prior to ignition and combustion. This metric is not completely reliable as geometric effects, such as compression ratio, or TDC clearance volume, can affect the compression spread even if trapped mass is equal. A better empirical method for investigating the differences in trapped mass is to utilize the PV diagram. The PV diagram includes effects of geometry in the form of cylinder volume versus crank angle degree. By plotting the PV data on a logarithmic scale, several effects can be distinguished.

The logP-logV diagrams from the GMVH-6 engine have consistently shown a “dip” in the region between intake port closing (IPC) to fuel valve closing (FVC) in all cylinders except 3L. This dip is illustrated in Figure 5-66 and Figure 5-67, which show the logP-logV diagrams

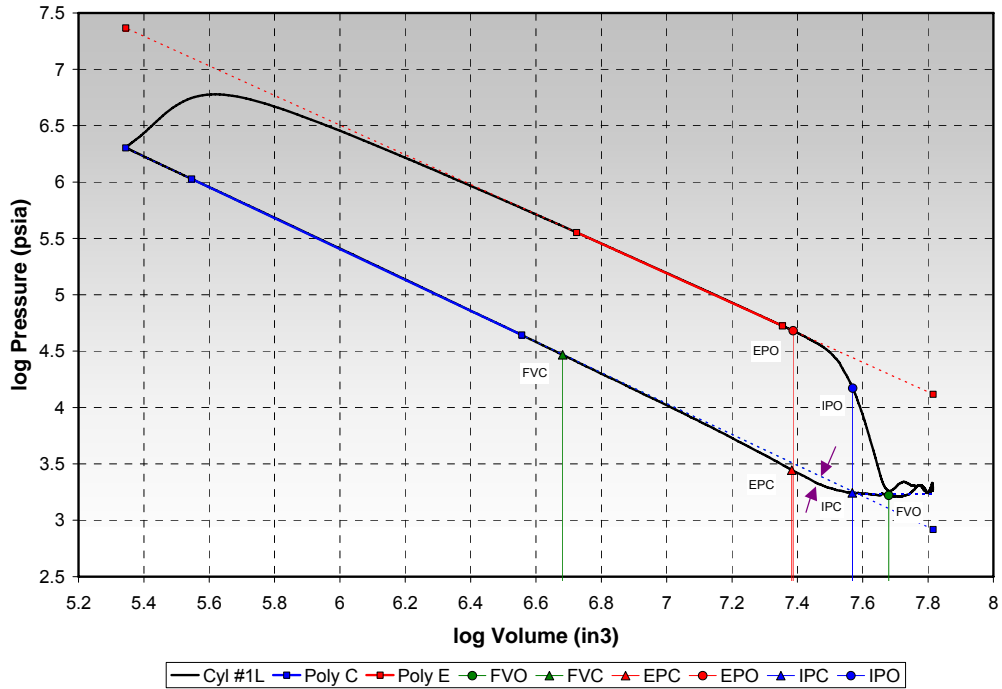


Figure 5-66. logP-logV Diagram for Cylinder 1L Showing “Dip” in Initial Compression

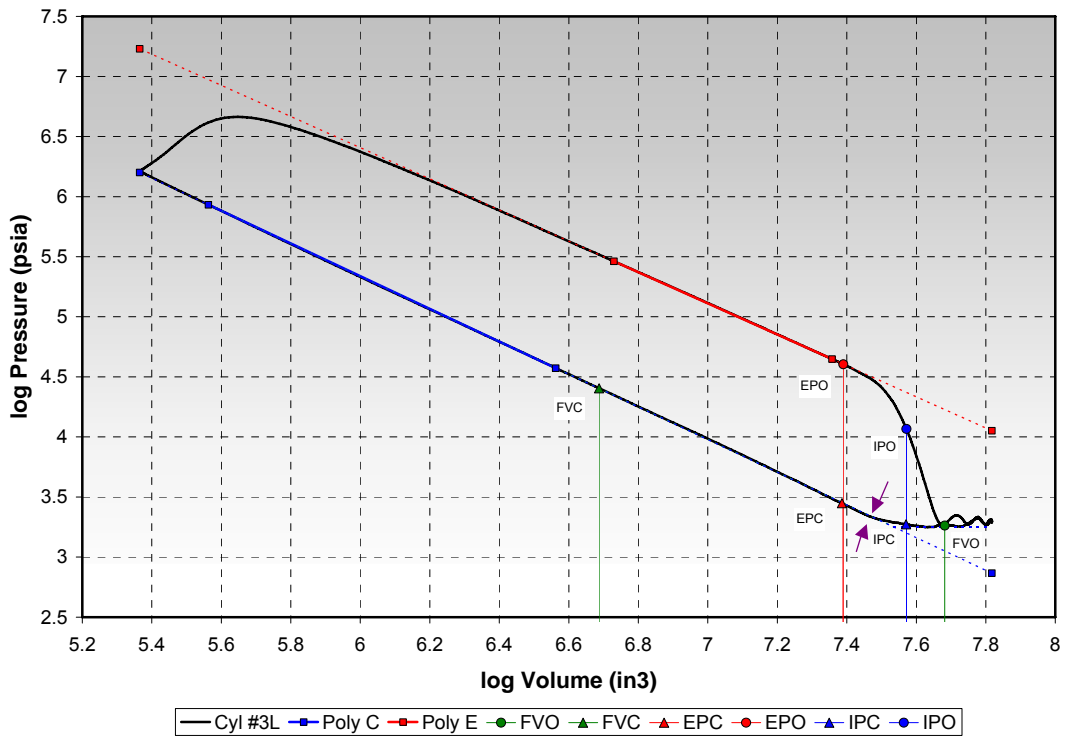


Figure 5-67. logP-logV Diagram for Cylinder 3L Showing No “Dip” in Initial Compression

for Cylinders 1L and 3L, respectively. The data in these figures are from 100-cycle averaged cylinder pressure recordings and calculated cylinder volume using dimensions derived in the geometric analysis. The dotted line on the compression stroke, where the dip is denoted by arrows, is an extension of the slope fit through the data points after FVC. The slope of this line is the polytropic compression coefficient. The logP-logV diagrams show that the polytropic compression and expansion relationship holds true for this engine, as it does for other reciprocating piston engines. The polytropic equation is shown below in Equation 1 and the derivation of the polytropic coefficient is given in Equation 2.

$$PV^n = \text{Constant} \tag{1}$$

$$n = -\frac{(\log(P_2) - \log(P_1))}{(\log(V_2) - \log(V_1))} \tag{2}$$

The “dip” illustrated in Figure 5-66 occurs between IPC and FVC where the cylinder mass is changing. Some of the cylinder mass is pushed into the exhaust until exhaust port closure (EPC) is reached, and fuel mass is being added to the cylinder until FVC. The pressure rise between IPC and EPC is less for Cylinder 1L than for Cylinder 3L, suggesting that either more mass is being displaced into the exhaust for Cylinder 1L or more fuel mass is being added to Cylinder 3L within this region. After EPC, the pressure rise for Cylinder 1L increases above that measured in Cylinder 3L, suggesting that more fuel mass is being added within this region to Cylinder 1L than is to Cylinder 3L. The pressure rise is constant after FVC for both cylinders as shown in Figure 5-68, where the logP-logV diagrams are overlaid. At the beginning of the polytropic compression region, Cylinder 1L has a higher pressure than Cylinder 3L for the same cylinder volume. This higher pressure indicates a higher trapped mass for Cylinder 1L.

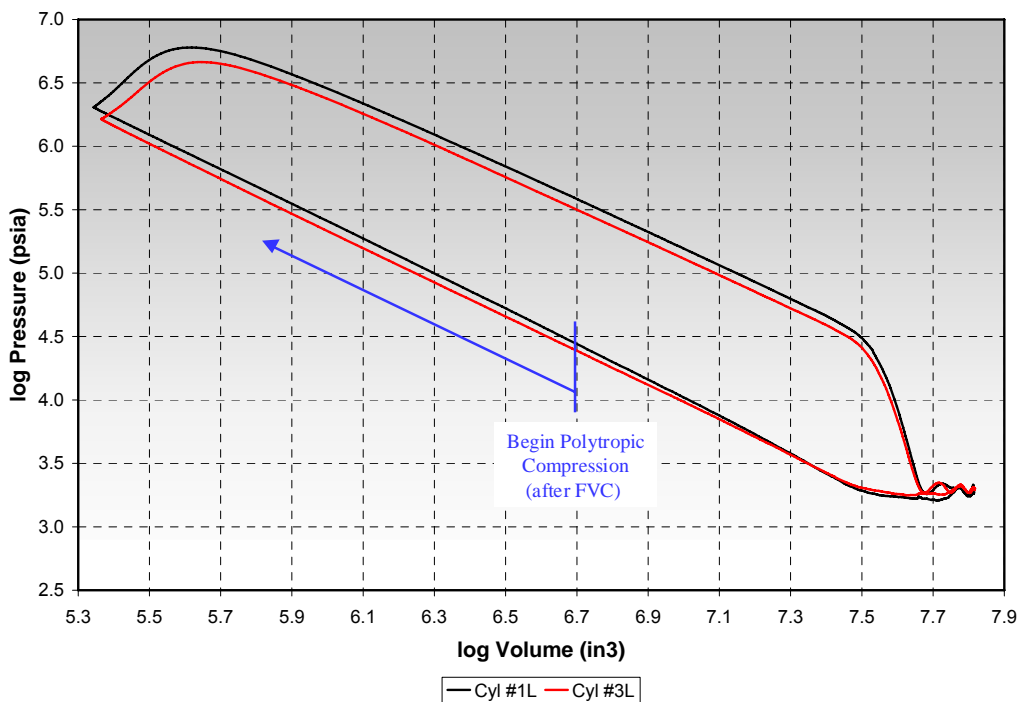


Figure 5-68. logP-logV Diagrams for Cylinders 1L and 3L Showing Effect of “Dip” on Resulting Compression Pressure

To fully quantify whether the effect is due to breathing or fueling rate differences, additional measurements must be performed. Measurement of the dynamic fuel valve pressure was, therefore, conducted and is discussed in the next section. Other factors that could affect the initial compression profiles include differences in heat transfer, blow-by, and initial mixture temperature.

5.1.8 INVESTIGATION OF FUEL VALVES AND FUELING RATE

The analysis of PV diagrams indicated that differences in fueling rate might be contributing to the spread in compression pressures initially blamed on perceived differences in breathing. The first test was to swap the fuel valves between Cylinders 1L and 3L. No change was made to the balance valves, and the engine was brought up to a repeat condition. The average cylinder pressure traces for all cylinders before and after the fuel valve swap are shown in Figure 5-69 and Figure 5-70, respectively. The engine was well balanced prior to the swap as shown in Figure 5-69. However, after the swap, Cylinder 3L experienced a drop in peak firing pressure and Cylinder 1L experienced a rise. This quick test indicated that the flow varied significantly between these fuel valves. Due to the significant rise in peak firing pressure for Cylinder 1L, the engine was not brought up to full rated conditions in fear that excessive detonation would occur. After acquiring the repeat data point, the balance valves were adjusted to bring these cylinders back in balance.

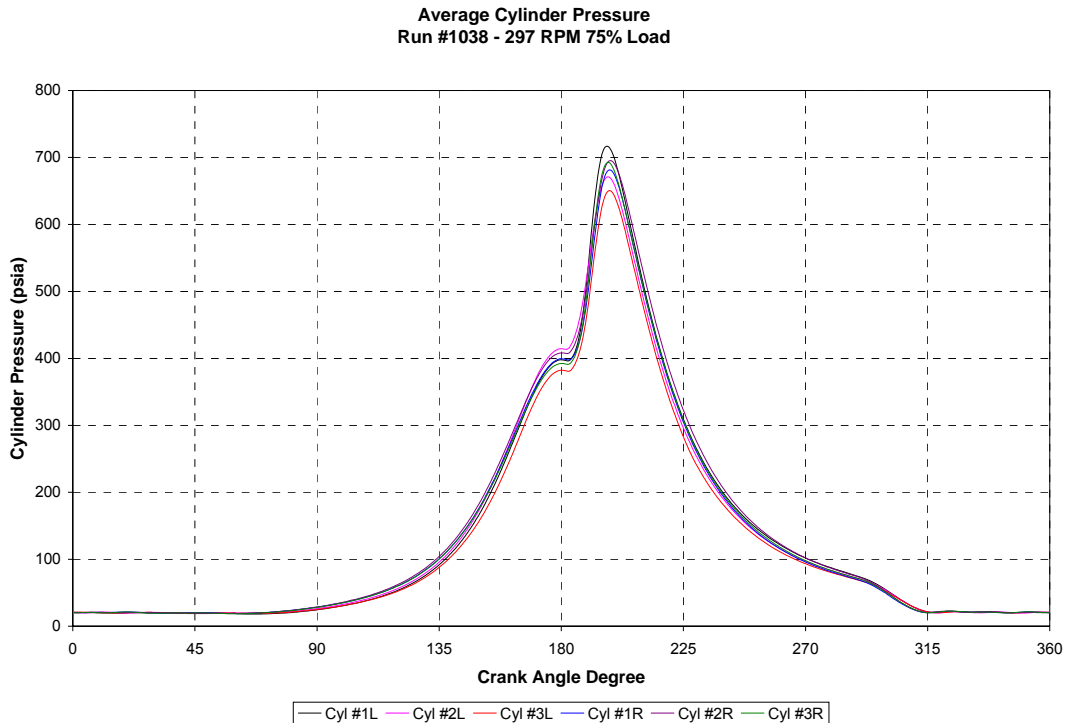


Figure 5-69. Cylinder Pressure for All Cylinders – Before 1L-3L Fuel Valve Swap

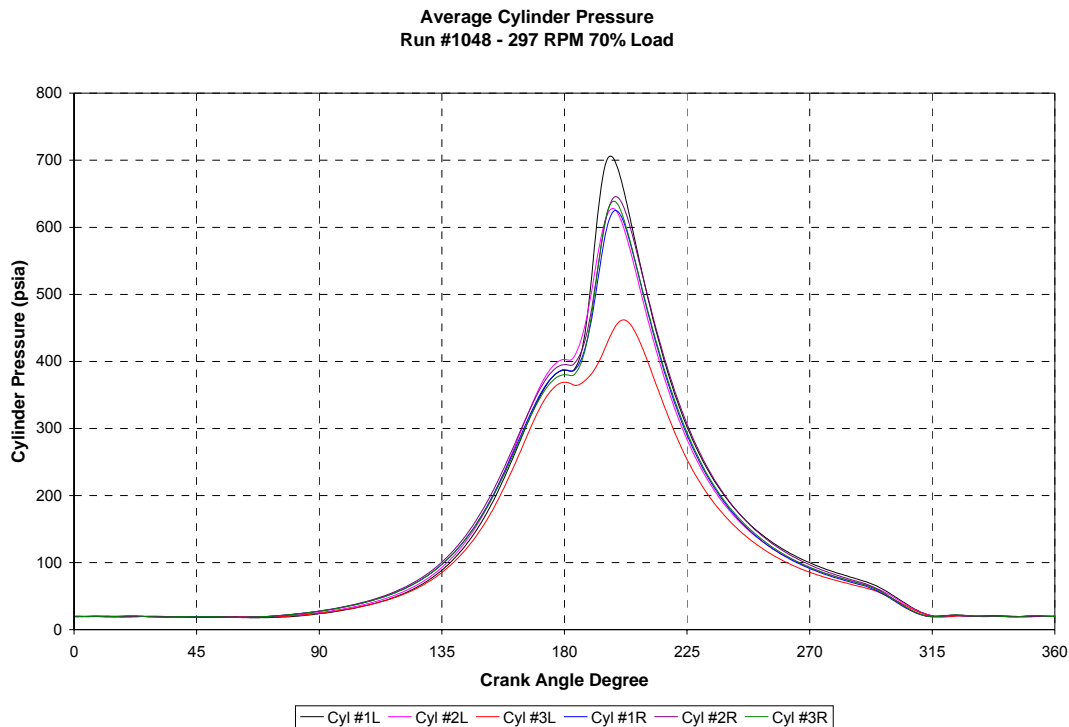


Figure 5-70. Cylinder Pressure for All Cylinders – After 1L-3L Fuel Valve Swap

After the quick test of swapping fuel valves, it was decided to measure the dynamic pressure in the fuel valves in Cylinders 1L and 3L. Dynamic pressure transducers were, therefore, installed in the supply elbow to the fuel valves in Cylinders 1L and 3L for investigation into potential fueling rate differences. The measurements under rated operating conditions are shown in Figure 5-71 and Figure 5-72 for Cylinders 1L and 3L, respectively. The dashed lines through the fuel pressure traces represent the mean value and the shading between the dynamic trace and mean value line was added between FVO and FVC to illustrate the pulsations occurring. The differences in the dynamic fuel valve pressures indicate that the fueling rates are slightly different. Flow testing of the fuel valves to develop discharge coefficients versus lift, and acquiring detailed dimensions to calculate the minimum areas versus lift is required to convert this pressure data into instantaneous flow data. The differences in dynamic pressures during the fueling event indicate that this system should be added to the engine simulation model for improved predictions. The differences in dynamic pressures also indicate that further research should be focused on the design of this system to determine if any improvements can be gained in terms of cylinder-to-cylinder fueling and fueling rate to better balance trapped air/fuel ratio.

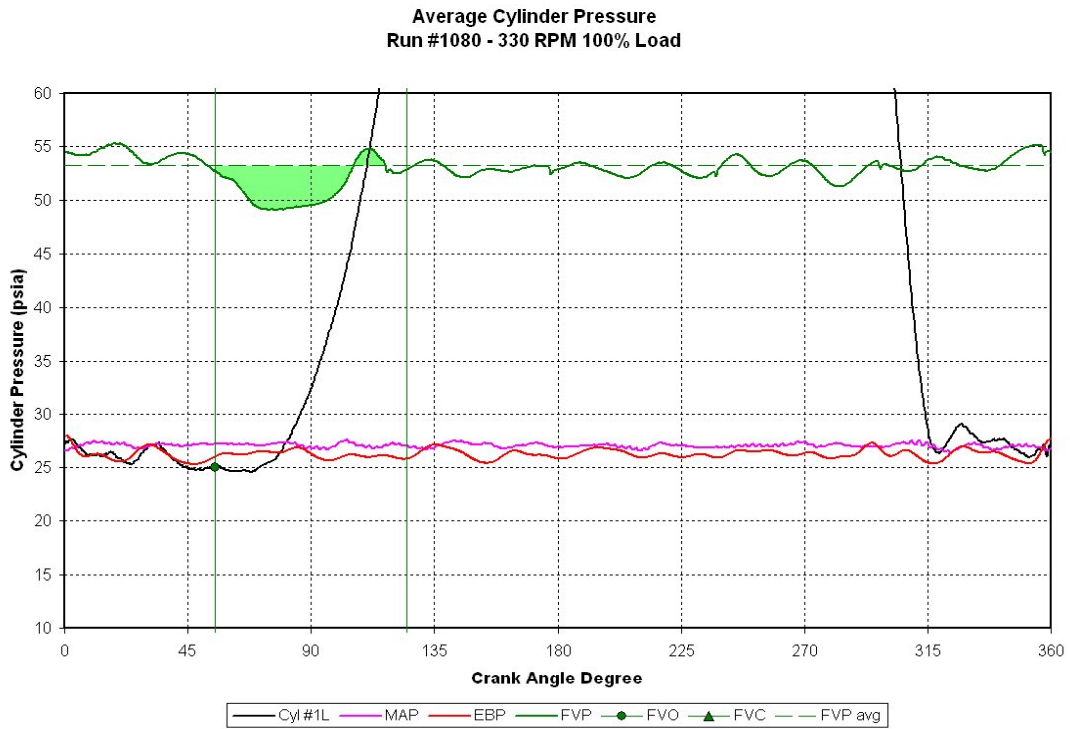


Figure 5-71. Cylinder Pressure and Fuel Valve Pressure for Cylinder 1L

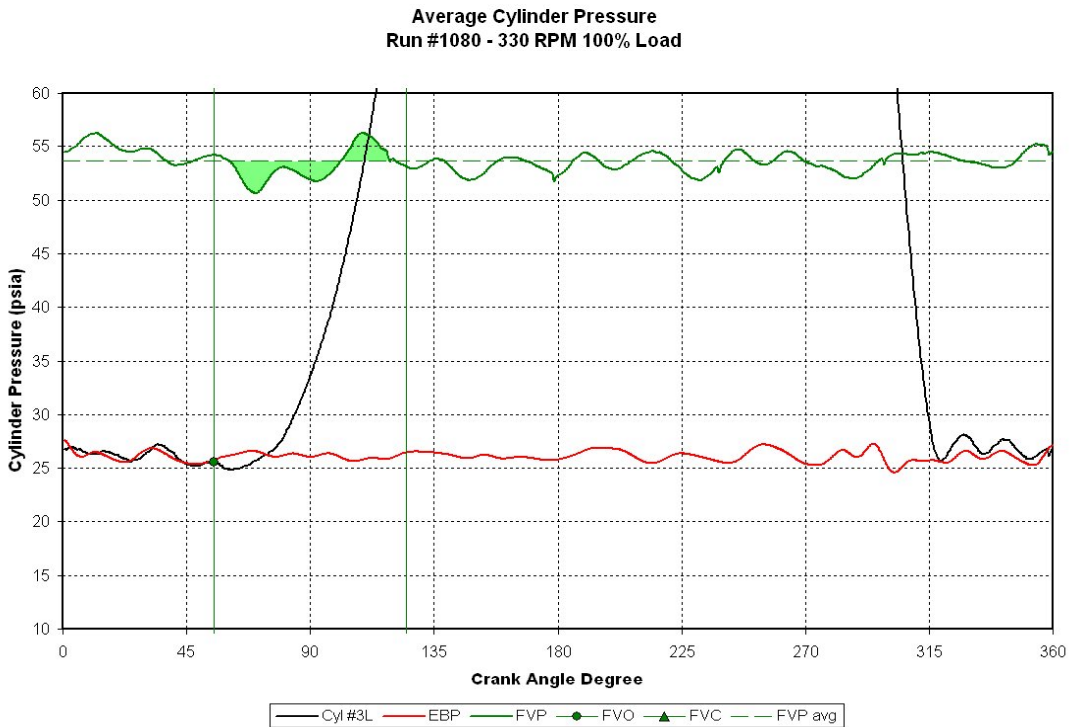


Figure 5-72. Cylinder Pressure and Fuel Valve Pressure for Cylinder 3L

5.2 CONCEPTUAL MANIFOLD DESIGNS

At the beginning of this program, it was anticipated that a new manifold(s) design would be developed to correct dynamic flow problems and balance the airflow and trapped mass between cylinders. This focus changed somewhat after testing, geometric analysis, and simulation. Simulation and geometric analysis results indicated that a large portion of the perceived air imbalance, as deduced from cylinder pressure data, was caused by geometric variation. However, there is still a discrepancy between test data and analysis that has yet to be explained and felt to be due to flow dynamics that could be caused by current manifold designs. It was also thought that different engine models might have worse and more obvious flow dynamic problems than the even firing GMVH-6. Therefore, developing a methodology for analysis and design is valuable even if the solution for the GMVH-6 is nominal.

The GMVH-6 features an even 60-degree firing interval, with each crankshaft throw coupled to a compressor. The exhaust manifold features a large diameter log, or plenum, connected to the cylinders at the bottom through runners. The exhaust manifold plenum features vertical support plates that effectively split the plenum at the runners and are slightly longer than the width of the exhaust runners with an open volume between the cylinder pairs. Therefore, the exhaust from each cylinder passes through the runners into individual volumes that merge into common volumes between cylinders and at the turbocharger turbine entrance. There are two intake manifolds, one for each bank, which are each comprised of a common log with rectangular runners to each cylinder airbox. The airbox in each cylinder is a volume that has connections to the intake runner, base air chest, and intake ports. The inlet air can pass through the airbox into either (or both) the base air chest or ports.

The exhaust ports are the last to close and the last to communicate with the combustion chamber during a cycle. Therefore, dynamics in the exhaust would seem to be more critical to scavenging than the intake side. Initial focus on conceptual manifold designs, therefore, focused on the exhaust. Though later, some of the focus switched to the intake side due to potential negative influences by having the intake manifolds and cylinder airboxes communicating through the base air chest. The resulting matrix of concepts for solution of the potential breathing issues involved a few different viewpoints on the solution. One viewpoint was that the concept should not only improve air balance but also provide improved performance. Another viewpoint was that the influence from one cylinder on another should be removed and each cylinder isolated. Yet another viewpoint was that if the original manifold designs are fine as they are, then develop retrofit concepts to mitigate the geometric influences. The original viewpoint was to design modifications or a new concept to mitigate flow imbalance and achieve equal breathing among cylinders. Designing devices to address a particular cylinder's geometric variation was thought to be too cumbersome and not pursued, as the variation would be random, not easily quantified without disassembly for measurement, and change when engine components are replaced. Thus, a series of concepts were developed and are shown in a flowchart in Figure 5-73.

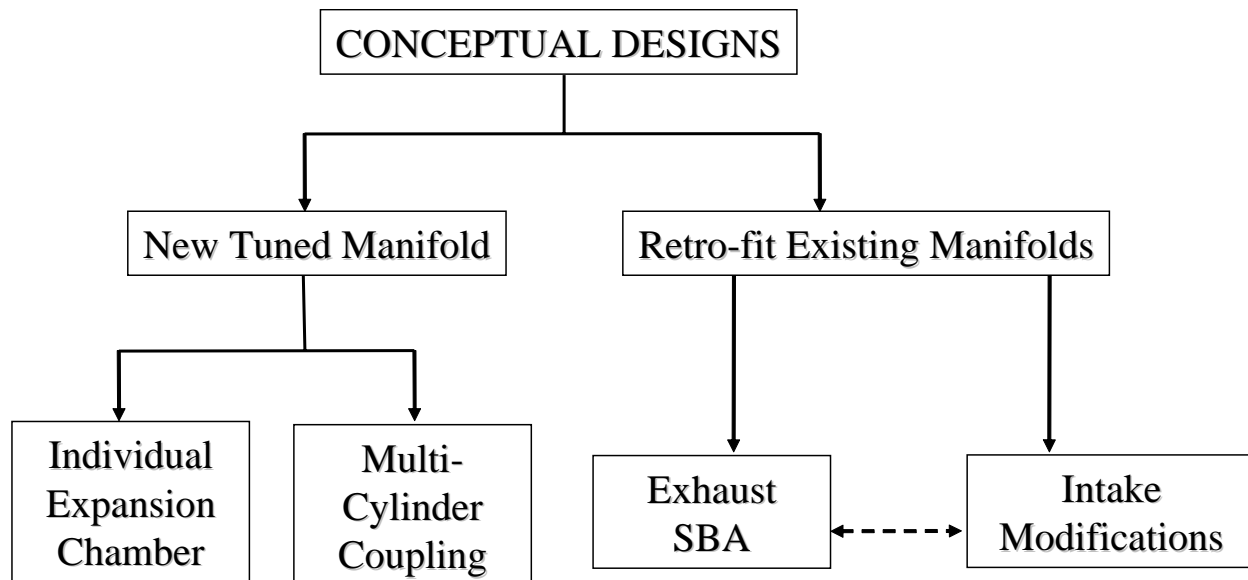


Figure 5-73. Flowchart of Current Conceptual Manifold Designs

5.2.1 INDIVIDUAL TUNED EXPANSION CHAMBER CONCEPT

The Individual Expansion Chamber concept involves the design and application of tuned expansion chambers for each cylinder. This concept would provide both cylinder isolation and could improve performance. Since this is a turbocharged engine, the individual expansion chambers would need to connect to a common plenum to maintain use of the constant pressure turbocharger. An expansion chamber is designed to first create a suction pulse that aids scavenge airflow, and then reflects a plugging pulse back to the exhaust ports at a time near port closing to supercharge or “pack” fresh charge mass into the cylinder. This causes an increase in trapped mass that is typically utilized for increased power output. An excellent description and schematic of an expansion chamber for a single cylinder is provided by Dr. Gordon Blair in his text, “Design and Simulation of Two Stroke Engines” [15]. This concept is most often applied to two-stroke performance or racing engines in applications, such as motorcycles and snowmobiles. These applications are mostly single or two cylinder engines. An application specific to gas compression engines was a design produced by Cooper Compression for the AJAX™ engine family [16]. Example photographs of Individual Expansion Chamber manifolds are provided in Figure 5-74.

The design of an expansion chamber has been simplified by Dr. Blair and the equations from this text were utilized for an initial design of individual expansion chambers for the GMVH-6 engine [15]. Figure 5-75 shows the various sections (lengths and diameters) specific to this design. The results of the initial design showed the overall length (LT) would be 60.2 feet, and the major diameter (d4) would be 16.9 inches.

The advantages of an Individual Expansion Chamber manifold for the GMVH-6 engine are as follows:

- Trapped mass increased for either leaner operation (if turbo-limited) or increased power.



Figure 5-74. Photographs of Expansion Chambers (Motorcycle Application at Left & AJAX™ Application on Right [16])

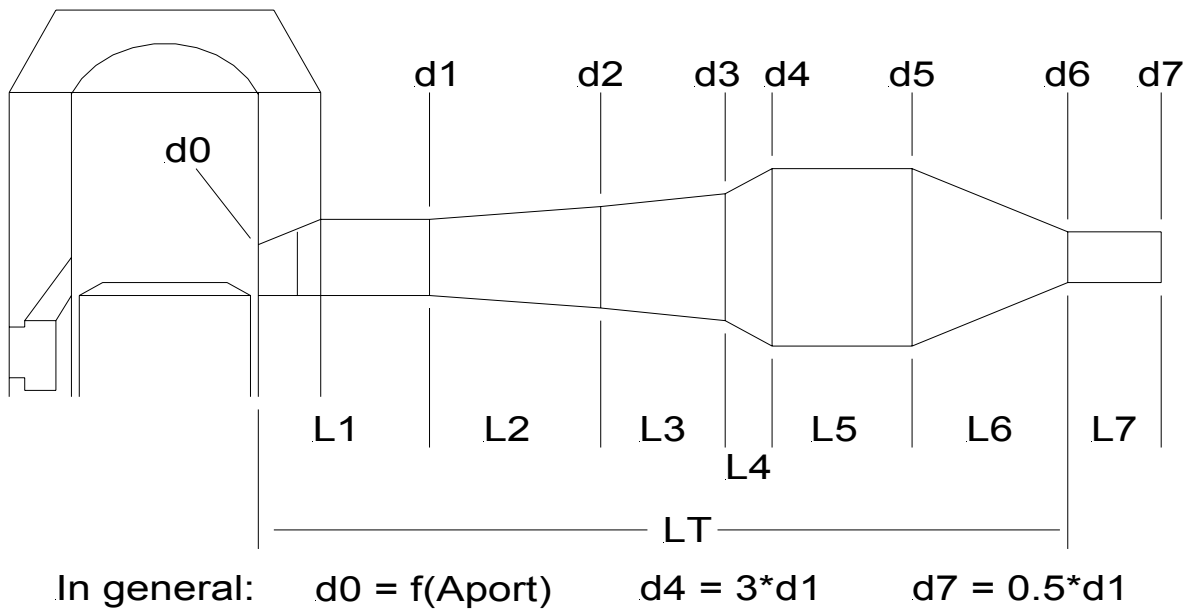


Figure 5-75. Design Parameters of an Individual Expansion Chamber Manifold

- Isolation between cylinders from adverse dynamics caused by combustion instability would be achieved.
- Potential exists for tunable section to compensate for cylinder geometric variability, potentially allowing for balancing of cylinders in terms of trapped mass.
- Basic design is applicable to all two-stroke engines, more so for non-turbocharged engines.

The disadvantages of an Individual Expansion Chamber manifold for the GMVH-6 engine are as follows:

- A common plenum is required to connect the turbocharger to all expansion chamber outlets. Packaging would be extremely challenging, likely requiring off-engine turbocharger mounting.
- Size and complexity would create a very expensive product.
- A tuned manifold has a very narrow operating band for efficient application. Performance may be worse than original manifold design at off-rated engine speed and load range.

The disadvantages for this concept outweigh the advantages, specifically in terms of cost and complexity. There was also concern that performance would be significantly degraded at operating conditions off-rated speed and load where the chambers would be tuned for maximum performance. Therefore, detailed design and optimization was not conducted for this concept.

5.2.2 MULTI-CYLINDER COUPLING TUNED MANIFOLD CONCEPT

The Multi-Cylinder Tuned Manifold concept follows the design for V-6 two-stroke engines typically used for outboard marine applications. This tuned manifold concept still utilizes a reflected pulse to supercharge the cylinder near port closure. The difference from the previous design is that this pulse is derived from another cylinder. The most attractive configuration would be three cylinders feeding into two plenums, which then feed into one junction to the turbocharger. This configuration, called the 3-2-1 arrangement, is depicted in Figure 5-76. This design would conveniently couple the cylinders by right bank and left bank due to the firing order and phasing inherent to the GMVH-6 design.

As mentioned previously, cylinder firing occurs evenly, every 60 crank angle degrees in the GMVH-6. The phasing of blowdown events is shown in Figure 5-77. In this image, the coupling of the left and right bank cylinders can be seen. The design process would, therefore, focus on runner lengths and diameters to achieve the optimum timing of the pulse from one cylinder to the next (i.e., 1L to 3L to 2L to 1L, etc.).

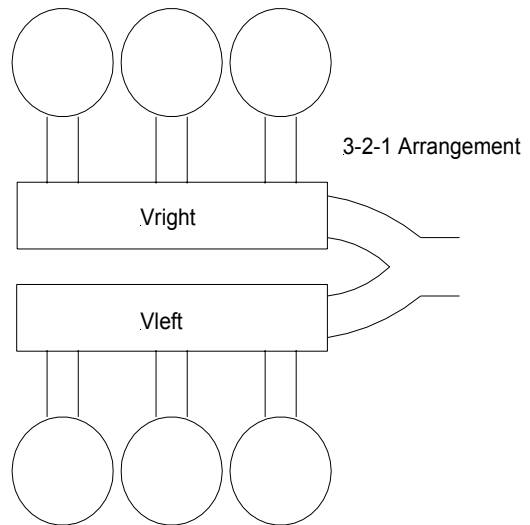


Figure 5-76. Multi-Cylinder Coupling Tuned Manifold Concept

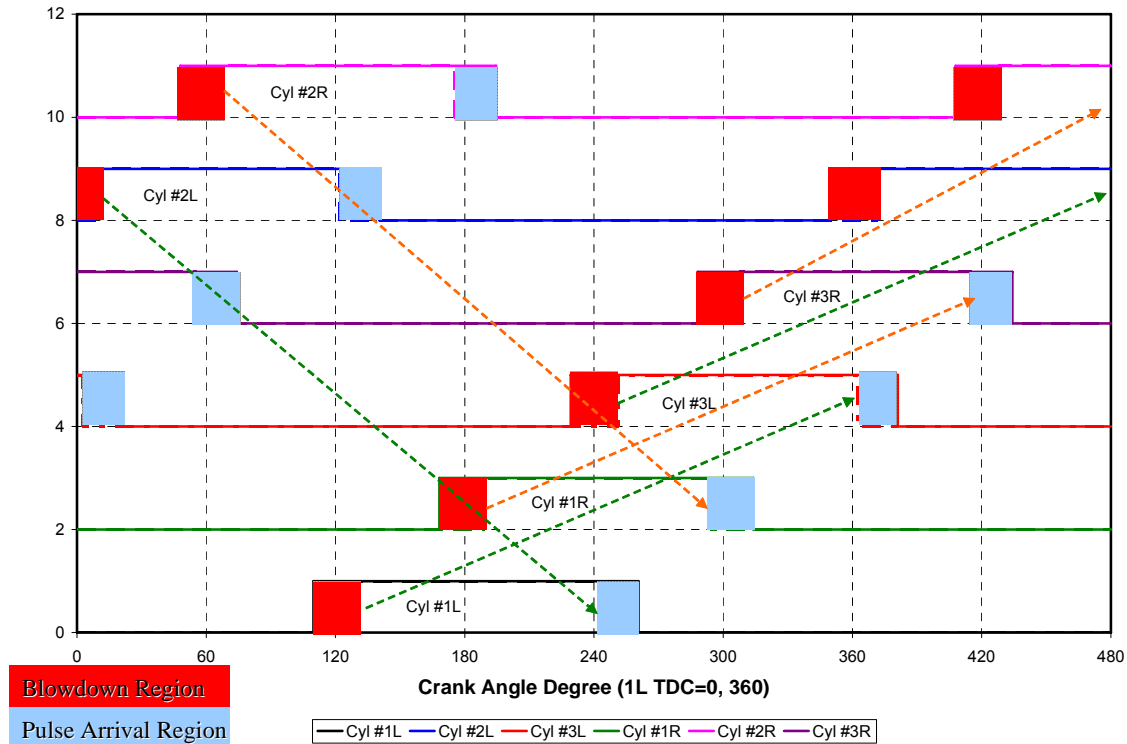


Figure 5-77. Phasing and Coupling of Cylinders on the GMVH-6 Engine

The design process for this concept utilized the Virtual 2-Stroke[®] software, and the optimization process was conducted by Optimum Power Technology. The results of this process showed an expected increase in engine BMEP of approximately 4% at rated conditions (330 RPM). The increase in BMEP is due to increased trapped mass and can be viewed as an ability to operate leaner at the same power output. The dimensions for this design are shown in Figure 5-78 for one bank (identical for opposing bank). The EMAN3 pipes from each bank would be coupled for a single EMAN4 pipe to the turbocharger.

The advantages of the Multi-Cylinder Coupled exhaust manifold for the GMVH-6 engine are as follows:

- Trapped mass increased for either leaner operation (if turbo-limited) or increased power.
- Smaller size and dimensions than the Individual Expansion Chamber design.
- Potential exists for tunable section to compensate for cylinder variability, allowing for balancing of cylinders in terms of trapped mass.
- Basic design is more suited for turbocharged engines and should be applicable to all two-stroke engines, more so for Vee engines.

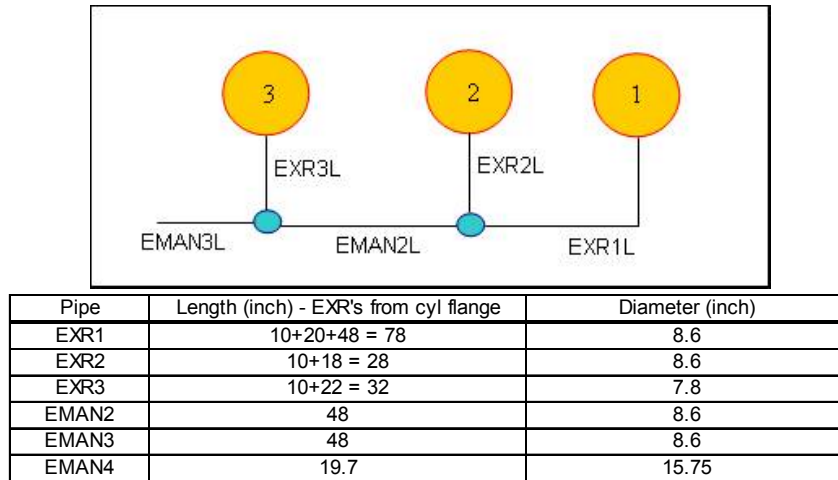


Figure 5-78. Dimensions for Optimized Multi-Cylinder Coupled Exhaust Manifold Concept

The disadvantages of the Multi-Cylinder Coupled exhaust manifold for the GMVH-6 engine are as follows:

- ❑ Completely new design would be an expensive product. It would likely require modification to turbocharger location/mounting and, in turn, the compressor outlet pipes.
- ❑ Since pulse charging depends on a previously firing cylinder, the effect of a misfire in one cylinder would more greatly affect the next cylinder dependent on this pulse.
- ❑ Design seems applicable to V-6 engines. Design for in-line engines would be more complex in terms of packaging due to cylinder spacing.
- ❑ A tuned manifold has a narrow operating band for efficient application. Performance may be worse at off-rated engine speed and load range.

The disadvantages for this concept appear to outweigh the advantages, specifically in terms of cost and potential performance degradation with unstable combustion seen in most open chamber engines operating lean for low NO_x emissions. There is also concern that performance would be degraded at operating conditions off-rated speed and load.

5.2.3 EXHAUST SIDE BRANCH ABSORBER (SBA)

As mentioned in the discussion of the tuned manifold concepts, unstable combustion will affect the dynamic pressures and flows in the exhaust manifold, and there is risk with a design that is dependant on these pulses. Therefore, a different approach was considered that would attempt to isolate the cylinders from the gas dynamics. One such approach was to incorporate a Side Branch Absorber (SBA) designed to dampen the specific frequency of pressure pulses caused by cylinder blowdown.

Data measured from the GMVH-6 for Cylinder 1 Left is plotted in Figure 5-79. The in-cylinder, intake runner, and exhaust runner pressures versus crank angle are shown. Noted on this graph are the pulses in this one exhaust runner caused by the blowdown of all the other cylinders. Also seen on the exhaust runner pressure trace are higher frequency pulsations, specifically during the scavenging region.

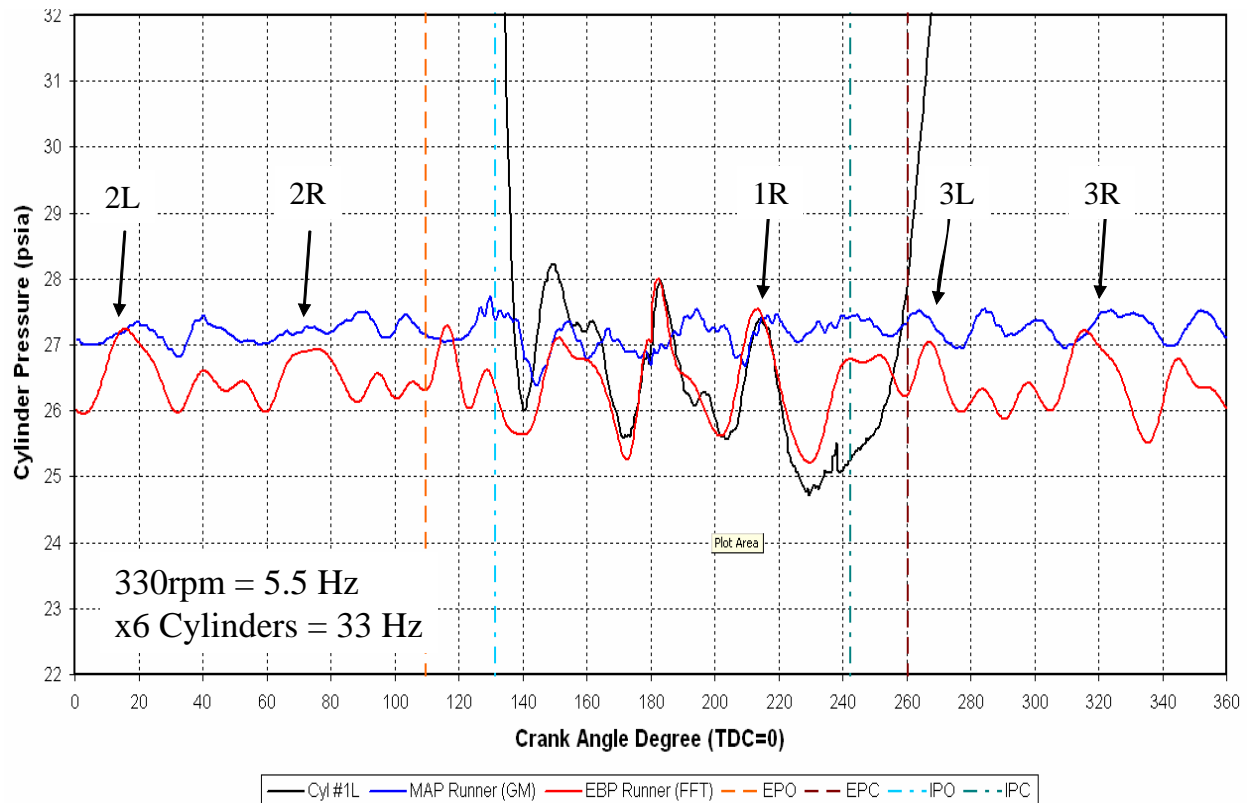


Figure 5-79. Dynamic Pressure Data Recorded on Cylinder 1L of the GMVH-6 Engine

An analysis on the exhaust dynamics was conducted with the SwRI developed IPPS model, which included derivation of the frequency modes and amplitudes of the measured exhaust pressures. Results of the data analysis are shown in Figure 5-80 for the left bank cylinders. The first mode of the length response of the exhaust chamber is seen in both the IPPS and engine data (near Cylinders 1L and 3L). The IPPS model predicted 64 Hz while the engine data showed 60 to 68 Hz. The second mode of the response is seen at the center of the chamber (near Cylinder 2 left). IPPS predicted 124 Hz, and the engine data shows a response at approximately 132 Hz. These results indicate that an SBA can be used to essentially eliminate the first mode of the response. Elimination of the pressure fluctuations during scavenging would be advantageous to increase scavenging and better isolate cylinders from each other for more consistent scavenging.

Acoustically, an SBA tries to create a velocity maximum at a point where a velocity minimum (pulsation maximum) exists. An SBA alters the acoustics, such that the response associated with the frequency to which the SBA is tuned is “split” into two responses. The SBA design developed from IPPS modeling to address the exhaust dynamic pressure measurements is shown in Figure 5-81. The IPPS simulation results with the SBA incorporated are shown in Figure 5-82 for Cylinder 1L.

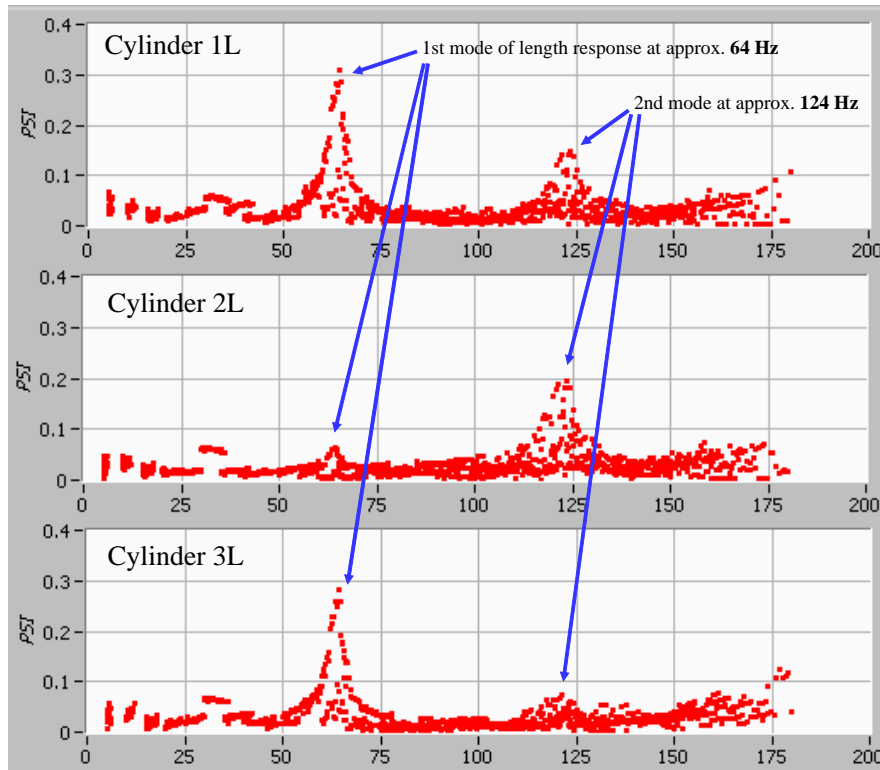


Figure 5-80. Frequency Analysis of Recorded Engine Data for Left Bank Cylinders

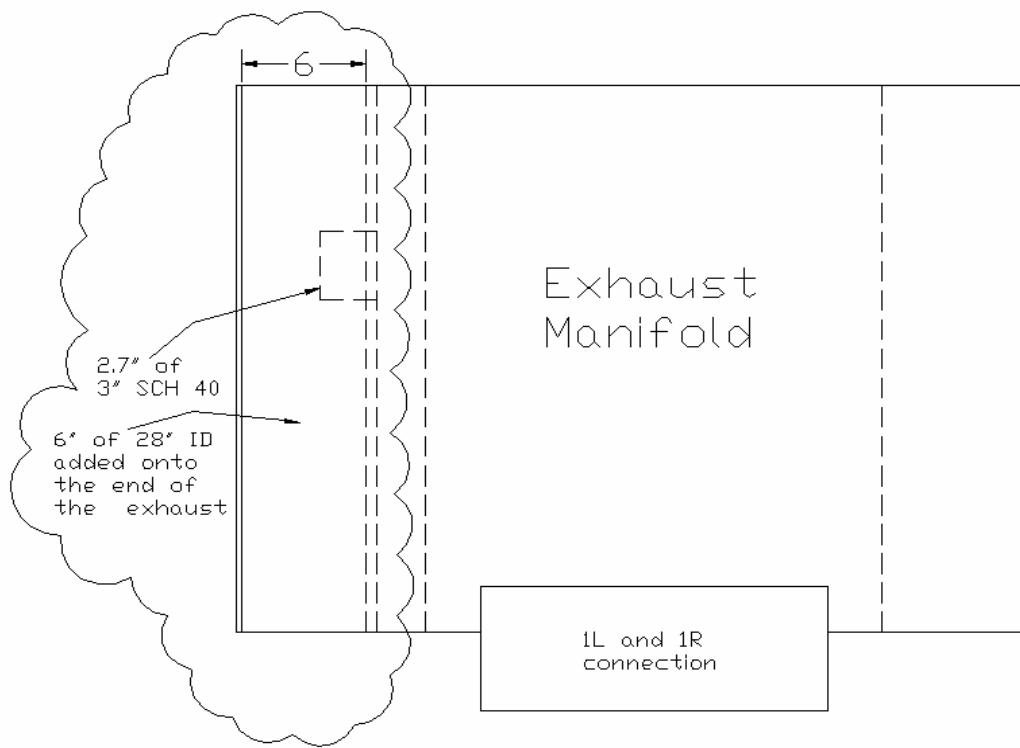


Figure 5-81. Conceptual Exhaust SBA Design for GMVH-6

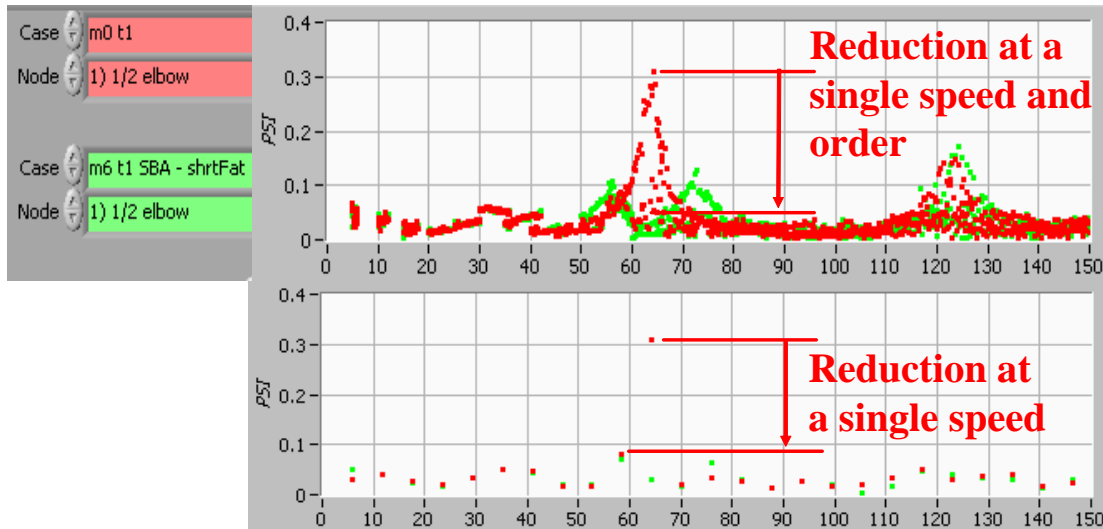


Figure 5-82. IPPS Model Results for SBA Concept

The advantages of the Exhaust SBA for the GMVH-6 engine are as follows:

- Cost-effective retrofit of existing manifold.
- Concept design should provide better cylinder isolation for more consistent scavenging and combustion.
- Some improvement in scavenging and, therefore, performance expected with pulsation attenuation.
- Can be designed to be tunable at different modes for best efficiency.
- Noise reduction would be expected as a side benefit.

The disadvantages of the Exhaust SBA for the GMVH-6 engine are negligible if the advantages can be achieved. If the mode changes at off-rated operating conditions, the SBA may become ineffective but will not alter engine performance from the original configuration. A more complex, but tunable design could be developed to address off-rated conditions.

The advantages for this concept make it very attractive. The next step was to conduct detailed analysis and optimization with the engine model. Initial modeling with the engine simulation showed only a small reduction in exhaust pulsations with the SBA. Iterations with SBA dimensions showed slight improvement in pulsation attenuation. It is currently uncertain if the engine model is accurately simulating the SBA. These devices have been designed and utilized in pipeline applications where they have successfully reduced resonant pulsations. SBA's are also used by the automotive industry on inlet air systems, such as late 1990's Chevrolet Pickups with V-8 engines. Therefore, more investigation was desired due to the cost-effective potential and testing of the concept is in progress. A prototype SBA was designed for easy changing of lengths and diameters and with only minor modifications required on the engine.

5.2.4 INTAKE MANIFOLD MODIFICATIONS

The last concepts considered were modifications to the intake manifold. One of the intake concepts included blocking the base air chest to ensure all inlet air is derived from the intake manifold and then modifying the intake manifold volume to dampen the resulting pulsations that will occur. The second intake concept is a modification to the plenum entry where the manifold is connected to the aftercooler.

The base air chest is a legacy design in the GMV from earlier versions where scavenging was accomplished with either pistons or blowers. In these earlier designs, air was fed to each cylinder through the air chest. The GMVH design is turbocharged with external intake manifolds, but the base air chest was left active and connected to all cylinders. In actuality, this air chest provides excellent dampening of intake pulsations. However, the air being fed into and out of this air chest undoubtedly is heated due to the very large surface area at or near oil temperatures. A concept was derived based on this to block the base air chest and reduce the actual air temperature entering the cylinder.

The first analysis was to determine what percentage of the total mass flow entering each cylinder is fed from the air chest. The engine simulation model was utilized for this analysis and results shown in Figure 5-83, where the instantaneous mass airflow from the air chest (plenum) and intake manifold runner is plotted with cylinder pressure. An integration of these traces shows that approximately 33% of the total mass airflow comes from the air chest, with the remainder coming from the intake manifold. This portion of the total mass flow was felt significant enough that eliminating the air chest flow would cause a significant reduction in inlet temperature. Simulation has shown that the air temperature entering the ports is approximately 20°F hotter than the air in the intake manifold log. A reduction in inlet air temperature would

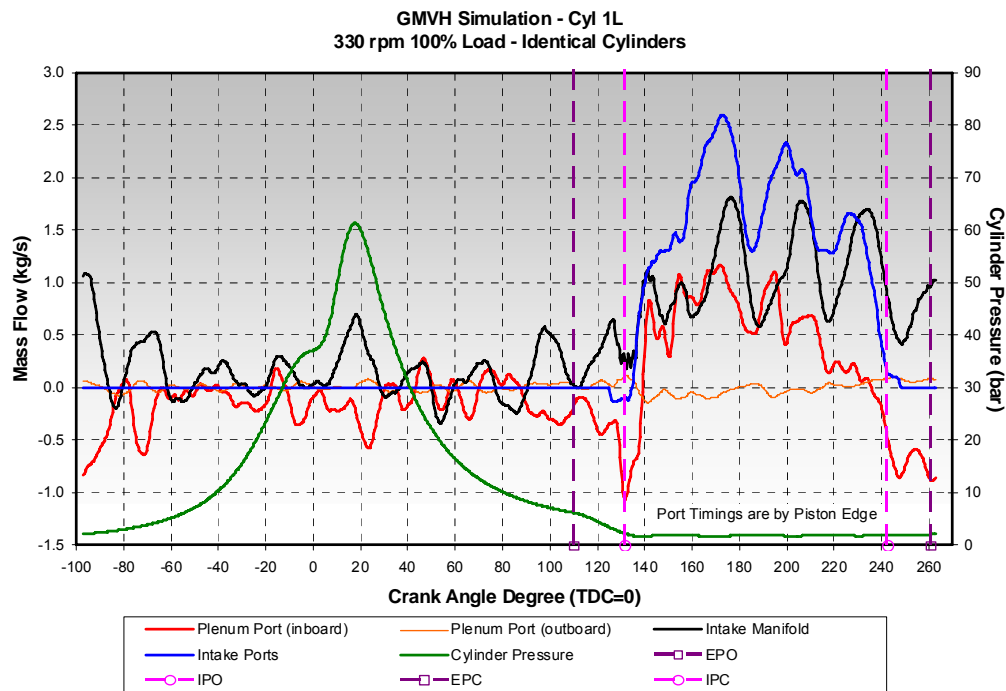


Figure 5-83. Simulated Mass Air Flow from Base Plenum, Intake Manifold, and Through the Intake Ports

provide reduction in both NO_x emissions and the tendency to knock. Prior test data from lean-burn natural gas engines indicates that a 10°F drop in inlet air temperature could achieve approximately 0.2 g/bhp-hr NO_x reduction in the GMVH-6. While not a significant reduction in total NO_x, an engine bordering on meeting permit levels would benefit in terms of efficiency with this amount of cushion or margin from the limit.

The next step in this analysis was to re-design the intake manifold to prevent the pulsations that will occur with the elimination of the base plenum. Earlier simulations with the base plenum not incorporated into the model were used to derive the expected pulsation amplitude and frequency. The IPPS model was then utilized to determine if this pulsation was resonant and could be addressed with an SBA, or if simple enlargement of the volume is required. The pulsation was determined to not be resonant and, therefore, the additional volume required for the intake manifold was derived. With the new intake volume determined, the engine simulation model was utilized to determine the potential temperature reduction with this concept.

The simulation results showed a disappointing reduction of only 4°F. This reduction is not felt sufficient to justify the cost of removing each power cylinder and capping the base plenum with special gaskets. An alternative approach was to reduce the large volume (large surface area) inside each cylinder's airbox, which is suspected to still cause significant air heating even with the base plenum disconnected. This alternative, however, would require a new cylinder casting and would become even more costly.

The next concept for intake manifold modification was not derived from simulation but rather engineering judgment. The intake manifolds on each bank are composed of a log with runners branching perpendicular to each cylinder. The entrance to each log is connected via bolted flange to a transitional duct on the aftercooler. The issues are with the bolted flange, which is internal to the manifold log and the short transitional duct from the aftercooler. The transitional duct does not appear optimum for flow, and the internal flange in the manifold log creates an orifice that is very close to the first cylinders' (3L and 3R) runners. A photograph and sketch of the left bank intake manifold and aftercooler duct are shown in Figure 5-84. The orifice created by the internal flange is likely creating a vena-contracta that may be restricting flow to the first cylinder runner. Cylinders 3L and 3R are the two lowest cylinders in terms of compression pressure as seen in Figure 5-9.

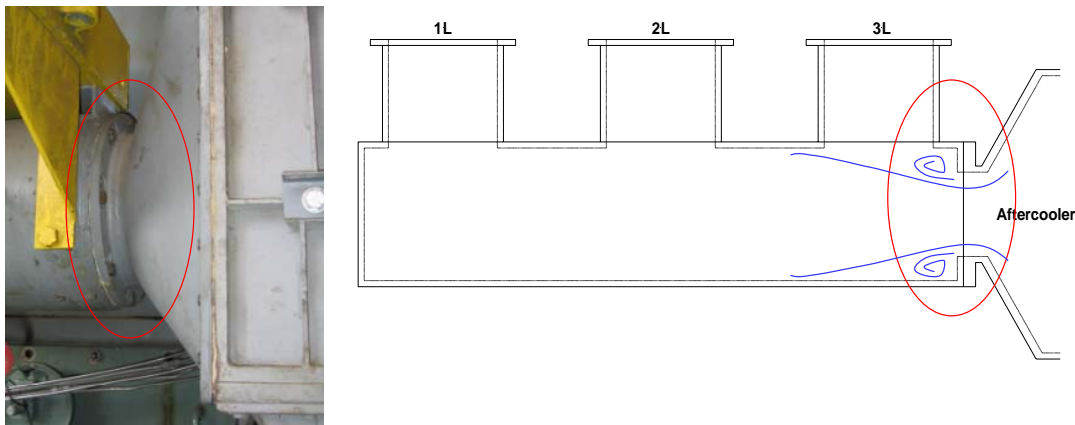


Figure 5-84. Photograph and Sketch of Intake Manifold Showing Region of Concern for Flow Disturbance and Restriction

If the vena-contracta is creating a flow structure that limits the flow to the first cylinders, then those cylinders will likely draw more air from the base air chest and may not trap as much total mass as the other cylinders. The air from the base is hotter than from the intake manifold air. This theory could explain the difference between measured data and simulation with geometric effects, which still cannot predict completely the spread in compression pressures. The flow phenomena suggested at the intake manifold entrance is highly dependent on the three-dimensional geometry. It is, therefore, suspected that a one-dimensional model may not completely capture the effects. The effect can either be simulated with a three-dimensional CFD program, or testing on the engine can determine if the suspected flow disturbance is significant in affecting the flow.

The engine test planned to address this suspicion is to add thermocouples in the base plenum access doors and probes in the inlet runners of Cylinders 1L and 3L. The thermocouples will provide the needed temperature measurement of base plenum air, and the probes will provide relative measurement of the dynamic airflow entering these cylinders. A significant reduction in airflow or velocity in Cylinder 3L compared to Cylinder 1L would validate that the intake manifold design is affecting flow and, therefore, trapped mass, among the cylinders.

The design concept would then involve removing the internal flange, possibly lengthening the intake log, adding an external flange, and possibly lengthening the aftercooler duct. The flange on the aftercooler duct will need to be redesigned for a larger bolt pattern matching the new external flange on the intake manifold log. This modification would also require a new mount design for the aftercoolers and modified turbocharger compressor outlet pipes.

The advantages of the Intake Entrance Modification for the GMVH-6 engine are as follows:

- Cost-effective retrofit of existing manifold, compared to new exhaust manifold.
- Concept design should provide better cylinder air balance. With cooler, denser charge to end cylinders. Potential for better air/fuel ratio balance.
- Can be coupled with and compliment exhaust manifold modifications.

The disadvantages of the Intake Entrance Modification are as follows:

- Potentially will affect only two of six cylinders, and performance gain would need to be determined for cost-effectiveness. However, on some engines, one poor performing cylinder (i.e., knocking or misfiring) would affect the overall engine performance if global spark timing and/or air/fuel ratio adjustment is required to compensate.

Additional testing was conducted at the end of the project schedule in an attempt to quantify whether the intake manifold design was in fact causing flow imbalances. It had been planned that such investigations would involve simulation rather than costly and time-consuming testing; however the simulation model, as constructed, was not successful in delineating any manifold flow issues. The testing involved the installation of pitot tubes into the intake runners of Cylinders 1L and 3L and connected to delta-pressure sensors that referenced the main manifold log. The testing involved rated operating conditions only. Initial results were disappointing as the long tube lengths induced high frequency “ringing” in the traces. The ringing was removed via FFT filtering, and a shift between the cylinder data became apparent.

The majority of the crank-angle-based data for Cylinder 3L was negative, while the Cylinder 1L data was mostly positive. A later test with the sensors swapped showed the data from Cylinder 3L now shifted positively. Therefore, the sensor used had an offset problem likely due to a floating ground. Time did not permit complete re-testing.

5.3 EXHAUST SIDE BRANCH ABSORBER DESIGN, CONSTRUCTION, AND VALIDATION TESTING

The results of testing showed that the air imbalance in the GMVH-6 engine was not as great as originally perceived, and that the spread in compression pressures was due in a large part to geometric variability. Communications with individuals in the industry and bits of data from various engines indicate that the manifolds on larger engines (increased number of cylinders) may have a greater effect on breathing than was found on the small GMVH-6 engine. The manifold designs on larger engines of the same model, such as the GMVH, are very similar and are mainly just lengthened for the increased number of cylinders. Given these presumptions and the results generated within this project, the exhaust SBA was felt to offer the greatest flexibility and cost effectiveness than any of the other designs. Installation of the SBA would require only minimal disassembly and modification to the engine and could be generally designed for a given engine model.

The prototype SBA designed for the GMVH-6 following dimensions (internal volume and choke tube dimensions) derived from the modeling above and is depicted in Figure 5-81. The housing design featured rolled and welded plate steel with an internal flange on one end. A blind flange was then bolted to the housing flange to provide an access port for potential modification to both the choke tube and internal volume by inserting a segment between the housing and blind flange. A production design is not expected to require the access flange and was only incorporated into the prototype for testing flexibility. The housing was mounted to the exhaust manifold by welding to the manifold log. Production design may involve the welding of an external flange to the exhaust manifold log so that the SBA could be bolted rather than welded in place. The choke tube was installed by inserting into a hole cut into the manifold log end cap and then welded in place. A three-dimensional CAD image of the design is depicted in Figure 5-85. Figure 5-86 is a photograph of the finished housing prior to installation. Photographs of the final installation are provided in Figure 5-87 and Figure 5-88.

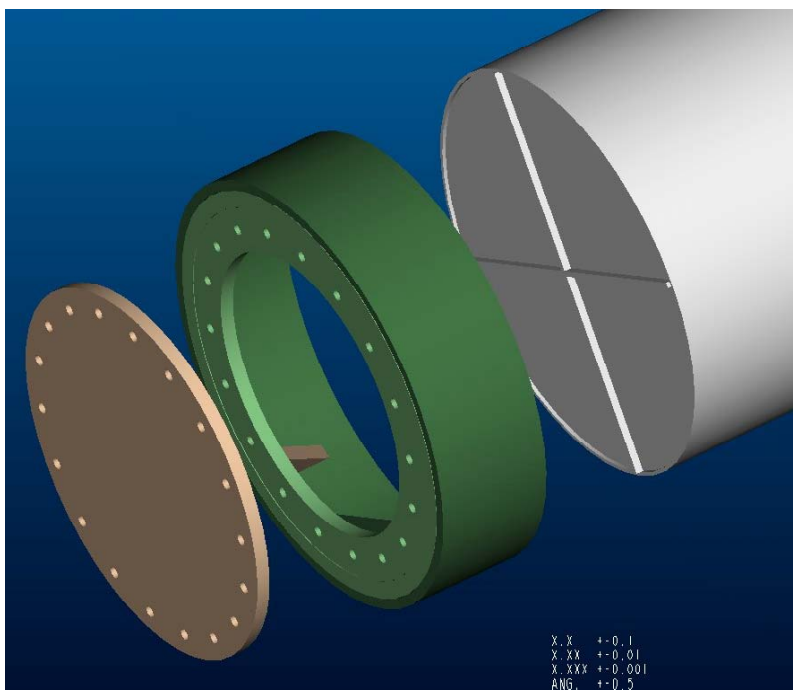


Figure 5-85. Three-Dimensional CAD Image of Prototype SBA Design



Figure 5-86. Photograph of Prototype SBA Housing Prior to Installation

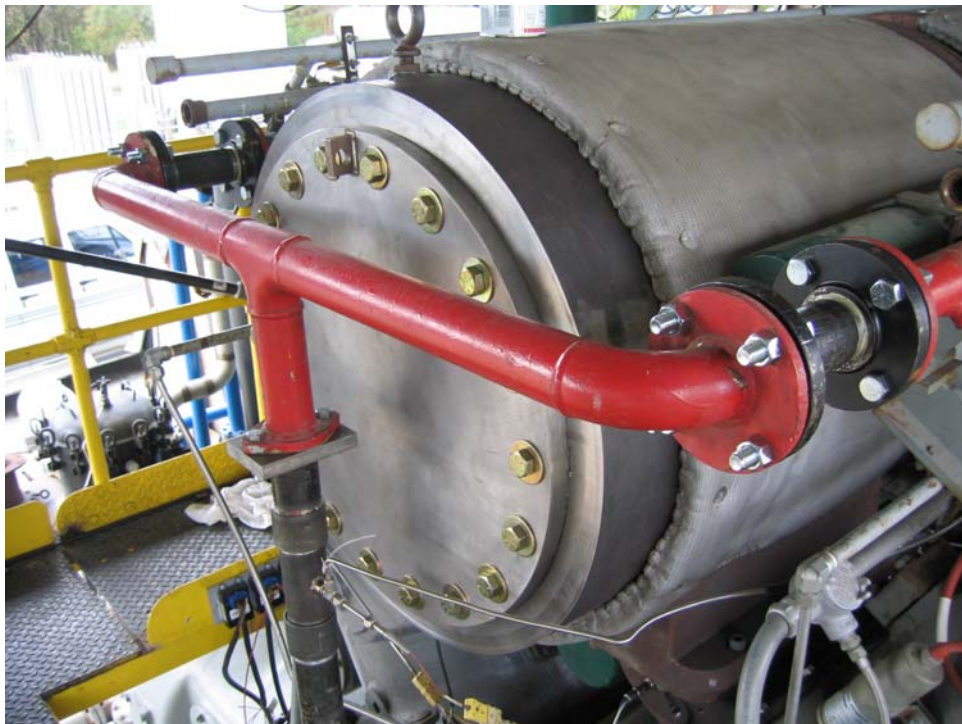


Figure 5-87. Photograph of Prototype SBA Housing Installed on Engine



Figure 5-88. Photograph of Prototype SBA Housing Prior Installed on Engine

To ensure access for good weld penetration, the end manifold segment was removed from the engine and then positioned vertically on the ground. Field installation may not require removal of the end segment, especially if an external flange is utilized to bolt the housing to the exhaust manifold. The only modification to the engine required for SBA installation was extending the fuel header. This extension was accomplished with flanged pipe inserts that can be seen in Figure 5-87 in the red-painted fuel header piping. A final installation step was to wrap the SBA with insulating material to prevent excess heating of the fuel header and for personnel safety.

The cost for fabrication and installation of the prototype SBA for this project was less than \$30,000. A production design may be more expensive due to the fact that it would incorporate features to enhance long-term reliability and typical variations among manifolds from a given engine model. The detailed design costs would also factor in the retail price, as well as profit for the manufacturer. Installation costs may be higher for equipping field engines due to transportation, personnel, and other costs related to construction in a compressor station as compared to a laboratory. However, it is anticipated that the total price for an installed unit would be less than \$50,000. Compared to fabrication and installation of a completely new manifold design, this estimated cost is likely an order of magnitude lower.

The SBA was tested over several engine speeds and loads, but focus was placed on rated conditions (design condition). Exhaust emissions were acquired during this testing, which was the first testing with emissions since before the engine was disassembled for geometric analysis. During reassembly the cylinder components between Cylinders 1L and 3L were swapped. Therefore, performance and pulsation data was compared with data acquired after reassembly. Emissions data and emissions-based calculations were compared to data prior to disassembly.

The pulsation data recorded by the dynamic sensors in each exhaust runner were compared first to ensure the SBA is having an effect. The data from Cylinder 1L is plotted in Figure 5-89, where exhaust runner pressure versus crank angle degree is shown for tests before and after SBA installation. A reduction in peak-to-peak amplitude can be seen in this comparison. A second data comparison plot is provided in Figure 5-90, where cylinder pressure data is plotted in addition to exhaust pressures. A significant reduction in pulsation amplitude can be seen near the end of the scavenging period (just after angle 225 degrees in Figure 5-90), which shows to affect the cylinder pressure at the beginning of compression as noted. The performance data showed an increase in the total mass flow for a given air manifold pressure and increased calculated scavenging ratio. The calculated scavenging efficiency, using the complete mixing model [13], showed an increase from approximately 65% to 68% with the SBA. The peak cylinder pressure was lower, location of peak cylinder pressure was slightly later, and the fuel efficiency was slightly decreased with the SBA. All performance indicators trended in the direction of a leaner trapped air/fuel ratio, for which optimization of spark timing may improve the efficiency to a point exceeding baseline conditions.

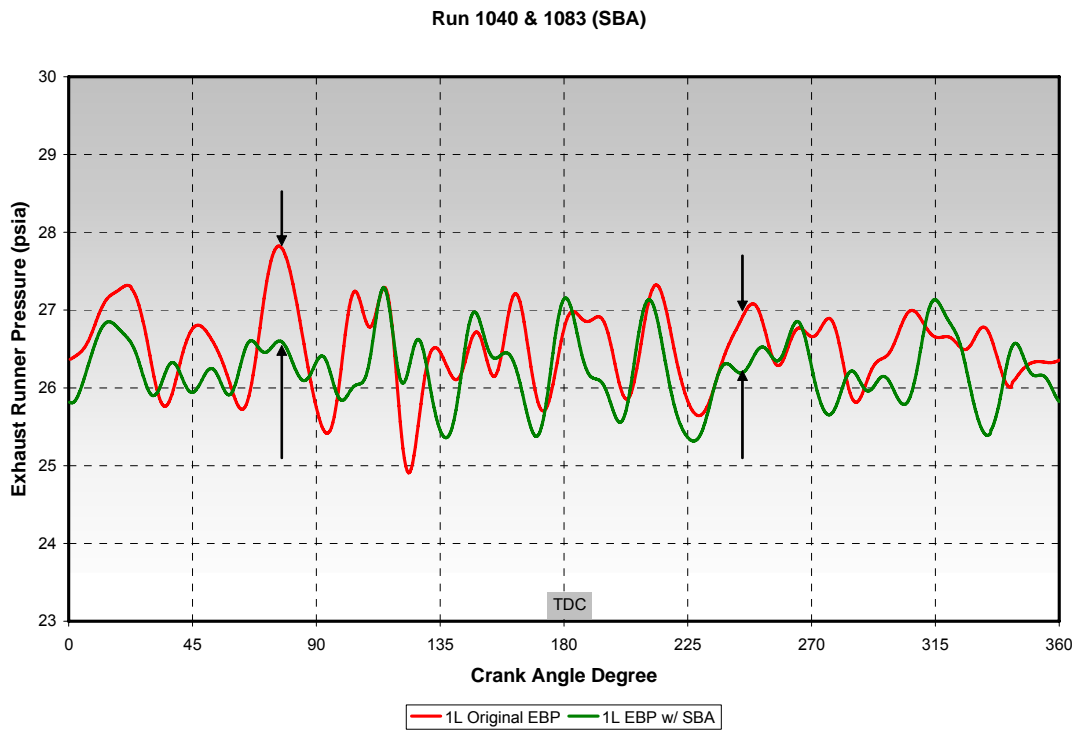


Figure 5-89. Comparison of Cylinder 1L Dynamic Exhaust Pressure Before and After SBA Installed

Run 1040 & 1083 (SBA)

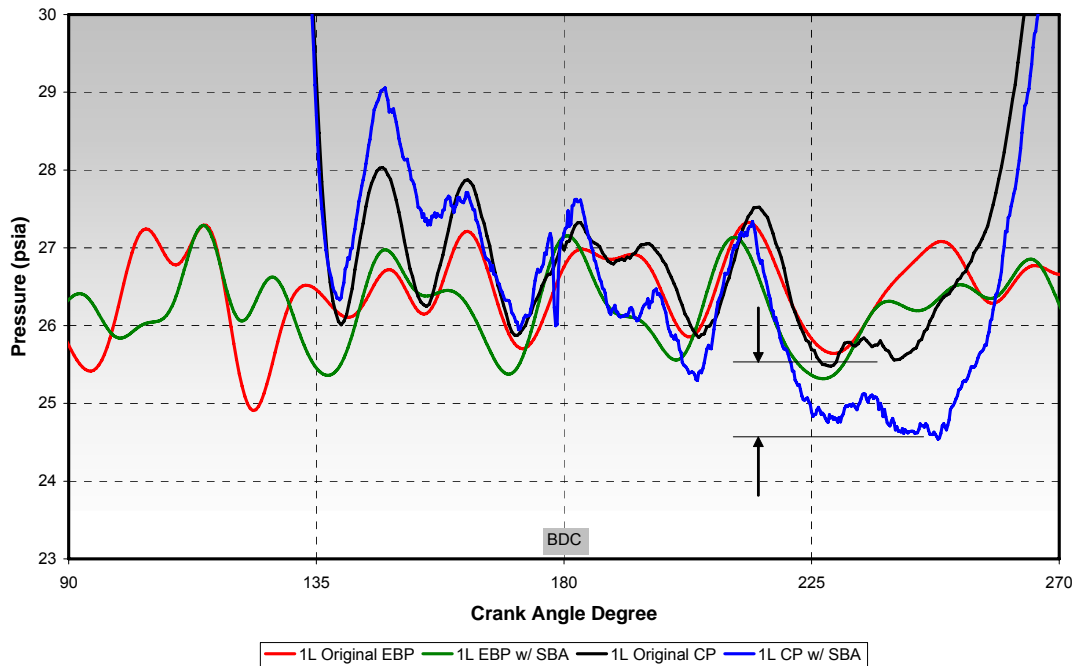


Figure 5-90. Comparison of Cylinder 1L Pressure and Dynamic Exhaust Pressure Before and After SBA Installed

The emissions data showed a more significant effect of the SBA. The exhaust O_2 was higher for repeat conditions, adding credence in the apparent improvement in airflow. The NO_x data was plotted versus air manifold pressure to incorporate data from air/fuel ratio sweeps, and shown in Figure 5-91. The operating conditions for this data comparison were rated engine speed and load with the same 4-degree BTDC ignition timing. The data in Figure 5-91 show a consistent reduction in NO_x emissions versus air manifold pressure for the SBA as compared to data obtained prior to engine disassembly. The NO_x data was corrected for ambient humidity using formulas given in CFR40 Part 1048 – “Control of Emissions from New, Large Non-Road Spark-Ignition Engines.” The humidity correction was necessary due to the large difference in ambient humidity between tests. The baseline data was acquired in late summer of 2004 when the ambient humidity was at its normal high (average 0.0137 gH₂O/gAir) for south central Texas. The SBA data was acquired in the winter of 2005 during abnormally dry conditions (average 0.0032 gH₂O/gAir). It is uncertain how applicable the humidity correction formulas apply to two-stroke integral engines, as no test has definitively derived an acceptable procedure.

While the drastic change in ambient humidity between the baseline and SBA tests causes some uncertainty in the optimistic emissions results, the entire data set trends favorable for the exhaust SBA. Much of the performance data acquired after engine reassembly was during the dry conditions, and correlates well with the baseline-SBA emissions data comparisons.

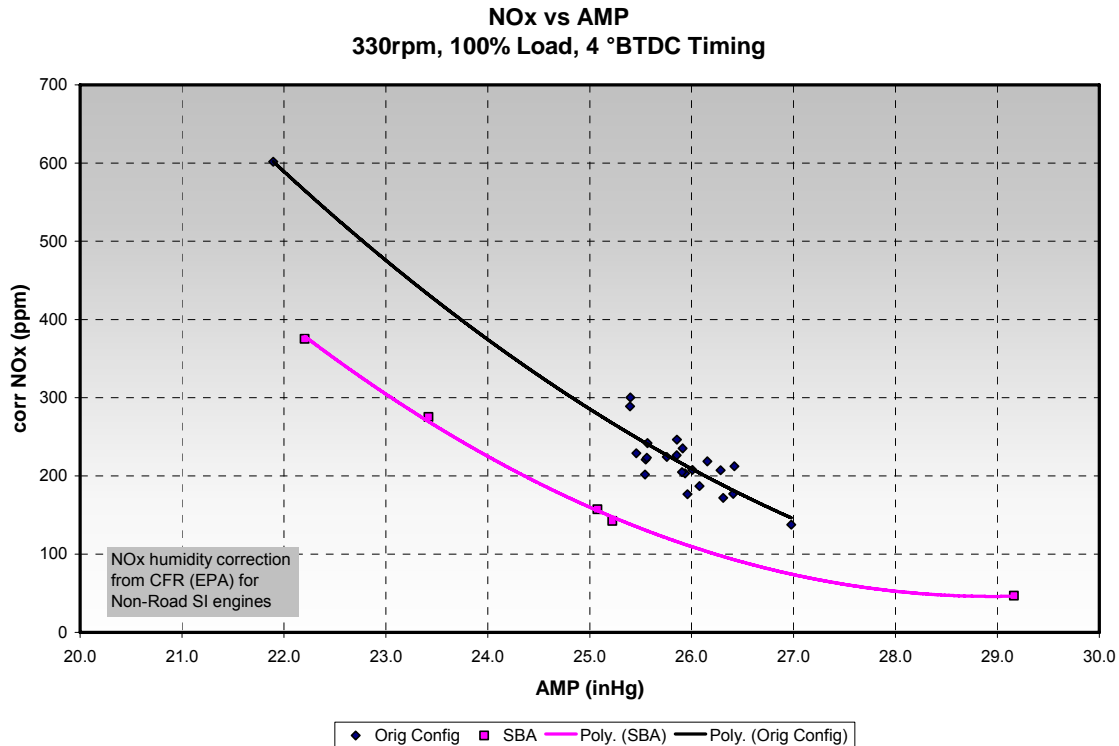


Figure 5-91. Comparison of Humidity Corrected NO_x versus Air Manifold Pressure Before and After SBA Installed

5.4 COMPONENT VARIABILITY

Simulation, measurement, and testing have shown a significant effect of component variation on the compression pressure and the resulting indicated performance. Realizing all engines cannot be “blueprinted” like was done on the laboratory GMVH-6, steps to alleviate geometry issues were evaluated. Various steps to consider during maintenance/repair include the following:

- Ensure matching components are installed—via casting or part numbers and from the same manufacturer.
- Use prior data to identify “outlier” cylinders and inspect/replace components when possible.
- Conduct basic measurements when cylinders are apart to correlate with performance data.
 - Port height – top of ports to top of cylinder (port timing and effective compression ratio indicator).
 - TDC piston height – piston top at TDC to cylinder top (compression ratio indicator).
 - Piston to head clearance – measured with clay or lead on piston crown (compression ratio indicator).

- Cylinder head (combustion chamber) volume – liquid volume (compression ratio indicator).
- Fuel cam profile – dial indicate travel versus crank angle degree.
- Perform detailed testing on engines with significant problems.
 - Flush-mount cylinder pressure transducers (where possible) for PV analysis.
 - Dynamic inlet, exhaust, and fuel valve pressures for pulsation analysis.

Casting numbers are visible on most major components of the GMVH-6 engine. Photographs of the cylinder and head casting numbers are provided in Figure 5-92 and Figure 5-93. These casting numbers allow for easy inspection of components to determine if mismatched components are installed on a given engine. A schematic of basic measurements that can be performed when a cylinder is disassembled is provided in Figure 5-94.

Performance data to review include cylinder pressure data and dynamic pressure data. Although the compression pressure prior to ignition has been shown to not be as good an indicator for air imbalance as originally perceived, it does provide a good indication of an outlier cylinder in terms of airflow, fueling rate, and component variability of which all affect indicated performance of that cylinder. The peak firing pressure stability (standard deviation or coefficient of variation) is a good indicator of trapped air/fuel variation, if one or two cylinders have a significantly different value than the other cylinders. The tendency to detonate or misfire more than the remaining cylinders should correlate with peak firing pressure stability differences. Cylinder pressure measured at the Kiene valve should be sufficient, assuming accurate sensor calibration, for determining the relative differences in cylinder pressure statistics.

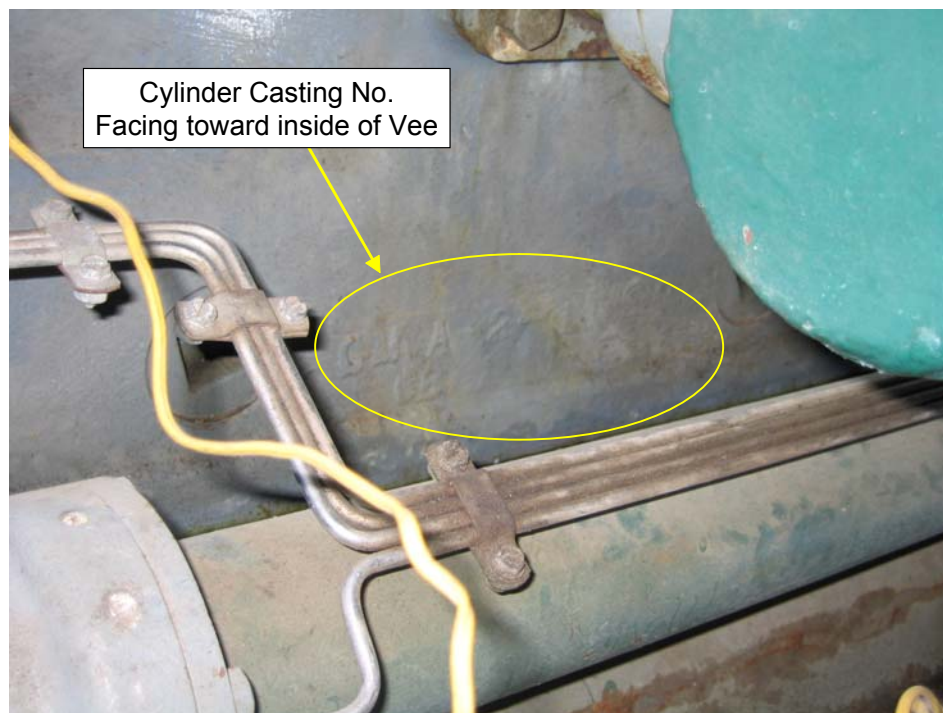


Figure 5-92. Photograph of Cylinder Showing Location of Casting Number



Figure 5-93. Photograph of Cylinder Head Showing Location of Casting Number

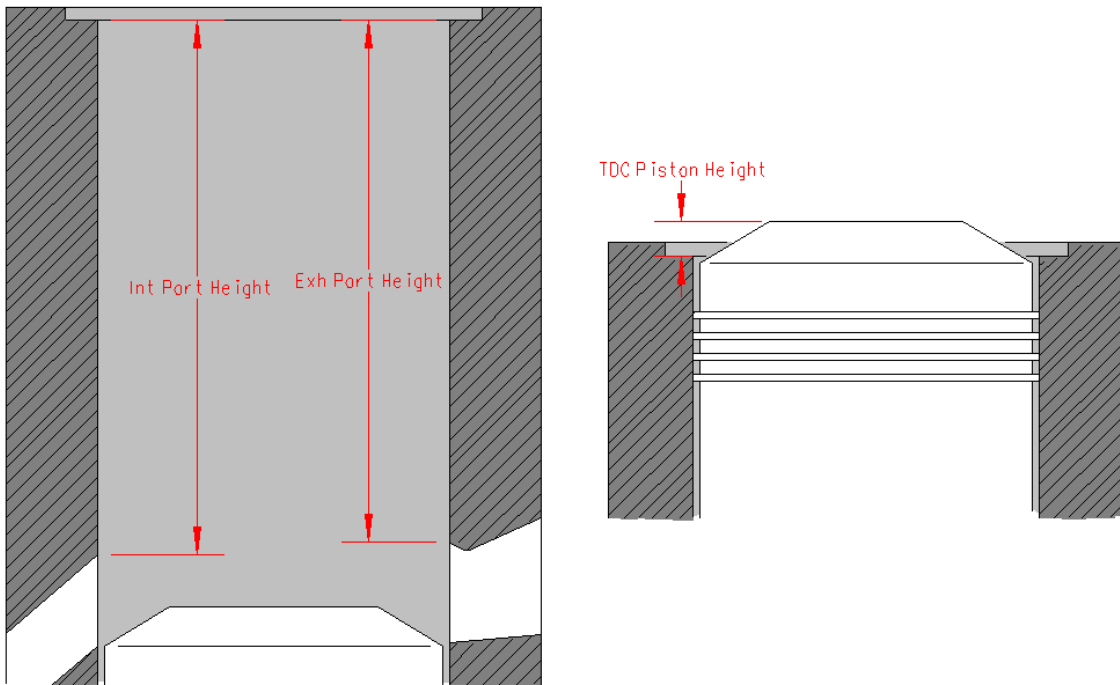


Figure 5-94. Schematic of Cylinder Measurements (with head removed) for Geometric Variability Investigation

6. CONCLUSIONS

Some form of combustion balancing is universally practiced on two-stroke engines. Most commonly, equal peak firing pressures are sought by adjusting fuel to each cylinder. However, analysis has shown that with cylinder-to-cylinder variations in trapped air, equal peak pressures mean unequal trapped air/fuel ratio and, hence, cylinder-to-cylinder inequality in combustion. A dominant and complicating characteristic of two-stroke engines is high cycle-to-cycle variability in combustion events for any cylinder. Average cycle-to-cycle standard deviations in peak firing pressures of 45 PSI, 58 PSI, and 60 PSI have been observed on three engines. The four-stroke engine tested also exhibited cycle-to-cycle variation between 10% and 15% of the average.

One alternative to peak firing pressure balancing is to equalize each cylinder's standard deviation in peak firing pressure over time. This method derives from the reasonable assumption that the standard deviation over time is a direct function of air/fuel ratio (richer combustion—within limits—is more stable). Reducing fuel to low standard deviation cylinders (or increasing it to high standard deviation cylinders) should equalize air/fuel ratio. Limited testing of this method indicated it helped control high excursions in crankshaft strain.

An alternative balancing method has been developed on the project, which adjusts individual cylinder fuel to equalize Combustion Pressure Ratio (CPR) across all cylinders. CPR is the ratio of peak firing pressure to compression pressure, calculated for each cylinder. Compression pressure is the pressure at a fixed angle ahead of Top Dead Center for that cylinder. The method's implicit goal, just as with standard deviation balancing, is to equalize air/fuel ratio. An application was made and a patent issued for CPR balancing. As practiced in a computer-assisted manual form on three engines, the quantity CPR is calculated each cycle, and then averaged over multiple cycles for all the cylinders. Evaluation has shown that averaging over 100 cycles provides a set of CPR values repeatable enough for balancing decisions. "Reducing" the fuel valve on the cylinder with the highest CPR leads to a readjustment and leveling of the CPR distribution. The method is significant because cylinder-to-cylinder variation in compression pressure between 6% and 12% has consistently been observed on the engines tested.

Tests on a GMW10 modified for high-pressure fuel and a turbocharger did show distinct reduction in crank strain following either standard deviation or CPR balancing—this is attributed to reduction in PFP of the richest cylinder as a result of either balancing method. Cycle-to-cycle variability imposes a limit on the benefits to be obtained by any type of combustion balancing. While average spread in peak firing pressure can be cut in half by peak firing pressure balancing, the instantaneous spread only drops by about 10%.

Significant imbalance from cylinder-to-cylinder in compression pressure is a consistent feature of slow-speed two-stroke engines. An additional feature is that compression pressures and their imbalance are much more consistent over time than combustion pressures (and their imbalances). Compression pressure standard deviations over time are smaller than the standard deviations in peak firing pressures by a factor of ten. Compression pressure imbalance can contribute to variability in equivalence ratio across the cylinders. Data measured on the project show that 25% to 50% dynamic variability in exhaust and air manifold pressure is typical, and by inference is a major contributor to compression pressure imbalance.

Longer-term data have shown how equivalence ratio (fuel-to-air ratio normalized by the stoichiometric valve) can vary over time—probably as a result of conditions changing, though random variation and hysteresis may contribute. Performance of engines is highly sensitive to this equivalence ratio and a need exists for a low-cost means to control equivalence ratio as conditions change. This need was particularly clear on the four-stroke engine tested, because such adjustment is currently made manually. This capability would allow more direct tuning to meet a particular goal, for example, to enhance combustion stability, heat rate, or emissions. The feasibility of a low-cost closed-loop control of waste-gate setting, which will maintain an equivalence ratio set point in turbocharged engines, has been demonstrated. With appropriate set point selection, this could be applied to meet a particular operational objective, such as minimum NO_x. The feasibility of maintaining a global equivalence ratio set point on a four-stroke engine by use of a control valve in a closed loop to modulate fuel rate has been demonstrated. This capability presents an option to replace manual adjustment based on an indirect measurement (manifold vacuum) and will enable alternatives in optimized operation (minimum heat rate, minimum emissions without a catalyst, or optimum operation of a catalyst, if installed).

The project has documented the strong dependence of heat rate on load—the HBA-6T tested showed 0.6% increase in heat rate for every 1% reduction in load. The KVG103 tested showed approximately a 0.4% increase in heat rate per 1% reduction in load. There is a strong need for convenient, accurate, and reliable measurement of actual brake power delivered to the compressor by the engine. Inferential methods evaluated under this project show variable accuracy, with as much as 10 or more percent discrepancy from indicated power. The achievement of high accuracy in inferential methods is possible, but requires extensive and costly mapping of each compressor in good condition, and errors can still result when malfunctions, such as a valve or ring leak occur.

The heat rate implications of not knowing power and torque accurately are clear; overload can also result. The GMRC Rod Load Monitor (RLM) promises to provide a means to measure power and torque directly, helping to optimize heat rate while avoiding overload. Evolving versions of the RLM have been evaluated under this program and results have guided refinements. A self-powered RLM with digital telemetry was demonstrated for the first time on a 300-RPM slow-speed integral HBA-6T. The self-powered RLM was also successfully demonstrated on a modified GMW10. Its inferred power based on measured strain, Young's modulus, and rod diameter were within 0.9% to 2.6% of indicated power.

The crankshaft Strain Data Capture Module (SDCM) has been used with success on tests of five different engines. It has shown sensitivity to changes in operating conditions and how they influence crankshaft bending strain, including: how standard deviation-based balancing reduced the frequency of high-strain excursions during the first HBA-6T test; how timing advance directly increased crankshaft dynamic strain; how reducing speed directly reduced crankshaft dynamic strain; how balancing reduced strain on the modified GMW10; and how high-pressure fuel injection reduced crankshaft strain slightly.

In recognition of the high sensitivity of heat rate to load, direct use of heat rate values in comparing operational conditions is subject to uncertainty when even small changes in load occur. However, the use of the heat rate versus load chart, as a reference for evaluating how changes influence heat rate, has shown promise on data from tests on a HBA-6T. On a second set of tests on the same HBA-6T showed a distinct reduction in heat rate after CPR balancing, by about 100 BTU/HP-Hr, when compared to the baseline heat rate versus load chart. Comparison

to the baseline heat rate versus load chart showed distinct heat rate reduction by about 100 BTU/HP-Hr for the HBA-6T tested when timing was advanced by 2 degrees. Immediate changes in heat rate after timing changes on GMW10 tests also showed that advancing timing reduces heat rate, and that retarding timing increases heat rate by several hundred BTU/HP-Hr. The KVG103 tested exhibited its lowest heat rate of 8,700 BTU/HP-Hr under advanced timing tests compared to 9,100 nominal. While increased timing reduces heat rate, it acts to increase NO_x concentration for all engines tested, two- and four-stroke. A series of tests on a GMW10, before and after modifications to add high-pressure fuel injection and a turbocharger, demonstrated a 7% reduction in heat rate, a 7% increase in thermal efficiency, and a 90% reduction in NO_x concentration; crankshaft strain was also reduced by a small amount.

One observed reason why timing is not advanced as much as it might be to reduce heat rate is the potential for detonation on hot days with advanced timing. If incipient detonation could be detected, it would allow active control to reduce timing immediately when detonation occurs, and allow the heat rate benefits to be realized safely. A low-cost knock detector has been evaluated on both an unmodified GMW10 and on an HBA-6T. The first test showed it could clearly detect audible detonation whenever it occurred. A second test on the HBA-6T showed that when timing was advanced, air manifold pressure reduced, and fuel supply to a cylinder increased; the detonation detector mounted on that cylinder responded with a steady increase in output even though no audible detonation was observed.

System thermal efficiencies in the range of 23.5% to 30% have been observed with “as found” timing. A high value of over 31% has been observed with an advance to 11-degree timing on a GMW10 with high-pressure fuel and a turbocharger. System thermal efficiency provides an effective way to assess a complete compressor package—usable for integral or separable compressor installations. It can be calculated from the inverse of compressor piston face heat rate multiplied by the compressor thermal efficiency. When investigating the influence of operating conditions (e.g., speed), system thermal efficiency combines heat rate, mechanical efficiency, and compressor thermal efficiency, using directly measured quantities. Compressor isentropic efficiencies in the range of 76% to 91% have been observed; compressor efficiency is an important benchmark for two reasons: first, because increasing efficiency reduces fuel consumption for a given amount of useful compression work; and secondly, it increases capacity because it allows more of the available engine power to provide useful compression work. Pulsations (which test results show can result from speed changes or load step changes) have been observed as a major contributor to increased losses. Attempts to assess the influence of speed on system thermal efficiency have emphasized the need for enhanced information on compressor mechanical efficiency. Tests on a KVG103 made combined use of the Rod Load Monitor power and indicated cylinder horsepower as speed was varied under no load conditions to prototype a means of inferring piston friction loss.

Many pipeline compressors have temperature measurement on each discharge nozzle. Temperature rise across each cylinder directly indicates the increase in enthalpy. Any losses in the cylinder increase the enthalpy rise above the ideal for the net pressure rise. Project results have confirmed cylinder temperature rise for a particular cylinder in a particular state of health is a direct and consistent function of compression ratio, and that consistent differences in discharge temperature can be observed between cylinders. With well-calibrated instrumentation and appropriate detection logic, these temperature differences can be used to detect a difference in efficiency from compressor cylinder to compressor cylinder. With appropriate statistical

analysis, the deviations between a cylinder's temperature rise and its expected value based on ratio provide a basis for assessing the condition of the cylinder.

Significant pressure drop in the compression pulsation control system reduces overall compressor efficiency. However, the dynamic pressure loss due to uncontrolled flow pulsation can cause an even larger reduction in efficiency. Excessive pulsation can create unacceptable vibrations that lead to pipeline failures. A second cause of low compressor efficiency is pressure drop across the compressor valves. To minimize pressure drop, the valve lift can be increased. However, excessive valve lift can greatly increase impact stress and significantly reduce valve life. In both cases (valves and installation losses), there is a critical trade-off between integrity/life and efficiency. New technology is required to de-couple this trade-off, thereby providing improved efficiency and integrity.

The Air Balance phase began with the presumption that flow variations and/or dynamic pulsations due to manifold design were causing the measured spread in compression pressure and, therefore, causing deviations in the scavenging and resulting trapped mass. A spread in trapped air mass and, therefore, trapped air/fuel ratio would lead to undesirable results, such as lower efficiency, higher NO_x production, increased crankshaft stress, increased vibration, and reduced operating margins from detonation and misfire. To add credence to the air imbalance theory, various field tests have shown the sensitivity of one or two cylinders per engine to adjustments in global air/fuel ratio. This sensitivity indicates that these cylinders are operating at or near the misfire or knock thresholds, which implies differences in trapped air/fuel ratio. In summary, the spread in compression pressure was found to not be the best parameter to gage air imbalance by itself. Factors, such as geometric variations, affect the compression pressure, as well as fuel admission variations. Compression pressure spread does, however, provide a good indication of deviations between cylinders that could be detrimental to overall performance of the engine. Extensive knowledge was gained throughout this project and detailed methods/procedures were developed for determining causes of cylinder deviations and performing manifold design. The GMVH six-cylinder engine is probably the best case for air balance as compared to similar engines with many more cylinders. Partial datasets from field engines and experiences by individuals with larger integral engines strongly indicate that air imbalance is a bigger issue with the larger engines. The effect of manifold design on air balance was not completely quantified on GMVH-6 engine due to geometric and fueling effects, but appears small.

This program has provided an in-depth assessment of operating methods and technologies that can, if implemented, enhance the operation of integral engine/compressors in natural gas pipeline service. This enhancement will improve integrity, extend life, improve efficiency, and increase capacity, while managing NO_x emissions. These benefits will translate into lower cost, more reliable gas transmission, and options for increasing deliverability from the existing infrastructure on high demand days.

7. REFERENCES

- [1] Smalley, A. J., Mauney, D. A., and Ash, D. I., (1997), Final Report PR-15-9529, “Compressor Station Maintenance Cost Analysis,” prepared for the Compressor Research Supervisory Committee of PRC International, SwRI Project No. 04-7424.
- [2] McKee, R. J., Smalley, A. J., Bourn, G.D., and Young, K. N., (2003), “Detecting Deterioration of Compression Equipment by Normalizing Measured Performance Relative to Expected Performance,” GMRC Gas Machinery Conference (GMC), Salt Lake City, Utah.
- [3] Harris, R. E., Edlund, C. E., Smalley, A. J., and Weilbacher, G., (2000), “Dynamic Crank Web Strain Measurements for Reciprocating Compressors,” presented at the GMRC Gas Machinery Conference (GMC), Colorado Springs, Colorado.
- [4] Smalley, A. J., McKee, R. J., Bourn, G. D., Smith, J. A., Truehaft, M. B., and Buckingham, J. P., “Engine/Compressor Performance Data Normalization,” Final Report, SwRI Project No. 18.05189, Prepared for Gas Research Institute, GRI Contract No. 8491, March 2003.
- [5] Koop, L., “Free Floating Piston, A Technology to Prevent Rider Ring Wear,” European Forum for Reciprocating Compressors – 2005 Conference, June 9-10, 2005, Hotel Corinthia, Antwerp Belgium.
- [6] Smalley, A. J., “Topical Report: Misalignment and Temperature Measurements on a Fully Grouted Reciprocating Compressor,” prepared for the Pipeline Research Committee of the American Gas Association, Project PR15-174, SwRI Project 04-7564, May 1985.
- [7] Smalley, A. J., Mandke, J. S., Pantermuehl, P. J., Drummond, R. D., “Reciprocating Compressor Foundations: Loading, Design Analysis, Monitoring & Repair,” GMRC Technical Assessment TA93-1.
- [8] Smalley, A. J., “Compressor Diagnostic Software: Development, Test, and Evaluation,” GRI Report No. GRI 95/0448.
- [9] Smalley, A. J., Harris, R. E., Lagus, P. L., Kothari, K. M., Wang, J. J., and Clowney, S. L., “Reciprocating Compressor Flow by Tracer Gas and Cylinder Pressure Measurement,” 1992 International Gas Research Conference.
- [10] Raymer, R., “Engine Tuning, Not Balance, is the KEY to Performance,” Gas Machinery Conference, Salt Lake City, Utah, October 6-8, 2003.
- [11] Heywood, J. and Sher, E., The Two-Stroke Cycle Engine, Taylor & Francis, 1999.
- [12] Heywood, J., Internal Combustion Engine Fundamentals, McGraw-Hill Publishing Company, 1988.

- [13] Taylor, C. F., The Internal Combustion Engine in Theory and Practice, Vol. 1, 2nd ED., MIT Press, 1985.
- [14] Blair, G. P., The Basic Design of Two-Stroke Engines, SAE International, 1990.
- [15] Blair, G. P., Design and Simulation of Two-Stroke Engines, SAE International, 1996.
- [16] Chrisman, B. M. and Bartos, J. C., “Development and Testing of an Expansion Chamber for the Reduction of NO_x Emissions in a Two-Stroke Lean Burn Gas Engine,” Gas Machinery Conference, Albuquerque, New Mexico, Oct. 4-6, 2004.
- [17] Randolph, A. L., “Methods of Processing Cylinder-Pressure Transducer Signals to Maximize Data Accuracy,” SAE Paper 900170, 1990.

8. LIST OF ACRONYMS AND ABBREVIATIONS

A/F	Air/Fuel Ratio
AGA	American Gas Association
AGA3	Gas Flow Measurement Standard
AMP	Air Manifold Pressure
BEI	Manufacturer's Trade Name for Encode Use
BHP	Brake Horsepower
BTDC	Before Top Dead Center
BTU	British Thermal Unit
COV	Coefficient of Variance
CPR	Combustion Pressure Ratio
DAS	Data Acquisition System
DOE	U.S. Department of Energy
EQ	Equivalence Ratio
FHP	Fuel Header Pressure
FIFO	First In, First Out
GMC	Gas Machinery Conference
GMRC	Gas Machinery Research Council
GMVH	Cooper Engine Model
GMVH-6	Cooper Engine Model
GMW10	Cooper Engine Model
HBA-6	Clark Engine Model
HBA-6T	Clark Engine Model
HBA8	Clark Engine Model
HP	Horsepower
HPFI™	Enginuity's High-Pressure Fuel Injection System
I/P	Current-to-Pressure Converter
IAC	Industry Advisory Committee
IMEP	Indicated Mean Effective Pressure
IRV	Instantaneous Rotational Velocity
LBSI	Lean-Burn Spark-Ignited
LHV	Lower Heating Value
mAmp	Milliamp
MMSCFD	Million of Standard Cubic Feet Per Day
MW	Megawatts
NGK	Manufacturer's Trade Name for NO _x and O ₂ sensor
NO _x	Oxides of Nitrogen
O ₂	Oxygen Molecule
OEM	Original Equipment Manufacturer
PCB	Manufacturer's Trade Name
PFP	Peak Firing Pressure
PID	Proportional-Integral-Differential
PPM	Parts Per Million
PSI	Pounds Per Square Inch

LIST OF ACRONYMS AND ABBREVIATIONS (CONT'D)

PSIA	Lb./Sq. Inch Absolute
PV	Pressure-Volume
RLM	Rod Load Monitor
RPM	Revolutions Per Minute
SCF	Standard Cubic Feet
SDCM	Strain Data Capture Module
Sdev	Standard Deviation
SwRI [®]	Southwest Research Institute [®]
TCF	Trillion Cubic Feet
TDC	Top Dead Center
TGP	Tennessee Gas Pipeline
TLA6	Clark Engine Model with Six Power Cylinders
UEGO	Universal Exhaust Gas Oxygen
V-10	10-Cylinder Engine with V Configuration